ANALYSIS OF THE ISO 9705 ROOM/CORNER TEST: SIMULATIONS, CORRELATIONS AND HEAT FLUX MEASUREMENTS

Scott Edward Dillon
University of Maryland
College Park, MD 20742

NIST

NIST-GCR-98-756

ANALYSIS OF THE ISO 9705 ROOM/CORNER TEST: SIMULATIONS, CORRELATIONS AND HEAT FLUX MEASUREMENTS

Prepared for
U.S. Department of Commerce
National Institute of Standards and Technology
Gaithersburg, MD 20899

By
Scott Edward Dillon
University of Maryland
College Park, MD 20742

August 1998

ANALYSIS OF THE ISO 9705 ROOM/CORNER TEST:

SIMULATIONS, CORRELATIONS AND HEAT FLUX MEASUREMENTS

by

Scott Edward Dillon

Thesis submitted to the Faculty of the Graduate School of the
University of Maryland, College Park in partial fulfillment
of the requirements for the degree of
Master of Science
1998

Advisory Committee:

Professor James G. Quintiere
Dr. Frederick W. Mowrer
Dr. Jose Torero

ABSTRACT

Title of Thesis:	AN ANALYSIS OF THE ISO 9705 ROOM-CORNER TEST: SIMULATIONS, CORRELATIONS AND HEAT FLUX MEASUREMENTS
Degree Candidate:	Scott Edward Dillon
Degree and Year:	Master of Science in Fire Protection Engineering, 1998
Thesis Directed by:	Professor James Quintiere Fire Protection Engineering

A simulation model is implemented in order to predict the fire performance of materials in the ISO 9705 Room-Corner Test. These materials were tested by the L S Fire Laboratories of Italy, and the data they provided is analyzed in this report. A method was established to define material properties including the heat of combustion, heat of gasification, thermal inertia, ignition temperature and the total energy released per unit area. These methods were developed from refinements in a theoretical model of ignition and in resolving time dependent effects in the Cone Calorimeter. The materials examined consist of some of the most difficult to analyze because they melt, drip, expand and de-laminate from the wall and ceiling configuration of the room-corner test. Corrections have been included in the simulation modeling to account for these effects. The correction involves reducing the total energy content per unit area

of the material to accordingly reduce its contribution as a wall-ceiling oriented element. An empirical correlation based on a linearized upward flame spread model is shown to provide excellent comparison to the flashover time in the full-scale ISO test. Accurate heat flux measurements from the ignition burner at an energy release of 100 and 300 kW were made from full-scale room-corner tests. Corrections to these heat flux measurements provide the incident heat flux from the burner fire plume and from a combination of the plume and the thermal feedback of the heated room. Detailed heat flux distributions along the walls and ceiling in the vicinity of the ignition burner are provided.

ACKNOWLEDGEMENTS

TABLE OF CONTENTS

LIST OF TABLES

LIST OF FIGURES

NOMENCLATURE

a	-	upward flame spread acceleration parameter (long burnout time)
A	-	surface area of sample
b	-	upward flame spread acceleration parameter
c	-	specific heat
d	-	sample dimension
D	-	burner dimension
g	-	acceleration due to gravity (9.807 m/s^2)
Gr	-	Grashof number
h_c	-	convection heat transfer coefficient
ΔH_C	-	effective heat of combustion
I	-	flame intermittency
k	-	thermal conductivity
kρc	-	thermal inertia
k_f	-	flame length coefficient (0.01 m^2/kW)
l	-	length (length scale for h_c calculation)
l_m	-	mean beam length
L	-	effective heat of gasification
m	-	mass
Nu	-	Nusselt number
Pr	-	Prandtl number
q	-	heat transfer
Q	-	energy
Ra	-	Rayleigh number
t	-	time
T	-	temperature
U	-	plume velocity
V	-	flame spread velocity
z	-	flame height in the Cone
Z	-	flame height/length
α	-	surface absorptivity
β	-	volumetric thermal expansion coefficient
δ	-	thickness, steel plate
Δ	-	distance, between thermocouple nodes
ε	-	emissivity
Φ	-	lateral flame spread coefficient
κ	-	absorption coefficient
ρ	-	density
σ	-	Stefan-Boltzmann constant (5.670 x 10^{-11} kW/m$^2 \cdot$K^4)
ν	-	kinematic fluid viscosity

Subscripts

0   - initial
a   - air
b   - burnout
c   - convective
cold   - incident to a cold surface
cr   - critical
eff   - effective
equil - equilibrium measurement
ext   - external
f   - flame or film (only in h_c calculation, Section 7)
fl   - fluid
fo   - flashover
h   - horizontal, flame extension
hot   - incident to a heated surface
i   - incident
ig   - ignition
inc   - through the ceramic fiber insulation
init   - initial measurement
k   - conduction
meas   - measured
min   - minimum
net   - net amount
p   - pyrolysis
pl   - plume
r   - radiation
rr   - re-radiation
R   - room
s   - surface
st   - steel
sto   - storage within the steel
v   - vaporization or vertical portion of flame length (Section 8)
∞   - ambient
peak   - at the peak energy release rate
peak avg.   - averaged over 80% above of the peak energy release rate
overall avg. - average of the overall properties during steady, sustained burning

Superscripts

(X'') - per unit area
$(\dot{X})$ - per unit time
$(\overline{X})$ - average value

1. INTRODUCTION

There are many different aspects of a fire event that can affect the final outcome. One means of expressing the overall hazard associated with a particular fire scenario is in terms of the size of the fire. The primary mechanism by which fires grow from a small incipient fire to a large, possibly fully involved, one is through the ignition and flame spread across the various fuels that are available. When attempting to determine or predict the growth rate potential and overall fire size for a space, the flame spread over the furnishings and interior finish materials will become significant. The fire growth of a fire can be considered to be a critical event in which the outcome can be based on several parameters. One method for determining the fire growth potential of interior finish materials is by the room-corner test. Unlike most other tests, materials in the room-corner test are exposed to a full-scale fire scenario: the materials are mounted in an orientation that is representative of there use in real situations and the ignition source is more consistent with realistic forms of ignition.

1.1 Room-Corner Tests

Several room-corner test protocols are currently in use and are listed by the American Society of Testing and Materials (ASTM), the National Fire Protection Association (NFPA), the Uniform Building Code (UBC) and the International Standards Organization (ISO). The tests arrangements and procedures are all similar, but have some differences that can significantly affect the performance of the sample material. These differences include the size, location and energy release rate of the ignition burner as well as the sample mounting.

1

The test method addressed in this analysis is the ISO 9705 Full-Scale Room Fire Test for Surface Products [22]or more simply the Room-Corner Test. The choice of this method was motivated by the fact that the ISO 9705 test is an internationally recognized standard and the availability of test data and a full-scale test facility.

The ISO 9705 test has the following criteria and can be seen in Figure 1.1:

- Room: 2.4 m x 3.6 m x 2.4 m high.

- Door on Short Wall: 2.0 m x 0.8 m wide.

- Ignition Burner: 17 cm x 17 cm square sand burner, top surface 30

                       cm above the floor, propane fuel.

- Burner Location: Corner, in contact with both walls.

- Burner Output: 100 kW for 10 minutes followed by 300 kW for an

                       additional 10 minutes.

- Material Mounting: On the 3 walls opposite the doorway and on the

                       ceiling if desired.

One useful way of ranking materials and determining the fire growth potential for a particular material is by the time to flashover under the conditions specified by the test standard. Flashover is an altogether complex process and is associated with different characteristics of the fire compartment: heat flux to the floor of approximately 20 kW/m^2, an upper layer temperature of 500 to 600 °C and flames emerging from the doorway [11]. Based on the standard room geometry of the test method, flashover conditions typically coincide with an

2

energy release rate of about 1,000 kW. It must be recognized that the presence or absence of the sample material on the ceiling of the room can be one of the most significant factors as to whether or not flashover occurs.
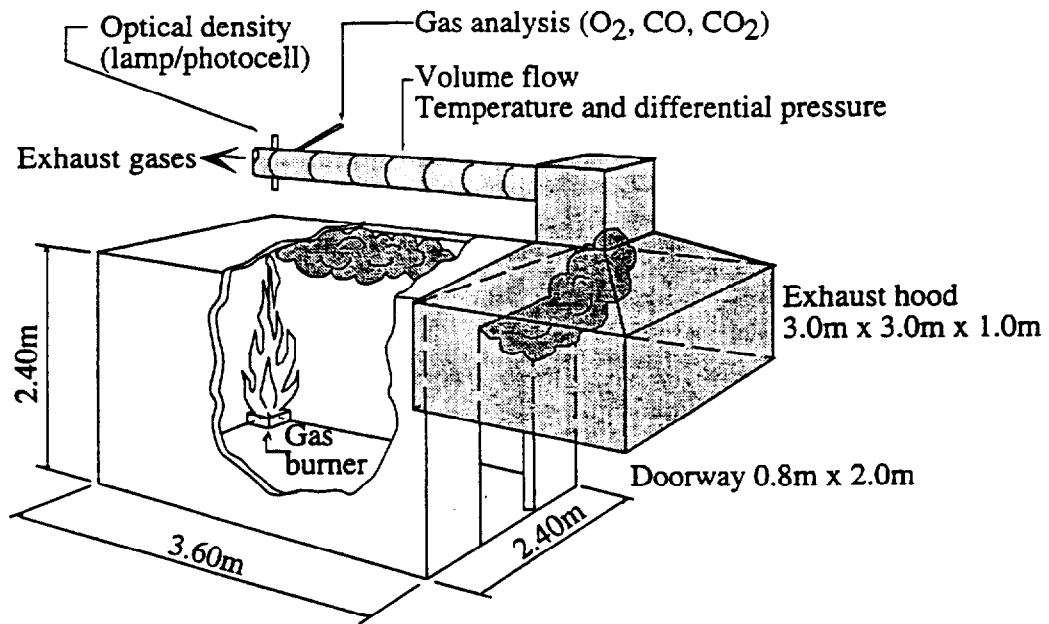
Figure 1. 1: Schematic Drawing of the ISO 9705 Room-Corner Test [49].

1.2 Modeling

A mathematical model to predict the fire growth of materials in a room-corner test has been developed by Quintiere [36]. The model utilizes derived material fire properties and simple equations that govern the physics of ignition and flame spread to predict the time dependent area of burning, upper gas layer temperature and energy release rate for a material in the room-corner test.

A primary difference between the different room-corner test methods is the ignition source. Test results indicate that the energy release rate of the burner, the associated heat flux to the sample material and the duration of the exposure influence the performance of the material. This is particularly true for thin materials and materials with a short burning duration. By adjusting the exposure conditions and material fire properties, the model can be used to indicate how sensitive a material is to producing flashover conditions. The model allows the performance of materials with different ignition sources and room geometries to be predicted without performing many expensive full-scale experiments. The model can also be adapted to wall fires and open pool fires, but will be confined to the prescriptions of the ISO standard for this analysis.

The materials evaluated represent traditional materials as well as materials that could be a potential challenge to the model. Previous analyses [23, 36, 37] have shown that charring materials like wood are typically well predicted by the model. However, thermoplastic materials can melt, deform and drip from the wall and ceiling which presents a significant modeling complexity. The series of materials evaluated in this analysis represent a wide range of realistic materials which should indicate the strengths and weaknesses of the model.

In order to analyze the performance of the materials, a systematic method will be developed for determining the material fire properties required by the model. This method will be based on small-scale test results like the Cone Calorimeter [2] and the LIFT [1] and medium-scale test methods like Roland [51]. Although the procedure for deriving the properties is not perfect for every material, it will be applied to each

4

material as a first step in developing a uniform system. Specific areas where the method breaks down will be indicated, analyzed. and explained.

Due to the critical nature of some materials, an empirical correlation by Cleary and Quintiere [9] will be applied to the materials. Using the same material properties used for modeling along with information regarding the ignition source, the flashover potential for the materials will be determined and presented in a format that allows materials to be compared.

Several aspects of the current model can be improved. Various studies have been conducted in order to examine the heat flux from controlled fires to vertical walls and corners [7, 23, 26, 31, 52, 53]. This heat flux information has been found to be very important to the performance of materials in the room-corner scenario and more generally for wall flame spread. More detailed experiments are needed in this area, especially for the exposure of materials in accordance with the standard test methods. It is recognized that theoretical determinations of these heat fluxes is beyond the current state of the art and experimentally based correlations will have to be utilized.

The incident heat flux to materials in the room-corner test is approximated in the model. In order to better understand the actual exposure conditions, full-scale heat flux measurements have been made and detailed heat flux profiles have been created as a part of this research. In addition, flame heights for the ignition burner in the corner have been determined. These factors will provide a tremendous amount of knowledge to what is currently known about the room-corner test and will enable Quintiere's model to be improved.

In response to the need for improved performance predictions, this research will attempt to provide a systematic method for determining material fire properties, assess the accuracy of a fire growth model for the room-corner test and determine aspects of the standard test that can be used to improve the current model.

2. DESCRIPTION OF MATERIALS

Thirteen materials were provided to the University of Maryland, for prediction of their performance in the full-scale room-corner test using Quintiere's fire growth model [36]. These materials are the same as the ones tested in the Cone Calorimeter [1] and Roland apparatus [51] at the L. S. Fire Laboratories (LSF), Moutano, Italy. Each material was tested in the Cone five times at four different external heat flux levels—25, 35, 40 and 50 kW/m^2—for a total of twenty tests for each material. These same materials were also tested using the ISO 9705 Room-Corner test protocol at the Swedish National Testing and Research Institute, Boras, Sweden [49]. These materials are listed below—the number preceding each material refers to the LSF designation for each material and will be used interchangeably with the full name. A brief description of the material properties and the manner in which the samples were mounted for the full-scale room-corner test are provided. All of the materials were conditioned at 20 ± 5 °C prior to the full-scale tests. Photographs of the samples are also provided.

R 4.01 Fire Retarded Chipboard

- Thickness: 12 mm

- Density: 805 kg/m^3

- Moisture content: 6.8 %

- Mounting: Nailed to the light weight concrete walls and ceiling.

4.01
F.R. Chipboard
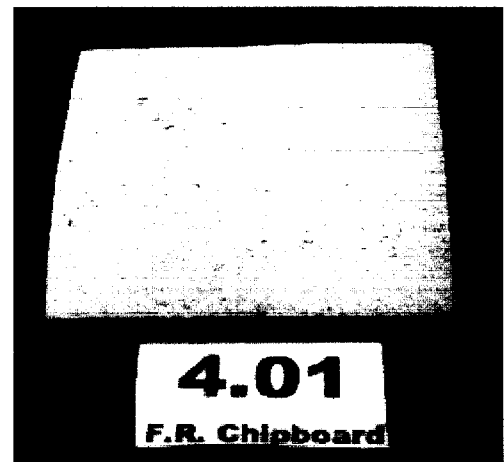
R 4.02 Paper Faced Gypsum Wallboard

- Thickness: 12.5 mm

- Density: 720 kg/m^3

- Mounting: Nailed to the light weight

  concrete walls and ceiling.
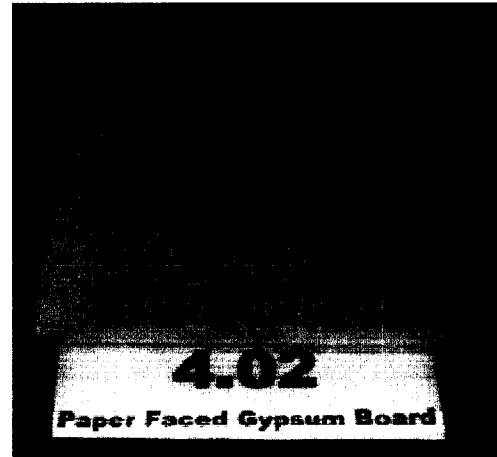
R 4.03 Polyurethane Foam Panel with Aluminum Paper Facing

- Thickness: 41 mm

- Density: 38 kg/m^3

- Area weight: 2.03 kg/m^2

- Mounting: Glued to a non-

  combustible board called "Promatek

  H", density 870 kg/m^3, with a water

  based contact adhesive called "Casco
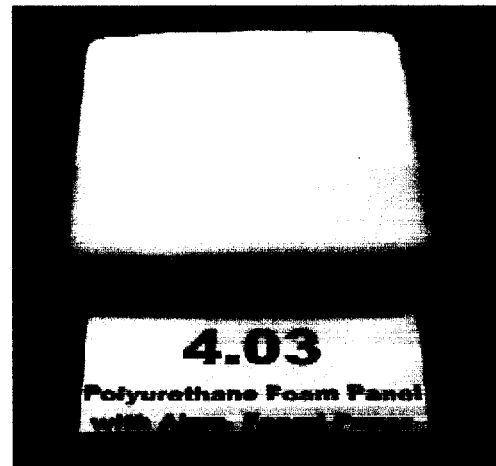
3880". The non-combustible boards were nailed to the light weight concrete

walls and ceiling before the polyurethane foam panels were glued.

R 4.04 Polyurethane Foam Panel with Paper Facing

- Thickness: 40 mm

- Density: 38 kg/m^3

- The properties for this material were used to predict the performance of the polyurethane foam panel with aluminum facing, R 4.03, due to the problems encountered in

extrapolating adequate material properties (see Section 3).
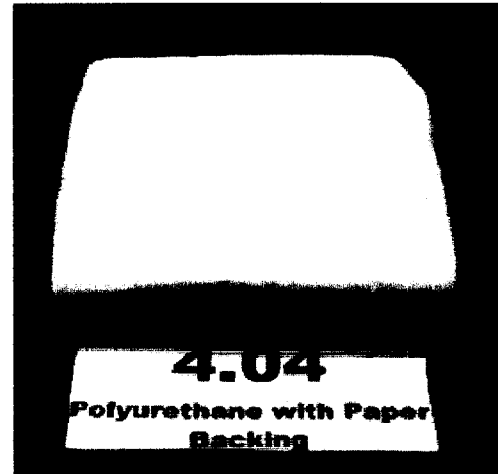
R 4.05 Fire Retarded, Extruded Polystyrene Board (40 mm)

- Thickness: 40 mm

- Density: 33 kg/m^3

- Mounting: Glued to a non-combustible board called "Promatek H", density 870 kg/m^3, with a water based contact adhesive called "Casco 3880". The non-combustible boards

were nailed to the light weight concrete walls and ceiling before the polystyrene boards were glued.
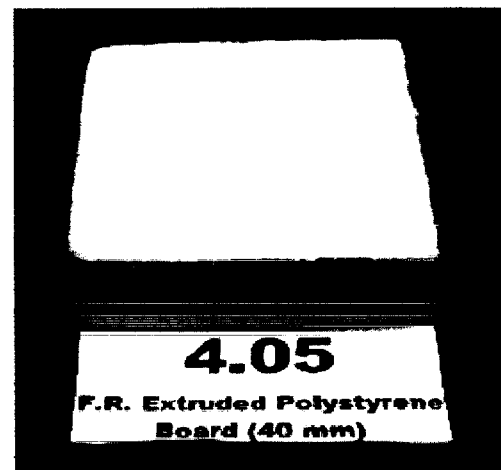
R 4.06 Clear Acrylic Glazing

- Thickness: 3 mm

- Density: 1150 kg/m^3

- Mounting: Screwed to a frame of light steel profiles spaced 40 mm from the light weight concrete walls and ceiling.
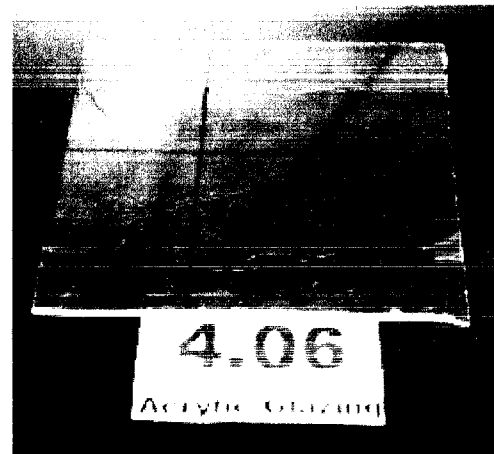
R 4.07 Fire Retarded PVC

- Thickness: 3 mm

- Density: 1505 kg/m^3

- Mounting: Screwed to a frame of light steel profiles spaced 40 mm from the concrete walls and ceiling.
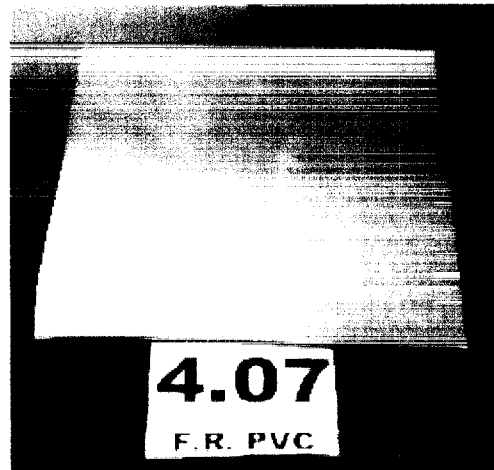
R 4.08 3-Layered Clear, Fire Retarded Polycarbonate Panel

- Thickness: 16 mm

- Density: 1200 kg/m^3

- Area weight: 2.9 kg/m^2

- Mounting: Screwed to a frame of light steel profiles spaced 40 mm from the light weight concrete walls and ceiling.
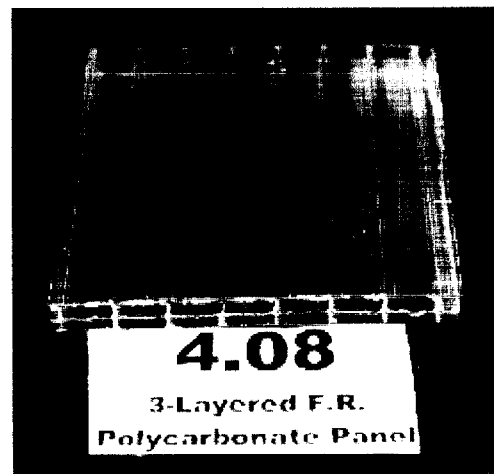
R 4.09 Varnished Massive Timber Paneling

- Thickness: 9 mm

- Area weight: 3.4 kg/m2

- Moisture content: 9.6 %

- Mounting: Nailed to the light weight

  concrete walls and ceiling.
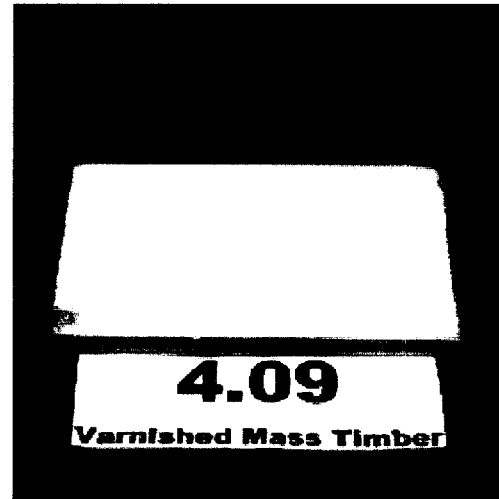
R 4.10 Fire Retarded Plywood

- Thickness: 15 mm

- Density: 460 kg/m^3

- Moisture content: 9.8 %

- Mounting: Nailed to the light weight

  concrete walls and ceiling.
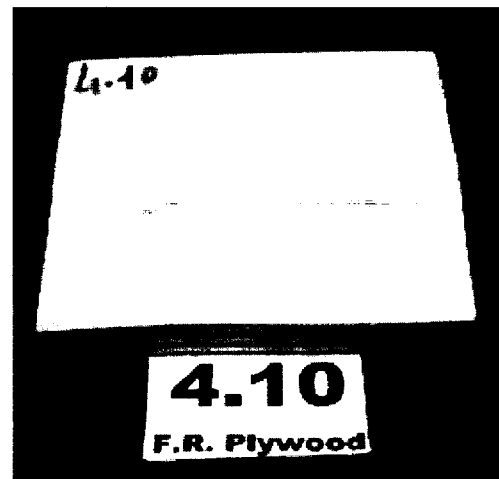
R 4.11 Normal, Untreated Plywood

- Thickness: 15 mm .

- Density: 440 kg/m^3

- Moisture Content: 11.3 %

- Mounting: Plywood was nailed to

  the light weight concrete walls and

  ceiling.
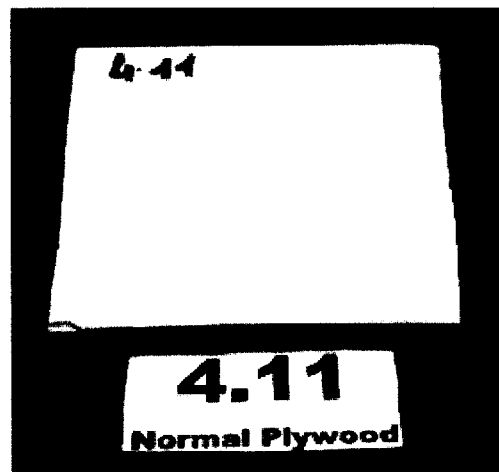
R 4.20 Fire Retarded, Expanded Polystyrene Board (40 mm)

- Thickness: 40 mm

- Density: 30 kg/m^3
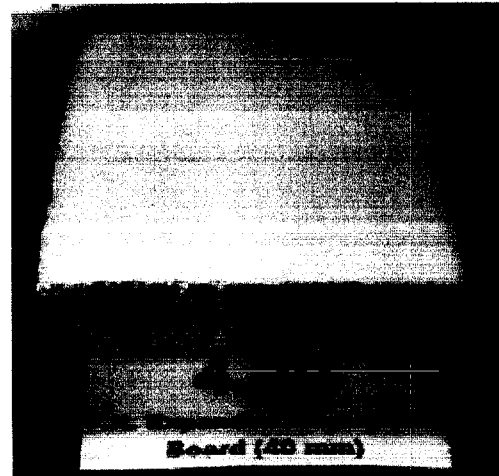
- Mounting: Glued to a non-combustible board called "Promatek H", density 870 kg/m^3, with a water based contact adhesive called "Casco 3880". The non-combustible boards were nailed to the light weight concrete walls and ceiling before the polystyrene boards were glued.

R 4.21 Fire Retarded, Expanded Polystyrene Board (80 mm)

- Thickness: 80 mm

- Density: 17 kg/m^3
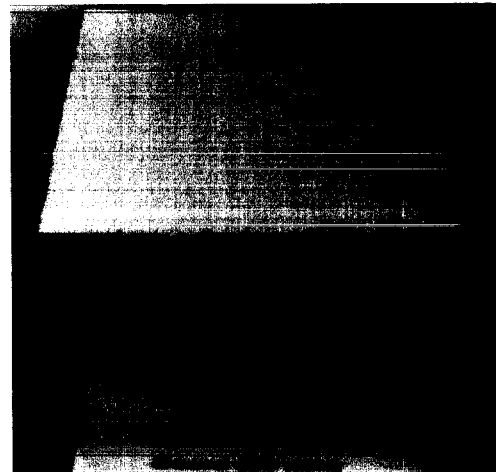
- Mounting: Glued to a non combustible board called "Promatek H", density 870 kg/m^3, with a water based contact adhesive called "Casco 3880". The non combustible boards were nailed to the light weight concrete walls and ceiling before the polystyrene boards were glued.

3. DETERMINING MATERIAL PROPERTIES

The material properties required to run the fire growth model are typically

derived from data provided by the Cone Calorimeter (ASTM E-1354 [2], ISO 5660) and

the Lateral Ignition and Flame Spread Test (LIFT, ASTM E-1321 [1], ISO 5658).

However, for this analysis the flame spread data was provided by the Roland apparatus

instead of the LIFT [46]. These modeling properties are listed in Table 3.1.

Table 3. 1: Material Modeling Properties.

	Material Property	Symbol	Test Method
1.	Ignition Temperature	T_{ig}	Cone, LIFT or Roland
2.	Minimum Temperature for Lateral Flame Spread	$T_{s, min}$	LIFT or Roland
3.	Thermal Inertia	$k\rho c$	Cone or LIFT
4.	Lateral Flame Spread Parameter	Φ	LIFT or Roland
5.	Effective Heat of Combustion	ΔH_C	Cone
6.	Effective Heat of Gasification	L	Cone
7.	Total Energy per Unit Area	Q''	Cone

Previous analyses of the performance of materials have used inconsistent methods for

determining the material properties. Therefore a more systematic method for accurately

determining these properties will be developed. This systematic method will then be

applied to all of the materials and used to predict the performance in the full-scale

room/corner test.

13

3.1 Ignition Properties

The ignition properties for the LSF materials were determined by Dillon, Kim and Quintiere [10] based on the Cone Calorimeter test results. In general the time to ignition (t_{ig}) can be expressed as

$$t_{ig} = C \cdot k\rho c \frac{(T_{ig} - T_\infty)^2}{(\dot{q}_i'' - \dot{q}_{cr}'')^2} \tag{3.1}$$

where T_∞ is the ambient temperature (K), $\dot{q}''_i$ is the incident radiant heat flux (kW/m^2), $\dot{q}''_{cr}$ is the critical heat flux for ignition (kW/m^2) and C depends on $\dot{q}''_i$. For the analysis by Dillon $et\ al.$, C was taken to be $\pi/4$ for high incident heat flux values. The critical heat flux for ignition can be expressed as

$$\dot{q}_{cr}'' = \sigma(T_{ig}^4 - T_\infty^4) + h_c(T_{ig} - T_\infty) \tag{3.2}$$

where σ is the Stefan-Boltzmann constant (5.670 x 10^{-11} kW/m$^2\cdot$K^4) and h_c is the convective heat transfer coefficient (kW/m$^2\cdot$K).

A plot of the inverse square root of the ignition times ($t_{ig}^{-1/2}$) with respect to the incident heat flux from the Cone is used to determine T_{ig} and $k\rho c$ (see Figure 3.1). The critical heat flux is the point at which t_{ig} is infinite and therefore $t_{ig}^{-1/2}$ is equal to 0. A value for $\dot{q}''_{cr}$ is determined by extrapolating the data at low heat fluxes as shown in Figure 3.1. The critical heat flux for each material is presented in Table 3.2. Using an h_c value of 10 kW/m$^2\cdot$K for the Cone, the critical heat flux is used in Equation 3.2 to calculate T_{ig}. The slope of the linear fit through the data points equals

$$\frac{1}{\left(\dfrac{\pi}{4} \cdot k\rho c\right)^{1/2} \left(T_{ig} - T_\infty\right)}$$

and is used to calculate $k\rho c$. The ignition data figures for all of the LSF materials are presented by Dillon *et al.*
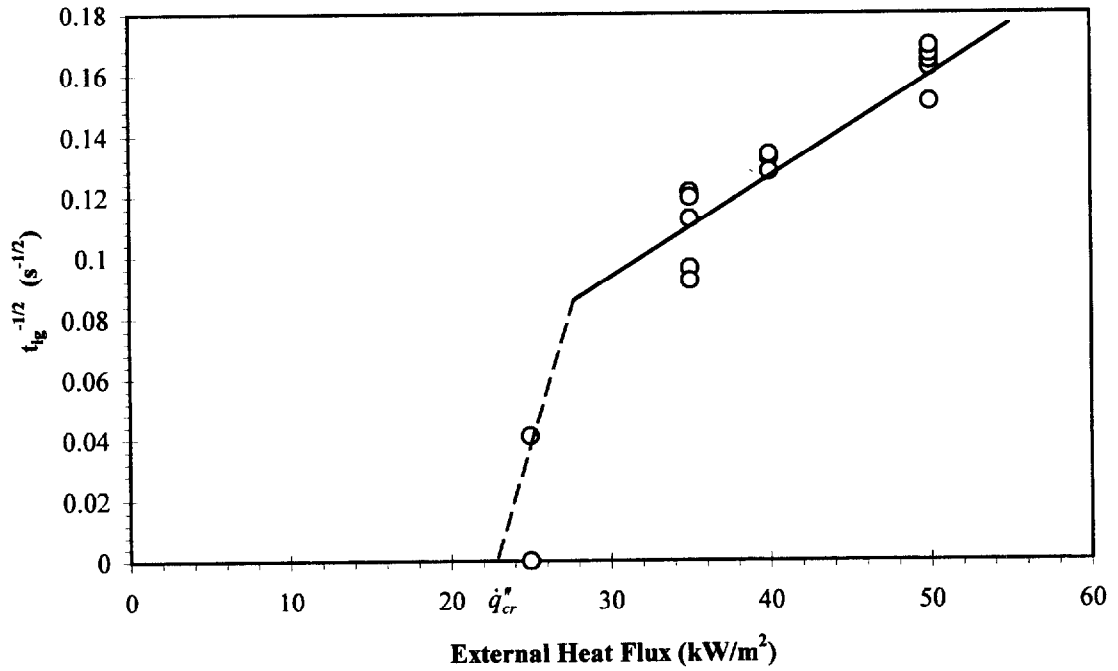
Figure 3. 1: Typical Interpretive Plot of Ignition Data in Order to Derive Properties: R 4.21, Fire Retarded Expanded Polystyrene Board.

Table 3. 2: Estimated Critical Heat Flux for Ignition

Material	$\dot{q}_{cr}''$
R 4.01, FR. Chipboard	25
R 4.02, Gypsum	26
R 4.03, PU/Alum.*	----
R 4.04, PU/Paper	6
R 4.05, Ext. PS40	7
R 4.06, Acrylic	4
R 4.07, FR. PVC	16
R 4.08, 3-Layer PC	24
R 4.09, Mass Timber	10
R 4.10, FR. Plywood	22
R 4.11, Plywood	8
R 4.20, Exp. PS40	8
R 4.21, Exp. PS80	23

3.2 Flame Spread Properties

The flame spread data for the LSF materials were also determined by Dillon *et al.* [10] and were obtained by using the Roland apparatus instead of the LIFT. A typical flame spread test using the Roland apparatus can be seen in Figure 3.2. The Equation for the flame spread velocity, V, is

$$V = \frac{\Phi}{k\rho c\left(T_{ig} - T_s\right)^2}$$

(3.3)

where Φ is the lateral flame spread parameter (kW^2/m^3) and T_s the surface temperature of the material caused by the incident heat flux (K). The location on the surface of the material at which lateral flame spread ceases can be used to determine $T_{s, min}$. The lateral flame spread parameter can then be calculated using Equation 3.3.
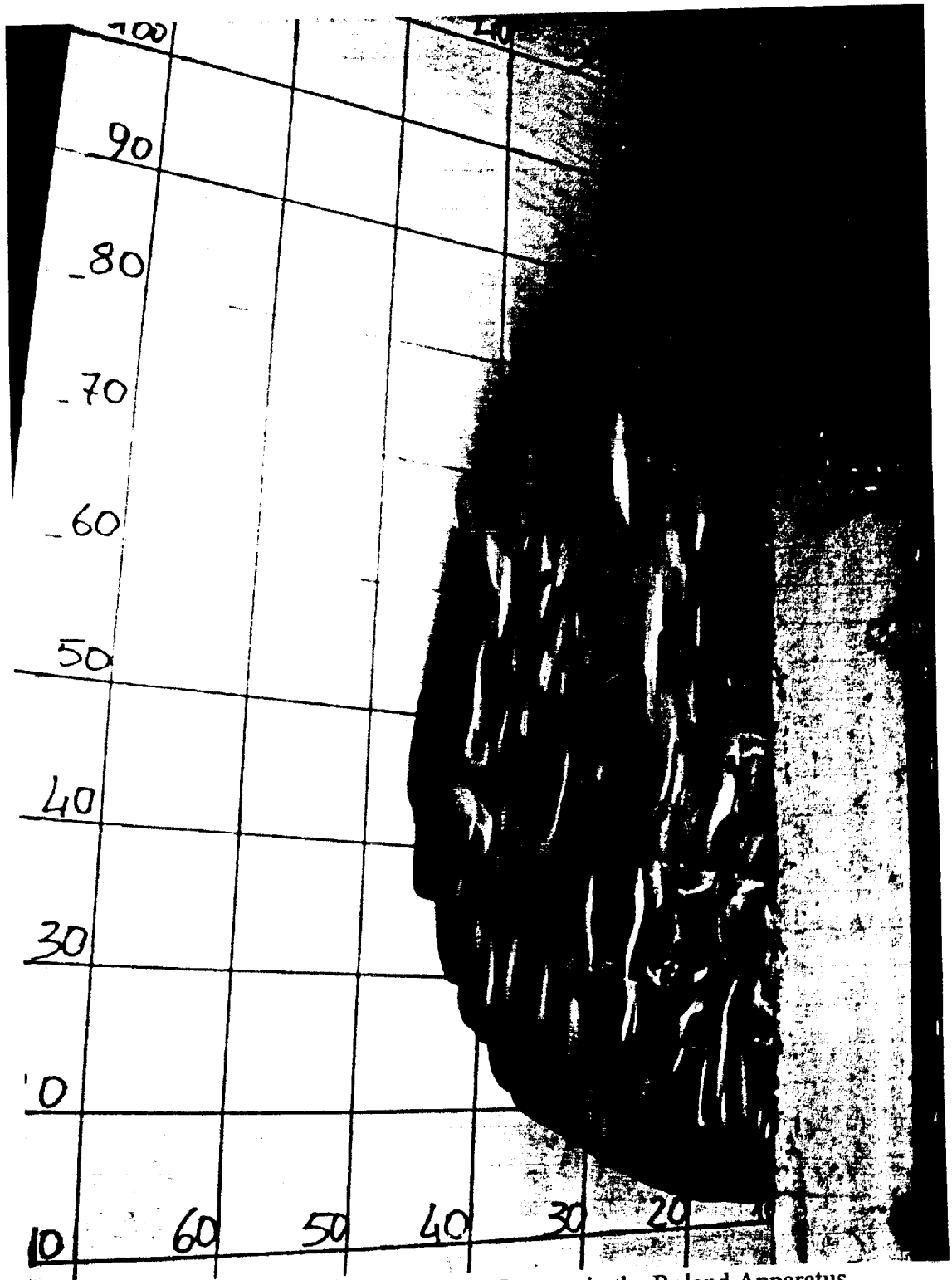
Figure 3. 2: A Typical Burning Process in the Roland Apparatus

17

The ignition and flame spread properties were derived by the methods presented in Sections 3.1 and 3.2 and are presented in Table 3.3.

Table 3. 3: Ignition and Flame Spread Properties of the LSF Materials.

Material	T_{ig} (°C)	$T_{s,min}$ (°C)	$k\rho c$ [(kW/m^{2}K)^{2}s]	Φ (kW^2/m^3)
R 4.01, FR. Chipboard	505	507	4.024	0.0
R 4.02, Gypsum	515	517	0.549	0.0
R 4.03, PU/Alum.*	---	---	---	0.0
R 4.04, PU/Paper	250	77	0.199	8.7
R 4.05, Ext. PS40	275	77	1.983	1.2
R 4.06, Acrylic	195	195	2.957	---
R 4.07, FR. PVC	415	352	1.306	0.2
R 4.08, 3-Layer PC	495	167	1.472	0.0
R 4.09, Mass Timber	330	77	0.530	6.9
R 4.10, FR. Plywood	480	197	0.105	0.7
R 4.11, Plywood	290	147	0.633	2.2
R 4.20, Exp. PS40	295	77	1.594	4.2
R 4.21, Exp. PS80	490	77	0.557	7.1

* Material properties could not be extrapolated from the test data

3.3 Heat of Combustion (ΔH_C)

3.3.1 Definition

The enthalpy of combustion or heat of combustion (ΔH_C) is a constant material property, representing the total amount of energy released by a unit mass of fuel (kJ/g) when it is completely oxidized through the combustion process. Heat of combustion values can be determined using an oxygen bomb calorimeter which forces all of the material to combust in a pure oxygen atmosphere while the vessel temperature and specimen mass loss are carefully monitored. Heat losses from the system are

18

minimized so that the heat release can be accurately determined by the temperature rise. The gross heat of combustion, $\Delta H_{C, gross}$, can then be calculated by dividing the total heat release by the total specimen mass loss. Gross heat of combustion values for many materials are presented by Tewarson [47]. However, complex materials like wood and composites like gypsum wallboard burning in more realistic conditions will not exhibit the gross heat of combustion values obtained in the oxygen bomb. Char formation, moisture evaporation and other complex effects will cause a reduced $\Delta H_{C, gross}$ to be observed. Therefore an effective heat of combustion, $\Delta H_{C, eff}$, which better represents the material burning in actual conditions needs to be determined. This effective value (simply referred to as ΔH_C for convenience) can be used to determine the energy release rate per unit area from a material based on the mass loss rate by:

$$\dot{Q}'' = \Delta H_C \cdot \dot{m}'' \tag{3.4}$$

where $\dot{Q}''$ is the energy release rate per unit area (kW/m^2) and $\dot{m}''$ is the mass loss rate per unit area (g/s·m^2). In this definition of the effective heat of combustion, $\dot{m}''$ of a burning material may not represent the mass of the fuel alone and can represent a loss of moisture or other products. This can result in complications in the determination of suitable values for predicting performance.

3.3.2 Determining ΔH_C

The time-varying and average effective heat of combustion were measured by LSF using the Cone Calorimeter. Each material was tested five times at each of the following incident heat flux levels: 25, 35, 40 and 50 kW/m^2. The Cone Calorimeter standard [2] specifies the time-varying heat of combustion value to be calculated by

19

$$\Delta H_C(t) = \frac{\dot{Q}''(t)}{\dot{m}''(t)}$$

where $\dot{Q}''(t)$ and $\dot{m}''(t)$ are the energy release rate and mass loss rate per unit area at time t. Similarly, the average heat of combustion is calculated by

$$\Delta H_C = \frac{Q}{\Delta m} \tag{3.5}$$

where Q is the total energy released during the test and Δm is the total specimen mass loss.

Because ΔH_C is typically considered to be a constant material property, it should not vary with temperature, burning rate or incident heat flux. Nevertheless, the Cone data indicates that the measured heat of combustion values were not constant with respect to time, and in some cases varied significantly throughout the test (see Figure 3.3). These fluctuations are most likely due to complex burning effects and inaccuracies in the oxygen consumption calorimetry method used to determine the values. Therefore three different methods will be utilized for determining constant effective heat of combustion values from the Cone Calorimeter data: based on (1) the peak energy release rate, (2) an average energy release rate around the peak and (3) the overall energy released during the test. Examples of these three energy release rates are presented in Figure 3.4.
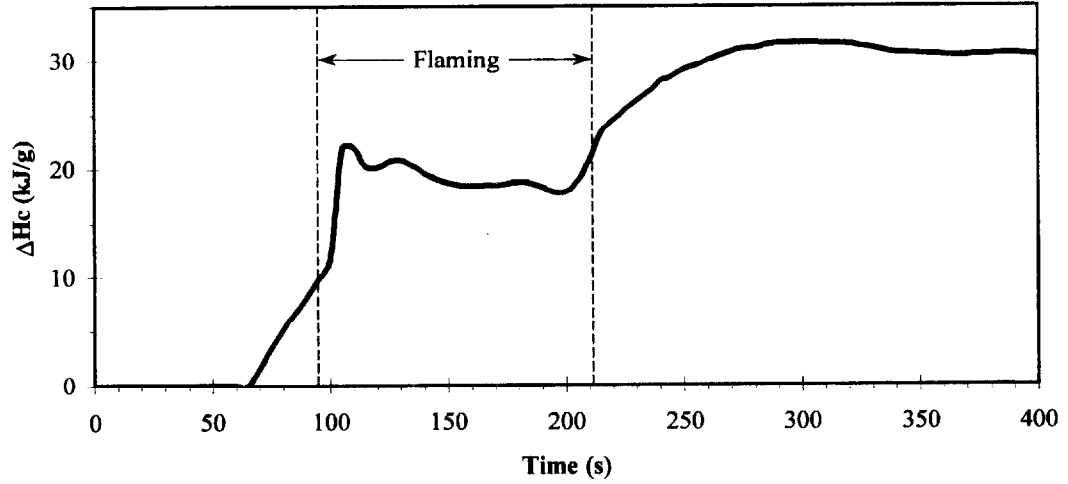
Figure 3. 3: Example of Time-Varying Heat of Combustion Measured in the Cone Calorimeter: R 4.08, 3-Layer Polycarbonate Panel at 50 kW/m^2 in the Cone Calorimeter.
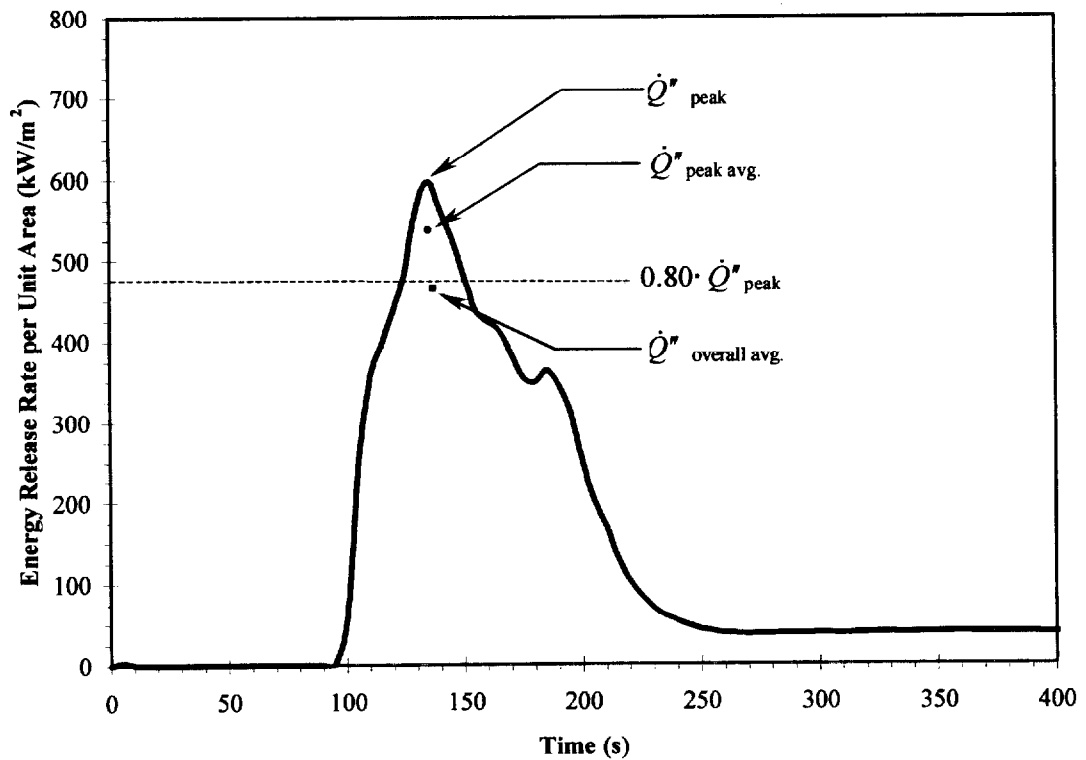
Figure 3. 4: Example of Peak, Peak Average and Overall Average Energy Release Rates per Unit Area Measured in the Cone Calorimeter: R 4.08 at 50 kW/m^2 in the Cone.

21

Due to the fact that not all of the samples ignited or exhibited continuous flaming, only the test data associated with ignition and sustained burning were used to determine the effective ΔH_C values. In a few tests the LSF data reports ignition of a sample, but inspection of the energy release rate versus time graphs clearly indicated that actual sustained flaming did not occur. Data from these types of tests will be omitted from the determination of the heat of combustion values.

Examples of $\Delta H_{C, peak}$, $\Delta H_{C, peak\, avg.}$ and $\Delta H_{C, overall\, avg.}$ values are shown graphically in Figure 3.5 and the three effective values for each material are presented in Table 3.4. Theoretically all three of these values should be identical, and as the table indicates there is reasonably good agreement between the values. The three methods for determining ΔH_C are explained below.

3.3.2.1 Peak Rate of Energy Release ($\Delta H_{C, peak}$)

For each Cone test in which the material ignited, a peak or maximum rate of energy release ($\dot{Q}''_{peak}$) occurs (see Figure 3.4). A heat of combustion value can be determined which directly coincides with the time at which the peak energy release rate occurs (see Figure 3.5). This "peak" value does not represent the maximum heat of combustion that was measured, but in fact represents the heat of combustion value associated with the peak energy releases rate.

All of the "peak" heat of combustion values measured for a particular material can then be averaged to determine an average, $\overline{\Delta H_{C,\, peak}}$, value. When plotted with respect to the external heat flux, the average value represents a horizontal "best-fit" line through the peak value data which can be seen in Figure 3.6. Figures for all of the

22

materials are presented by Dillon *et al.* [10]. These average heat of combustion values are listed in Table 3.4. This average peak heat of combustion value can be used in Equation 3.4 to determine the typical peak energy release rate associated with a material.
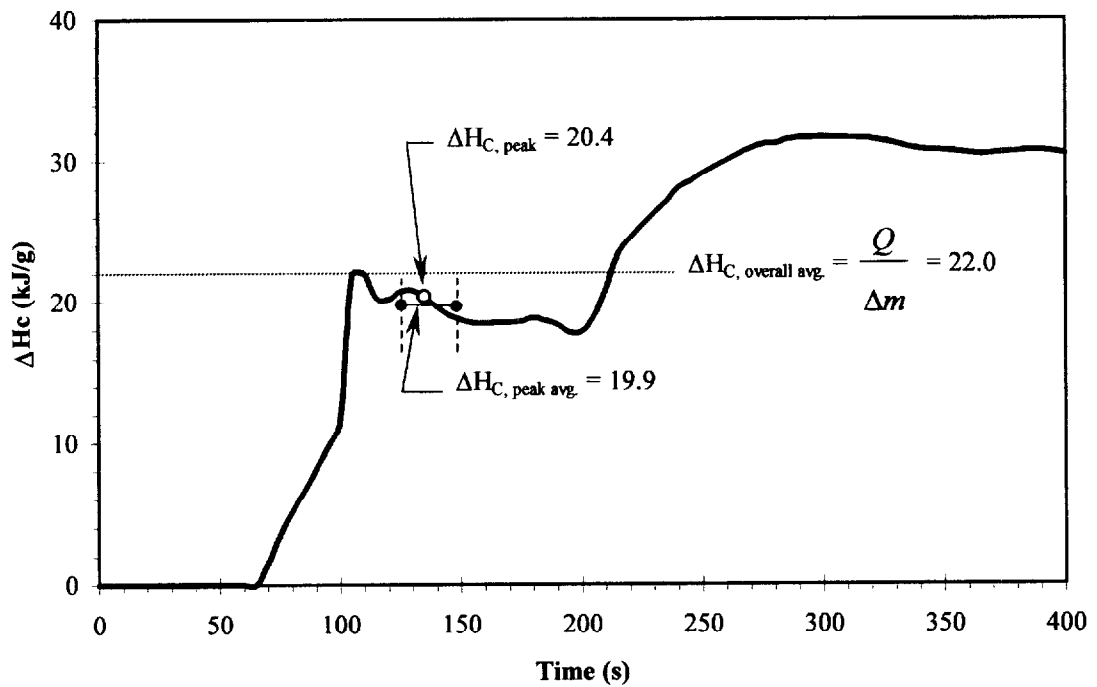
Figure 3. 5: Method of Determining the Peak, Peak Average and Overall Average Heat of Combustion Values: R 4.08, 3-Layer Polycarbonate Panel at 50 kW/m^2 in the Cone Calorimeter.

3.3.2.2 Average Rate of Energy Release ($\Delta H_{C, peak\ avg.}$)

Another method of using the peak energy release rate as a basis for determining the effective heat of combustion is to take an average energy release rate per unit area around the peak value. For this analysis, it is estimated that an average peak energy

23

release rate occurs approximately 20% below the peak value. Therefore, the $\dot{Q}''_{\text{peak avg}}$ shown in Figure 3.4 is an integrated average of the measured energy release rates above 80% of the peak value. The "peak average" value is intended to represent an energy release rate that is more consistent with steady burning as opposed to an instantaneous maximum value. This averaging method reduces the effects of a sudden, possibly uncharacteristic spike in the energy release rate and smoothes the data while still taking into account the most intense burning of the material.

The peak average heat of combustion, $\Delta H_{C,\,peak\,avg.}$, is taken to be a numerical average of the measured heat of combustion values over the same time interval that the energy release rate is averaged. The time period over which the heat of combustion values are averaged is illustrated in Figure 3.5. An average value, $\overline{\Delta H_{C,\,peak\,avg.}}$, is calculated to be a numerical average of the individual peak average values from each test.
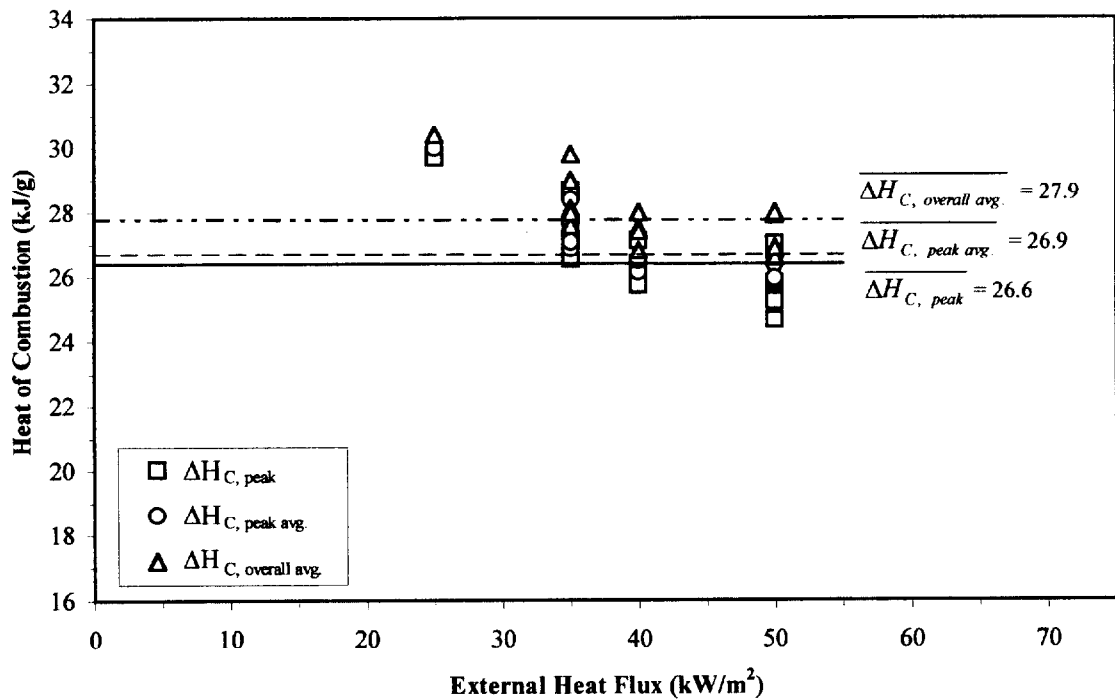
Figure 3. 6: Example of a Typical Average Heat of Combustion ($\overline{\Delta H_C}$)
Determination: R 4.08 at 50 kW/m^2.

3.3.2.3 Overall Energy Release ($\Delta H_{C, \, overall \, avg.}$)

The overall heat of combustion values, $\Delta H_{C, \, overall \, avg.}$, were calculated by LSF by

dividing the total heat evolved from each sample, Q, by the total specimen mass loss,

Δm, as in Equation 3.5. This is the typical method of determining an effective heat of

combustion value by the Cone Calorimeter test standard [2]. This "overall average"

value represents an average of the burning characteristics over the entire test duration.

As with the previous two methods, the average overall value, $\overline{\Delta H_{C, \, overall \, avg.}}$, for

a particular material is determined by taking the numerical average of the values

calculated from each Cone test.

Table 3. 4: Average, Effective Heat of Combustion (ΔH_c) Values Calculated by Three Methods.

Material	$\overline{\Delta H}_{C,\ peak}$ (kJ/g)	$\overline{\Delta H}_{C,\ peak\ avg.}$ (kJ/g)	$\overline{\Delta H}_{C,\ overall\ avg.}$ (kJ/g)
R 4.01, FR. Chipboard	9.6	9.2	7.9
R 4.02, Gypsum	6.7	6.4	3.2
R 4.03, PU/Alum.	16.3	16.3	18.2
R 4.04, PU/Paper	19.3	18.9	18.0
R 4.05, Ext. PS40	28.5	27.8	28.2
R 4.06, Acrylic	24.2	24.1	24.0
R 4.07, FR. PVC	10.2	9.9	6.8
R 4.08, 3-Layer PC	19.5	19.5	21.5
R 4.09, Mass Timber	17.3	16.3	15.7
R 4.10, FR. Plywood	11.6	11.2	10.3
R 4.11, Plywood	12.1	11.9	10.8
R 4.20, Exp. PS40	27.4	27.5	27.8
R 4.21, Exp. PS80	26.6	26.9	27.9

3.4 Heat of Gasification (L)

3.4.1 Definition

When exposed to an incident heat flux, materials will vaporize at a certain rate. The rate of this vaporization can be expressed in terms of the mass loss rate per unit area of material ($\dot{m}''$) and is dependent on the magnitude of the heat flux. The heat of gasification (L) value is an effective property that describes the energy required to produce the fuel volatiles per unit mass of the material and is typically expressed in the units kJ/g. The effective L value represents the average effects of vaporization of the fuel and does not include transient burning effects. Typical heat of gasification values have been determined by Tewarson [47].

26

The burning of a material is a relatively complex and unsteady process. However, a constant, steady burning rate per unit area can be approximated using constant net heat flux and heat of gasification values:

$$\dot{m}'' = \frac{\dot{q}''_{net}}{L} \qquad (3.6)$$

where $\dot{q}''_{net}$ is the net heat flux to the material (kW/m^2). This approximation assumes that at ignition (t_{ig}) the burning rate becomes $\dot{q}''_{net}/L$ and at the burnout time (t_b) it drops to zero. This burning rate approximation is illustrated in Figure 3.7, where the area under the predicted curve is equivalent to the area under the experimental curve. The predicted ignition time in the figure is approximated using the following expression:

$$t_{ig} = \frac{\pi}{4} \cdot k\rho c \frac{(T_{ig} - T_\infty)^2}{(\dot{q}''_{net})^2}$$

and the burnout time is approximated by

$$t_b = \frac{L}{\Delta H_C} \frac{Q''}{\dot{q}''_{net}}$$

where Q'' is the total energy per square meter of material (see Section 3.5). Therefore in order to estimate the steady burning rate of materials, an effective heat of gasification value needs to be determined.
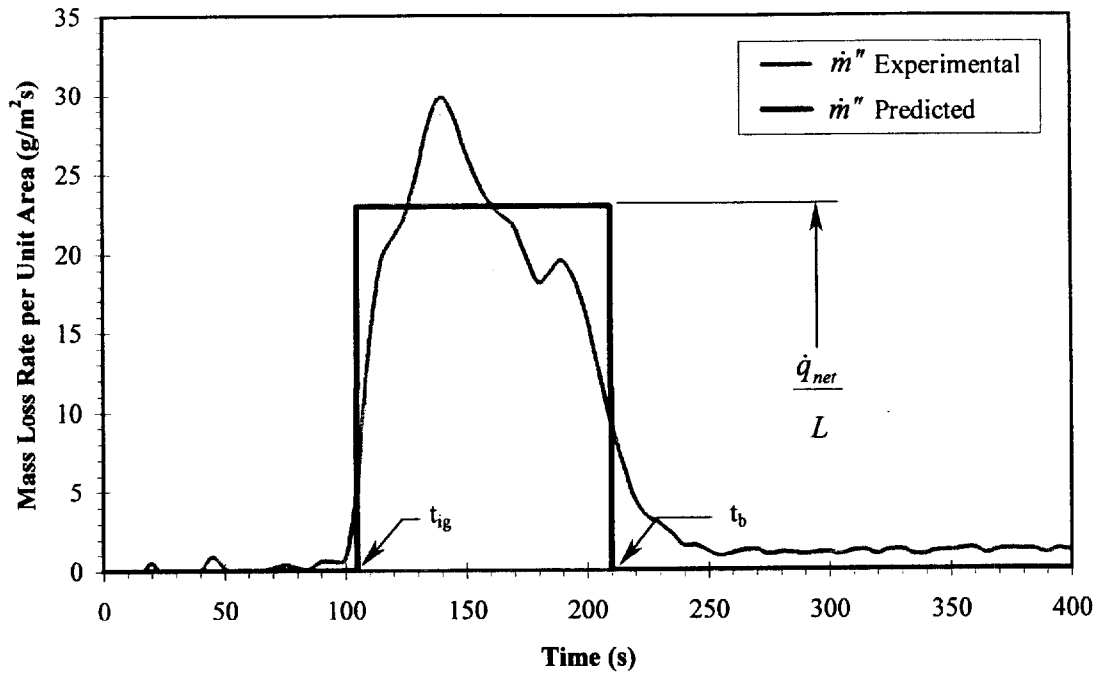
Figure 3. 7: Example of a Typical Burning Rate per Unit Area ($\dot{m}''$) Prediction: R 4.08, 3-Layer Polycarbonate Panel at 50 kW/m² in the Cone Calorimeter.

Using mass loss rate data from the Cone Calorimeter, estimations of the heat of gasification can be made. This effective L value can then be used to predict the rate of burning of a material over a range of external heat flux values.

The heat of gasification also allows the energy release rate of a material to be predicted. Equation 3.4 indicates that the energy release rate per unit area can be determined by multiplying the mass loss rate per unit area by the heat of combustion thereby allowing Equation 3.6 to be expressed as:

$$\dot{Q}'' = \dot{q}''_{net} \frac{\Delta H_C}{L} \tag{3.7}$$

where $\dot{Q}''$ is the energy release rate per unit area of burning material (kW/m²) and ΔH_C is the heat of combustion—as calculated in Section 3.3.2. The predicted energy release

28

rate will become equal to the right hand side of Equation 3.7 at ignition and remain constant over the burning time. Figure 3.8 shows a comparison of a typical predicted energy release rate versus an actual experimentally measured rate. The predicted energy release rate and burnout time, t_{bo}, are calculated such that the area under the predicted curve, Q'', is equivalent to the area under the experimental curve.

3.4.2 Cone Calorimeter Heat Flux

Equations 3.6 and 3.7 indicate that the mass loss rate and energy release rate per unit area may be linearly dependent on the net heat flux. In the Cone Calorimeter, the net heat flux to the sample is

$$\dot{q}''_{net} = (1 - \alpha_f)\dot{q}''_{ext} + \dot{q}''_f - \dot{q}''_{rr} \tag{3.8}$$

where α_f is the flame absorptivity, $\dot{q}''_{ext}$ is the external heat flux provided by the Cone heater (kW/m^2) and $\dot{q}''_f$ is the total incident heat flux from the flame including both radiant and convective heating (kW/m^2):

$$\dot{q}''_f = \dot{q}''_{f,r} + \dot{q}''_{f,c}$$

and $\dot{q}''_{rr}$ is the heat flux lost due to re-radiation (kW/m^2) from the heated material surface. Therefore, it would be advantageous if the heat flux from the flame, $\dot{q}''_f$, and the re-radiant losses, $\dot{q}''_{rr}$, can be determined to be constant over a range of external heat fluxes thereby producing a heat of gasification value that is linearly dependent on the external heat flux alone. This linear dependence will allow effective heat of gasification values to be extracted from the Cone data.

29
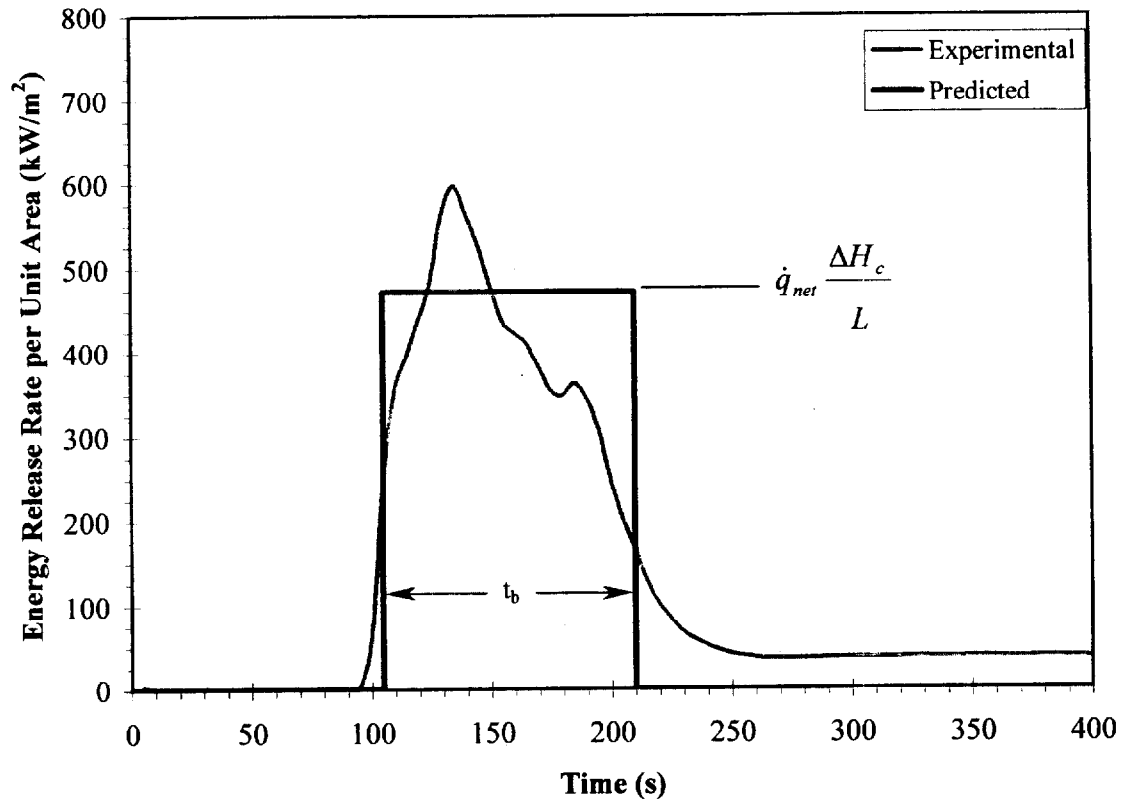
Figure 3. 8: Example of a Typical Energy Release Rate per Unit Area ($\dot{Q}''$) Prediction: R 4.08, 3-Layer Polycarbonate Panel at 50 kW/m^2 in the Cone Calorimeter.

Using Kirchhoff's law [20] the absorptivity of the flame can be determined to be equal to the flame emissivity:

$$\alpha_f = \varepsilon_f$$

where ε_f is the emissivity of the flame. Quintiere and Rhodes [42] and Rhodes [43] demonstrated that the flame volume for materials burning in the Cone Calorimeter can be approximated as a tall, vertical cylinder and that the emissivity can be approximated by:

$$\varepsilon_f \cong 1 - e^{-\kappa d_m}$$

30

where κ is the absorption coefficient (m^{-1}) and l_m is the mean beam length (m). For tall, semi-infinite cylindrical flames with height (z) greater than twice the sample width (d), the mean beam length for radiation to the base of the cylinder (the surface of the sample material) is approximately $0.65 \cdot d$ [20]. Therefore for flames of height z greater than $2d$, the flame emissivity is approximately constant and a relatively low value—Rhodes calculates 0.09 for PMMA burning in the Cone Calorimeter. Since the flame emissivity is so low, the flames are very transparent and very little of the external heat flux from the Cone heater is absorbed. Therefore most of the external heat flux is transmitted to the sample.

Quintiere and Rhodes also indicate that the total flame heat flux ($\dot{q}''_f$) from thermoplastic materials burning in the Cone Calorimeter can be considered to be constant for different external heat fluxes. The radiant portion of the flame heat flux is

$$\dot{q}''_{f,\,r} = \varepsilon_f \sigma T_f^4$$

where σ is the Stefan-Boltzmann constant (5.670×10^{-11} kW/m$^2 \cdot$K^4) and T_f is the flame temperature (K). The average flame volume temperature for a burning material can be considered to be relatively constant resulting in a constant $\dot{q}''_{f,\,r}$ value. For example, black PMMA burning in the Cone has a constant flame temperature of approximately 1400 K and an associated radiant flame heat flux of approximately 20 kW/m^2 [43]. This does not imply that all materials have identical radiative heat fluxes from the flames, but that for a particular burning material, the radiant heat flux is relatively · constant.

Rhodes work also indicates that the convective heat flux to a sample in the Cone Calorimeter is relatively constant as well, but can decrease slightly as the burning rate

increases. An increase in the burning rate will produce a "blocking factor" which acts to effectively reduce the convective heat transfer coefficient (h_c). Rhodes determined a convective heat flux of 15 kW/m² for black PMMA in the Cone, assuming a blocking factor of 1 (the burning rate, $\dot{m}''$, approaches 0).

The burning rate of the LSF materials does increase with the external heat flux, however this increase appears to be small enough that this decrease in $\dot{q}''_{f,c}$ can be neglected. Therefore, since both the radiative and convective portions of the flame heat flux are approximately constant for tall flames ($z > 2d$), the net flame heat flux incident to materials burning in the Cone Calorimeter, $\dot{q}''_f$, can be considered to be constant.

The re-radiant heat losses from the material surface ($\dot{q}''_{rr}$) can be expressed as

$$\dot{q}''_{rr} = \varepsilon_s \sigma T_s^4$$

where ε_s is the emissivity of the material surface and T_s is the surface temperature of the material (K). For this analysis the surface emissivities of the burning materials are approximated as being equal to 1. Since most materials will either darken, warp, melt and even char when burning, this is a reasonable approximation.

Rhodes work and work done by Hopkins and Quintiere [19] suggests that the surface temperature for burning thermoplastic materials in the Cone is constant. This surface temperature represents the vaporization temperature of the material (T_v) which is approximately constant and can be approximated as being equal to the ignition temperature (T_{ig}). Although the vaporization temperature is slightly higher than the ignition temperature for most thermoplastic materials, this appears to be a reasonable assumption based on the currently available data for thermoplastics. This implies that the reradiation losses from the sample are relatively constant over different external heat

32

fluxes. However further surface temperature data for non-charring as well as charring materials would help to reinforce this hypothesis. The surface temperature of charring materials is typically much higher than the ignition temperature, especially after a significant char layer has developed and been heated by the incident heat flux. Therefore using the ignition temperature to represent the surface temperature for all materials represents an approximation which may provide some error in the final prediction of the fire growth.

To predict the burning rate per unit area, $\dot{m}''$, using Equation 3.6, we need to determine an appropriate L value. In order to do this we consider the flame emissivity, flame heat flux and re-radiant heat loss for each material burning in the Cone Calorimeter to be constant. We can therefore assume that the $\dot{q}''_{net}$ in Equation 3.8 is only linearly dependent on $\dot{q}''_{ext}$. Therefore, since the effective heat of combustion and heat of gasification values are also taken to be constant, the burning rate and energy release rate per unit area will become linearly dependent on the external heat flux from the Cone heater:

$$\dot{m}'' \approx \dot{q}''_{ext} \frac{1}{L} \qquad (3.9) \qquad\qquad \dot{Q}'' \approx \dot{q}''_{ext} \frac{\Delta H_C}{L} \qquad (3.10)$$

This linear dependence of $\dot{m}''$ and $\dot{Q}''$ on the external heat flux allows the heat of gasification to be to be evaluated through methods similar to those for calculating the different ΔH_C values. The exception being that the peak, peak average and overall average energy release rates will be used on both an energy release rate basis as well as a specimen mass loss basis.

3.4.3 Energy Release Rate Methods

The effective heat of gasification values calculated based on energy release rates are based on Equation 3.10. Since ΔH_c and L are constants and are not dependent on the external heat flux, this Equation can be differentiated into the following form:

$$\frac{d\dot{Q}''}{d\dot{q}''_{ext}} = \frac{\overline{\Delta H_C}}{L}$$

where $\overline{\Delta H_C}$ indicates an average heat of combustion value, as listed in Table 3.4.

The peak, peak average and overall average energy release rate values ($\dot{Q}''$) are plotted with respect to the external heat flux ($\dot{q}''_{ext}$) from the Cone heater. Only the samples where ignition and sustained burning occurred were plotted. Since $d\dot{Q}'' / d\dot{q}''_{ext}$ is assumed to be linear, a least squares fit line was drawn through the data points and the slope of the linear fit was determined. The numerical value for the slope is simply equal to $\Delta\dot{Q}'' / \Delta\dot{q}''_{ext}$ allowing the effective heat of gasification to be calculated by

$$L = \frac{\overline{\Delta H_C}}{\left(\Delta\dot{Q}''/\Delta\dot{q}''_{ext}\right)} \tag{3.11}$$

which can be seen graphically in Figure 3.9. Graphical representations for all of the materials are presented by Dillon *et al.* [10].

3.4.3.1 Peak Energy Release Rate (L_{peak})

The $\dot{Q}''_{peak}$ value from each test is taken directly from the LSF data and plotted

against the external heat flux from the Cone heater. Using the $\overline{\Delta H_{C,\ peak}}$ values in

Table 3.4, an effective L_{peak} value is calculated for each material based on

$$L_{peak} = \frac{\overline{\Delta H_{C,\ peak}}}{\left(\Delta \dot{Q}''_{peak} / \Delta \dot{q}''_{ext}\right)}$$
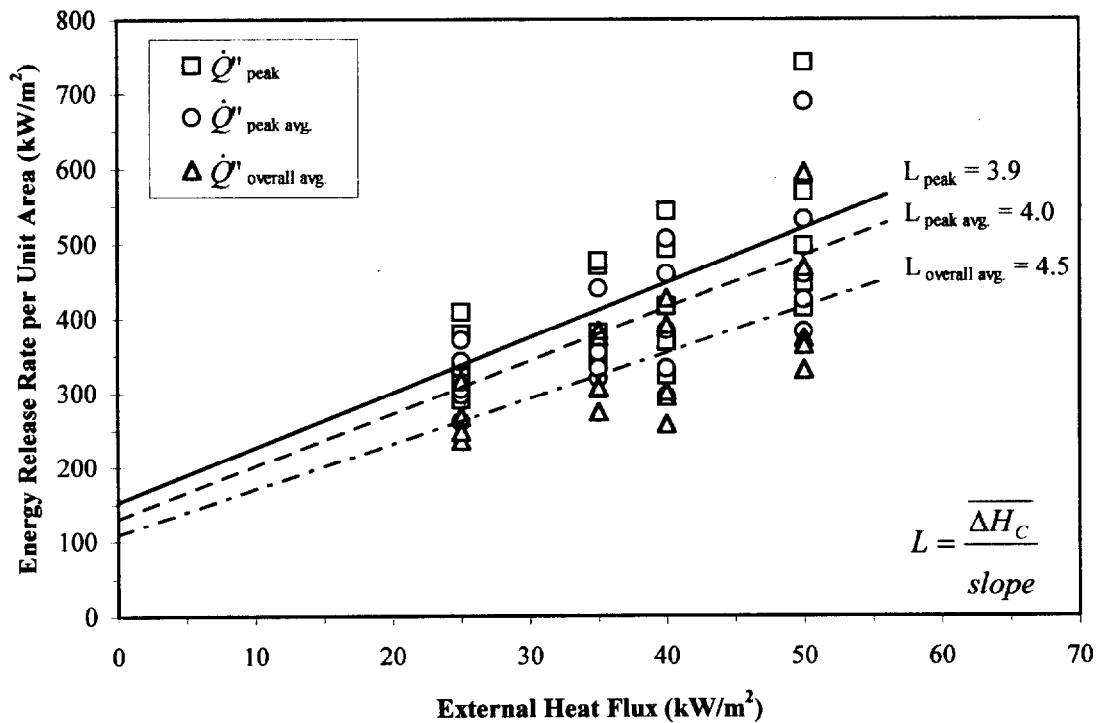
Figure 3. 9: Example of a Typical Heat of Gasification (L) Determination Using
Energy Release Rates per Unit Area with Respect to the External Heat Flux in the Cone
Calorimeter: R 4.05, Fire Retarded Extruded Polystyrene.

3.4.3.2. Average Energy Release Rate Around the Peak ($L_{peak\ avg.}$)

This method is identical to the one used to determine L_{peak} except that the "peak average" values are used:

$$L_{peak\ avg.} = \frac{\overline{\Delta H_{C\ peak\ avg.}}}{\left(\Delta \dot{Q}''_{peak\ avg.} \Big/ \Delta \dot{q}''_{ext} \right)}$$

3.4.3.3. Average Overall Test Results ($L_{overall\ avg.}$)

For this method the total steady burning of the sample material from each test is used to determine the effective heat of gasification value. This results in a more global value as opposed to a value based on an instantaneous or local occurrence. As in the previous two methods, the overall energy release rate for each test, $\dot{Q}''_{overall\ avg.}$, needs to be plotted against the associated external heat flux level from the Cone heater. The overall energy release rate can be determined from

$$\dot{Q}''_{overall\ avg.} = \Delta H_{C,\ overall\ avg.} \cdot \dot{m}''_{overall\ avg.} \tag{3.12}$$

The overall heat of combustion values used in Equation 3.12 represent values calculated from individual tests as opposed to the average values listed in Table 3.4.

In order to determine a heat of gasification value over the region of steady burning, the total specimen mass loss from the Cone data can not be used. This is done in order to eliminate mass loss from non-burning phenomenon, *e.g.* moisture evaporation. For example, gypsum wallboard undergoes a rather brief burning period after the paper facing ignites, but the specimen mass will continue to decrease past the point of flame extinction. This continued mass loss is due to the evaporation of the water trapped within the gypsum by the applied heat flux. Therefore, the steady mass

36

loss rate per unit area value ($\dot{m}''_{overall\ avg.}$) will be determined over this sustained burning region.

In order to determine this steady burning mass loss rate, the slope of the specimen mass versus time curve (dm/dt) is determined over the region where sustained burning was believed to occur. The steady burning region is taken as the ignition time until the point at which the mass versus time curve appears to curve towards a horizontal line—indicating a significant reduction in the burning rate. A typical steady burning rate determination can be seen in Figure 3.10.

The times at which the different specimens ignite were provided by LSF. The data also includes the time at which flaming ends, but it is unclear if this time represents a sudden end of flaming or a gradual reduction of the flame size until it becomes undistinguishable. There are tests where the reported end of flame time does not reasonably correspond with the end of significant mass loss or energy release. There are also cases where a material underwent ignition and extinguishment several times, and it was unclear as to what end of flaming time to choose. Since these values will be used to predict the burning of materials in actual scenarios, the time at which the burning rate is seriously reduced can be used to represent an approximate point at which steady, sustained burning might have ended. Therefore the change in the slope of the mass loss versus time curve is implemented here for determining the end of steady burning.

The mass loss rate ($\dot{m}$) is approximately linear over this steady burning region. Therefore, $\dot{m}''_{overall,avg.}$ can be determined from the slope of the linear fit through the

specimen mass versus time curve during steady burning divided by the surface area of

the specimen:

$$\dot{m}''_{overall\ avg.} = \frac{\dot{m}}{A_s} = \frac{-dm/dt}{A_s}$$

where A_s is the surface area of the sample which is reported by LSF to be 0.0088 m^2 for

all of the samples tested.
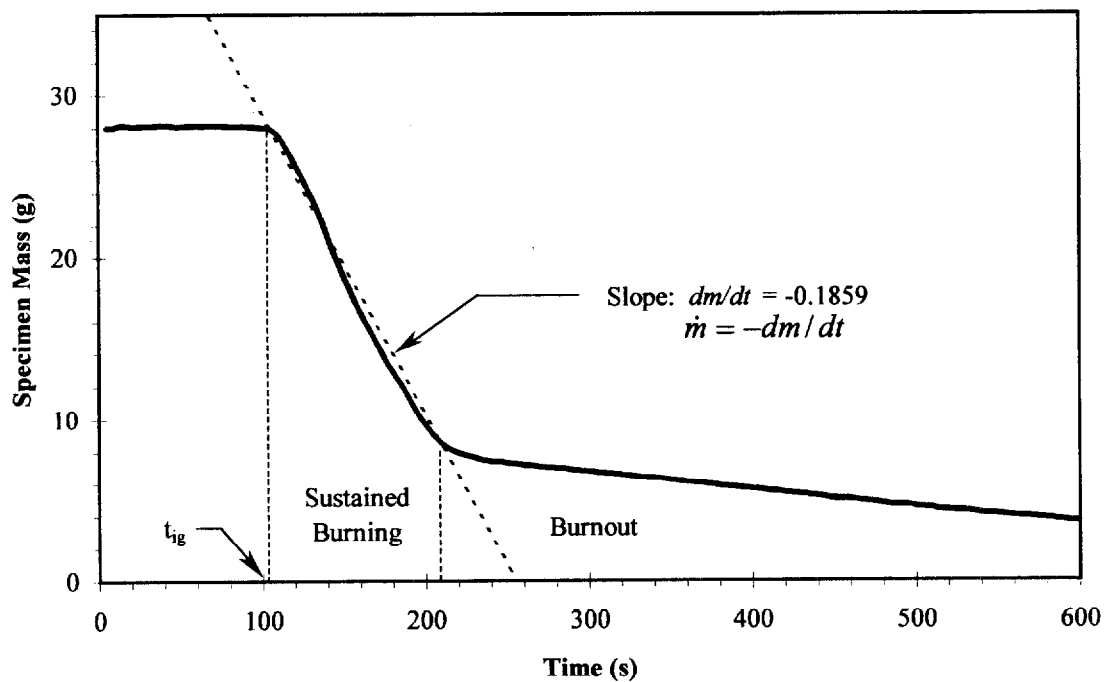
Figure 3. 10: Example of Steady Burning Rate ($\dot{m}$) Determination: R 4.08, 3-Layer
Polycarbonate Panel.

Using $\dot{m}''_{overall,avg.}$, the overall energy release rate per unit area is determined for

each test using Equation 3.12 and plotted with respect to the external heat flux from the

heater as in Figure 3.9. The slope of the linear fit and $\overline{\Delta H_{C, \, overall \, avg}}$ are used to

determine the L value:

$$L_{overall \; avg.} = \frac{\overline{\Delta H_{C, \, overall \; avg.}}}{\left(\Delta \dot{Q}''_{overall \; avg.} \Big/ \Delta \dot{q}''_{ext} \right)}$$

3.4.4 Specimen Mass Loss Methods

Heat of gasification values determined on a specimen mass loss basis are

calculated using Equation 3.9. Differentiation produces

$$\frac{d\dot{m}''}{d\dot{q}''_{ext}} = \frac{1}{L}$$

As with the energy release rate, the mass loss rate per unit area is taken to be linearly

dependent on the external heat flux and can be expressed as

$$\frac{\Delta \dot{m}''}{\Delta \dot{q}''_{ext}} = \frac{1}{L} \tag{3.13}$$

Therefore, the effective L value is the inverse of the slope of the linear fit through the

specimen mass loss rate per unit area data plotted against the external heat fluxes for

each test:

$$L = \frac{1}{\left(\Delta \dot{m}'' / \Delta \dot{q}''_{ext} \right)} \tag{3.14}$$

A graphical representation of the determination of the heat of gasification using the

specimen mass loss rate per unit area is shown in Figure 3.11.

39

3.4.4.1 Peak Energy Release Rate (L_{peak}) by Mass Loss

The peak mass loss rate per unit area for each tested specimen was determined by using a form of Equation 3.4:

$$\dot{m}''_{peak} = \frac{\dot{Q}''_{peak}}{\Delta H_{C, \, peak}}$$

$$(3.15)$$

The heat of combustion values used here are the actual peak values that were determined for each Cone test (as opposed to the average values from Table 3.4). The peak mass loss rates are then plotted against the external heat fluxes as in Figure 3.11 and the heat of gasification is determined by

$$L_{peak} = \frac{1}{\left(\Delta \dot{m}''_{peak} / d\Delta \dot{q}''_{ext}\right)}$$
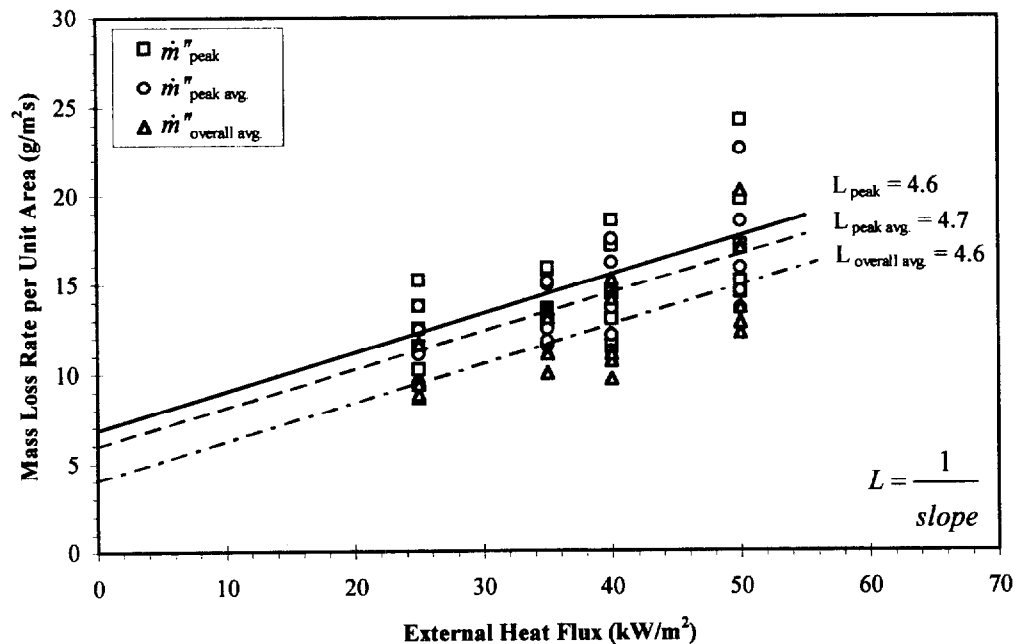
Figure 3. 11: Example of a Typical Heat of Gasification (L) Determination Using Specimen Mass Loss Rates per Unit Area with Respect to the External Heat Flux in the Cone Calorimeter: R 4.05, Fire Retarded Extruded Polystyrene.

3.4.4.2 Average Energy Release Rate Around the Peak ($L_{peak\,avg.}$) by Mass Loss

This method is the same as the previous method except that the $\dot{Q}''_{peak\,avg.}$ and $\Delta H_{C,\,peak\,avg.}$ from each test are used in Equation 3.15 to determine the peak average mass loss rate per unit area. The effective heat of gasification is also found in a similar manner:

$$L_{peak\,avg.} = \frac{1}{\left(\Delta \dot{m}''_{peak\,avg.} / \Delta \dot{q}''_{ext}\right)}$$

3.4.4.3 Average Overall Test Results ($L_{overall\,avg.}$) by Mass Loss

This method uses the same $\dot{m}''_{overall\,avg.}$ values for the region of steady, sustained burning determined in Section 3.4.3.3 plotted against the external heat flux levels.

$$L_{overal\,avg.} = \frac{1}{\left(\Delta \dot{m}''_{overall\,avg.} / \Delta \dot{q}''_{ext}\right)}$$

3.4.5 Heat of Gasification Value Analysis

The six calculated effective heat of gasification values for the different materials are presented in Table 3.5. Theoretically, all six heat of gasification values that have been calculated should be identical. It can be seen that for some materials, the calculated L values are reasonably consistent. However for other materials there is a great deal of discrepancy between the values and some of the values do not make a great deal of sense. These discrepancies are due to moisture evaporation, char formation, unsteady burning rate and difficulties in determining appropriate mass loss rates and will be described in more detail below.

41

Negative heat of gasification values were calculated for the Paper Faced

Gypsum Board (R 4.02). This is most likely due to the effects of the rapid burning of

the paper facing followed by the evaporation of the moisture contained within the

gypsum itself. The continuous mass loss causes the effects of the burning paper to

become relatively insignificant to the mass loss rate when determining $L_{overall, avg.}$ by the

energy release method. The rapid burning of the paper facing produces very low energy

release rate (≈ 100 kW/m^2) and a minimal increase in the mass loss rate over a very

short time period as can be seen in Figure 3.12. Therefore, inconsistencies appear in the

determination of the peak and peak average mass loss rates leading to errors in the

development of L due to the linear fit through the data.

Table 3. 5: Effective Heat of Gasification (L) Values Calculated by Six Methods.

Material	Energy Release Rate			Mass Loss Rate		
	L_{peak} (kJ/g)	$L_{peak\ avg.}$ (kJ/g)	$L_{overall\ avg.}$ (kJ/g)	L_{peak} (kJ/g)	$L_{peak\ avg.}$ (kJ/g)	$L_{overall\ avg.}$ (kJ/g)
R 4.01, FR. Chipboard	9.3	10.0	4.5	13.4	12.4	9.4
R 4.02, Gypsum	4.6	4.8	-693.5	-27.9	-10.6	13.0
R 4.03, PU/Alum. *	---	---	---	---	---	---
R 4.04, PU/Paper	5.0	5.5	---	5.9	5.6	1.0
R 4.05, Ext. PS40	3.9	4.0	4.5	4.6	4.7	4.6
R 4.06, Acrylic	1.5	1.6	3.0	1.4	1.6	2.7
R 4.07, FR. PVC	9.3	10.4	4.2	2.1	2.2	2.4
R 4.08, 3-Layer PC	3.2	3.3	3.6	4.4	3.6	4.8
R 4.09, Mass Timber	22.9	17.5	6.5	147.1	41.8	6.9
R 4.10, FR. Plywood	8.9	9.3	8.8	12.7	13.4	15.5
R 4.11, Plywood	7.5	7.3	3.9	6.9	8.0	7.8
R 4.20, Exp.PS40	7.1	7.3	11.2	9.2	8.5	11.5
R 4.21, Exp.PS80	13.5	12.7	9.4	8.0	8.5	7.5

* Material properties could not be extrapolated from the test data
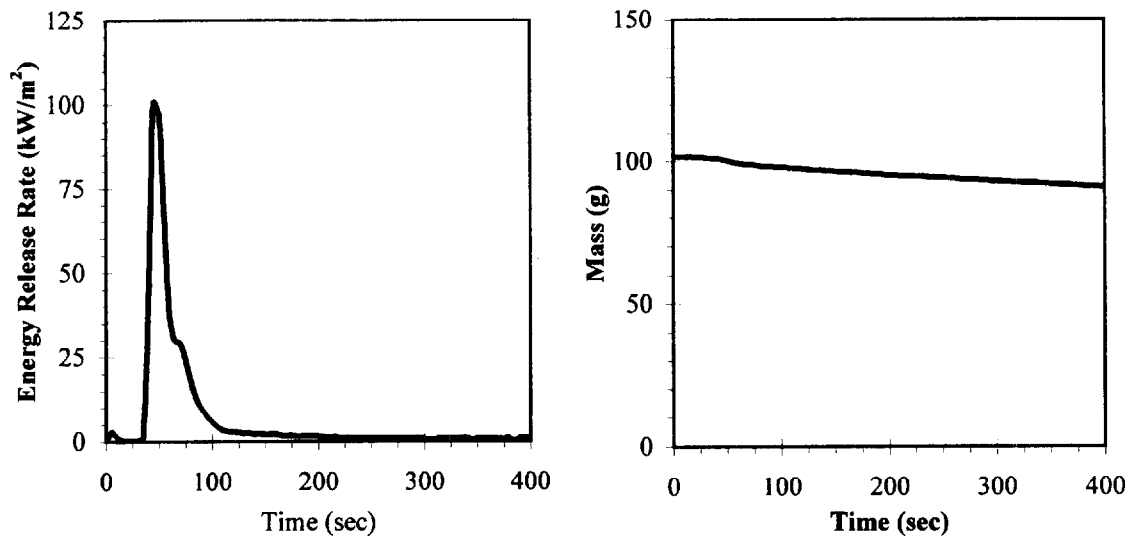
Figure 3. 12: Typical Energy Release Rate per Unit Area and Specimen Mass for Gypsum Board, R 4.02, in the Cone Calorimeter.

The $L_{overall\ avg.}$ value by the energy release rate method for the polyurethane foam panel with paper facing, R 4.04, is missing due to missing data from LSF. Without the $\Delta H_{C,\ overall\ avg.}$ values, this L value could not be calculated. The $L_{overall\ avg.}$ value by the mass loss rate also appears to be very low while the other four values are relatively consistent. This was due to difficulties in determining the region of steady mass loss by the method in Section 3.4.3.3 above. For most other materials the region of steady burning is clearly marked by a steady specimen mass loss followed by a sharp transition in the specimen mass with respect to time graph. However as Figure 3.13 indicates, the specimen mass follows more of a curve with respect to time therefore making it difficult to accurately determine this transition point. Using the point at which the energy release rate begins to rapidly decline ($\approx$ 115 seconds in Figure 3.13) as the end of steady burning would have provided a line with a higher mass loss rate. This may provide a

more appropriate L value when a linear fit is drawn through the mass loss rate per unit area data plotted versus the external heat flux.
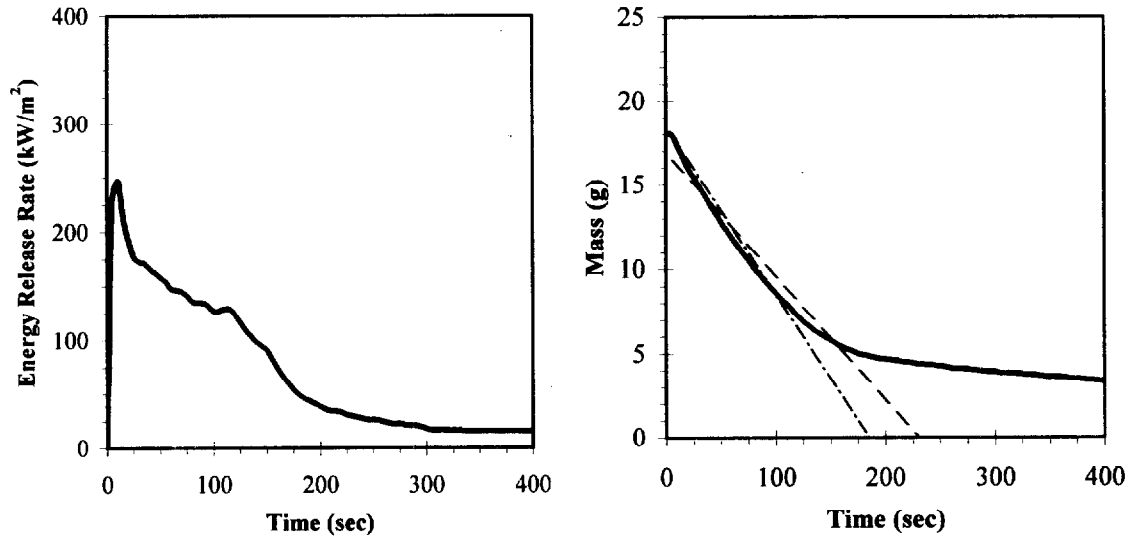
Figure 3. 13: Typical Energy Release Rate and Specimen Mass for Polyurethane Foam Board with Paper Facing, R 4.04, in the Cone Calorimeter.

The L values determined by the energy release rate method for fire retarded PVC, R 4.07, are much higher and less consistent than those calculated by the mass loss rate method. These high values are most likely due to the large amount of scatter that exists for the heat of combustion values, especially for the peak and peak average values at low external heat flux levels (see Figure 3.14). This type of scatter was not seen in the analysis of the other materials. The reason for this scatter is most likely due to the inconsistent burning characteristics of PVC as seen in Figure 3.15. The existence of both single and multiple peak energy release rates produces inconsistent data which therefore produces higher average ΔH_C values thereby producing high L values. The overall average heat of combustion has a lower, more constant value which explains

why the $L_{overall\ avg.}$ value is closer to the mass loss rate values. The use of a lower heat of combustion value may be appropriate for determining L as well as for predicting the performance of fire retarded PVC.
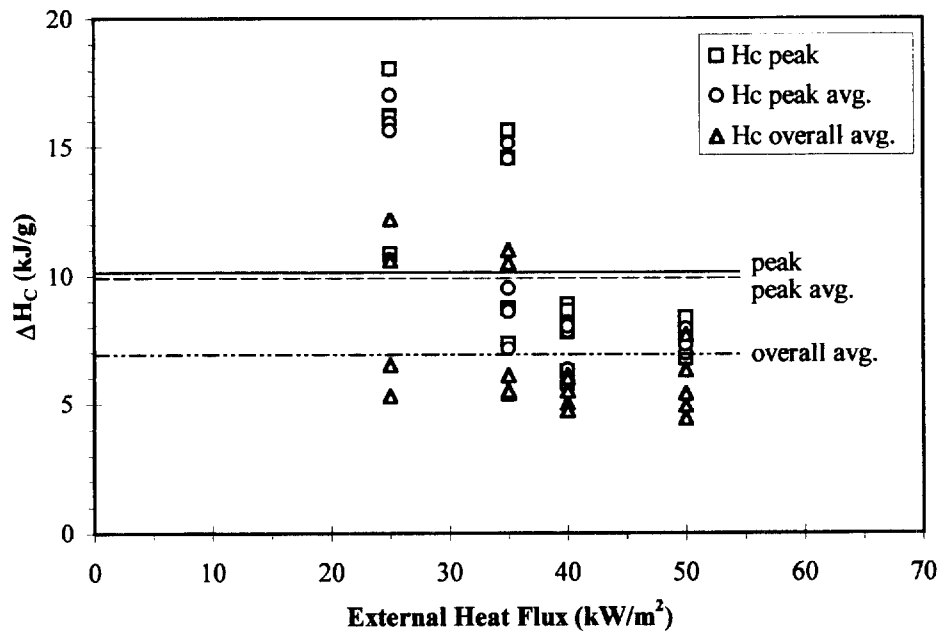
Figure 3. 14: Average Heat of Combustion Values for Fire Retarded PVC, R 4.07.

The heat of gasification values for varnished massive timber, R 4.09, indicate a great deal of fluctuation. The L_{peak} and $L_{peak\ avg.}$ by mass loss rate values seem particularly high and the energy release rates are high as well. Upon ignition the massive timber rapidly releases a large amount of energy, which is most likely due to the varnish burning away. This initial peak energy release rate is relatively constant for the different external heat flux levels and the mass loss rate associated with this peak appears to be constant as well (see Figure 3.16). This type of burning is atypical for wood samples burning in the Cone Calorimeter and confirms that the burning varnish has a constant energy release rate and mass loss rate regardless of the external heat flux.

For typical wood samples both the initial and secondary energy release rate peaks are proportional to the external heat flux.
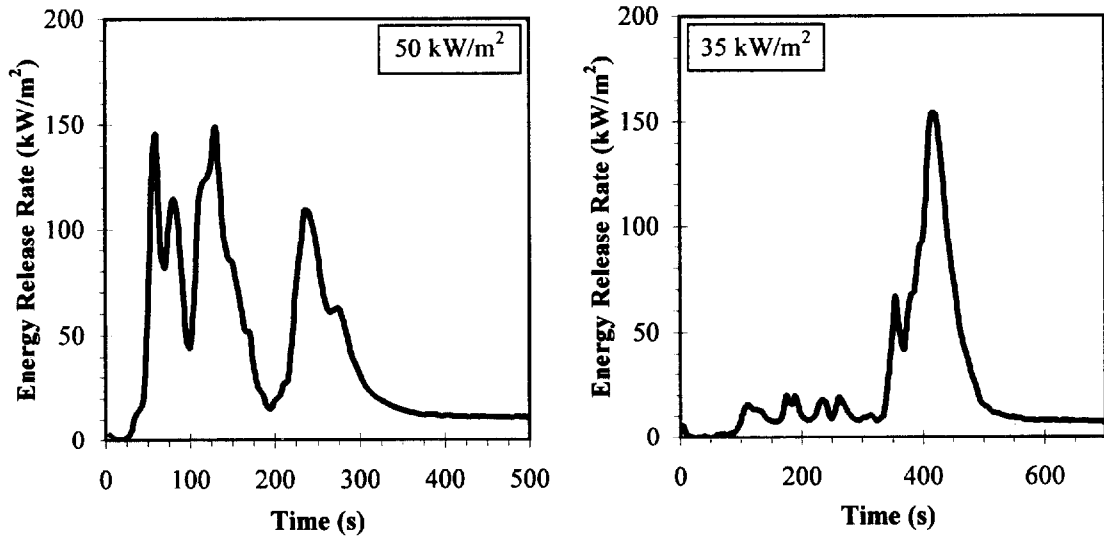
Figure 3. 15: Various Energy Release Rates for Fire Retarded PVC, R 4.07, in the Cone Calorimeter
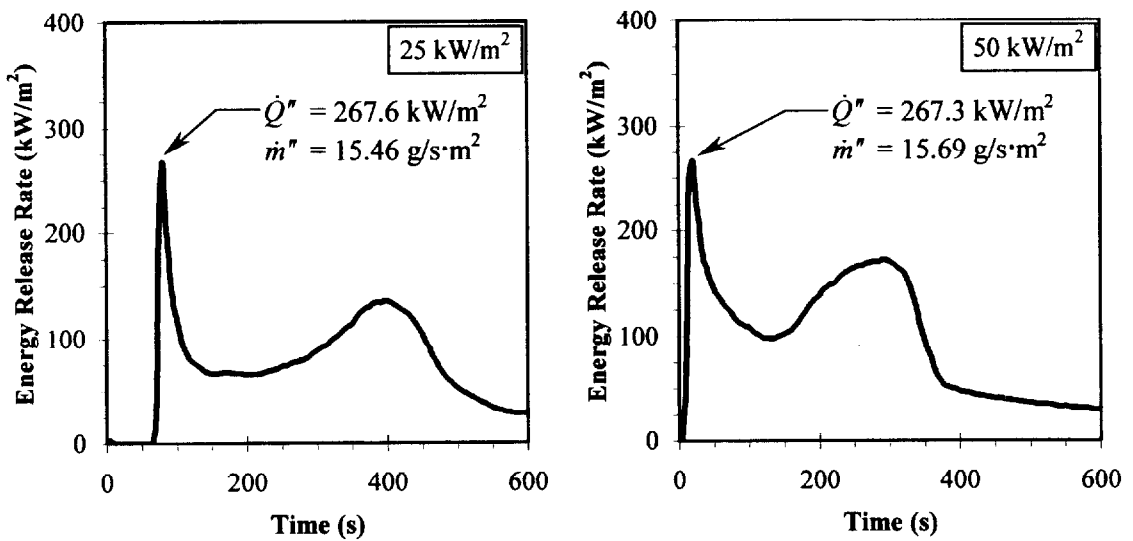
Figure 3. 16: Peak Energy Release and Mass Loss Rates for Varnished Massive Timber, R 4.09, at Different External Heat Flux Levels in the Cone Calorimeter.

46

Constant mass loss and energy release rates results in a linear fit through the peak and peak average data that is almost horizontal. Therefore, the inverse of the slope of this fit produces a high L value that does not appear to be appropriate for the material.

Fire retarded chipboard, R 4.01, and normal plywood, R 4.11, demonstrate slightly reduced $L_{overall\,avg.}$ by energy release values. This seems to be typical for cellulosic-type materials and is most likely due to char formation. At lower heat fluxes, a layer of char can develop over the surface of normal charring materials, like wood, long before ignition. However, as the wood is continually heated, it pyrolizes and continues to lose mass even though there is no flame present. At much higher heat fluxes, ignition usually occurs before a significant char layer can develop. Due to the mass loss prior to ignition at lower heat fluxes, the overall energy release rate will be reduced, therefore producing a linear fit through the data that has a higher slope. The inverse of this higher slope will produce a reduced L value as can be seen in Table 3.5. The fire retarded plywood does not show this significantly low $L_{overall\,avg.}$ value mostly due to only some of the samples igniting at 25 kW/m^2 and less importance being placed on these data points when taking a linear fit through the data. It is important to note that charring materials will show this sort of char layer development dependence at different low heat flux levels and this level will depend on sample orientation, fire retardant additives and material properties (critical heat flux for ignition, density, thermal conductivity, etc.).

3.5 Total Energy Per Unit Area (Q'')

Samples tested in the Cone Calorimeter release a certain amount of energy (Q) over the duration of the test. In order to predict the performance of materials in full-scale scenarios, this total evolved energy term is needed. However, it is desirable to eliminate thickness and density factors in the expression of this energy. Therefore the total amount of energy that can be released from a material when it is burning is expressed in terms of a unit area (Q''). The total energy per unit area can be calculated by:

$$Q'' = \frac{Q}{A_s}$$

where Q is the total heat evolved from the sample material and A_s is 0.0088 m^2.

Like the heat of combustion and heat of gasification, Q'' is regarded as a constant material property that is independent of the incident heat flux. Therefore in order to calculate an effective Q'' value for a material, the numerical average of all the Q'' values measured in the Cone is calculated. This average value effectively represents the total energy available from a square meter of the material and is expressed graphically in Figure 3.17—the horizontal line indicating the average Q'' value. Figures for the remainder of the LSF materials are presented by Dillon *et al.*The average values determined for all of the materials are presented in Table 3.6.
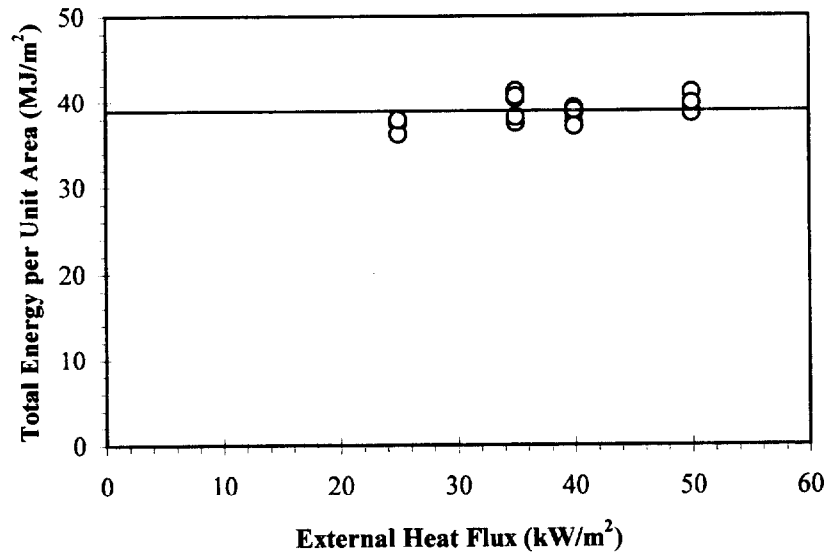
Figure 3. 17: Typical Total Energy per Unit Area (Q'') Determination: R 4.05, Extruded Polystyrene Board.

Table 3. 6: Total Energy per Unit Area of Material.

Material	Q'' (MJ/m²)
R 4.01, FR. Chipboard	34.2
R 4.02, Gypsum	2.2
R 4.03, PU/Alum.	32.9
R 4.04, PU/Paper	30.8
R 4.05, Ext. PS40	38.7
R 4.06, Acrylic	89.5
R 4.07, FR. PVC	16.1
R 4.08, 3-Layer PC	58.1
R 4.09, Mass Timber	68.2
R 4.10, FR. Plywood	51.8
R 4.11, Plywood	64.6
R 4.20, Exp. PS40	33.9
R 4.21, Exp. PS80	25.5

3.6 Material Property Conclusion

In order to appropriately model the performance of the materials, the properties that best represent the burning characteristics under actual conditions must be determined. It is also desirable to determine these properties in a systematic manner that will allow consistent predictions of material properties. For this analysis, the "peak average" heat of combustion and heat of gasification by the energy release rate method appear to be the most appropriate. This is a judgement that was made based on the desire to most accurately represent full-scale conditions with the fire growth model.

The properties evaluated at the peak energy release rate are not used because it is believed that momentous burning effects are not necessarily consistent with the actual performance of the material. The peak values are based on the burning of the material at one point in time during the entire test. This instantaneous value will most likely produce an energy release rate prediction that is too high which will cause the prediction of excessive, unrealistic flame spread and fire growth. The values based on the "overall average" energy release rate are not used because non-burning effects such as moisture evaporation can cause errors in the determination of the material properties.

A comparison of some typical energy release rate predictions for a thermoplastic and charring material in the Cone are presented in Figures 3.14 and 3.15, respectively. The energy release rates were predicted using the peak, peak average and overall average material properties in Equation 3.7 with the flame heat flux for the materials burning in the Cone approximated as being equal to 35 kW/m^2 (see Section 3.4.2). The area under the rectangular predicted curves are equivalent to the area under the experimental curve. As the Figures indicate, the peak average values appear to give the

best representation of the experimental energy release rate for both types materials.

Therefore, the peak average properties for all materials were used. This method of

determining properties may not be completely appropriate for all of the materials but

appears to be the most appropriate systematic method to apply to all of the materials.
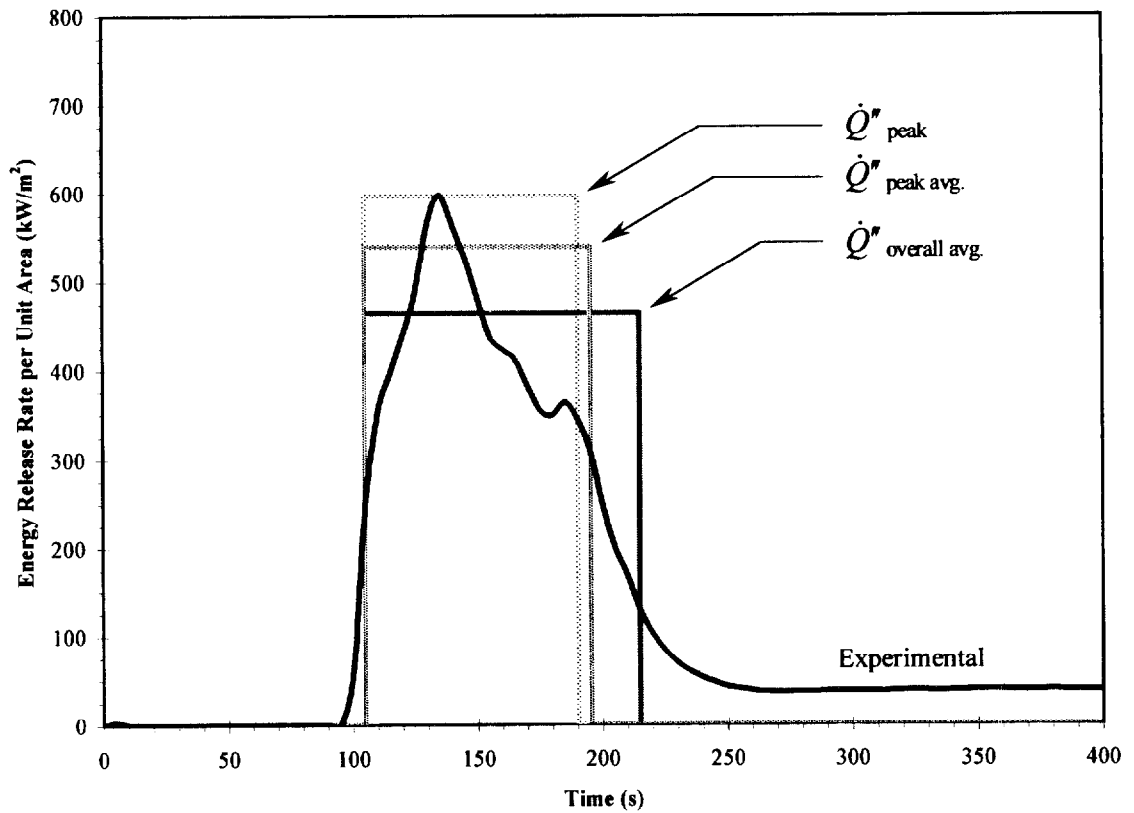
Figure 3. 18: Comparison of Methods for Predicting the Energy Release Rate of a Thermoplastic Material in the Cone Calorimeter: R 4.08, 3-Layer Polycarbonate Panel at $50 \, kW/m^2$.
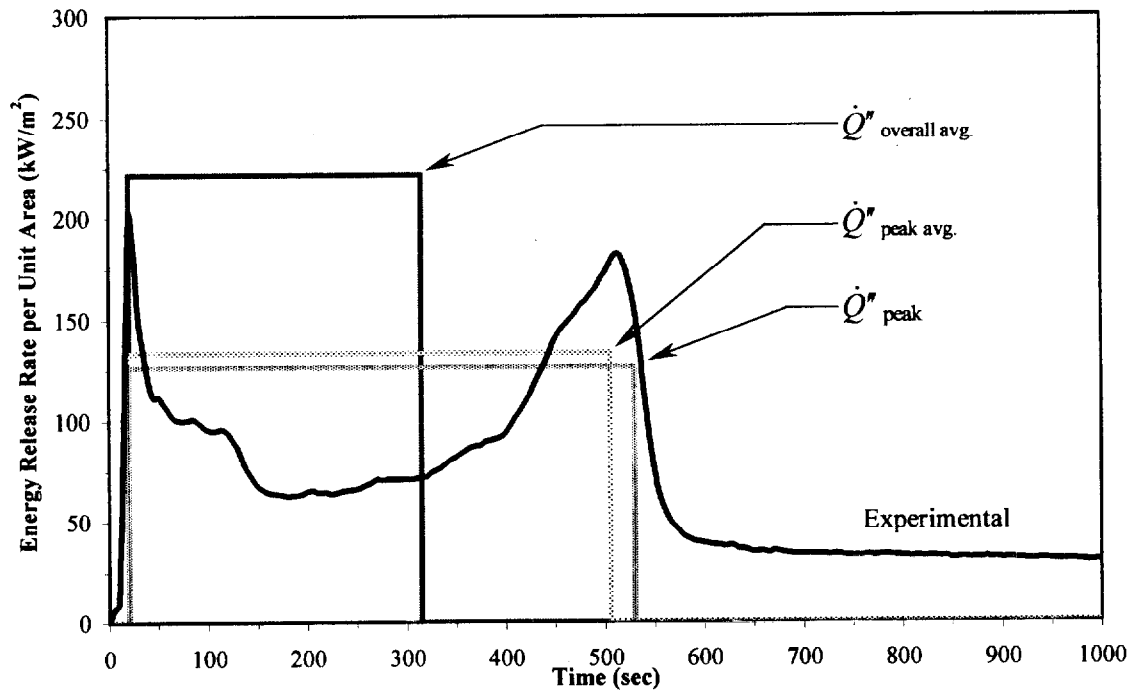
Figure 3. 19: Comparison of Methods for Predicting the Energy Release Rate of a Charring Material in the Cone Calorimeter: R 4.11, Normal, Untreated Plywood at 50 kW/m^2.

4. FIRE GROWTH PREDICTIONS

4.1 Fire Growth Model

The model used for predicting the performance of the LSF materials in the room-corner test was developed by Quintiere [36]. Previous literature has been published which describes the physics of the model and its application [16, 23, 33, 37] therefore only a brief description is provided here. However, important aspects of the model that were taken into consideration in the analysis of the materials will be provided at the appropriate points.

Quintiere's fire growth model computes the wind-aided (upward and ceiling jet) and opposed flow (lateral and downward) flame spread front as well as the associated burn-out fronts. The pyrolysis and burn-out fronts are then used to compute the burning total area as shown in Figure 4.1. The model also predicts the upper gas layer temperature and the rate of energy release as a function of time. Enhanced flame spread due to thermal feedback effects from the room are included but oxygen depletion is not. More detailed approximations of these two effects could be included however it has been found that the flame spread process is relatively insensitive to the room conditions until flashover is attained.

To predict the growth of fire in the ISO 9705 room-corner test the model requires input data regarding the following:

- Initial room temperature: 20 °C
- Room geometry: 2.4 m x 3.6 m x 2.4 m high with a 2.0 m x 0.8 m door/vent.

- Ignition burner output: 100 kW for 10 minutes followed by 300 kW for

  an additional 10 minutes.

- Calculation Parameters

- Material Property Data

Material fire properties can be derived from small-scale tests such as the Cone Calorimeter and the LIFT apparatus, as describes in Section 3. These seven properties are as follows:

1. Ignition temperature (T_{ig})

2. Minimum temperature necessary for lateral flame spread ($T_{s,\,min}$)

3. Thermal inertia ($k\rho c$)

4. Lateral flame-heating parameter for lateral flame spread (Φ)

5. Heat of combustion (H_C)

6. Heat of gasification (L)

7. Total energy per unit area of material ($Q"$)

Previous comparisons of model predicted energy release rates and the results of full-scale room-corner tests have shown good, but not perfect, results. It has also been found that for some materials small changes in the material properties and even exposure conditions can led to dramatic differences in the predictions. This has been shown to be especially true for thin materials or materials with a short burnout time. As

opposed to being some sort of mathematical artifact, this seems to indicate that some

materials are on the threshold of a critical condition—the onset of flashover.
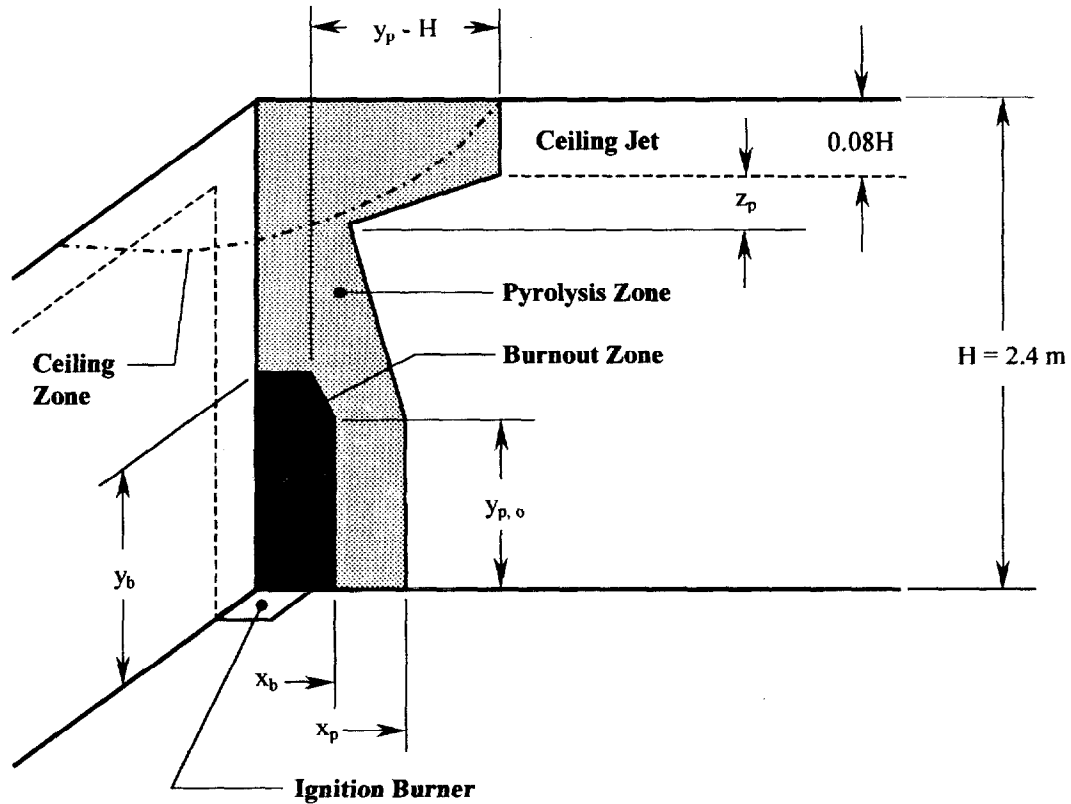
Figure 4. 1: Features of Quintiere's Fire Growth Model.

4.2 Material Properties Used

The material properties used for modeling the flame spread are presented in

Table 4.1. There is no lateral flame spread parameter, Φ, for the acrylic glazing (R

4.06) since the ignition temperature and minimum temperature for spread are the same.

The lack of data for the polyurethane foam panel with aluminum facing, R 4.03, is due

to the lack of material ignition at all incident heat fluxes except 50 kW/m^2. Due to the reflective nature of the aluminum facing ignition only occurred at the highest external heat flux in the Cone Calorimeter and material properties could not be extrapolated. Therefore the material properties developed for the polyurethane foam panel with paper facing, R 4.04, were used to predict the performance of the aluminum faced foam in the full-scale test. The room-corner test ignition burner will quickly coat the aluminum facing with soot thereby causing a significant increase in the absorptivity of the aluminum and an increase in the heat transfer to the polyurethane. This will cause the aluminum faced foam to perform much like the paper faced foam and allows for a fire growth prediction to be made. Observations from the full-scale test indicate that the aluminum facing began to become damaged in the region around the ignition burner after approximately 14 seconds. This damage to the aluminum facing allowed the polyurethane foam to be exposed to the igniter flames which allowed rapid ignition, unlike in the Cone Calorimeter.

As mentioned in the previous section, the "peak average" heat of combustion and heat of gasification values are used for the basic material performance prediction However, modifications to the properties will made to account for potential errors in the properties (as discussed in Section 3.4.5) and unusual performance in the room-corner test, *i.e.*, melting.

4.2.1 Adjusted Properties for Melting/Dripping Materials

In order to account for the melting of thermoplastic materials the burnout time of the material (t_b) can be approximated as being the time at which the material began to

melt in the full scale tests. This approximation assumes that when a material melts, drips and/or falls from the walls and ceiling, it is burned away and no longer present and available to burn. The model calculates the burnout time of a material by

$$t_b = \frac{Q''}{\dot{Q}''}$$

(4.1)

where Q'' is the total energy per unit area of the material (kJ/m^2) and $\dot{Q}''$ is the energy release rate per unit area (kW/m^2) which can be calculated by

$$\dot{Q}'' = \dot{q}''_{net} \frac{\Delta H_C}{L}$$

(4.2)

where $\dot{q}''_{net}$ represents the net heat flux to the material. This net heat flux is approximated as the total heat flux from the flame minus any re-radiation from the material surface:

$$\dot{q}''_{net} = \dot{q}''_f - \dot{q}''_{rr}$$

(4.3)

Quintiere [36] considers the flame heat flux to be constant over the pyrolysis (burning) region and over the extended flame length. The net flame heat flux over the pyrolysis zone is taken as being 60 kW/m^2. This represents the heat flux to the material surface over the height of the ignition burner flame and the heat flux from the flames over the region of material that is burning. Quintiere also selects the extended wall flame heat flux to the unburned material above the pyrolysis region to have a constant value of approximately 30 kW/m^2. The idealized heat flux distributions from the ignition burner and the extended wall flame can be seen in Figure 4.2.

(a) Ignition Burner   (b) Wall Flame
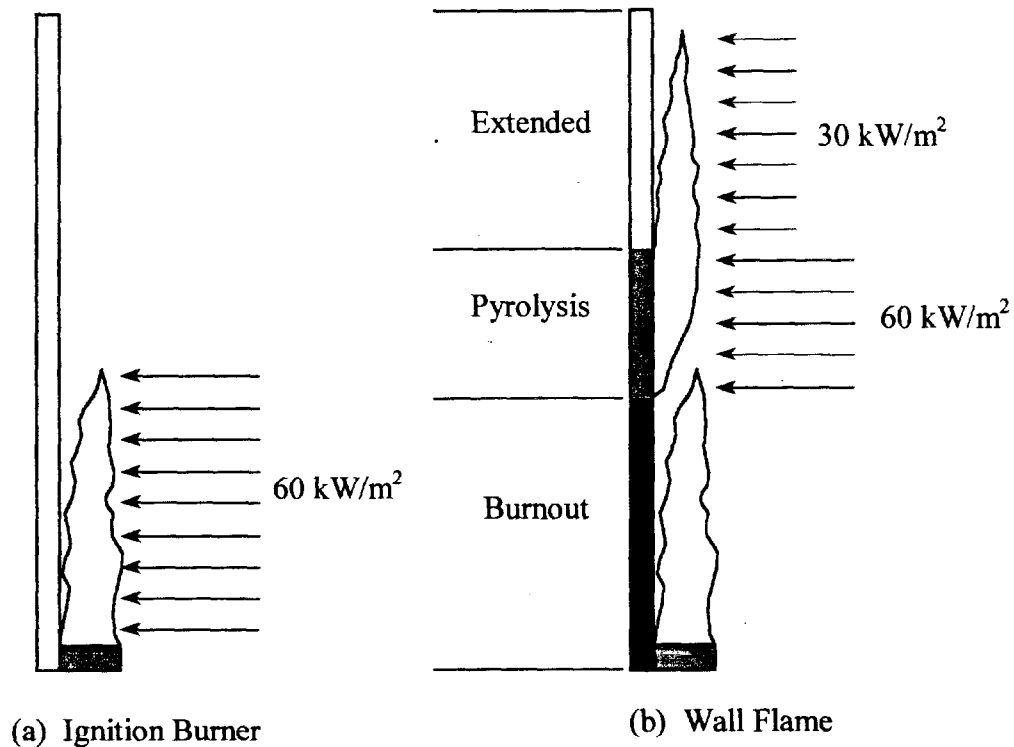
Figure 4. 2: Idealized Heat Flux Distributions Used in Quintiere's Fire Growth Model.

Using Equations 4.1 to 4.3, an approximate burnout time for the material can be calculated. The model treats the burnout time as the time at which the material is no longer present and available to burn, which is also the case when the material melts or falls off of the wall and the ceiling. Therefore the time for a material to begin melting in the full-scale experiments was taken to be an "effective burnout time". In order to achieve these effective times, the total energy per unit area of material (Q'') was reduced by a fraction which caused the burnout time to be similar to the melting time. This reduced Q'' is then taken to be an approximation of the actual energy available from melting materials.

58

This approximation method seems to work relatively well. However, for some

materials the reduced Q'' prediction did not produce enough of a reduction in the heat

release to accurately simulate the full-scale test. For those materials, the Q'' value was

further decreased until a representative prediction was achieved. Therefore, it can be

seen that this method is not a completely accurate method of approximating the melting

of actual materials, but it does help in showing the sensitivity of the model and

identifying the hazards and processes that are involved in melting materials.

4.3 Results

The material performance predictions by Quintiere's fire growth model were

compared with full-scale ISO 9705 room-corner tests performed at the Swedish

National Testing and Research Institute [49]. Graphical comparisons of the predicted

and full-scale test energy release rates are presented in Figures 4.2 through 4.13.

A key factor for determining material performance in a room configuration is

the amount of time that it takes the burning material to take the room to flashover.

Because flashover is a complex phenomenon, the time to onset in the 9705 room-corner

test is associated with an energy release rate of 1,000 kW which is based on flames

emerging from the door and floor heat flux. This 1 MW criterion is for the most part

independent of the material and only a property of the room geometry. Other factors

effect the overall performance of a material, but for the most party the time for the

energy release rate to reach 1,000 kW will be analyzed.

Predictions made by the model using the properties presented in Table 4.1 are simply identified in the figures as "Prediction". For some materials, especially thermoplastic materials that tended to melt and drip, key observations from the full-scale tests are presented in these figures. The figures also show predictions that were made using adjusted material properties, which will be discussed below. The adjusted properties for these predictions are identified in the legends of the appropriate figures.

It should be noted that for the full-scale test results there appears to be a consistent lag between the beginning of the test and the time at which 100 kW from the ignition burner is measured. This lag is between 20 and 60 seconds for each test (see Figure 4.3 to 4.14) and indicates an important characteristic of the SP oxygen consumption calorimeter. This lag time has some significance in the result comparisons which follow.

Table 4. 1: Ignition, Flame Spread and Energy Release Properties of the LSF Materials used for Modeling.

Material	T_{ig} (°C)	$T_{s,min}$ (°C)	$k\rho c$ [(kW/m^{2}K)^{2}s]	Φ (kW^2/m^3)	ΔH_c (kJ/g)	L (kJ/g)	Q'' (MJ/m^2)
R 4.01, FR. Chipboard	505	507	4.024	0.0	9.2	10.0	34.2
R 4.02, Gypsum	515	517	0.549	0.0	6.4	4.8	2.2
R 4.03, PU/Alum.	---	---	---	0.0	16.3	---	32.9
R 4.04, PU/Paper	250	77	0.199	8.7	18.9	5.5	30.8
R 4.05, Ext. PS40	275	77	1.983	1.2	27.8	4.0	38.7
R 4.06, Acrylic	195	195	2.957	---	24.1	1.6	89.5
R 4.07, FR. PVC	415	352	1.306	0.2	9.9	10.4	16.1
R 4.08, 3-Layer PC	495	167	1.472	0.0	19.5	3.3	58.1
R 4.09, Mass Timber	330	77	0.530	6.9	16.3	17.5	68.2
R 4.10, FR. Plywood	480	197	0.105	0.7	11.2	9.3	51.8
R 4.11, Plywood	290	147	0.633	2.2	11.9	7.3	64.6
R 4.20, Exp. PS40	295	77	1.594	4.2	27.5	7.3	33.9
R 4.21, Exp. PS80	490	77	0.557	7.1	26.9	12.7	25.5

4.3.1 R 4.01, Fire Retarded Chipboard.

The results of the room-corner test show a low energy release rate with minimal flame spread for the first ten minutes. After the ignition burner was increased to 300 kW, the energy release increased to approximately 700 kW after about 5 minutes. However, a flashover energy release rate of 1,000 kW was never achieved. The model prediction shows a similar trend as the full-scale prediction except that the maximum predicted energy release rate is approximately 400 kW. The general performance of the fire retarded chipboard is predicted, however the quantity of the energy released is substantially under-predicted.

The under-prediction by the model may be a direct result of the calculation of the heat of gasification. If the $L_{peak\ avg.}$ value used for the basic prediction (10.0 kJ/g) is too high, the energy release rate may be lower than expected:

$$\dot{Q}'' = \dot{q}''_{net} \frac{\Delta H_C}{L}$$

Therefore the overall average value, 4.5 kJ/g, was input into the model. As Figure 4.3 indicates, this L value allows the fire retarded chipboard to reach 1 MW. This indicates that a lower heat of gasification value may be more appropriate for the chipboard, but that the overall value is too low.
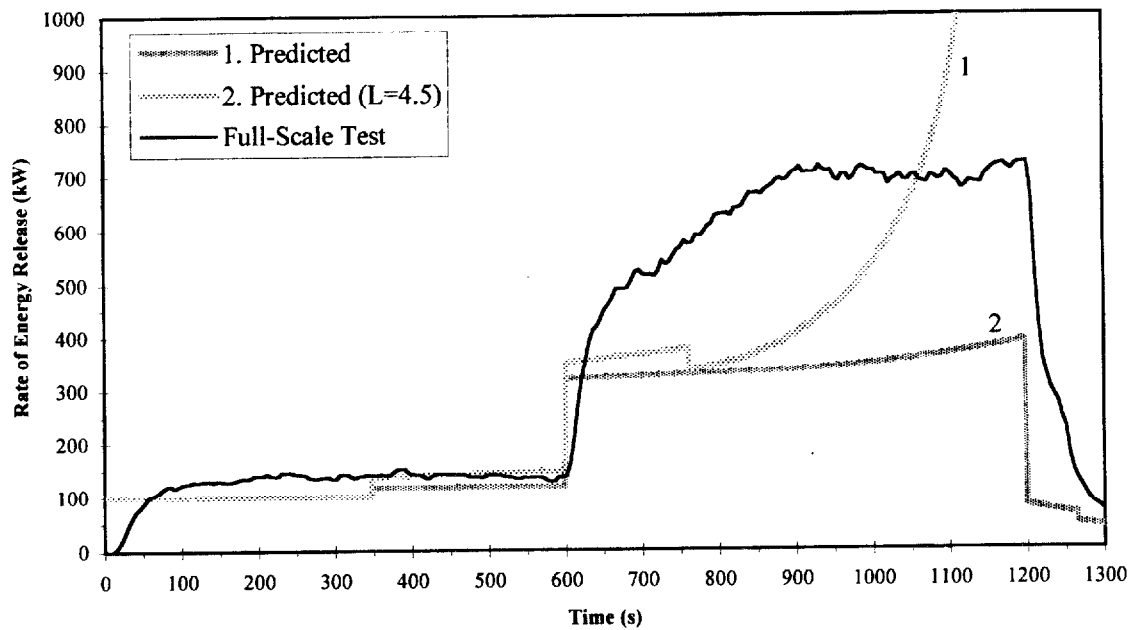
Figure 4. 3: Full-Scale Energy Release Rate for Fire Retarded Chipboard, R 4.01.

4.3.2 R 4.02 Paper Faced Gypsum Board.

Observations from the full-scale test indicate minimal heat release and flame spread during the first ten minutes. After the ignition burner was increased to 300 kW, there was some flame spread along the ceiling resulting in a slight increase in energy release. However, this diminished as the paper facing stopped burning.

The basic prediction shows minimal energy release during the first ten minutes followed by a tremendous increase in the energy release rate approximately 1 minute after the ignition burner is increased. As mentioned previously, thin materials are difficult to predict and the paper facing is basically a thin covering over a non-combustible material. Furthermore, the rapid burning of the paper and the slow, steady

moisture evaporation make paper faced gypsum board an extremely difficult material to model.

In order to predict the performance of the gypsum board the heat of gasification (L) is increased by 50% (i.e. 1.5·L) and the total energy per unit area (Q") is reduced by 50% (i.e. 0.5·L). Figure 4.4 indicates that both adjustments provide similar predictions of the performance. However, these adjustments were arbitrarily determined and were merely an attempt to measure the sensitivity of the model for such a complex material.
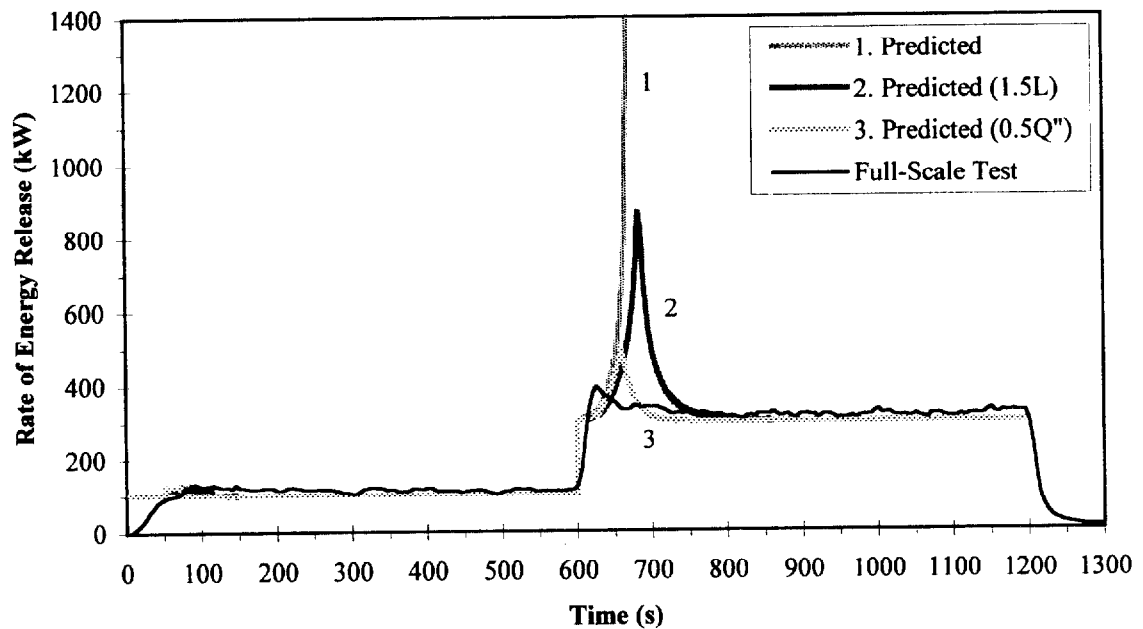
Figure 4. 4: Full-Scale Energy Release Rate for Paper Faced Gypsum Board, R 4.02.

4.3.3 R 4.03 Polyurethane Foam Panel with Aluminum Facing

Since material properties could not be extrapolated from the Cone tests for the aluminum faced foam, the properties for the paper faced foam, R 4.04, are used.

In the room-corner test, the aluminum facing near the ignition burner became damaged after about 14 seconds. This allowed the polyurethane to become exposed to direct flame impingement by the ignition burner. After 27 seconds large portions of the ceiling were ignited and after about 40 seconds the energy release rate reached 1 MW and flames were observed coming out the doorway.

The model predicts the ignition of the material after about 2 to 3 seconds and after 9 seconds the energy release rate is above 1,000 kW. To account for the melting of the foam, the total energy per unit area (Q'') is reduced by 70% to 9.9 MJ/m^2 and the model predicts a similar fire growth. This indicates that even with a large portion of the material gone, the fire will still tend to grow at an amazingly fast rate.

The heat of gasification is then increased by a factor of 2 in order to possibly account for some of the initial reflection of the incident heat flux by the aluminum facing. As Figure 4.5 indicates, this prediction produces a 1 MW energy release rate after 22 seconds. This, therefore indicates that although the calculated heat of gasification values for the paper faced foam are very consistent, they may be too low to predict the performance of the aluminum faced polyurethane foam. These discrepancies are most likely due to the use of the paper faced foam properties to predict performance in the full-scale test. The aluminum facing no doubt delayed the ignition of the foam producing some of the differences seen in the Figure.
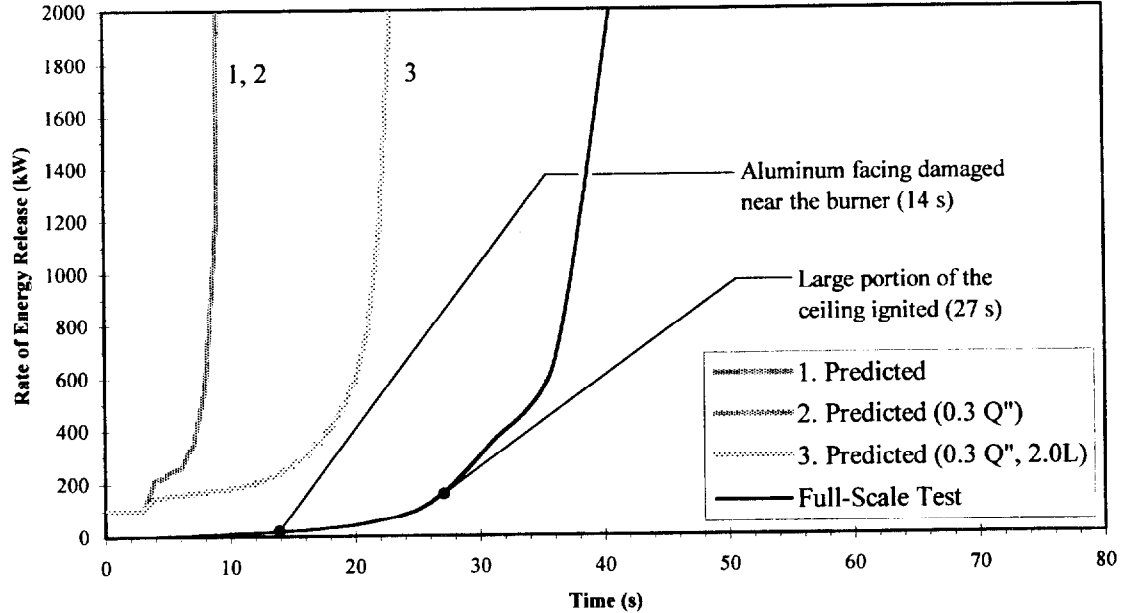
Figure 4. 5: Full-Scale Energy Release Rate for Polyurethane Foam Panel with Aluminum Facing, R 4.03, Using Material Properties for Polyurethane Panel with Paper Facing, R 4.04.

The polystyrene foam clearly indicates a material that melts and drips from the walls and ceiling. However as Figure 4.6 indicates, the model prediction with the unadjusted Cone properties appears to do a reasonable job of predicting the initial peak in the energy release rate. There is approximately 30 seconds difference between the prediction and experimental test results.

To simulate melting, the total energy per unit area is reduced to 30% of the original value: 11.6 MJ/m². This adjusted prediction provided the same rapid fire growth as the original. The total energy is then further reduced by a factor of 1/2, to 15% of the original value. This adjustment indicates a slight rise in the energy release rate immediately after ignition followed by a decay to the baseline energy release rate from the burner. As in the full-scale test when the ignition burner output is increased,

66

there is a tremendous increase in the energy release rate and 1,000 kW is reached at 614 seconds.

In an attempt to better predict the actual performance of the material a total energy per unit area value between the previous two is chosen: 22%. This value predicts the initial energy release rate peak extremely well, but does not indicate the decrease in energy release or the increase associated with the burner output increase.

The vigorous melting of polystyrene foam indicates that it is extremely difficult to model. However, by reducing the total energy per unit area in order to simulate melting effects, reasonable predictions can be achieved.

4.3.4 R 4.05, Fire Retarded Extruded Polystyrene Board

The 40 mm thick extruded polystyrene board ignited after 20 seconds in the room-corner test. After 85 seconds, the material on the ceiling was melting and dripping onto the floor. Fifteen seconds later the energy release rate reached 1 MW. Flames could not be seen coming from the doorway, however thick, black smoke emanating from the room may have obscured them. After about 2 minutes, the energy release rate began to reduce and after 3 minutes only the flames from the corner ignition burner were present. The burner heat output was increased to 300 kW at 10 minutes. Twenty seconds later the energy release rate was above 1,500 kW and melted, burning polystyrene droplets were falling from the ceiling. Flames could still not be observed out the doorway, but thick black smoke was once again emanating from the opening. After the fire was extinguished almost all of the material was either burned or melted.

2000
1800
1600
1400
1200
1000
800
600
400
200
0

Rate of Energy Release (kW)

1, 2   3   4

Melted, burning
droplets falling from the
ceiling (620 s)

Ceiling material
melting (85 s)

1. Predicted
2. Predicted (0.3Q")
3. Predicted (0.22Q")
4. Predicted (0.15Q")
Full-Scale Test

0   100   200   300   400   500   600   700   800   900   1000

Time (s)
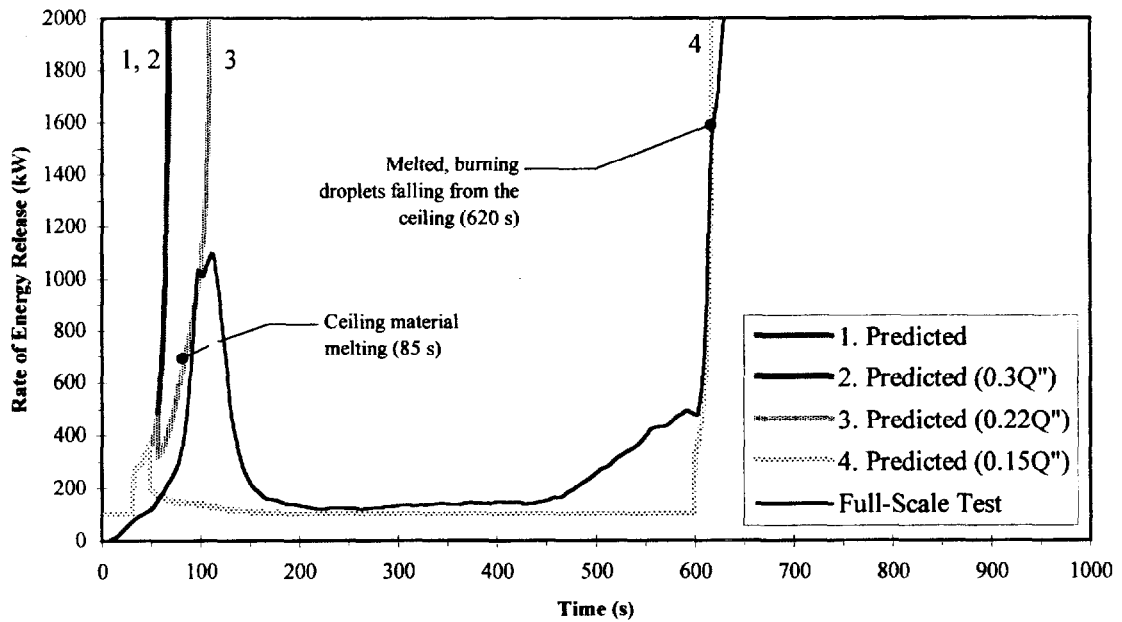
Figure 4. 6: Full-Scale Energy Release Rate for Extruded Polystyrene Board, R 4.05.

4.3.5 R 4.06, Clear Acrylic Glazing

The sheets of acrylic glazing ignited after 1 minute in the full-scale room-corner test. Once ignited, the acrylic began to melt and form a small burning pool near the burner. After 90 seconds the ceiling material had ignited and 15 seconds later burning, melted droplets were falling to the floor. After 130 seconds, an approximately 2 m² pool of melted acrylic was burning on the floor near the ignition burner. About 5 seconds later the energy release rate reached 1 MW. After extinguishment it was observed that most of the material was burnt or melted and melted acrylic covered about half of the floor area. Unlike the extruded polystyrene which had a tendency to melt and form droplets, the acrylic mostly appeared to melt and flow away from the wall and ceiling in sheets.

This material also represents a significant challenge for the fire growth model. The basic prediction identifies ignition after 21 seconds and a 1 MW energy release rate 6 seconds later. This prediction underestimates the "flashover" of the space by about 2 minutes. Therefore, the Q" value is reduced to 25% of the original value in order to simulate the significant melting that occurred. As Figure 4.7 indicates, this reduction of the amount of energy available from the acrylic had no effect on the prediction. This indicates that even with 75% of the material gone, the model still predicts the same rapid fire growth and flashover. The heat of gasification value is then arbitrarily increased by a factor of 3 to determine the sensitivity of the model and to determine if a more appropriate L value should be used. This increased L value provides the same rapid fire growth only it takes 50 seconds to reach 1,000 kW, indicating that the calculated L value may in fact be lower than that of the actual material. However the highest calculated value from Table 3.5 is only twice as large as the peak average value used. This discrepancy remains unexplained although the rapid flashover of the acrylic glazing is predicted and represents a worst-case scenario.

Although the full-scale fire growth for acrylic is rapid by typical room-corner test standards, the predicted growth is much more rapid. The more gradual growth in the test is no doubt due to the melting and falling away of the acrylic. Materials such as this are even more difficult to model due to the very rapid reduction in material available for burning. It is difficult to accurately determine when a section of acrylic will begin to melt and then to predict how much of the material will ooze from the walls and ceiling. The current predictions are reasonable and identify the potential for rapid fire growth. However, they do not necessarily account for the actual performance of

acrylic glazing. With repeated full-scale testing and modeling of similar materials a
method of determining the material properties may be developed which will allow for a
more appropriate prediction. At this time no further conclusions regarding the material
properties of the acrylic glazing and there applicability to this type of modeling can be
made.
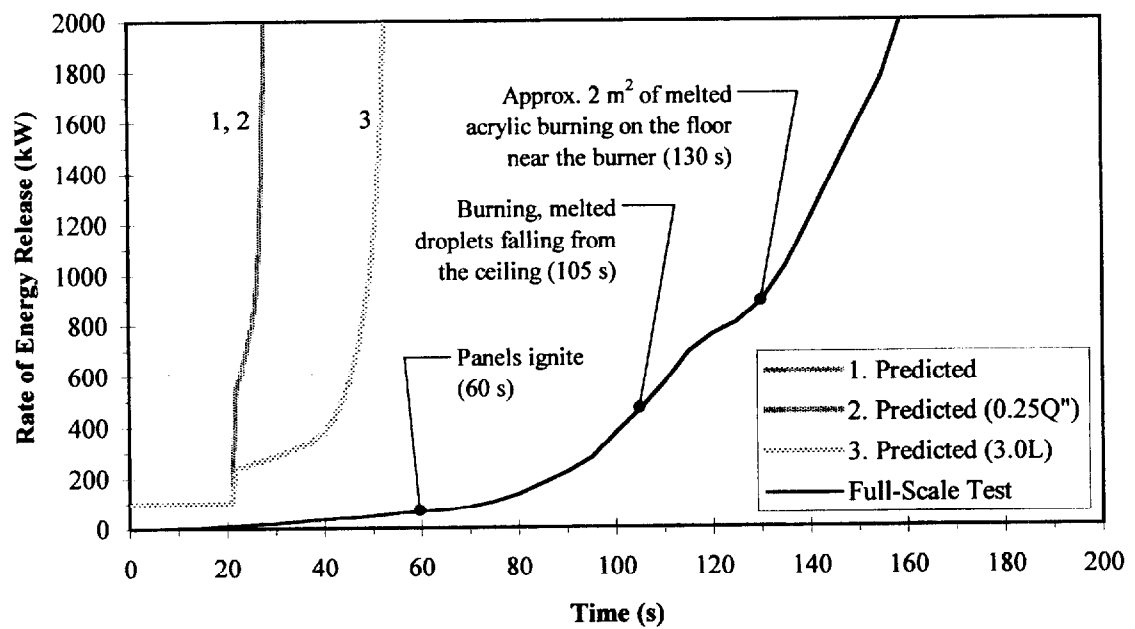
Figure 4. 7: Full-Scale Energy Release Rate for Acrylic Glazing, R 4.06.

4.3.6 R 4.07, Fire Retarded PVC

Thirty seconds after the ignition burner was ignited, the ceiling panels in the
corner began to deform. After 85 seconds, the material in the corner was melted. This
melting continued throughout the test and after 9 minutes, most of the ceiling material
was melted and fallen to the floor. One minute after the ignition burner was increased

to 300 kW, all of the ceiling material had fallen to the floor. The test went for the full 20 minutes without reaching the 1,000 kW indicative of flashover. In fact as Figure 4.8 indicates, the energy release rate never rose above 400 kW. This material acted much the same way as the clear acrylic glazing, R 4.06, in that it melted and fell off the walls and ceiling in soft sheets. At the conclusion of the test the ceiling panels and most of the wall panels had melted and were lying on the floor in piles.

The prediction of the fire growth for the PVC indicates very little energy release rate during the early portion of the test. However after the ignition burner is increased, the model predicts flashover after 2 minutes. The Q" value was reduced by 50% and 70% to determine if the extensive melting and softening of the PVC sheets could be predicted. As Figure 4.8 suggests, the adjusted Q" values better predict the fire growth, but still indicate peak energy release rates of 1100 and 900 kW, respectively.

As mentioned above, materials that tend to melt, soften and pull away from the walls and ceiling are extremely difficult to model. The methodology of reducing the energy available as the material melts is not very appropriate when entire sheets of the material melt and fall to the floor. The procedure for developing adjusted properties for these types of materials needs to be seriously addressed if any attempt at accurate modeling is going to be conducted.
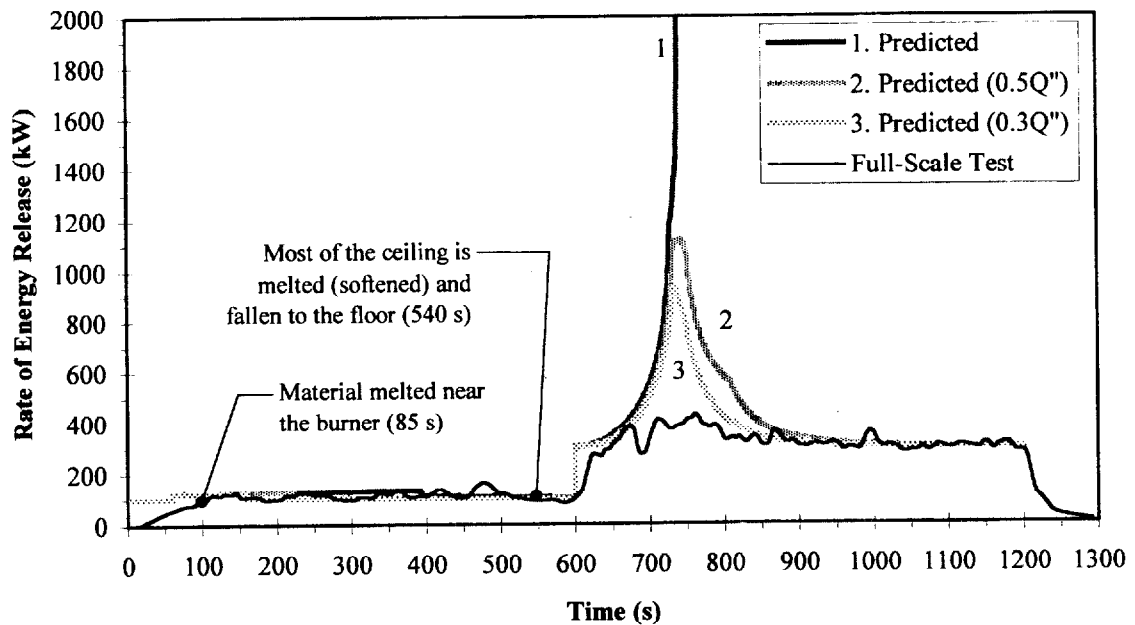
Figure 4. 8: Full-Scale Energy Release Rate for R 4.07 Fire Retarded PVC.

4.3.7 R 4.08, 3-Layered, Fire Retarded Polycarbonate Panel

The ceiling panels above the ignition burner began to deform 15 seconds after ignition of the burner. After 60 seconds melted material from the walls and ceiling were forming into droplets. There did not appear to be ignition or burning of any material besides in the vicinity of the ignition burner. This limited burning allowed the energy release rate to reach approximately 275 kW, but this rate quickly reduced to a level just above the baseline energy release rate from the burner. After the energy release rate increase of the ignition burner at 10 minutes, the polycarbonate panels began to soften and move away from the burner flame. Figure 4.9 reveals that very little burning occurred throughout the duration of the test except for a small burning pool of melted material near the burner. After the test all of the ceiling and a majority of the walls had melted and fallen to the floor.

72

Three-layered polycarbonate paneling poses a similar modeling challenge to the acrylic glazing and the PVC. The initial run of the model predicted material ignition after 120 seconds and a 1 MW energy release rate after 230 second. As before, the total energy per unit area value was reduced by 50% to simulate the melting of the panels. This adjustment provided the same prediction as with the original value. Decreasing Q" further (20% of the original value) indicated a slight energy release rate increase followed by burnout and no significant heat release. However, after 10 minutes, the 300 kW ignition burner cause flashover after 70 seconds. Therefore, Q" was reduced further still. At 10% of the original value, 5.8 MJ/m^2, the model predicted an increase to a peak energy release rate of about 800 kW after 700 seconds followed by a decrease and no significant heat release for the duration of the test.

4.3.8 R 4.09, Varnished Massive Timber

The lacquer finish ignited after 25 seconds and after 45 seconds the ceiling above the ignition burner had ignited. At approximately 90 seconds, flame spread down the walls clearly observed. Ten seconds later, the energy release rate was over 1 MW and ten seconds after that flames were observed out the doorway. After extinguishment, the entire ceiling and about 50% of the walls were charred. The lower half of the walls were slightly discolored but generally undamaged.
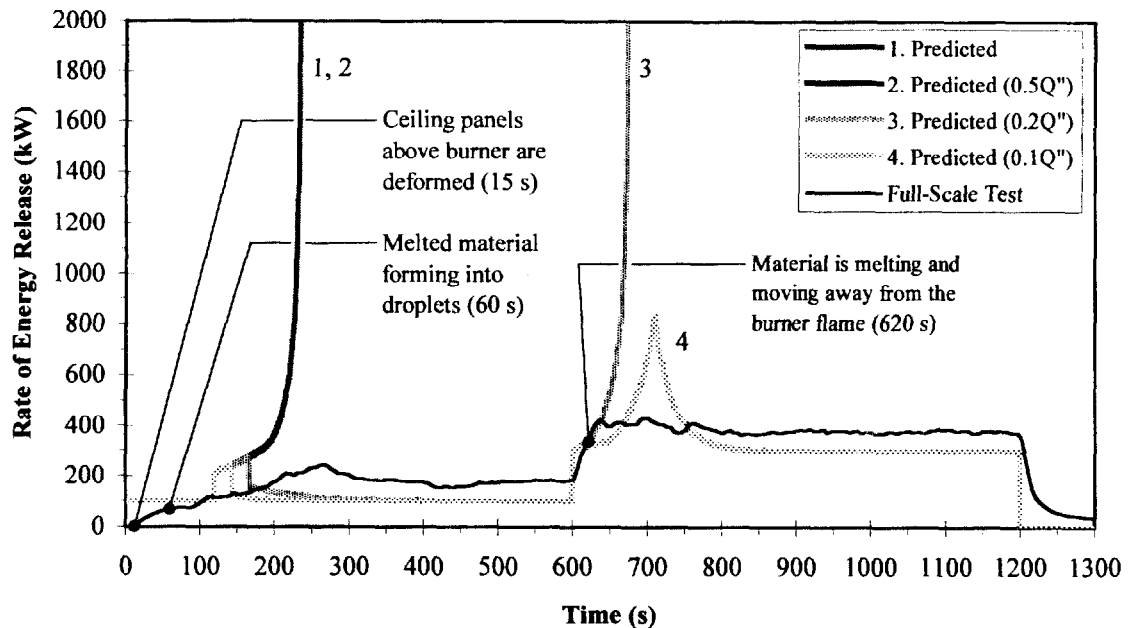
Figure 4. 9: Full-Scale Energy Release Rate for 3-Layered, Fire Retarded Polycarbonate Panel, R 4.08.

The initial run of the model predicts a minimal energy release rate (approximately 160 kW) during the first ten minutes of the test. Twelve seconds after the ignition burner heat flux is turned up, the energy release rate exceeds 1,000 kW. This poor fire growth prediction is no doubt due to the unusually high peak and peak average heat of gasification values for massive timber (as mentioned in Section 3.5). Therefore the overall average value of 6.5 kJ/g was used. This value provided a fire growth prediction that was more consistent with the full-scale test data but with an approximately 35 second difference in the times to flashover. The heat of gasification was then arbitrarily increased to 9.0 kJ/g in order to determine the appropriateness of the overall average value and the sensitivity of the model. As Figure 4.10 indicates, this increased L value provides an extremely accurate prediction of the full-scale test. A

heat of gasification value of 9.0 kJ/g is completely arbitrary but indicates that although

the $L_{overall\ avg.}$ used is not too far off, a higher value may be more appropriate.
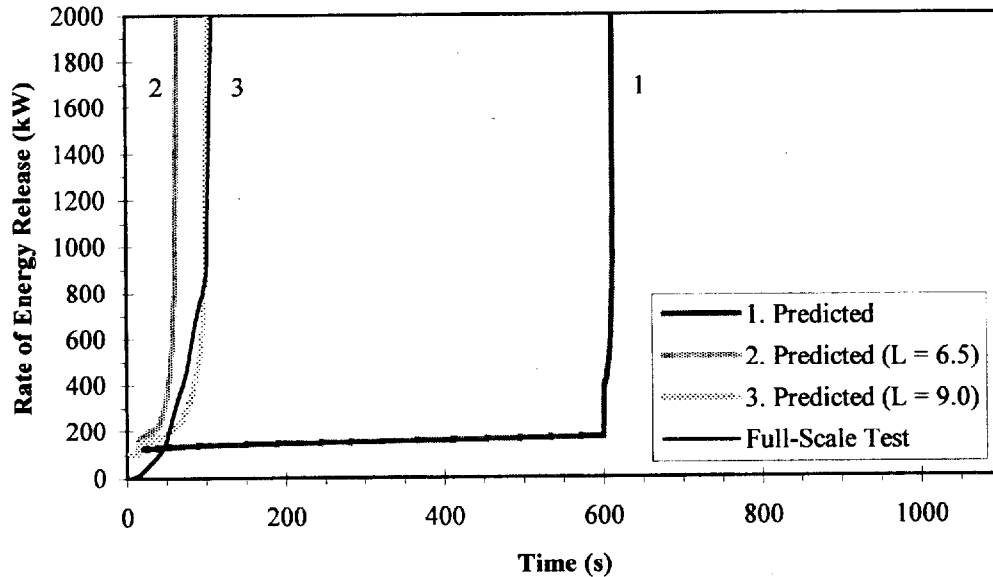
Figure 4. 10: Full-Scale Energy Release Rate for Varnished Massive Timber, R 4.09.

4.3.9 R 4.10, Fire Retarded Plywood

The room-corner test for fire retarded plywood showed a limited energy release

rate for the first ten minutes. The ignition burner flames merely darkened and charred

the material located in the corner. Ten seconds after the ignition burner was increased

to 300 kW, extensive flame spread across the ceiling was observed. After 630 seconds

the energy release rate reached 1 MW and 5 seconds later, flames were observed

coming out the door. After 645 seconds, flames were spreading down the walls.

As Figure 4.11 indicates, the model does a good job of predicting the

performance of the fire retarded plywood. However, the dependence of flashover on

the increase of the energy release rate form the ignition burner does not provide a great deal of insight into the appropriateness of the material properties used. Therefore it must be assumed that the properties derived for the Cone for fire retarded plywood are reasonably legitimate and can be used to predict performance in the ISO 9705 room-corner test.
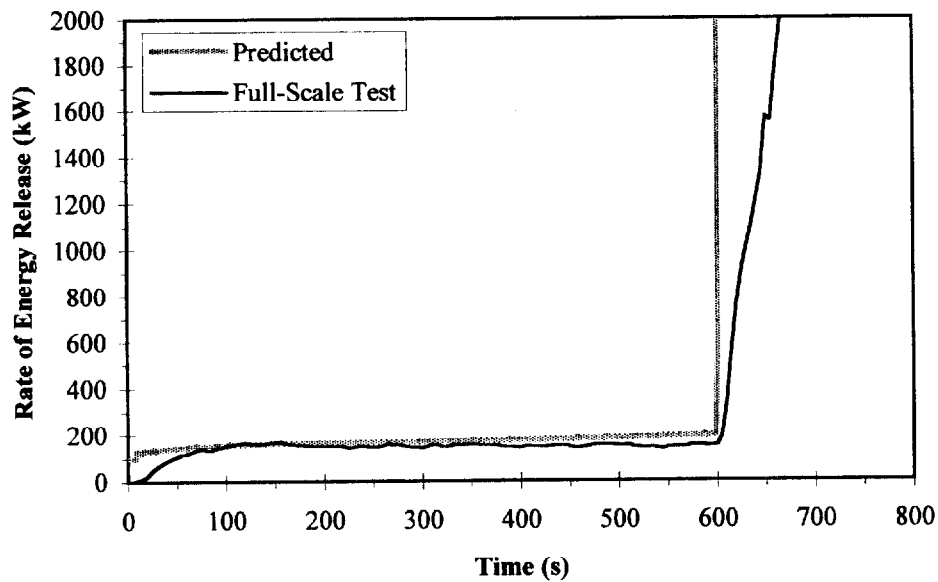
Figure 4. 11: Full-Scale Energy Release Rate for Fire Retarded Plywood, R 4.10.

4.3.10 R 4.11, Normal Plywood

The plywood ignited 45 seconds after ignition of the burner. Another 45 seconds later 50% of the ceiling was ignited and flames were beginning to spread down the walls. At 134 seconds flames were observed out the door and after another 4 seconds the energy release rate reached 1,000 kW. After the test, most parts of the walls and ceiling were charred.

The model does a reasonable job of predicting the flashover of the plywood but underestimates the time by about 30 seconds. To determine the appropriateness of the $L_{peak\,avg.}$ by the energy release rate method and the sensitivity of the model to this value, the $L_{peak\,avg.}$ value by the mass loss rate method (8.0 kJ/g) is used. Figure 4.12 reveals that this increased L value provides a slightly better prediction of the performance of the plywood. Although the heat of gasification derived from the mass loss data provides a better prediction than the energy release rate data, both predictions demonstrate the hazardous nature of normal plywood and the rapid flashover that results.
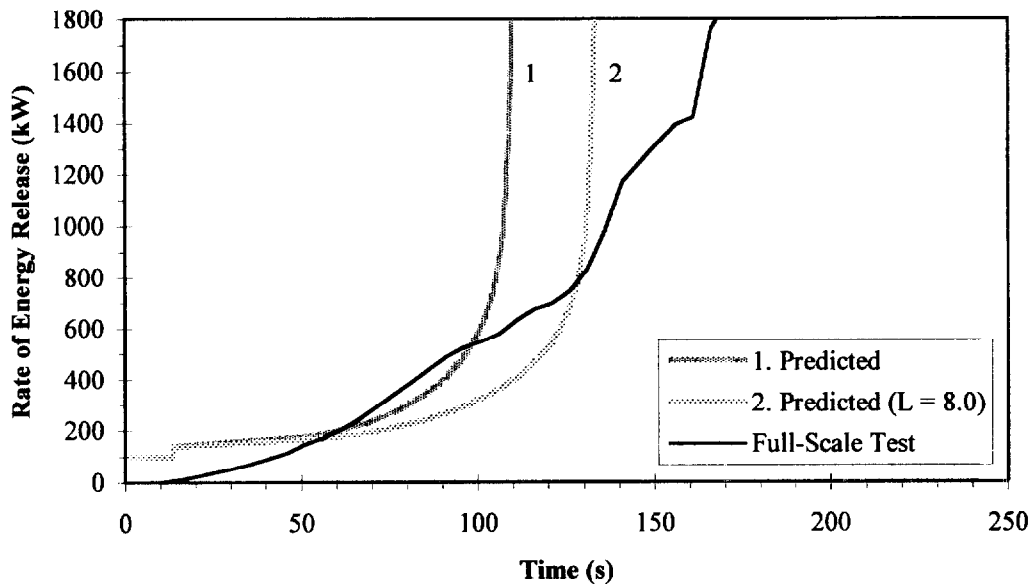
Figure 4. 12: Full-Scale Energy Release Rate for Normal Plywood, R 4.11.

4.3.11 R 4.20, Fire Retarded Expanded Polystyrene Board (40 mm)

The expanded polystyrene board began to melt quickly after the ignition burner was ignited. Burning, melted droplets were observed after 20 seconds and melted

material was running down the walls after 40 seconds. After 80 seconds, polystyrene was dripping from the entire ceiling. About 4 seconds later the energy release rate reached 1 MW and a few flames were observed coming from the doorway. As Figure 4.13 indicates, the energy release rate from the fire then quickly reduced and remained close to the ignition burner energy release rate for the duration of the test. A slight increases occurred immediately after the increase of the ignition burner due to melting material burning away, but this increase was small and short lived. After the test almost all of the polystyrene was burned or melted from the walls and ceiling.

Despite the substantial melting that occurred, the model does an excellent job of predicting the performance of the expanded polystyrene with flashover occurring after 90 seconds. The reduced Q'' value which was used to simulate melting—30% of the original value—also provides a reasonable prediction, but with a slightly longer time to flashover. The model is able to accurately predict the flashover of the expanded polystyrene because although the material begins to melt soon after the test begins, it does not fall from the walls and ceiling in large pieces or sheets. Although melting droplets begin to fall from the entire ceiling, there is still enough material available to produce an energy release rate above 1 MW. However, once this high energy release rate is reached, most of the material has melted away and there is not enough to sustain burning.
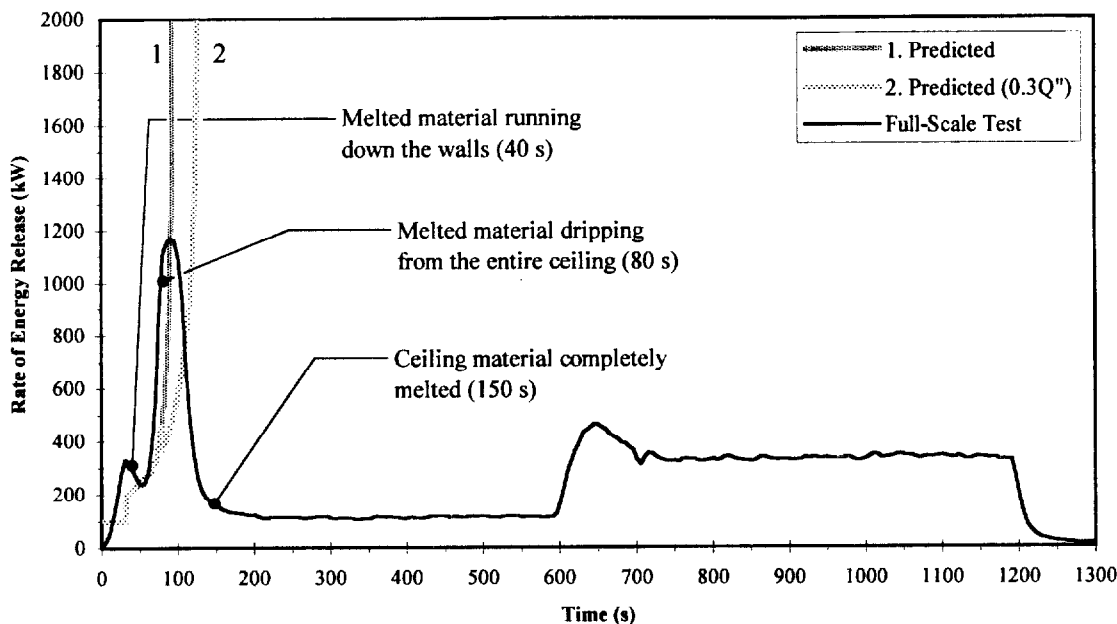
Figure 4. 13: Full-Scale Energy Release Rate for Fire Retarded Expanded Polystyrene Board (40 mm), R 4.20.

4.3.12 R 4.21, Fire Retarded Expanded Polystyrene Board (80 mm)

Like the 40 mm board, the 80 mm expanded polystyrene began to melt quickly in the room-corner test. After 15 seconds the material above the ceiling began to melt and melted material was running down the walls after 30 seconds. After approximately 105 seconds material was dripping from the entire ceiling, flames were coming out the doorway and the energy release rate reached 1 MW. Immediately after flashover the energy release rate rapidly reduced—approximately 50% of the walls had been consumed or melted. For the next 7 minutes burning polystyrene was minimal and could only be seen in the ignition burner corner. After the ignition burner was increased to 300 kW, the melted material immediately next to the burner ignited and caused a slight increase in the energy release rate. As Figure 4.14 indicates, the fire began to

decay just like the 40 mm polystyrene board but then rapidly grew and exceeded 1,000 kW again at 798 seconds.

The initial prediction made by the model shows the same rapid fire growth as the full-scale test but happening approximately 3 minutes later. The heat of gasification used for this prediction, 12.7 kJ/g, seemed relatively high, especially when compared to the L value for the 40 mm board, 7.3 kJ/g. Therefore, in order to determine the accuracy of the heat of gasification, the lower value was used. This prediction provided good agreement with the initial energy release rate peak from the test, but did not demonstrate the decay and subsequent rise. This seems to indicate that the $L_{peak\,avg.}$ by the energy release rate method used may be too high for the material. Since there seems to be no consistency between the L values for the 40 and 80 mm polystyrene boards, no definitive judgement can be made on which value represents the most appropriate value for this type of material.

The total energy per unit area was reduced to simulate the melting of the polystyrene, but did not provide an accurate prediction. As with the 40 mm expanded polystyrene board, the melting of the material does not seem to be as critical a factor as with the extruded polystyrene, R 4.05. This difference remains unexplained.
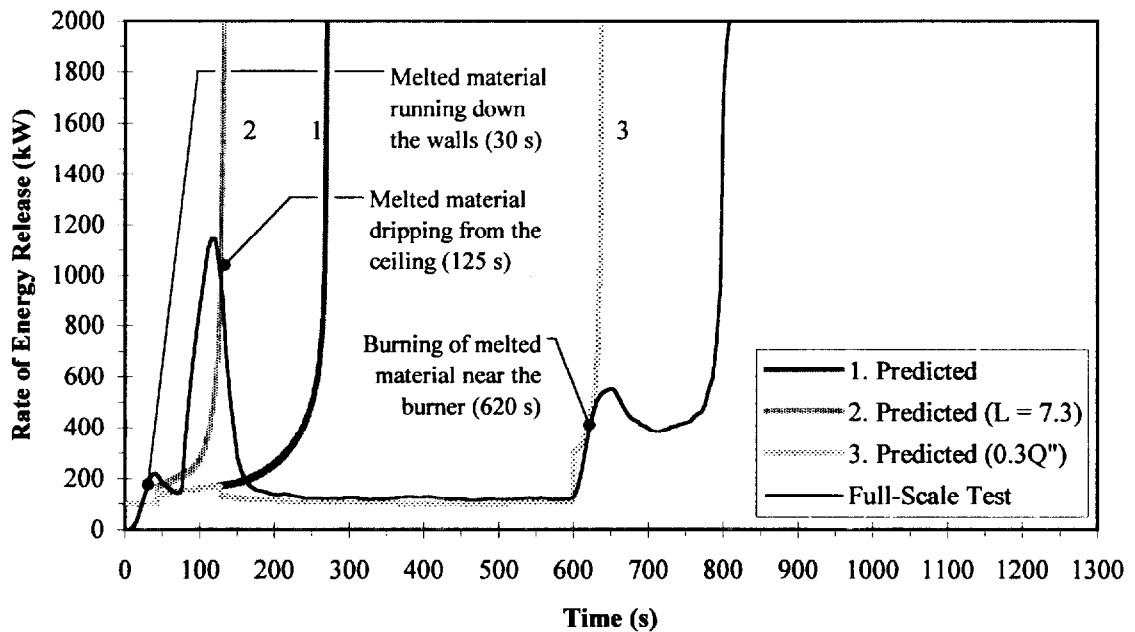
Figure 4. 14: Full-Scale Energy Release Rate for Fire Retarded Expanded Polystyrene Board (80 mm), R 4.21.

4.3.13 Time to Reach Flashover

As mentioned above the key factor for determining material performance in the room-corner test is the amount of time that it takes the burning material to take the room to flashover or an energy release rate of 1,000 kW. Table 4.2 shows the time to reach 1 MW for the full-scale tests and the predictions by the model. The "Basic Predictions" represent the use of the "peak average" heat of combustion and heat of gasification values for all materials. The "Adjusted Predictions" represent the time associated with a particular adjusted material property. The purpose of these adjusted predictions is to indicate the sensitivity of the model, analyze potentially erroneous material properties and to provide a possible means for handling materials that melt, drip and are generally poorly represented in the room-corner test. It should be noted that an adjusted

81

prediction that is in excellent agreement with the full-scale test might be due to an

arbitrary sensitivity adjustment to a material property and might not be necessarily

legitimate.

Table 4. 2: Comparison of the Time to Reach Flashover (1,000 kW) for the Full-Scale Room-corner Tests and the Model Predictions.

Material	Time to Flashover, $\dot{Q}$ = 1,000 kW (s)			
	Full Scale	Basic Prediction	Adjusted Prediction	Adjusted Material Property
R 4.01, FR. Chipboard	∞	∞	1113	$L = 4.5$ kJ/g
R 4.02, Gypsum	∞	666	∞	$1.5 \cdot L$ or $0.5 \cdot Q''$
R 4.03, PU/Alum.	40	----	----	----
R 4.04, PU/Paper	----	9	22	$0.3 \cdot Q''$ & $2.0 \cdot L$
R 4.05, Ext. PS40	96 & 614*	64	99 616	$0.22 \cdot Q''$ $0.15 \cdot Q''$
R 4.06, Acrylic	141	27	50	$3.0 \cdot L$
R 4.07, FR. PVC	∞	726	730 ∞	$0.5 \cdot Q''$ $0.3 \cdot Q''$
R 4.08, 3-Layer PC	∞	230	669 ∞	$0.2 \cdot Q''$ $0.1 \cdot Q''$
R 4.09, Mass Timber	104	612	62 100	$L = 6.5$ kJ/g $L = 9.0$ kJ/g
R 4.10, FR. Plywood	631	601	----	----
R 4.11, Plywood	138	108	131	$L = 8.0$ kJ/g
R 4.20, Exp.PS40	84	90	118	$0.3 \cdot Q''$
R 4.21, Exp.PS80	107 & 798*	268	129 636	$L = 7.3$ kJ/g $0.3 \cdot Q''$

* Energy release rate ($\dot{Q}$) exceeded 1,000 kW more than one time.

4.4 Lateral Flame Spread

In order to determine the sensitivity of the lateral flame spread, the material's were modeled with the minimum temperature necessary for flame spread ($T_{s, min}$) reduced to ambient (20 °C). The results of these predictions were almost identical to those presented above—using the $T_{s, min}$ determined from test methods. In fact, the times for the room to reach 1 MW were identical or within ±1 second. This indicates that the lateral flame spread does not play a very significant role in the predicted performance of the LSF materials in the ISO 9705 protocol. This may be true for all materials, however further testing and analysis would have to be conducted to eliminate lateral flame spread as a significant form of flame spread and fire growth.

4.5 Large-Scale Room Fire Experiments

Previous room-corner testing has typically been conducted using the standard 2.4 m x 3.6 m x 2.4 m room. In an attempt to determine whether Quintiere's fire growth model can accurately predict the fire growth of materials in a different size compartment, results from a significantly larger test room are compared to results provided by the model.

Large-scale room fire experiments were conducted by Kokkala, Göransson, and Söderbom at the Technical Research Center of Finland [28]. These experiments involved a test room which was 4.9 m high, 9.0 m wide and 6.75 m deep. A 2.0 m by 2.0 m door was provided in the center of the longer wall. The ignition source consisted of three 0.17 m x 0.17 m propane gas burners, as specified by the ISO 9705 Room-

Corner Test standard [22] and as shown in Figure 4.15. The ignition source for the first

twenty minutes of the test are identical to the procedure proposed by the ISO standard:

100 kW for 10 minutes followed by 300 kW for an additional 10 minutes from the

central burner. However, after 20 minutes the energy release rate was increased to 900

kW using all three of the burners.

Single 0.17 m Square
Propane Gas Burner:
Used for 100 & 300 kW

All Three Burners:
Used for 900 kW
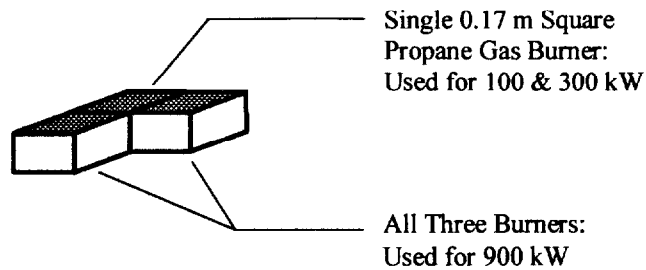
Figure 4. 15: Large-Scale Test Ignition Burner Used by Kokkala *et. al.*

The five materials tested in the large-scale room experiments are as follows:

- Textile wall covering on gypsum board.

- Combustible facing on mineral wool.

- Fire retarded particle board, Type B1.

- Ordinary birch plywood.

- PVC wall covering on gypsum board.

The walls and ceiling of the large room were lined with material except for the lower

portions of the wall farthest from the ignition burner corner. The ignition, flame spread

and energy release properties for the materials were obtained from the work by

Quintiere, Haynes and Rhodes [37] and are presented in Table 4.3.

Table 4. 3: Ignition, Flame Spread and Energy Release Properties of the EUREFIC Materials.

Material	T_{ig} °C	$T_{s,min}$ °C	$k\rho c$ (kW/m²K)²s	Φ kW²/m³	ΔH_c kJ/g	L kJ/g	Q'' MJ/m²
TEXT./GYP BOARD	386	189	0.97	7.7	7.5	3.1	9.5
Comb. Min. Wool	354	263	0.11	0.86	11.0	9.2	1.7
FR Part. Board	482	482	0.29	---	3.9	1.4	5.5
Birch Plywood	392	164	0.99	13	11.9	6.2	75.5
PVC/Gyp Board	391	367	0.69	8.2	6.5	3.3	11.0

The flame height for a 900 kW ignition source using the burner shown in Figure 4.15 is determined using the correlation by Hasemi provided in Section 6.1.1. The flame heights typically used in the model for 100 kW and 300 kW (1.3 m and 3.6 m respectively) are based on approximations of the continuous flame region [36]. Therefore the continuous flame height for the 900 kW fire was determined to be 5.86 m above the burner which represents a height of 5.94 m above the floor.

The full-scale test results are compared with the model predicted results in Figures 4.16 to 4.20. The comparisons are merely based on a visual comparison of the energy release rate since the 1,000 kW flashover criteria for the standard room is based on geometry and not on ignition burner exposure. No flashover criteria for the large room used in these experiments was available to provide a more detailed analysis. However, the model predicted results seem to provide good agreement with experiments for the combustible faced mineral wool, fire retarded particle board and the PVC wall covering.

The textile wall covering shows reasonable agreement, but the times to a peak energy release rate differ by about 15 minutes. The model predicts an energy release rate in excess of 1200 kW after the ignition burner was increased to 900 kW after 20

minutes while a rate of over 3 MW was measured in the full-scale test. The model predicts incredibly rapid fire growth after about 35 minutes but the full-scale experiments had been stopped by that point due to a substantial decrease in the energy release rate. The reasons for these differences remain unexplained and may possibly be due to the thermoplastic nature of the material. However, the results obtained are the opposite of what has typically seen for foam and plastic materials—the full-scale results are usually much lower than the predicted results due to melting, deformation and dripping.

Surprisingly, the predicted fire growth for the birch plywood is inconsistent with the full-scale results. The model predicts "flashover" immediately following the ignition burner energy release rate to 300 kW while the plywood in the large-scale room did not reach a peak rate until after 19 minutes. The standard room test predictions indicated excellent agreement for normal plywood (R 4.11) and other charring materials. These differences, as well as the differences seen with the textile wall covering, may also be due to the method in which the flame height from the 900 kW burner was determined. A detailed analysis of the ignition burner flame height and incident heat flux is provided in Section 6.
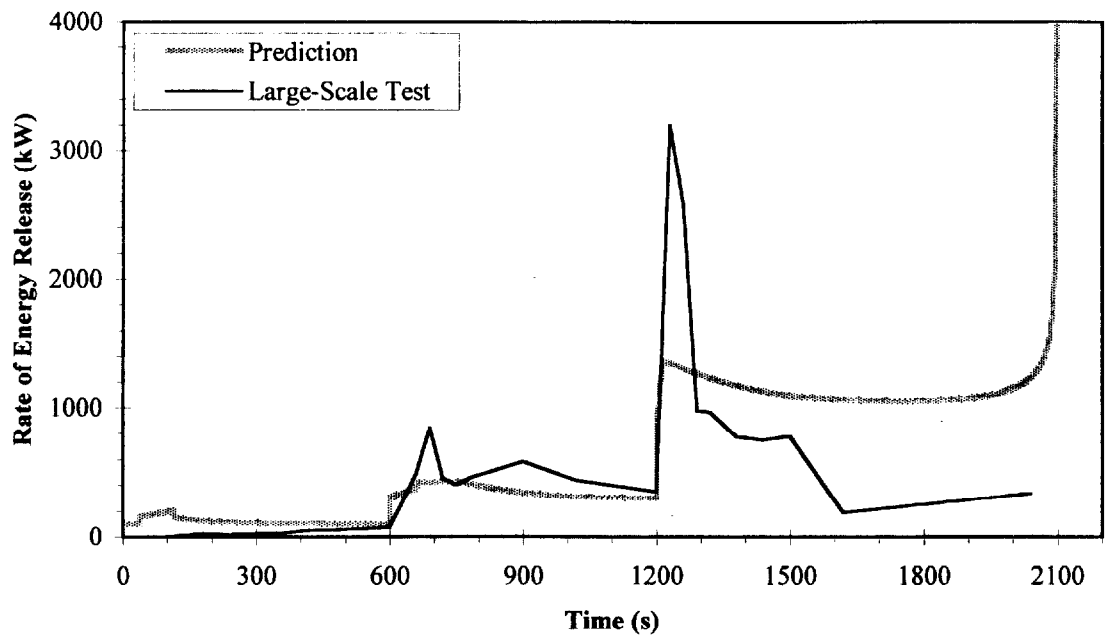
Figure 4. 16: Large-Scale Energy Release Rate for Textile Wall Covering on Gypsum Board.
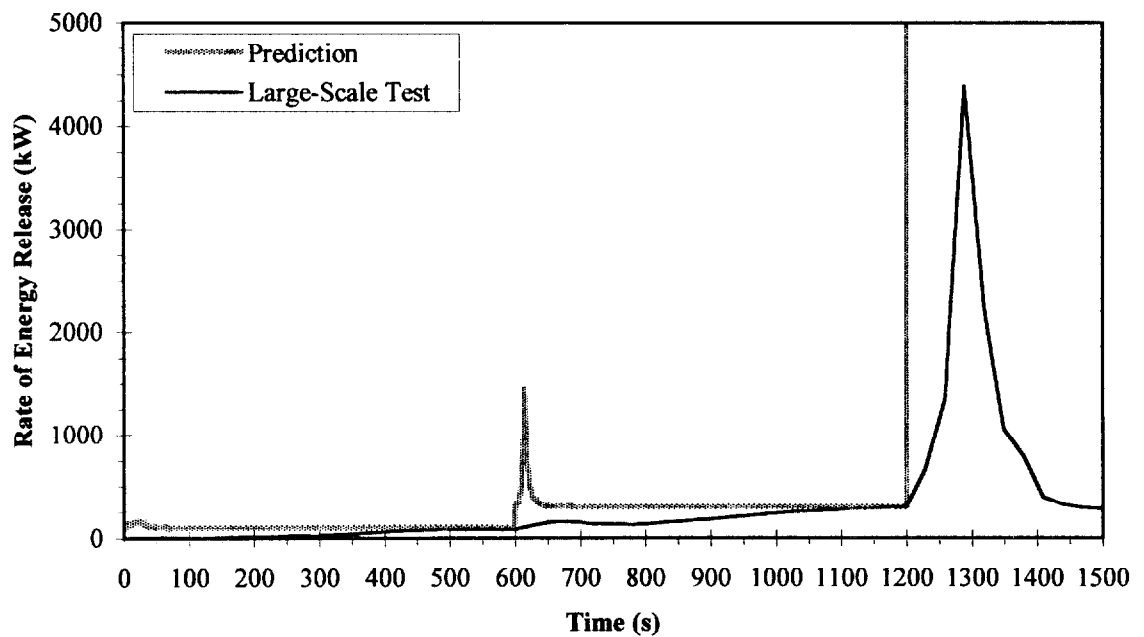
Figure 4. 17: Large-Scale Energy Release Rate for Combustible Facing on Mineral Wool.
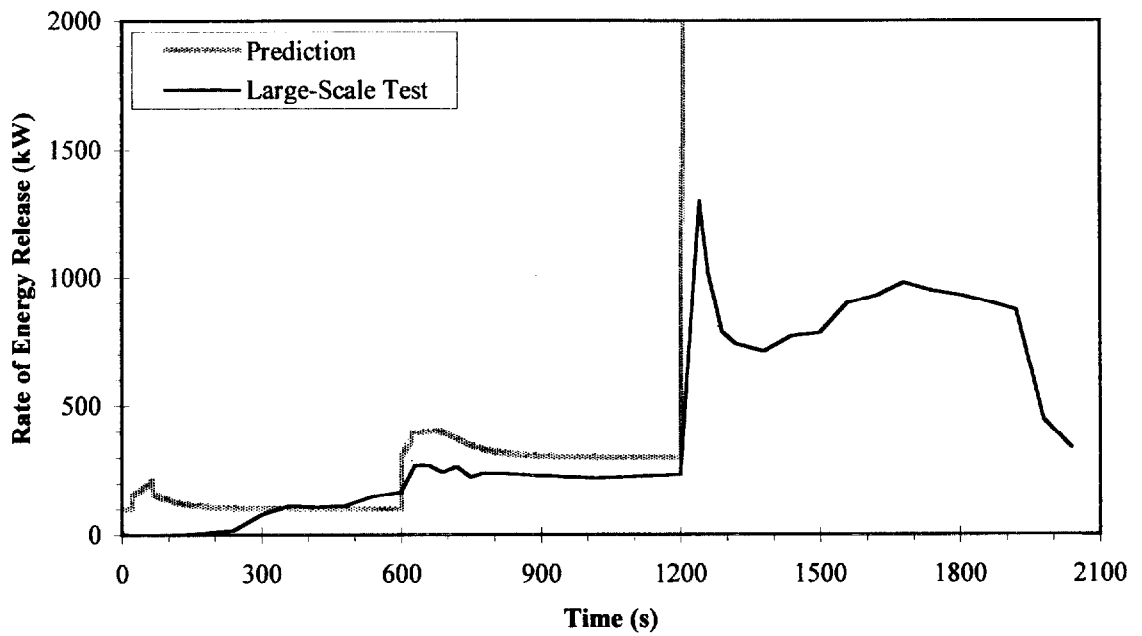
Figure 4. 18: Large-Scale Energy Release Rate for Fire Retarded Particle Board, Type B1.
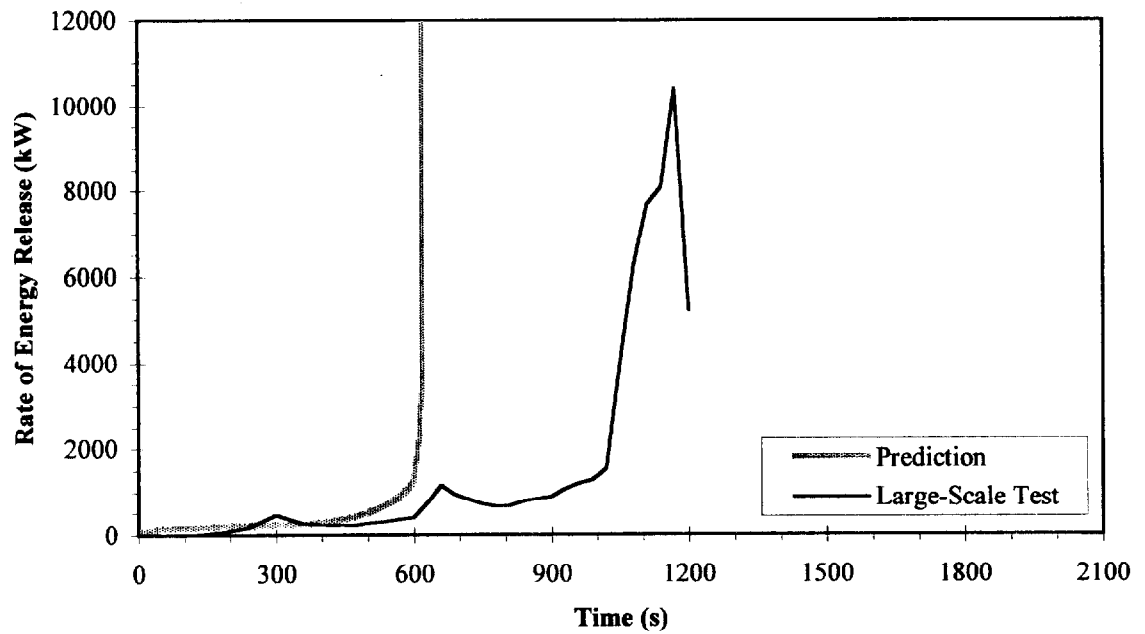
Figure 4. 19: Large-Scale Energy Release Rate for Ordinary Birch Plywood.
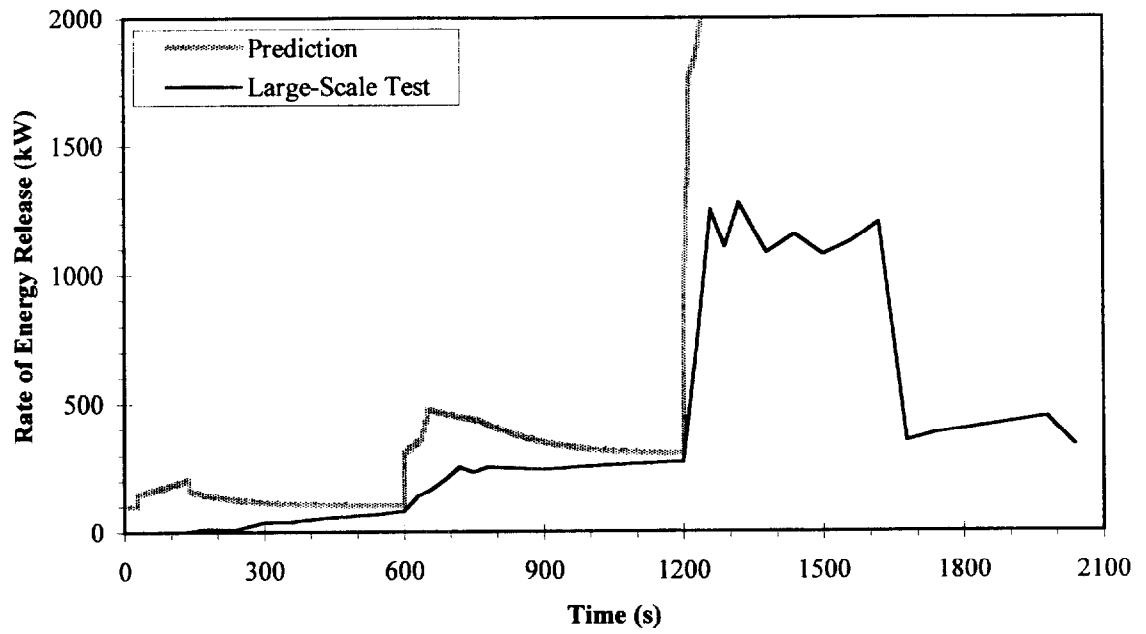
Figure 4. 20: Large-Scale Energy Release Rate for PVC Wall Covering on Gypsum Board.

5. FIRE GROWTH CORRELATION

5.1 Upward Flame Spread Acceleration Factor

The spread of flame can be viewed as a critical event that is dependent on the exposure conditions and material properties. This idea of criticality is that a burning material reaches a point at which it will either grow exponentially or burn out. The potential for the flames to spread becomes a balance of the fuel being heated to ignition, the consumption rate of the fuel and the amount of fuel available [31]. The ability of a material to take a room to flashover and the time associated with the onset of that flashover can be expressed in terms of the upward acceleration of the flame spread. Cleary and Quintiere [9] have developed an empirical parameter (*b*) which can be used to examine the growth of a flame in the standard 2.4 m x 3.6 m x 2.4 m room based on material fire properties:

$$b = k_f \dot{Q}'' - 1 - t_{ig}/t_b$$

where k_f is a flame length coefficient (m^2/kW), $\dot{Q}''$ is the energy release rate per unit area (kW/m^2), t_{ig} is the predicted time to ignition (s) and t_b is the predicted burnout time or burning duration (s). The flame length coefficient is based on a linear approximation of the flame length based on wall fire data and is approximately equal to 0.01 m^2/kW [9].

The energy release rate per unit area of material is calculated by

$$\dot{Q}'' = \frac{\Delta H_C}{L} \left(\dot{q}''_{ig} - \sigma T_{ig}^4 \right)$$

where ΔH_C and L are taken as "peak average" values (from Table 4.1), σT_{ig}^4 represents re-radiant heat flux loss from the surface of the material and $\dot{q}''_{ig}$ is the incident heat flux to the pyrolysis region from the ignition burner flame. This heat flux controls the ignition

of the material and is taken to be constant over the height of the ignition burner flame and equal to 60 kW/m² [36].

The time to material ignition for the spread of flame can be predicted by

$$t_{ig} = \frac{\pi}{4} k\rho c \left(\frac{T_{ig} - T_s}{\dot{q}''_f} \right)^2 \tag{5.1}$$

where $k\rho c$ and T_{ig} come from Table 4.1, T_s is the original surface temperature of the material ($\approx 20\ °C$) and $\dot{q}''_f$ is the heat flux from the extended wall flame. This extended flame heat flux controls upward flame spread and is taken to be approximately 30 kW/m² [36].

The burnout time for a material can be predicted by

$$t_b = \frac{Q''}{\dot{Q}''}$$

where Q'' is the total energy per unit area of material calculated in Section 3.5.

The b parameter for a material can indicate the tendency of the flame to accelerate towards flashover ($b > 0$) or decay until the material burns itself out ($b < 0$). Values of b that are close to zero are considered to be "borderline" materials. This borderline region represents materials where small changes in either the material properties or the exposure conditions can affect the outcome. The time to flashover from the full-scale experiments (t_{fo}) is plotted against the upward flame spread factor in Figure 5.1. The small cluster of points just above $t_{fo} = 600$ s are those materials that did not flashover until the ignition burner was increased to 300 kW.

The time to flashover can also be normalized by dividing it by the time to ignition which is represented by

$$\tau_{fo} = \frac{t_{fo}}{t_{ig}}$$

This dimensionless relationship is plotted with respect to b in Figure 5.2

Figures 5.1 and 5.2 represent the culmination of b values for 13 materials tested in Sweden, 10 materials from the EUREFIC program [25, 37] along with the 12 LSF materials analyzed here: the material numbers are proceeded by an "S", an "E" and an "R", respectively. The EUREFIC material results from the large-scale experiments presented in Section 4.5 are not included in this correlation.

It can be seen that the materials generally follow the empirical correlation. At low, negative b values, most of the materials will not go to flashover ($t_{fo} \rightarrow \infty$). As the b number increases towards positive, the time to flashover decreases. For increasing positive b values the time to flashover appears to be asymptotically decreasing towards 0. The region of borderline materials can also be seen between b values of approximately -1 and 1.

The only materials that do not seem follow the empirical correlation are the polyurethane foam panel with aluminum facing, R 4.04, and acrylic glazing, R 4.06. The polyurethane foam does not fall in line with the other data points only in Figure 5.2. This is due to the incredibly low ignition time of 2 seconds which is calculated from Equation 5.1 using the material properties for the paper faced foam, R 4.03. Since ignition of the foam did not occur in the room-corner test until after the aluminum facing became damaged at 14 seconds, the calculated τ_{fo} value is much lower than expected.

The acrylic glazing did not exhibit a huge deviance from the correlation but a shorter time to flashover was expected for such a high b number. This difference is most

92

likely due to the glazing being such a thin material. As mentioned previously, thin materials tend to have short burn times and are therefore sensitive to changes in material properties and exposure conditions. The glazing probably experienced a great deal of local melting in the vicinity of the ignition burner, which most likely extended the times to ignition and flashover beyond the predicted value.

Surprisingly, even materials that tended to melt, soften, deform and fall off of the walls are well predicted by the b factor correlation. Therefore, it can be implied that this empirical result gives an extremely good categorization of the flashover potential in the ISO 9705 room/corner test.
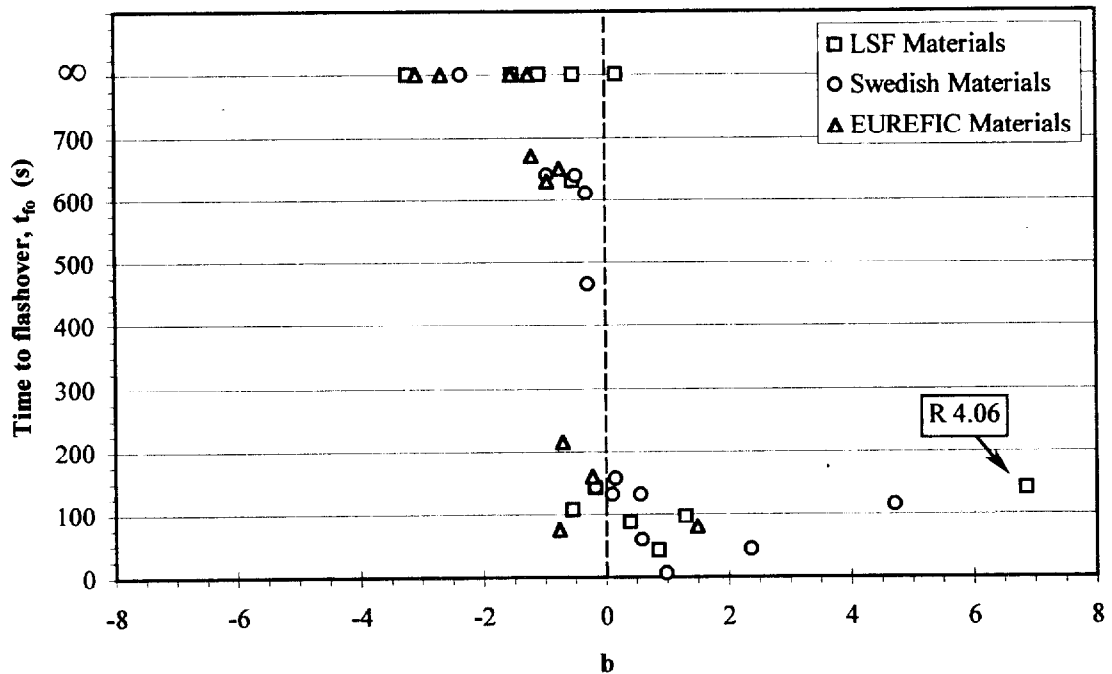
Figure 5. 1: Time to Flashover as a Function of the Flame Spread Acceleration Factor.
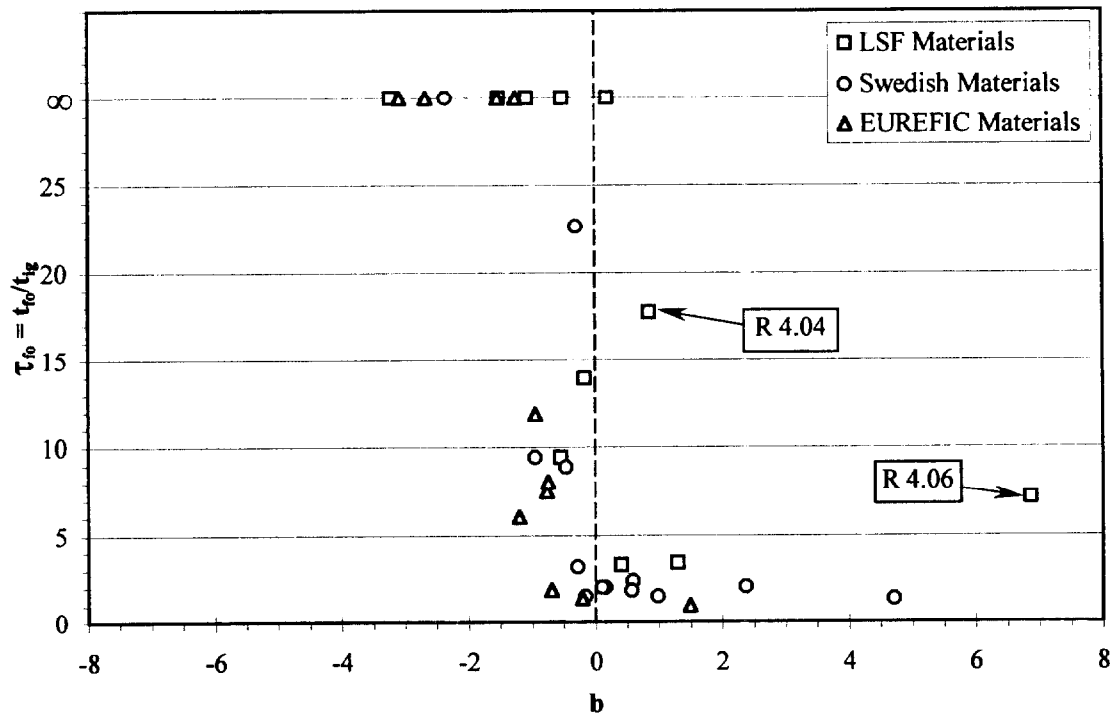
Figure 5. 2: Dimensionless Time as a Function of the Flame Spread Acceleration Factor.

5.2 Burnout Time Considerations

The correlation by Cleary and Quintiere [9] indicates that the ratio of the energy release rate of the material, $\dot{Q}$, to the energy release rate of the burner, $\dot{Q}_o$, is equal to

$$\frac{\dot{Q}}{\dot{Q}_o} = \frac{\left[(1+a)^2 \cdot e^{a(\tau-1)} - 1\right]}{a} \qquad \text{for } 1 \le \tau \le \tau_b + 1$$

$$\text{for } \tau > \tau_b + 1$$

$$\frac{\dot{Q}}{\dot{Q}_o} = \left\{ \frac{\left[(1+a)^2 \cdot \left(e^{a \cdot \tau_b} - 1\right)\right]}{a} \right\} \cdot e^{b(\tau-1-\tau_b)}$$

(5.2)

where τ and τ_b are the dimensionless time and burnout time, respectively:

$$\tau = \frac{t}{t_{ig}} \cdot \qquad\qquad \tau_b = \frac{t_b}{t_{ig}}$$

The dimensionless parameter a is calculated by

$$a = k_f \dot{Q}'' - 1$$

with k_f equal to 0.01 m^2/kW, and

$$b = a - \frac{1}{\tau_b}$$

Kim [25] also shows that $\dot{Q}/\dot{Q}_o$ is a function of the material fire properties:

$$\frac{\dot{Q}}{\dot{Q}_o} \approx f\{a,\ a(\tau\text{-}1),\ a\cdot\tau_b,\ b(\tau\text{-}1\text{-}\tau_b)\}$$

where the empirical b parameter is based on the final parameter, $b\left(\tau_{fo} - 1 - \tau_b\right)$. For a

typical flashover energy release rate of 1,000 kW

$$\frac{\dot{Q}}{\dot{Q}_o} = \text{constant}$$

Therefore, for small values of τ_b:

$$b\left(\tau_{fo} - 1 - \tau_b\right) \approx \text{constant} \qquad\qquad \text{for } \tau_{fo} > (\tau_b + 1)$$

Based on this empirical correlation, when $\tau_{fo} - 1 - \tau_b$ is plotted with respect to b, the

data should provide a hyperbolic relationship with the y-axis, x = 0, being the vertical

asymptote. As Figure 5.3 indicates, the data does indeed indicate a hyperbolic

relationship with those values below approximately -1.25 indicating infinite values.

95

However, the figure indicates a vertical asymptote of approximately -0.75 to -1.0 as opposed to 0.
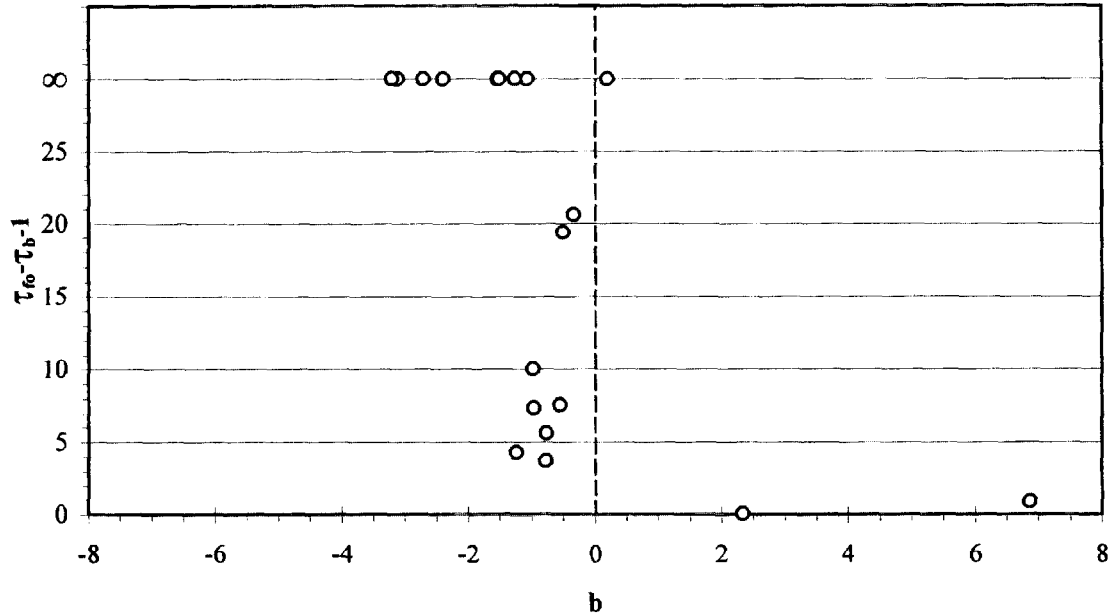
Figure 5. 3: Small Dimensionless Burnout Time [$T_{fo} > (T_b + 1)$], $T_{fo} - 1 - T_b$ versus b.

On the other hand, for materials with long burnout times, the dimensionless time T_b will be large and the value $1/T_b$ is approximately equally to zero. This results in b becoming the parameter a ($b \rightarrow a$)and :

$$a\left(\tau_{fo} - 1\right) \approx \text{constant} \qquad \text{for } T_{fo} \le (T_b + 1)$$

The a parameter is plotted with respect to ($T_{fo} - 1$) in Figure 5.4 which also shows the asymptotic relationship indicated by the correlation. However the vertical asymptote appears to be equal to -0.5 as opposed to the y-axis ($a = 0$). The horizontal asymptote is clearly equal to the x-axis, which indicates that ($T_{fo} - 1$) tends toward zero. This requires

that t_{fo}/t_{ig} is equal to 1 and that the time to flashover is approximately equal to the time to ignition. This implies that there is a direct correlation between the time to flashover and the time to ignition.
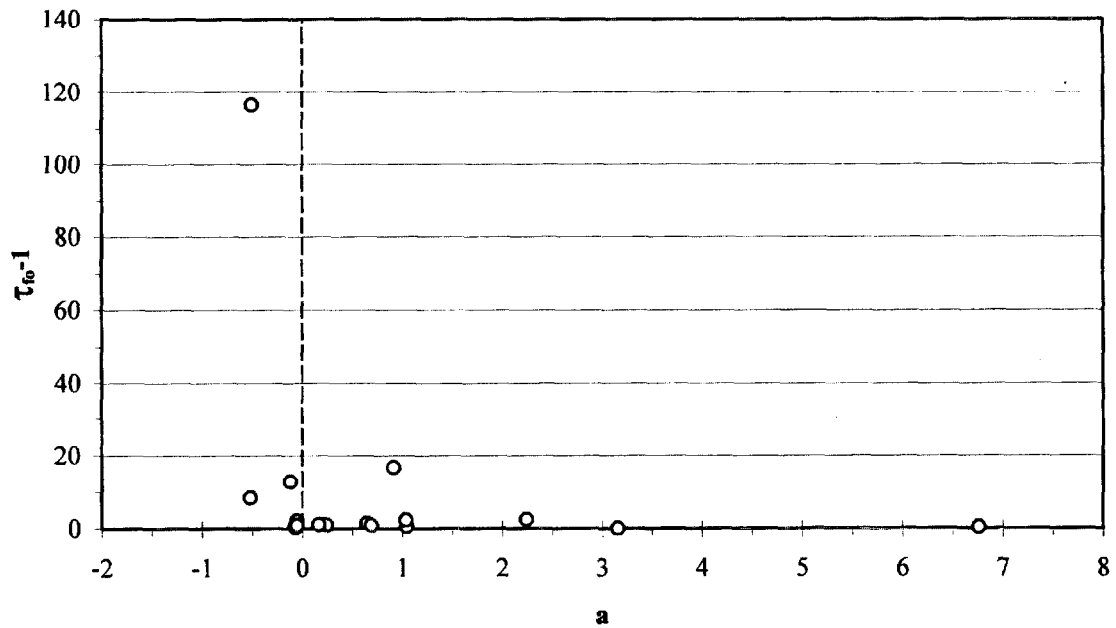
Figure 5. 4: Large Dimensionless Burnout Time [$\tau_{fo} \leq (\tau_b + 1)$], $\tau_{fo} - 1$ versus a.

The previous analysis provides further indication that the empirical correlation which has been presented provides an accurate method for categorizing materials in terms of there potential to burnout or take a room to flashover. However, the current data indicates that a and b values closer to approximately -0.5 to -0.7 are more consistent with "borderline" materials which are more sensitive to the ignition burner output and material properties.

Table 5. 1: Fire Growth Correlation Parameters for Swedish, EUREFIC and LSF Materials.

Material	t_{fo} (s)	t_{ig} (s)	t_b (s)	τ_{fo}	τ_b	a	b
S1, Ins. Fiberboard	59	25	413	2.36	16.52	0.65	0.59
S2, Med. Den. Fiberbrd	131	72	590	1.82	8.20	0.69	0.57
S3, Particle Board	157	79	964	1.99	12.20	0.24	0.16
S4, Gypsum	∞	89	45	∞	0.50	-0.38	-2.35
S5, PVC/Gyp. Board	611	27	27	22.63	1.02	0.67	-0.30
S6, Paper/Gyp. Board	640	68	70	9.41	1.03	0.02	-0.95
S7, Tex/Gyp. Board	639	72	20	8.88	0.28	3.16	-0.46
S8, Tex/Mineral Wool	43	21	21	2.05	1.01	3.37	2.37
S9, Mel/Part. Board	465	147	631	3.16	4.29	-0.05	-0.28
S10, Exp. PS	115	85	41	1.35	0.49	6.76	4.71
S11, PU Foam	6	4	68	1.50	17.09	1.05	0.99
S12, Wood Panel	131	66	1026	1.98	15.55	0.17	0.11
S13, Pap/Part. Board	143	95	1076	1.51	11.33	-0.07	-0.16
E1, Painted Gyp. Board	∞	176	86	∞	0.49	-0.61	-2.67
E2, Birch Plywood	160	116	804	1.38	6.93	-0.06	-0.21
E3, Tex/Gyp. Board	670	111	80	6.04	0.72	0.19	-1.20
E4, Mel/Non-Comb Brd	∞	102	130	∞	1.28	-0.46	-1.25
E5, PF Steel/Min. Wool	∞	162	260	∞	1.61	-0.90	-1.53
E6, FR Part. Board, B1	630	53	47	11.89	0.90	0.16	-0.95
E7, Comb. Min. Wool	75	10	28	7.50	2.77	-0.39	-0.76
E8, FR Part. Board	∞	669	294	∞	0.44	-0.80	-3.08
E9, PF Steel/PU	215	115	179	1.87	1.56	-0.05	-0.69
E10, PVC/Gyp. Board	650	81	114	8.02	1.41	-0.04	-0.74
E11, Ext. PS	80	80	48	1.00	0.60	3.16	1.49
R 4.01, FR. Chipboard	∞	234	948	∞	4.05	-0.64	-0.84
R 4.02, Gypsum	∞	33	43	∞	1.28	-0.49	-1.40
R 4.03, PU/Alum.	41	2	----	17.72	----	0.92	1.04
R 4.04, PU/Paper	----	----	161	----	69.51	----	----
R 4.05, Ext. PS40	96	28	119	3.38	4.19	2.25	2.27
R 4.06, Acrylic	141	19	104	7.12	5.24	7.63	7.83
R 4.07, FR. PVC	∞	47	343	∞	7.30	-0.55	-0.61
R 4.08, 3-Layer PC	∞	81	244	∞	3.00	1.38	1.88
R 4.09, Mass Timber	107	11	1394	9.41	122.69	-0.51	-0.46
R 4.10, FR. Plywood	631	5	1029	117.44	191.58	-0.50	-0.32
R 4.11, Plywood	142	10	729	13.92	71.47	-0.11	-0.04
R 4.20, Exp. PS40	87	26	166	3.26	6.23	1.04	1.07
R 4.21, Exp. PS80	∞	30	290	∞	9.65	-0.14	0.06

6. IGNITION BURNER FLAME HEIGHT AND HEAT FLUX

The purpose of this section is to provide some of the available flame height and heat flux correlations for flames produced by square propane burners of different sizes and output levels positioned in the corner of a room. Different forms of the room-corner test require various burner sizes and output levels. The ISO 9705 Room-Corner Test standard [22] calls for the use of a 0.17 m square Nordic propane burner which is operated at 100 kW for ten minutes followed by 300 kW for an additional 10 minutes. The ASTM test standard requires a 0.3 m square burner operated at 40 kW for 5 minutes followed by 160 kW for 10 minutes. Other test methods require varied burner geometries and heat outputs. For example, the work by Kokkala, Göransson and Söderbom as a part of the EUREFIC program [27, 28] in Europe to evaluate the performance of materials exposed to larger fires in larger compartments uses three 0.17 m burners operated at 100 kW, 300 kW and 900 kW.

Accurate correlations for ignition burner flame heights and heat fluxes will provide a much needed advancement to Quintiere's fire growth model. The current flame height used by the model for a 0.17 m square burner, is 1.3 m at 100 kW and 3.6 m at 300 kW. These values were assumed by Cleary and Quintiere [9], based on an early correlation for flame tip heights by Hasemi and Tokunaga [14]. These values are not consistent with observations made from ISO 9705 room-corner tests and indicate that a more detailed study is required. In addition the model does not provide values for different flame heights or heat fluxes or for the 0.3 m ASTM burner. This section will address other correlations that exist for the flame height and heat flux for corner positioned ignition burners. The following sections will address the determination of

99

the actual flame height and heat flux that is incident to the walls and ceiling in the vicinity of the burner in the standard room.

6.1 Flame Height

6.1.1 Open Corner

It is generally well recognized that the dimensionless flame height (Z_f/D) for a pool fire is dependent on a dimensionless energy release parameter:

$$Q^* = \frac{\dot{Q}}{\rho_\infty c_{p,\infty} T_\infty g^{1/2} D^{5/2}}$$
(6.1)

where $\dot{Q}$ is the burner energy release rate, T_∞ is the ambient air temperature (300 K), ρ_∞ is the density of ambient air (1.16 kg/m^3), $c_{p,\infty}$ is the specific heat of ambient air (1.01 kJ/kg·K), g is acceleration due to gravity (9.807 m/s^2) and D is the pool diameter (m), or in this case the side dimension of the burner. This Q^* parameter is the square root of the Froude number, Fr, which is the ratio between inertial and buoyant forces:

$$Fr = \frac{U^2}{gD}$$

where U is the velocity of the gasses flowing from the top surface of the fuel or in this case the burner surface. Although this analysis deals with propane burners, the flame mechanics of the pool fire are similar and allow an equivalent comparison to be made. Inputting ambient air properties into Equation 6.1 results in the following expression:

$$Q^* = \frac{\dot{Q}}{1100 \cdot D^{5/2}}$$
(6.2)

which is consistent with the work by Gross [12], in which the ambient air properties

used resulted in a value of 1116 in the denominator. Equation 6.2 indicates that the

dimensionless heat release parameter, Q^*, is directly dependent on the ratio between the

burner energy release rate and the size of the burner.

Using Equation 6.2, dimensionless heat release rates were calculated for various

burner outputs and sizes. These values are presented in Table 6.1. Note that the three

0.17 m burner scheme used by Kokkala, *et al.* [27, 28] to achieve a 900 kW energy

release rate is roughly equivalent, in terms of overall surface area, to a 0.3 m square

burner as seen in Figure 6.1. Therefore the flame height for this burner configuration

will be calculated based on the equivalent square burner.

Table 6. 1: Dimensionless Energy Release Rate Parameters for Different Burner Sizes and Energy Output Levels.

Burner Size, *D* (m)	Q^*				
	50 kW	100 kW	160 kW	300 kW	900 kW
0.17	—	7.64	—	22.9	—
0.30	0.92	—	2.95	—	16.6
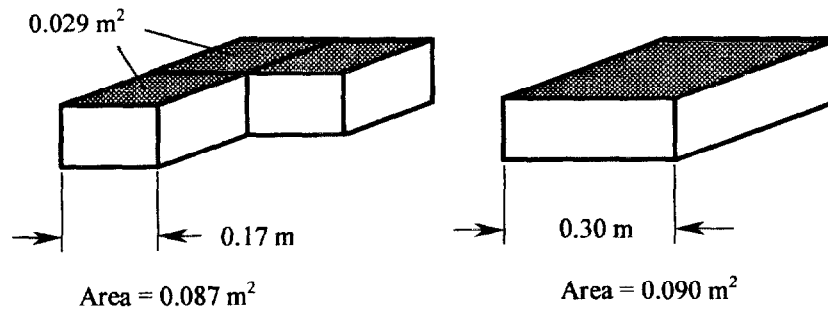
Figure 6. 1: Corner Burner Configurations.

6.1.1.1 Hasemi and Tokunaga

Hasemi [13] and Hasemi and Tokunaga [14, 15] performed several analyses into the flame heights of ignition burners, Z_f, located along walls and in corners. Their analysis produces the following correlation for the dimensionless flame height (Z_f/D) [15]:

$$\frac{Z_f}{D} = CQ*^{2/3}$$

where: C = 4.3 for the flame tips (tip of the intermittent region)

   C = 3.0 for the continuous flame region (bottom of the intermittent region)

The average flame height can therefore be calculated by taking an average height of the intermittent region:

$$\frac{Z_f}{D} = 3.65Q*^{2/3}$$

There are some potential limitations to using Hasemi and Tokunaga's analysis to evaluate the flame heights at high burner heat outputs: the tests conducted in the formation of this correlation were for low heat output levels in an open corner with no ceiling. When the flame tips reach the ceiling they will curve away from the walls and form a horizontal ceiling jet. Therefore this correlation may not be appropriate once the calculated flame height reaches a height just below the ceiling.

6.1.1.2 Kokkala

Kokkala's [27] flame height correlation is also based on the dimensionless energy release rate of the burner. He proposes that the average visible flame height can be directly related to the temperature in the plume and therefore can be expressed in

terms of $Q*$. Two gas temperature profiles developed by Kokkala are presented in Figure 6.2. Based on a visible flame boundary temperature of between 400 and 500 °C Kokkala reports that based on the $Q*$ value, a ratio between the average flame height (Z_f) and the burner size (D) can be determined:

$$Q* < 8.6 \qquad \frac{Z_f}{D} = -1.73 + 4.96(Q*)^{2/3}$$

$$Q* > 8.6 \qquad \frac{Z_f}{D} = 15.6 + 0.40Q*$$

It should be noted that although Kokkala's experiments were carried out over a wide range of burner sizes (0.17 to 0.5 m) and energy release rates (40 to 300 kW) the tests involved an open corner configuration. He used a 4.5 meter high corner constructed with 2 wall segments in an 18m high laboratory hall. Therefore, there were no ceiling effects.

6.1.1.3 Revised Heskestad Correlation

In the same experimental work mentioned above, Kokkala also provides a revised version of the open pool fire expression developed by Heskestad:

$$(Open\ Pool) \qquad \frac{Z_f}{D} = -1.02 + 3.7(Q*)^{2/5}$$

By "modifying the expression to correspond to the imaginary fire source of four-fold area... where $Q*$ now corresponds to that of the burner in the corner" [26] he develops the following revised corner burner flame height equation:

$$\frac{Z_f}{D} = -2.04 + 6.62(Q*)^{2/5}$$

103
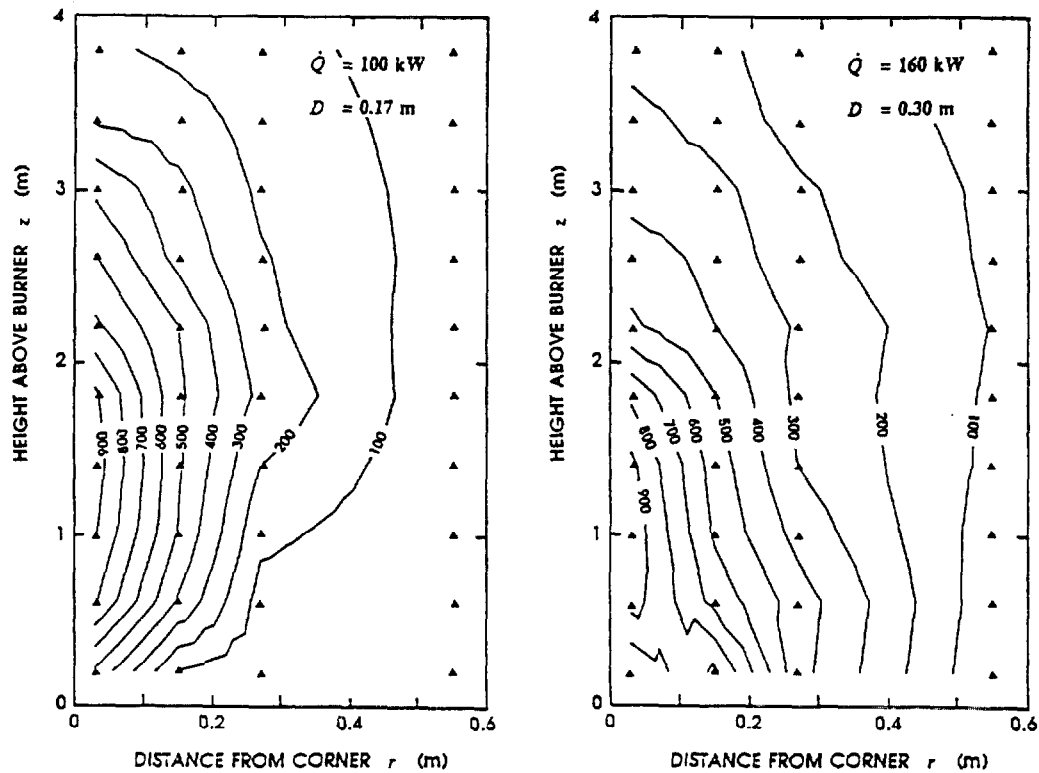
Figure 6. 2: Flame Temperature Distributions 3 cm from the Wall for a 17 cm x 17 cm Burner at 100 kW and a 30 cm x 30 cm Burner at 160 kW [26].

6.1.1.4 Janssens

Janssens [23] developed specific flame height values for the heat fluxes of the ISO and ASTM ignition burners in order to improve the accuracy of Quintiere's fire growth model [36]. He wanted to determine the initial pyrolysis area caused by the burner based on the flame height, Z_f, and the width of the flame at half weight, $W_{1/2}$. Using Kokkala's experimental flame temperature profiles from Figure 6.2 and implementing a flame boundary temperature of 600 °C Janssens determined the flame heights for the ISO and ASTM burners. His results are presented in Figure 6.3.

104

Table 6. 2: Flame Height for 17 and 30 cm Square Ignition Burners at 40 to 300 kW Energy Release Rates, Calculated by Janssens [23].

Burner	$\dot{Q}$ (kW)	Z_f (m)
17 cm	100	1.96
	300	4.0
30 cm	40	0.7
	160	1.79

6.1.1.5 Comparison of Corner-Flame Height Determinations

A comparison of the different flame height expressions and calculations is presented in Figure 6.3. It is clear that the different methods provide different results especially at higher heat output levels. It should be noted that for the 17 cm burner, a Z_f/D difference of about 5 represents a flame height difference of almost 1 meter. Due to the discrepancies between the work by the different researchers it is apparent that further observations and research need to be conducted into the heights of ignition burner flames in corners before they can be appropriately modeled. A study by Beyler [8] of different flame height correlations indicates that there is even a great deal of discrepancy between the correlations for open pools fires, which have received a great deal more attention than fires in open corners or room corners. Determining an appropriate correlation for determining the flame length in the room-corner test becomes further complicated by the presence of the ceiling.
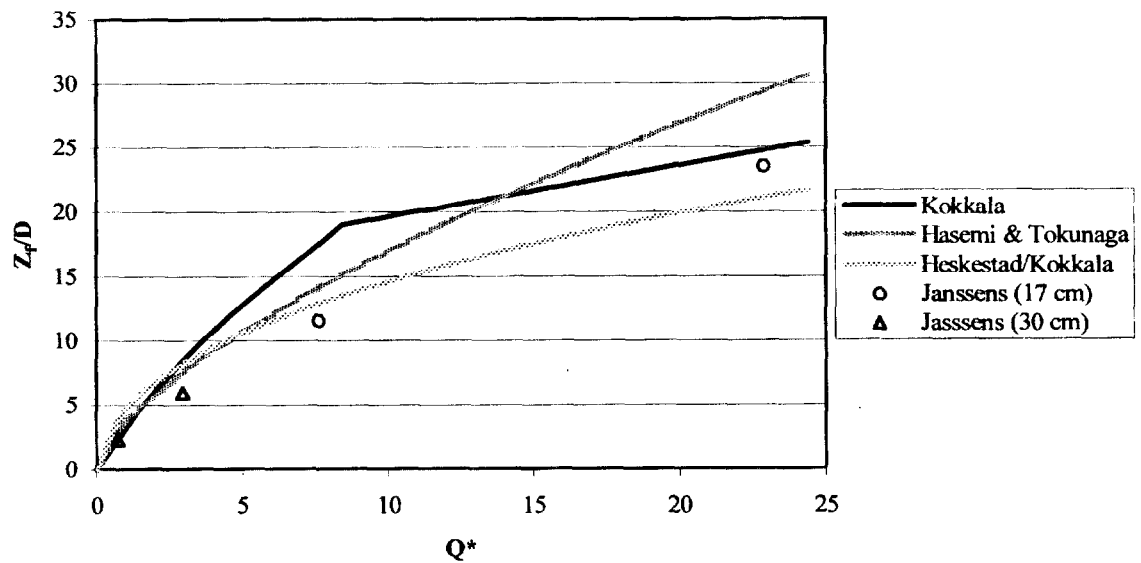
Figure 6. 3: Dimensionless Average Flame Height (Z_f/D) in a Corner as a Function of the Dimensionless Energy Release (Q^*).

6.1.2 Ceiling Jets

Due to the presence of the ceiling in the standard room, the flames from the ignition burner will be deflected and form a horizontal ceiling jet emanating from the wall corner intersection. This can be distinctly seen in the full-scale room-corner test results, Figure 8.14 (b).

A method by Babrauskas [6] can be used to determine the ceiling flame extension of an axisymmetric ceiling jet based on the amount of air that is entrained by the fire being equal to that of free fires. He approximates the ceiling-corner configuration by using the method of images for the entire plume by which the corner plume is assumed t be 1/4 of a free plume. However this method is fuel dependent and proved to be too complex for calculating the ceiling flames in Quintiere's fire growth model.

Thomas and Karlsson [48] use correlations for the temperature rise, ΔT, as a function of the ceiling jet radius, r, by Alpert and by Heskestad and Delichatsios to determine the horizontal flame extension (Z_h) under a ceiling from a corner burner:

$$\textit{Alpert} \qquad \frac{Z_h}{H*} = \left(\frac{250}{\Delta T}\right)^{3/2} 15.6 Q_H^* - 0.15$$

and

$$\textit{Heskestad \&}$$
$$\textit{Delichatsios} \qquad \frac{Z_h}{H*} = 6.39\sqrt{Q_H^*}\left(\frac{250}{\Delta T}\right)^{3/4} - 0.60$$

where Z_h is the horizontal flame extension and Q_H* is

$$Q_H^* = \frac{\dot{Q}}{\rho_\infty c_{p,\infty} T_\infty g^{1/2} H*^{5/2}} \qquad (6.3)$$

The parameter $H*$ is the height of the ceiling above a virtual flame source which is approximated as

$$H* = H + 3D$$

where H is the height of the ceiling above the fuel source and D is the burner dimension.

Using a temperature rise, ΔT, of 180 ° provided good agreement between the correlations and corner-ceiling flame length data collected by Gross [12]. The Alpert correlation provides a reasonable fit of the data up to $Q*_H = 0.1$ $(Z_h/H* > 2.0)$. However the Heskestad and Delichatsios correlation provides much better agreement for $Q*_H$ less than 0.06. The two expressions are graphically presented in Figure 6.4. Since $Q*_H$ is equal to 0.022 for the 300 kW burner in the ISO room-corner test, the Heskestad and Delichatsios expression is probably the most appropriate.
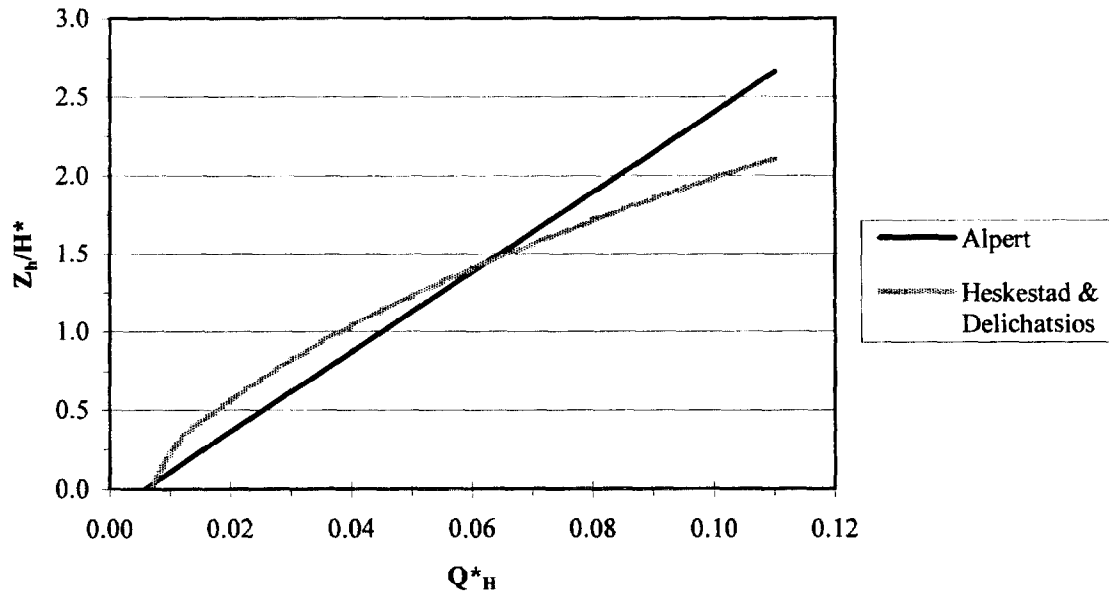
Figure 6. 4: Horizontal Flame Lengths Under a Ceiling From a Corner Ignition Burner [48].

6.2 Heat Flux

The incident heat flux from the ignition burner is one of the most critical factors that effects the ignition of a sample material in the room-corner test. However, little study has been done to determine exactly what the incident flux from the corner ignition burner is.

6.2.1 Kokkala

Kokkala [26] and Kokkala *et al.* [27] used heat flux meters in 100 different positions to determine heat flux distributions for 100 and 300 kW burners using a 0.17 m square propane gas burner located 14.5 cm above the floor. These distributions are presented here in Figure 6.5. These distributions are for a burner in a 4.5 m high corner

without a ceiling tested in an 18 m high test bay. Kokkala's data is limited so no

correlations have been developed. The distributions will also be inconsistent with

fluxes in the standard room since there are no ceiling or room feedback effects.

Kokkala's data is compared with room flux distributions in Section 8.4.1.
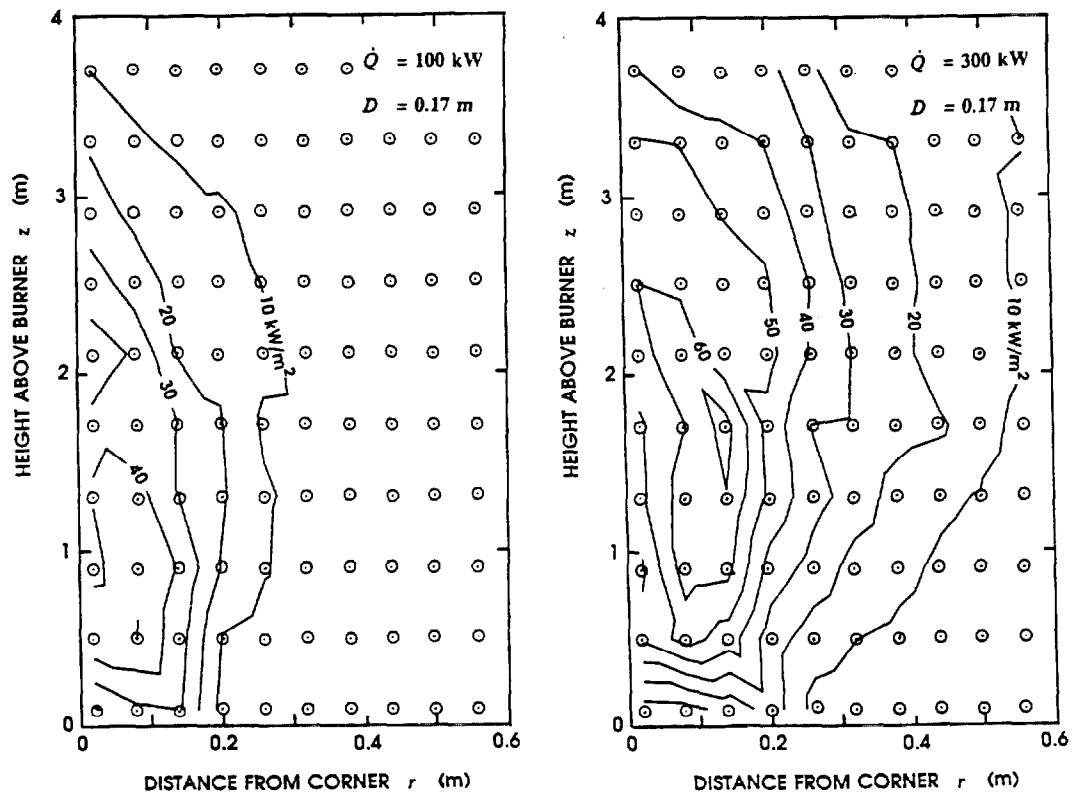
Figure 6. 5 (a & b): Heat Flux Distributions to the Wall from a 17 cm x 17 cm
Propane Gas Burner Located in the Corner with Energy Release Rates of 100 and 300
kW [26, 27].

6.2.2 Janssens

Janssens [23] also calculated the incident heat flux from a propane ignition

burner by determining the radiative and convective components. The radiant portion is

based on the combustion efficiency of propane (X = 0.95) and the percentage of the

energy release rate, $\dot{Q}$, lost by radiation ($X_r \approx 0.30$). The convective heat transfer was

determined based on the velocity and temperature of the plume gasses and the surface

temperature of the walls. The incident heat fluxes to the corner ($\dot{q}''$) calculated by

Janssens are provided in Table 6.3. His data indicate good agreement with Kokkala's

distribution for the 100 kW Burner but the 300 kW Burner Flux is extremely low.

Table 6. 3: Incident Heat Flux to the Corner from 17 and 30 cm Square Ignition
Burners at 40 to 300 kW Energy Release Rates, Calculated by Janssens [23].

Burner	$\dot{Q}$ (kW)	$\dot{q}''$ (kW/m^2)
17 cm	100	44.4
	300	47.1
30 cm	40	29.9
	160	38.5

6.2.3 Conclusion

There appears to be very little data regarding the heat flux to a corner from an

ignition burner. The data that do exist are not completely consistent and do not

necessarily fully represent the corner-ceiling configuration of the test standard. There is

also very little data regarding the incident heat flux to the ceiling above the burner. Due

to the buoyancy effects of the fire plume, this region is expected to be exposed to

significant heat flux levels. Therefore accurate measurements of the heat flux to the

walls and ceiling in the room-corner test must be made. Testing over a wide range of

burner sizes and energy release rates should allow simple correlations to be developed

that can be incorporated into Quintiere's fire growth model and make it more accurate.

7. SMALL-SCALE STEEL PLATE VALIDATION

A limited amount of data exists for the flame height and incident heat flux for an ignition burner in a corner. Even less data exists for a corner-ceiling configuration of an actual room. Quintiere's model assumes that the heat flux to the wall is 60 kW/m^2 over the height of the ignition burner flame however there is little data to support this value. Therefore in order to increase the power and validity of the room-corner test model, the actual ignition burner exposure must be determined.

Using an arrangement of large steel plates with thermocouples attached to the unexposed surface, the incident heat flux from the burner flames can be accurately determined. This procedure follows work by Ingason and de Ris [21] and was validated using the following series of small-scale experiments.

7.1 Experiments by Ingason and de Ris

In order to determine the incident heat flux from flames within a rack storage configuration, Ingason and de Ris [21] used thermocouples spot welded to the back of steel sheets. Using the measured temperatures of the steel the total heat flux was determined using the following equation:

$$\dot{q}''_{tot} = \rho c_p \delta \frac{dT}{dt}$$

where ρ is the density, c_p is the specific heat and δ is the thickness of the steel. Heat flux losses due to conduction were determined to be small and were neglected. Re-

radiation was determined to be the largest sources of heat loss and could be easily corrected.

Their experimental results indicate good agreement with measured values from a Schmidt Boelter heat flux gauge. Therefore a similar methodology will adopted to determine the incident heat flux to the walls and ceiling of the room corner test. However a more detailed heat transfer analysis will be performed in order to reduce potential sources of unknown losses. Before full-scale testing was performed, small-scale procedure validation tests were performed using the LIFT apparatus.

7.2 Experimental Set-Up and Procedure

In order to verify the applicability of the method used by Ingason and deRis a small steel plate was placed in the LIFT apparatus and exposed to various radiant heat fluxes. The rate of temperature rise of thermocouples spot welded to the back of the plate were used to calculate the total incident heat flux to the center of the plate.

The plate used was a 15.24 cm (6 inch) square by 4.7 mm thick piece of C-1018 AISI-SAE grade carbon steel. The thickness of the steel was specifically chosen to be sensitive to the changes in the heat transfer, but not so sensitive that wild fluctuations are recorded. The time constant for the steel plate is determined by the following expression [44]:

$$t_{o,st} = \frac{\delta^2}{\alpha}$$

where δ is the thickness of the plate (m) and α is the thermal diffusivity of the steel (m^2/s). Using the properties of steel at ambient temperature provides a time constant of

$t_{o,st} \approx 2$ seconds. This indicates that the incident heat flux to the exposed surface will reach the unexposed surface in approximately 2 seconds. This time constant is appropriate for this small-scale analysis and the full-scale measurements of the flux from actual flames. A thicker plate will give a much longer time delay while a thinner plate will be incredibly sensitive to small changes in the incident flux.

Five 24 gauge, Type-K, Chromel-Alumel thermocouples were spot welded to the back of the steel plate: one in the center and the other 4 in the corners of the plate, 7.7 cm from the center. The area where a thermocouple was to be attached was polished prior to spot welding. Figure 7.1 shows the geometry of the plate and the thermocouples. Unfortunately, prior to testing, one of the thermocouples became detached from the plate as indicated by the figure.

In order to reduce the reflectivity of the exposed plate surface, the steel was roughened using a pneumatic, glass bead blaster. This provided a coarse surface with a substantially reduced reflectivity.
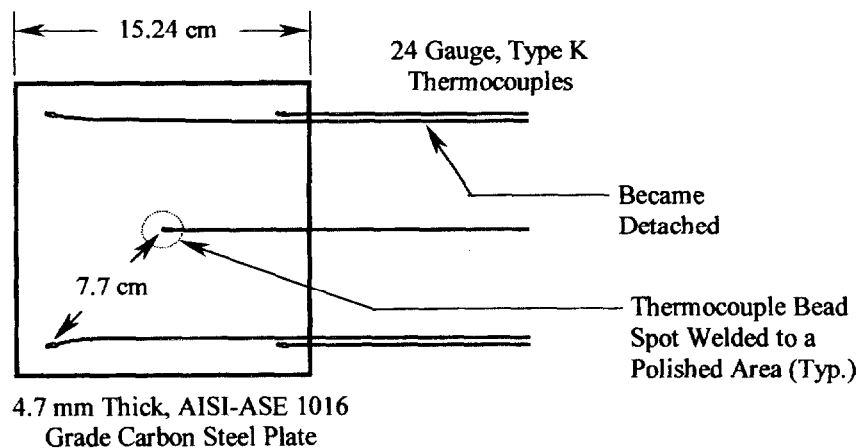
Figure 7. 1: Small-Scale Steel Plate Thermocouple Geometry.

The plate was then placed within the LIFT sample holder with a thin strip of ceramic fiber insulation placed between the edges of the plate and the metal holder. This was done to reduce conductive heat losses from the plate to the holder. Thin layers of the ceramic fiber blanket were also placed between the thermocouple wires and the steel plate up to the spot welded bead in order to reduce damage to the thermocouple wire insulation during testing. A 15.5 cm wide by approximately 65 cm long piece of 1" (2.54 cm) non-combustible marinite board was placed in the sample holder next to the steel plate in order to protect the thermocouple wires from the incident heat flux. Two 15.5 cm square pieces of 1/2" (1.27 cm) ceramic fiber insulation blanket were then layered on top of the steel plate with a thermocouple centered between the two layers (See Figure 7.2). A 15.5 cm square piece of 1" marinite board was placed on top of the ceramic fiber blankets and a 15.5 by 65 cm piece of gypsum board was placed over the first marinite board with the thermocouple wires sandwiched in between. The entire assembly was then held in place within the sample holder using the LIFT sample support which is not shown in the figures. A cut away section of the back side of the test assembly can be seen in Figure 7.3.

Prior to placing the steel plate assembly in the LIFT, the reflectivity was further reduced in order to provide a surface absorptivity, α, of as close to 1 as possible. To do this the entire test assembly was positioned horizontally with the face of the steel plate facing downward over a small gasoline pool fire. The soot from the gasoline pool fire produced an even layer of soot over the entire surface of the plate. Siegel and Howell [45] list the emissivity of candle soot and lampsoot as approximately 0.95. Similarly,

114

Kutateladze and Borishanskii [29] list the emissivity of soot deposited on a solid surface to be 0.96 which is approximately equal to 1.
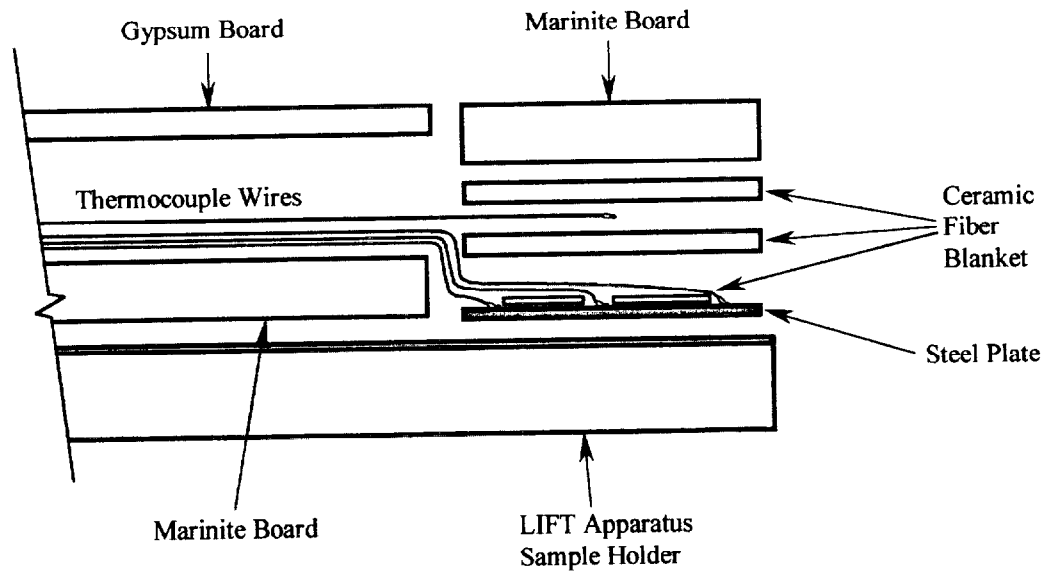
Figure 7. 2 Small-Scale ,Steel Plate LIFT Apparatus Test Assembly (Exploded View).
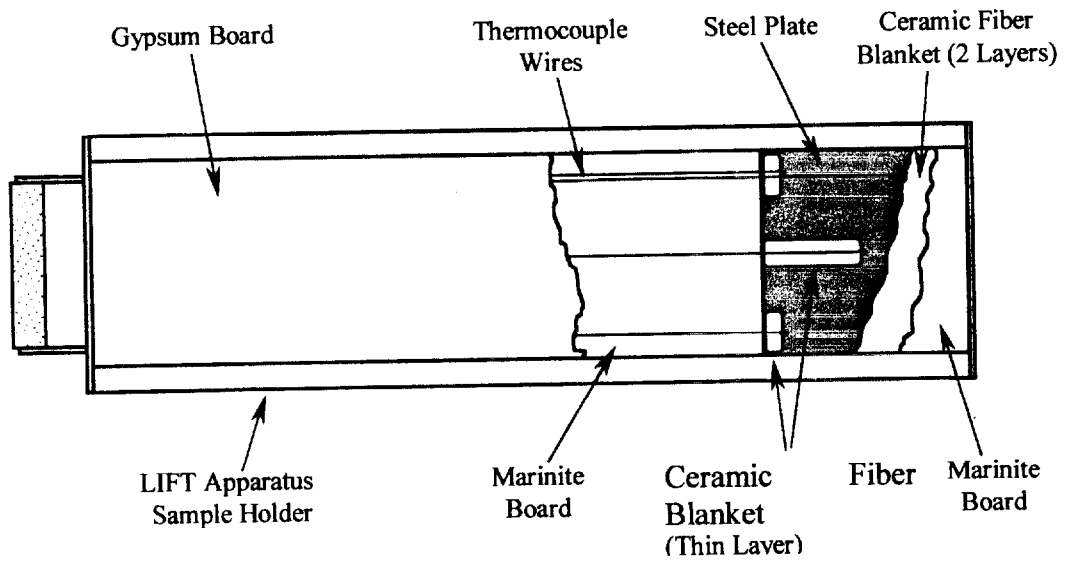
Figure 7. 3 Small-Scale, Steel Plate LIFT Apparatus Test Assembly (Rear View).

115

The radiant panel on the LIFT apparatus was ignited and allowed to equilibrate

for approximately 30 minutes with a dummy sample in place. The heat flux from the

radiant panel was measured throughout each test using a Honeywell Type RL-2

Radiamatic Pyrometer. As Figure 7.4 indicates, the pyrometer was positioned so that

the viewing angle captured the heat radiating from the panel which was directly incident

to the steel plate. According to the LIFT standard [1], the heat flux over the first 15.5

cm of the sample holder is exposed to a nearly uniform heat flux. Therefore the

measured flux from the pyrometer is taken as being the actual flux to the plate.

The thermocouple wires were input into an Omega® CIO-EXP32 multiplexer

board which was connected to an Omega® CIO-DAS08 data acquisition card. The data

acquisition was handled using Laboratory Technologies Corporation©, LABTECH

Version 9.0 software. The data acquisition system was set up to take temperature

measurements and write them to an output file every second. A thermocouple was also

positioned in the vicinity of the LIFT apparatus and was configured to record the

ambient temperature.
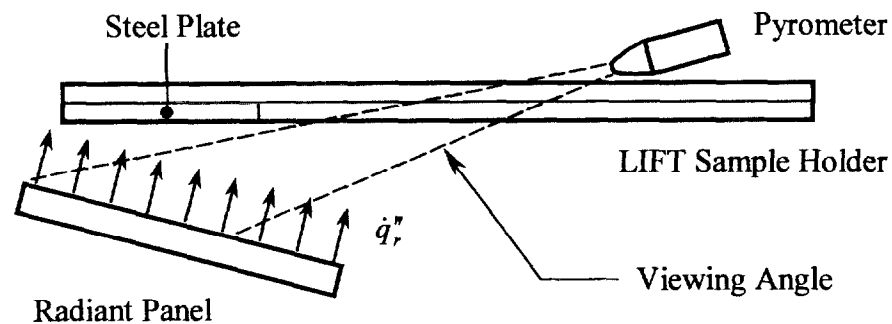
Figure 7. 4: Small-Scale Steel Plate Test Arrangement.

116

After allowing the radiant panel to come to a steady heat flux, the data acquisition system was started, the dummy sample was removed and the steel plate was inserted. Temperature and heat flux data were taken until the temperature of the center thermocouple became relatively constant. At steady conditions the sample was either removed or the heat flux was increased and allowed to once again reach steady state. These increases were implemented in order to verify that the plate can accurately measure the change in the incident heat transfer.

This test method was repeated 7 times at various incident heat fluxes: 7 to 48 kW/m². With the exception of one test, the steel plate was coated with a thin layer of soot and the sample assembly was allowed to cool to ambient room temperature prior to each test. For the seventh test the surface of the plate was coated with Medtherm Corporation© high temperature optical black coating. This coating is typically used for coating the surfaces of heat flux meters and according to Medtherm it has an emissivity, ε, value of 0.92 from 0.5 to 20 microns.

7.3 Heat Transfer Analysis

In order to accurately determine the incident heat flux from the radiant panel to the center of the steel plate, $\dot{q}''_i$, the energy storage within the steel as well as the convective, re-radiant and conductive heat transfer must be calculated and combined into the following expression:

$$\dot{q}''_i = \dot{q}''_{sto} + \dot{q}''_c + \dot{q}''_{rr} - \dot{q}''_{k, st} + \dot{q}''_{k, ins}$$

This heat transfer analysis will then be applied to a large number of thermocouples in a grid layout. The total heat flux at each node will be calculated based on the time temperature curve of that node combined with the temperature of the four surrounding nodes.

7.3.1 Conduction—Steel Plate

Due to temperature differences within the plate, heat will be transferred by conduction, $\dot{q}''_{k,\,sl}$. The conduction heat transfer within the plate will be determined using a two dimensional finite-difference method, as demonstrated in Figure 7.5 with the distance between the thermocouples denoted by Δ. The central thermocouple represents the node of interest while the four surrounding thermocouples represent the differential increment boundary nodes to which heat is being conducted. It is important to note that prior to testing in the LIFT, the thermocouple located at (x, y-Δ) became detached from the plate (it is shown in the Figure 7.5 as O). The test data indicates that the temperatures at this location were relatively consistent with the temperatures measured at the (x+Δ, y) thermocouple. Therefore, the temperatures from (x+Δ, y) are also used at (x, y-Δ). This approximation is not expected to provide a significant amount of error.

In order to analyze the conduction heat transfer of the incident heat flux at the central node (x,y), the heat flow in the x and y directions must be determined. The heat transfer in the x-direction will be analyzed and will be taken as being similar in the y-direction.
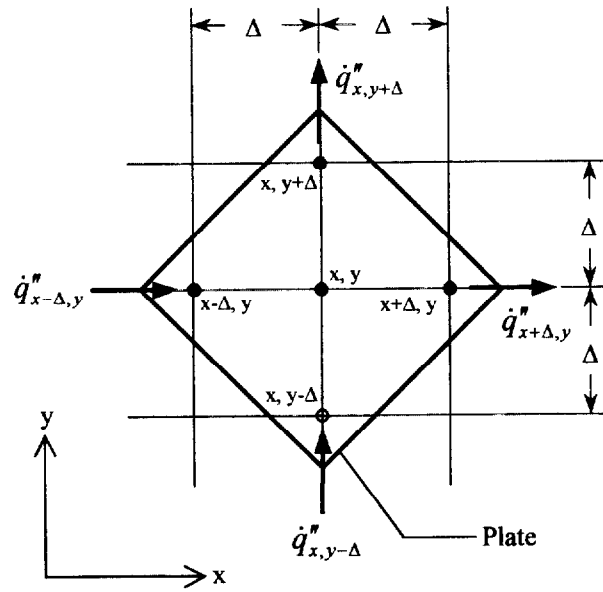
Figure 7. 5: Steel Plate Nodes for Numerical Analysis of Conduction Heat Transfer.

Heat transfer in the x-direction can be expressed using Fourier's law:

$$\dot{q}''_{x,y}{}_{\longrightarrow x} = -k_{st}\frac{\partial T}{\partial x} \tag{7.1}$$

where k_{st} is the thermal conductivity of the steel (W/m·K). The heat transfer at the two

boundary nodes (x-Δ, y and x+Δ, y) can be approximated using Taylor series

expansions of Equation 7.1:

$$\dot{q}''_{x+\Delta,y} = \dot{q}''_x + \frac{\partial \dot{q}''_x}{\partial x}\Delta + \frac{\partial^2 \dot{q}''_x}{\partial x^2}\Delta^2 + \cdots \tag{7.2a}$$

$$\dot{q}''_{x-\Delta,y} = \dot{q}''_x - \frac{\partial \dot{q}''_x}{\partial x}\Delta - \frac{\partial^2 \dot{q}''_x}{\partial x^2}\Delta^2 - \cdots \tag{7.2b}$$

Therefore, using the first two terms from Equation 7.2 a and 7.2b, the net heat flux in

the x-direction can be approximated as

119

$$\underline{\dot{q}''_{net}}_x = \dot{q}''_{x+\Delta,y} - \dot{q}''_{x-\Delta,y} = \frac{\partial \dot{q}''_{x,y}}{\partial x} 2\Delta \qquad (7.3)$$

Using Equations 7.1 and 7.3, the net heat transfer in the x-direction can be expressed as:

$$\underline{\dot{q}''_{net}}_x = \frac{\partial}{\partial x}\left(-k_{st}\frac{\partial T}{\partial x}\right)2\Delta = -k_{st}\frac{\partial^2 T}{\partial x^2}2\Delta$$

Finite-difference approximations allow the temperature gradients in the x-direction to be expressed as [18]

$$\left[\frac{\partial T}{\partial x}\right]_{x+\Delta,y} \approx \frac{T_{x+\Delta,y} - T_{x,y}}{\Delta}, \qquad \left[\frac{\partial T}{\partial x}\right]_{x-\Delta,y} \approx \frac{T_{x,y} - T_{x-\Delta,y}}{\Delta}$$

and

$$\left[\frac{\partial^2 T}{\partial x^2}\right]_{x,y} \approx \frac{\left[\frac{\partial T}{\partial x}\right]_{x+\Delta,y} - \left[\frac{\partial T}{\partial x}\right]_{x-\Delta,y}}{\Delta} = \frac{T_{x+\Delta,y} + T_{x-\Delta,y} - 2T_{x,y}}{\Delta^2}$$

thereby allowing the net conduction heat transfer in the x-direction to be approximated by the following expression:

$$\underline{\dot{q}''_{x,y}}_x \approx -2k_{st}\left(\frac{T_{x+\Delta,y} + T_{x-\Delta,y} - 2T_{x,y}}{\Delta}\right)$$

Since conduction heat transfer acts through the plate and the incident heat flux acts normal (perpendicular) to the plate surface, the conduction from the central node must be represented as an incident flux. Therefore, the conduction heat flux per unit area in the x-direction must be multiplied by the area over which conduction is occurring, $\delta \cdot 2\Delta$, and divided by the area over which the heat flux is incident, $(2\Delta)^2$. This results in the following expression for the conduction heat transfer of the incident heat flux in the x-direction

$$\dot{q}''_{k,\,st}{}_x \approx -k_{st}\left(\frac{T_{x+\Delta,y}+T_{x-\Delta,y}-2T_{x,y}}{\Delta^2}\right)\delta \tag{7.4a}$$

Similarly, the conduction heat transfer of the incident heat flux in the y-direction can be approximated by:

$$\dot{q}''_{k,\,st}{}_y \approx -k_{st}\left(\frac{T_{x,y+\Delta}+T_{x,y-\Delta}-2T_{x,y}}{\Delta^2}\right)\delta \tag{7.4b}$$

These two expressions can be combined to produce an expression for the net conduction heat transfer:

$$\dot{q}''_{k,\,st} \approx -k_{st}\left(\frac{T_{x+\Delta,y}+T_{x-\Delta,y}+T_{x,y+\Delta}+T_{x,y-\Delta}-4T_{x,y}}{\Delta^2}\right)\delta \tag{7.4c}$$

The thermal conductivity of steel is temperature dependent. The properties for C-1018 carbon steel were obtained from the *ASM Metals Reference Handbook* [3] and are presented if Figure 7.6. The following expression represents the equation of the line through the data points which was used to calculate k_{st} at all steel temperatures:

$$k_{st} = -3\times10^{-5}\cdot T^2 - 0.0115\cdot T + 51.9 \ \text{W/m·K} \tag{7.5}$$

where T is the temperature of the steel in °C.
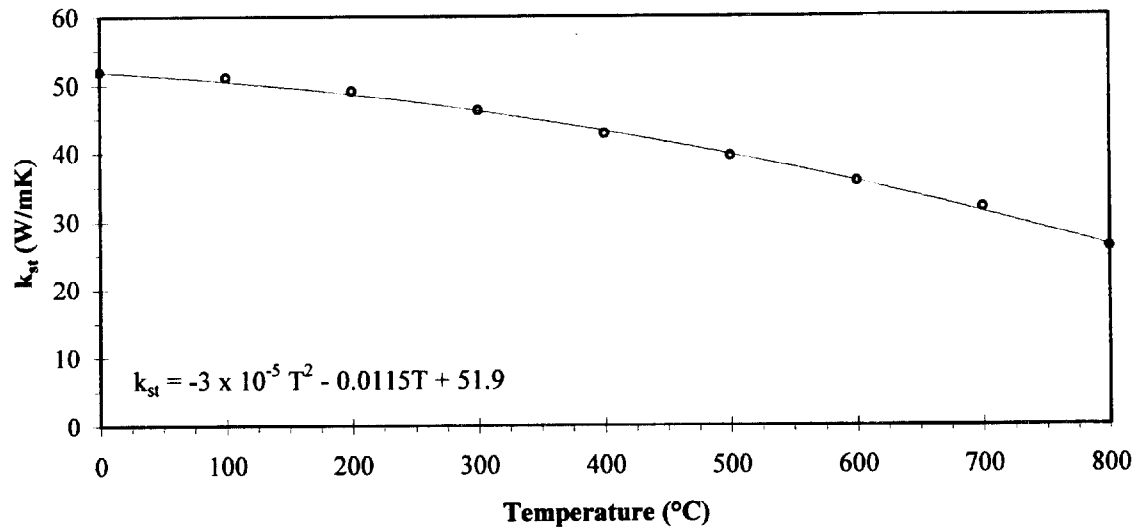
Figure 7. 6: Thermal Conductivity of C-1018 Carbon Steel.

$$k_{st} = -3 \times 10^{-5} \, T^2 - 0.0115T + 51.9$$

7.3.2 Conduction—Insulation

The ceramic fiber insulation will become heated due to being in contact with the heated plate. However, the insulation temperature will increase at a much slower rate thereby creating a temperature difference. This temperature difference between the steel and the ceramic fiber insulation, will cause heat to be conducted away from the unexposed side of the plate and into the insulation, $\dot{q}''_{k, ins}$. Fourier's law can be used to express this conduction heat transfer.

$$\dot{q}''_{k, ins} = -k_{ins} \frac{\Delta T}{\Delta z} \tag{7.6}$$

where k_{ins} is the thermal conductivity of the ceramic fiber insulation, ΔT is the difference between the central thermocouple temperature and the temperature measured between the layers of insulation and Δz is the thickness of a layer of insulation, which is approximately 1 cm (after being slightly compressed within the sample holder).

The temperature dependent thermal conductivity of the ceramic fiber insulation

was obtained from the manufacturer's literature and is presented in Figure 7.7. The

equation of the line through the data points is determined to be

$$k_{ins} = 3 \times 10^{-7} \cdot T^2 + 9.41 \times 10^{-5} \cdot T + 0.035252 \text{ W/m·K}$$

where T is the temperature measured between the insulation layers in °C. This equation

is used to determine the thermal conductivity of the insulation at all temperatures.
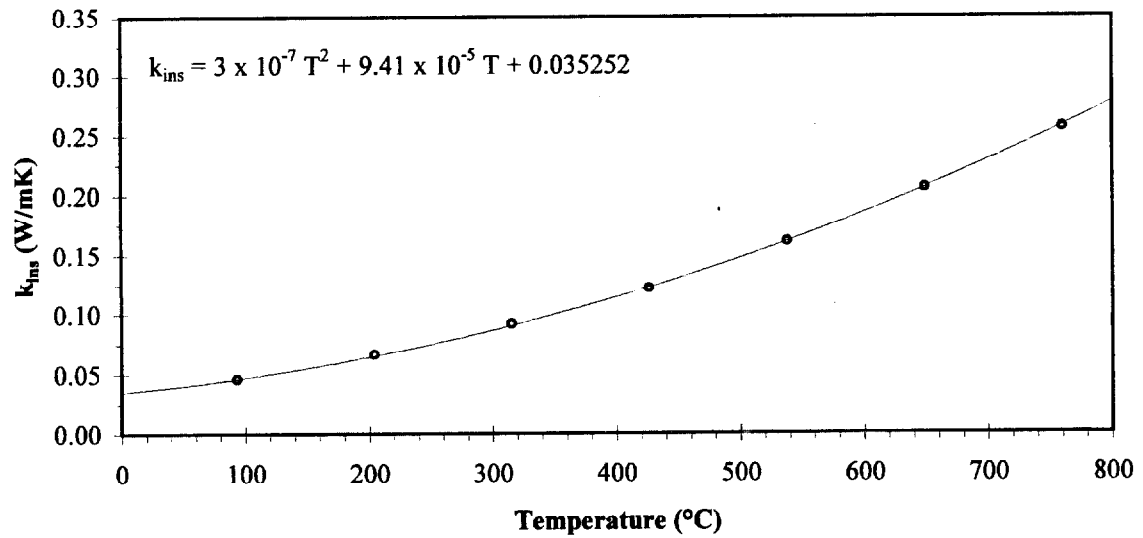
Figure 7. 7: Thermal Conductivity of Ceramic Fiber Insulation

7.3.3 Convection

The heated steel plate will also transfer heat to the cooler surrounding air by

convection heat transfer, $\dot{q}_c''$. Convection heat transfer can be expressed as

$$\dot{q}_c'' = h_c(T_s - T_\infty) \tag{7.7}$$

where h_c is the convection heat transfer coefficient (W/m^2·K), T_s is the surface temperature of the steel plate (K) and T_∞ is the ambient temperature (K).

In order to determine the convective heat flux, an appropriate h_c value must be determined for the steel plate being heated in the LIFT apparatus. There is no applied flow across the surface of the sample in the LIFT, therefore the plate will undergo natural convection. Typical h_c values for natural convection are between approximately 10 and 25 W/m^{2}K [20]. However, in order to accurately calculate the convective heat transfer, temperature dependent expressions for h_c are used.

An average heat transfer coefficient can be calculated by

$$\overline{h_c} = \frac{\overline{Nu} \cdot k_a}{l} \tag{7.8}$$

where $\overline{Nu}$ is the average Nusselt number, k_a is the thermal conductivity of the fluid in contact with the plate (air) and l is effective length scale, which is the height of the plate (15.24 cm).

The Nusselt number "is equal to the dimensionless temperature gradient at the surface, and it provides a measure of the convection heat transfer occurring at the surface." [20]. An average Nusselt number, provides an average heat transfer coefficient, which is reasonable for this analysis. The average Nusselt number for a flat, vertical plate undergoing free (unforced) convection can be expressed as [4].

$$\overline{Nu} = \left\{ 0.825 + \frac{0.387 \cdot Ra^{1/6}}{\left[1 + (0.492/Pr)^{9/16} \right]^{8/27}} \right\}^2$$

where Ra and Pr are the Rayleigh number and the Prandtl number, respectively.

The Rayleigh number is the ratio of inertia and viscous forces and can be expressed as the product of the Grashof number and the Prandtl number:

$$Ra = Gr \cdot \mathrm{Pr}$$

The Grashof number, Gr, is a dimensionless parameter which provides a ratio between buoyancy and viscosity forces that act on a fluid. Since there is no significant forced air flow present in the LIFT apparatus buoyancy driven flow becomes the primary mode of convective heat transfer [30]. The Grashof number for a vertical flat plate can be expressed as

$$Gr = \frac{g\beta(T_s - T_\infty)l^3}{\nu^3} \tag{7.9}$$

where g is the acceleration due to gravity (9.807 m/s^2), β is the volumetric thermal expansion coefficient (1/K), ν is the kinematic fluid viscosity (m^2/s) and T_s is the surface temperature of the plate which is approximately equal to the measured temperature of the central thermocouple.

The volumetric thermal expansion coefficient, β, provides a measure of the change in density of a fluid, at constant pressure, based on the temperature change. For an ideal gas, β depends on the absolute temperature of the fluid:

$$\beta = -\frac{1}{\rho}\left(\frac{\partial \rho}{\partial T}\right)_p = \frac{1}{\rho}\frac{p}{RT^2} = \frac{1}{T}$$

where ρ is the fluid density (kg/m^3), p is the pressure, R is the specific gas constant (J/kg·K) and T is the absolute fluid temperature (K). However a boundary layer exists over the vertical plate, and the temperature varies across that layer. Therefore a mean average boundary layer temperature, or film temperature (T_f), must be used to determine the thermal expansion coefficient.

125

$$T_f \equiv \frac{T_s + T_\infty}{2}$$

Therefore β can be expressed as

$$\beta = \frac{2}{T_s + T_\infty}$$

The Prandtl, Pr, number is a dimensionless parameter which relates the molecular momentum and the thermal diffusivity of a fluid and "provides a measure of the relative effectiveness of momentum and energy transport by diffusion in the velocity and thermal boundary layers" [20].

$$\text{Pr} = \frac{\nu}{\alpha} \qquad (7.10)$$

where α is the thermal diffusivity (m^2/s) of the fluid.

The thermo-physical properties of air used in Equations 7.8, 7.9 and 7.10, are also temperature dependent and must be determined in order to accurately calculate h_c. The thermal conductivity, thermal diffusivity and kinematic viscosity were obtained from Atreya [4] and are presented in Figures 7.8, 7.9 and 7.10. The temperature dependent equations derived from the data are as follows:

$$k_a = -3 \times 10^{-8} \cdot T^2 + 7.76 \times 10^{-5} \cdot T + 0.024281 \quad \text{W/m·K}$$

$$\alpha = 7 \times 10^{-11} \cdot T^2 + 1.562 \times 10^{-7} \cdot T + 1.8176 \times 10^{-5} \quad m^2/s$$

$$\nu = 7 \times 10^{-5} \cdot T^2 + 0.0974 \cdot T + 13.159 \quad m^2/s$$

Due to boundary layer effects, these properties are evaluated at the film temperature, T_f.

Therefore, using the heat transfer coefficient calculated with Equation 7.8, the convection heat transfer from the center of the heated plate to the surrounding air can be precisely calculated.

$$k_a = (-3 \times 10^{-5} T^2 + 0.0776T + 24.281) \times 10^{-3}$$
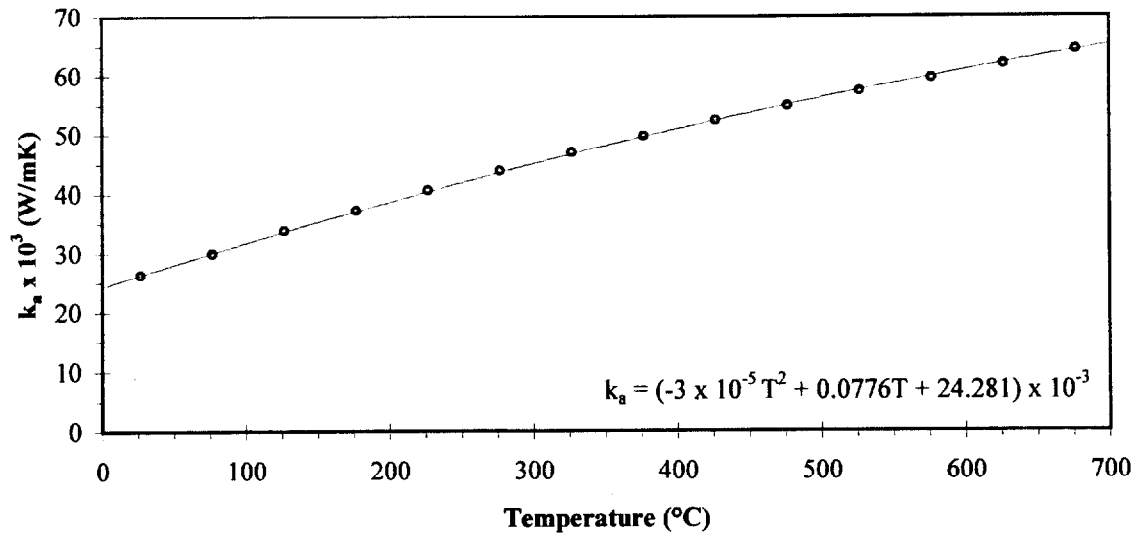
Figure 7. 8: Thermal Conductivity of Air.

$$\alpha = (7 \times 10^{-5} T^2 + 0.1562T + 18.176) \times 10^{-6}$$
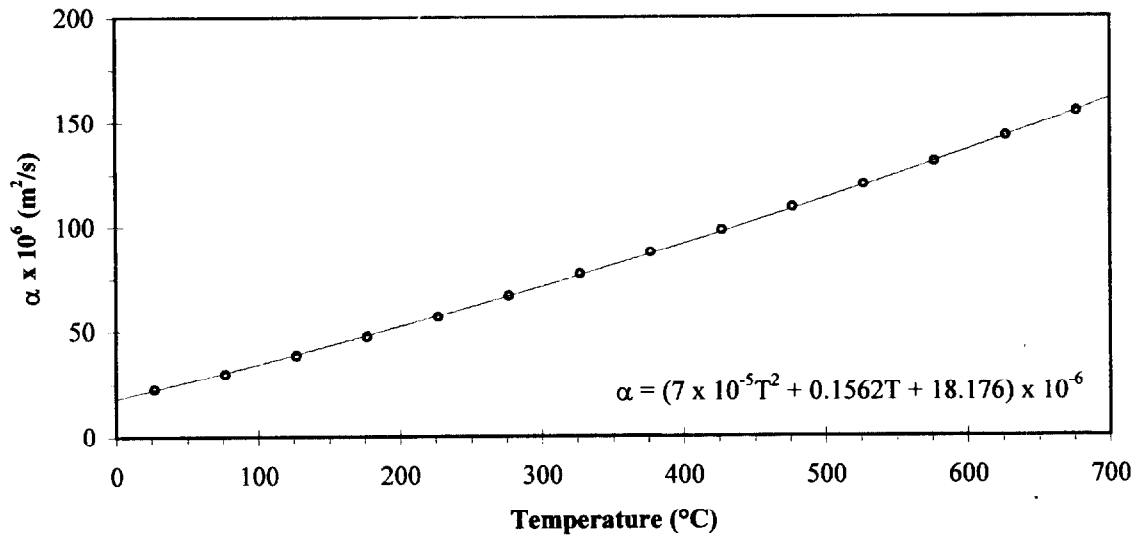
Figure 7. 9: Thermal Diffusivity of Air.

127

$$v = 7 \times 10^{-5} T^2 + 0.0974T + 13.159$$
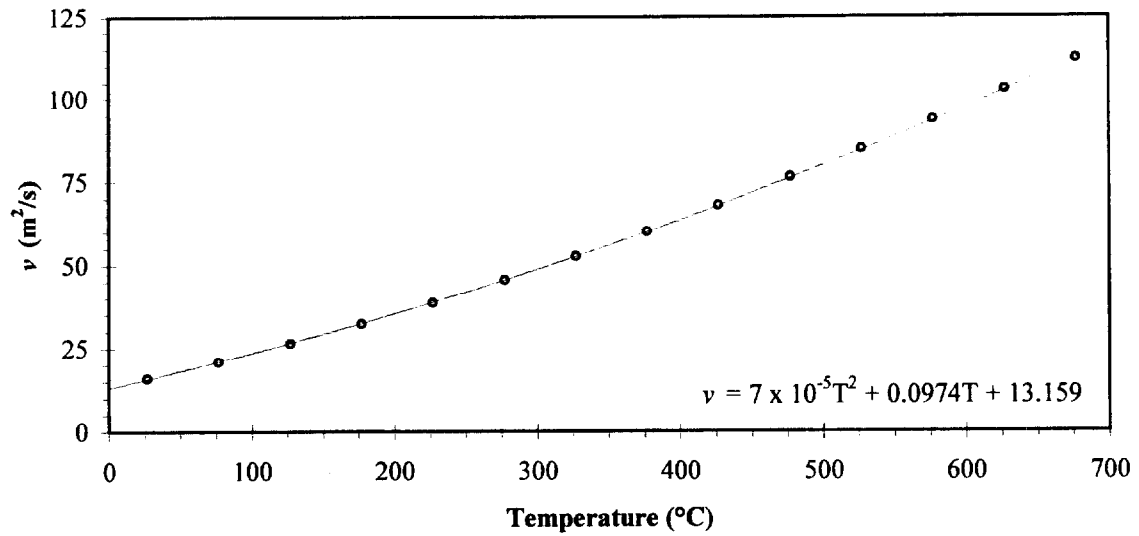
Figure 7. 10: Kinematic Viscosity of Air.

7.3.4 Re-Radiation

The heated steel plate will radiate energy to the environment according to the following expression:

$$\dot{q}''_{rr} = \varepsilon\sigma\left(T_s^4 - T_\infty^4\right) \tag{7.11}$$

where σ is the Stefan-Boltzmann constant (5.67 x 10^{-11} kW/m^2·K^4) and ε is the emissivity of the steel surface which is taken to be 1 due to the surface being coated with soot. Taking the temperature of the central thermocouple node as being an approximation of the surface temperature, the re-radiation with respect to time can be calculated. Although small differences between the temperature of the surface of the steel and the thermocouple positions are expected, the magnitude of these differences will be negligible.

128

7.3.5 Energy Storage Term

The rate of change of thermal energy stored within a unit volume can be expressed as

$$\dot{q}''' = \rho c \frac{\partial T}{\partial t} \qquad (7.12)$$

assuming that the density, ρ, and the specific heat, c, remain relatively constant. In order to calculate the rate of change per unit area of the steel plate, Equation 7.12 can be multiplied by the plate thickness, δ to obtain

$$\dot{q}''_{sto} = \rho c \delta \frac{\partial T}{\partial t} \qquad (7.13)$$

The density of C-1018 steel is 7,860 kg/m^3 and is constant over the range of temperatures reached in this series of experiments. However as the data in Figure 7.11 indicates, the specific heat of steel, c, is temperature dependent. The specific heat data follows a quadratic equation up to 700 °C and the subsequent temperature dependent increase and decrease is approximated linearly:

$$c = 0.0007 \cdot T^2 - 0.0058 \cdot T + 486 \ \text{J/kg·K} \qquad 0 \ °\text{C} < T < 700 \ °\text{C}$$

$$c = 11.72(T - 700) + 846 \ \text{J/kg·K} \qquad 700 \ °\text{C} < T < 750 \ °\text{C} \qquad (7.14)$$

$$c = -9.64(T - 750) + 1432 \ \text{J/kg·K} \qquad 750 \ °\text{C} < T < 850 \ °\text{C}$$

The slope of the time-temperature curve, or the derivative with respect to time, is simply approximated as being the temperature difference over an incremental period of time.

$$\frac{\partial T}{\partial t} \cong \frac{\Delta T}{\Delta t}$$

129

Due to slight fluctuations in the plate temperature and the precision of the data acquisition system, this time period is chosen to be 10 seconds. This value provides a limited amount of fluctuation in the heat flux calculation while still providing an accurate approximation of the slope. This results in the following expression for the amount of thermal energy that is stored per unit area of the steel plate:

$$\dot{q}''_{sto} = \rho c \delta \frac{\Delta T}{\Delta t} \qquad \Delta t = 10\text{s} \qquad (7.15)$$

where Equation 7.14 is used to determine the appropriate specific heat.
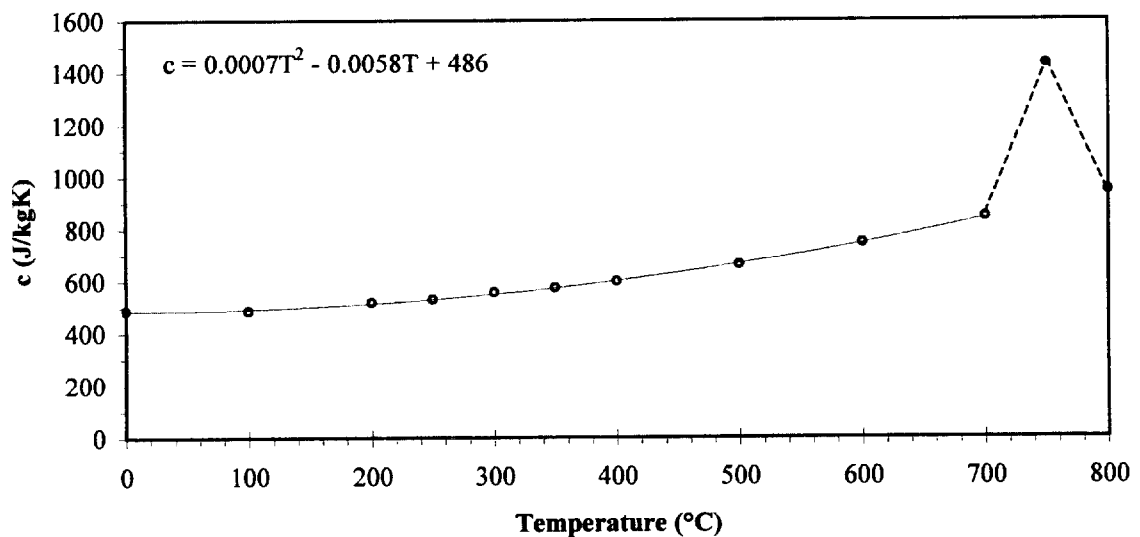
Figure 7. 11: Specific Heat of C-1018 Carbon Steel.

7.4 Incident Heat Flux Equation

The incident heat flux from the radiant panel of the LIFT apparatus can be calculated by combining the energy storage, convection, re-radiation and conduction heat transfer terms:

$$\alpha \dot{q}_i'' = \dot{q}_{sto}'' + h_c(T_s - T_\infty) + \varepsilon\sigma(T_s^4 - T_\infty^4) + \dot{q}_{k,\ ins}'' - \dot{q}_{k,\ st}'' \qquad (7.16)$$

Using Equations 7.4, 7.6 and 7.13 as inputs into Equation 7.16, the incident heat flux to the center of the steel plate can be calculated by the following expression

$$\dot{q}_i'' = \left[\rho c \delta \frac{\Delta T}{\Delta t} + h_c(T_s - T_\infty) + \varepsilon\sigma(T_s^4 - T_\infty^4) - k_{ins}\left(\frac{\Delta T}{\Delta z}\right) - k_{st}\left(\frac{T_{x+\Delta,y} + T_{x-\Delta,y} + T_{x,y+\Delta} + T_{x,y-\Delta} - 4 \cdot T_{x,y}}{\Delta^2}\right)\delta \right] \Big/ \alpha \qquad (7.17)$$

It should be noted that the symbol "Δ" used for ΔT, Δt and Δz indicates change and not the distance between the thermocouples as in the denominator of the final term

Equation 7.17 indicates that determination of the incident heat flux to the steel plate, $\dot{q}''_i$, is dependent on the absorptivity, α, of the plate surface. However, since the emissivity of the surface is approximately equal to 1 due to the soot coating and the roughened surface, the numerator of the right hand side of Equation 7.17 is approximately equal to the actual incident heat flux. For the test where the plate was coated with the high temperature optical black coating the right side of the equation must be divided by the emissivity, which is 0.92.

7.5 Small-Scale Steel Plate Test Results

Using Equation 7.17, the temperature profiles of the four thermocouples welded to the plate (recall that one of the thermocouples became detached prior to testing) and the thermocouple within the ceramic fiber insulation, the incident heat flux from the radiant panel can be calculated. Figures 7.12 through 7.25 show the temperature profiles from the central thermocouple, the heat flux measured by the pyrometer and the heat flux calculated using Equation 7.17. The step-like nature of the measured heat flux curve is due to the sensitivity of the voltmeter used to measure the output from the pyrometer.

The figures indicate that this method is extremely accurate for determining the incident heat flux to a small vertical steel plate and provides evidence that large scale-testing should provide equally accurate results. The slight drop in the calculated heat flux immediately after the initial increase is most likely due to a slight decrease in the heat flux from the radiant panel following removal of the dummy sample and insertion of the sample holder. Small errors are also expected due to the approximations used for calculating the conduction losses and the convection heat transfer coefficient. However, the discrepancies are minimal and are within the amount of error expected for this type of analysis.

132
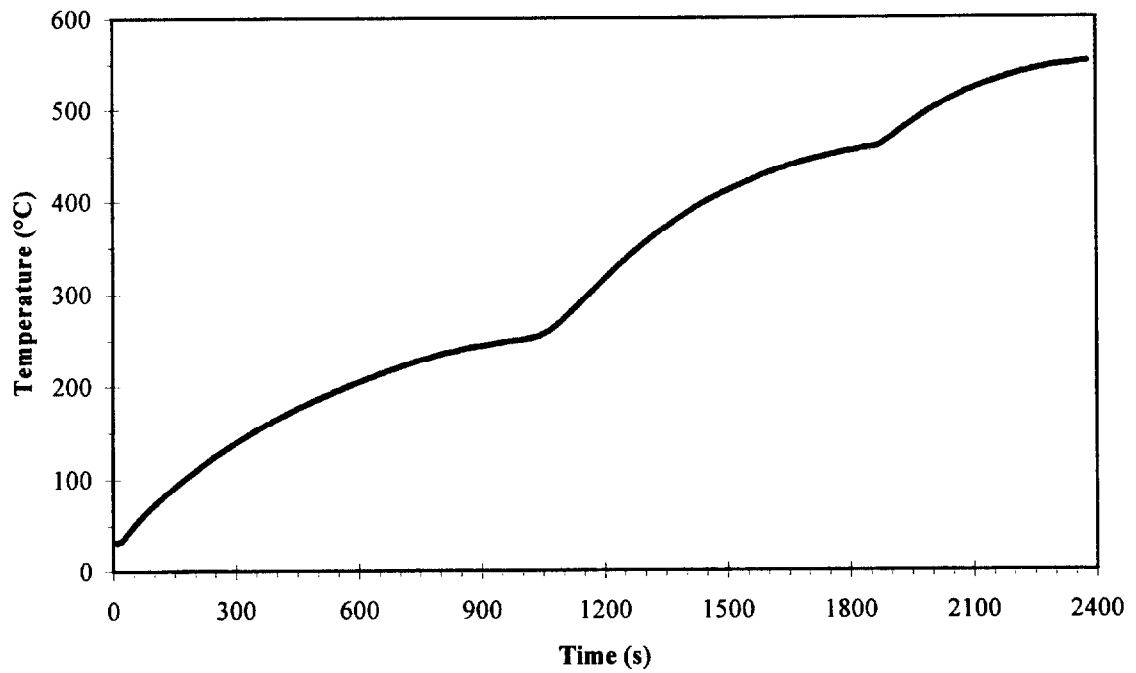
Figure 7. 12: Temperature with Respect to Time – 7.2 kW/m² Increased to 24.6 and 37.6 kW/m².
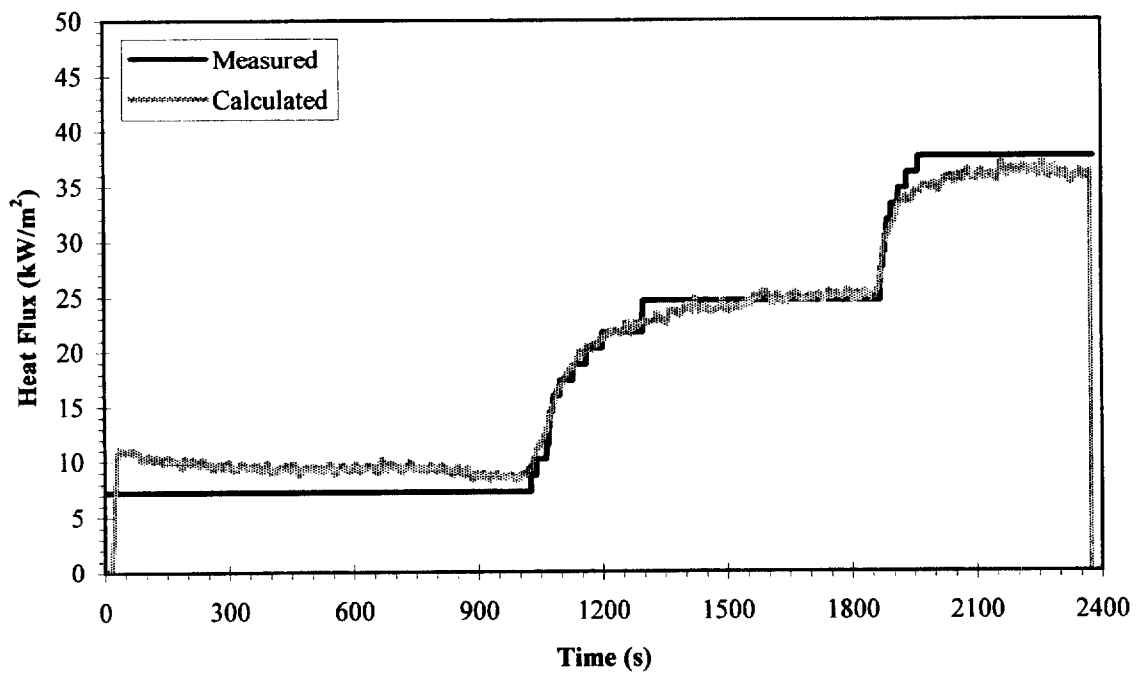
Figure 7. 13: Measured and Calculated Heat Flux – 7.2 kW/m² Increased to 24.6 and 37.6 kW/m².
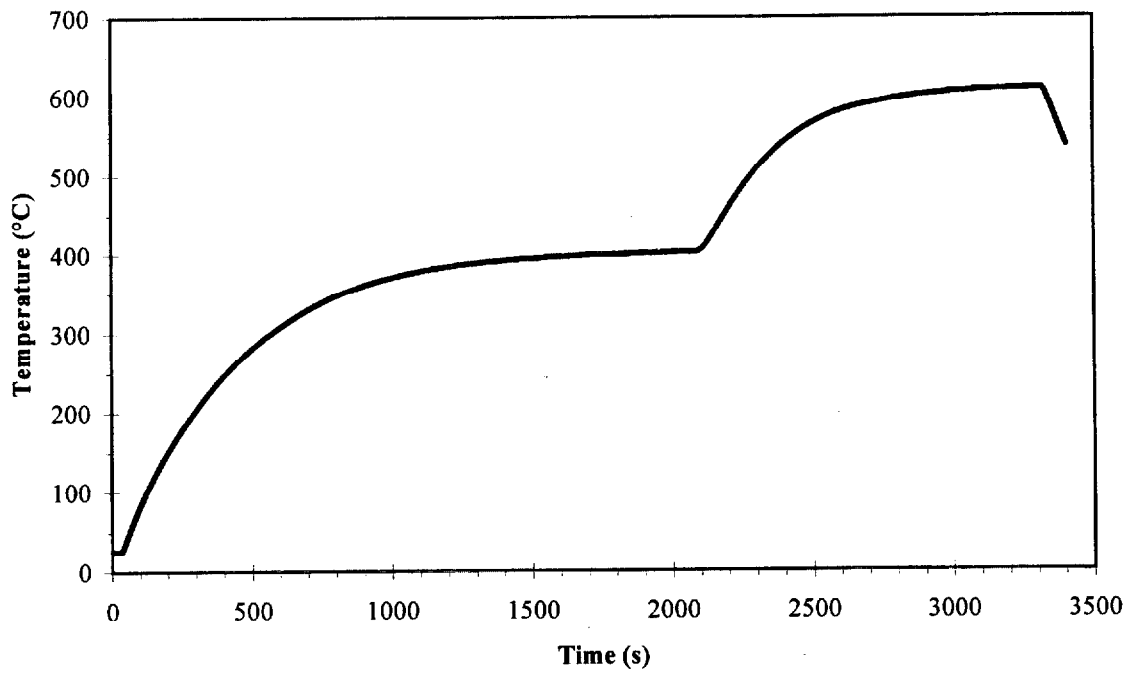
Figure 7. 14: Temperature with Respect to Time – 17.8 kW/m² Increased to 43.0 kW/m².
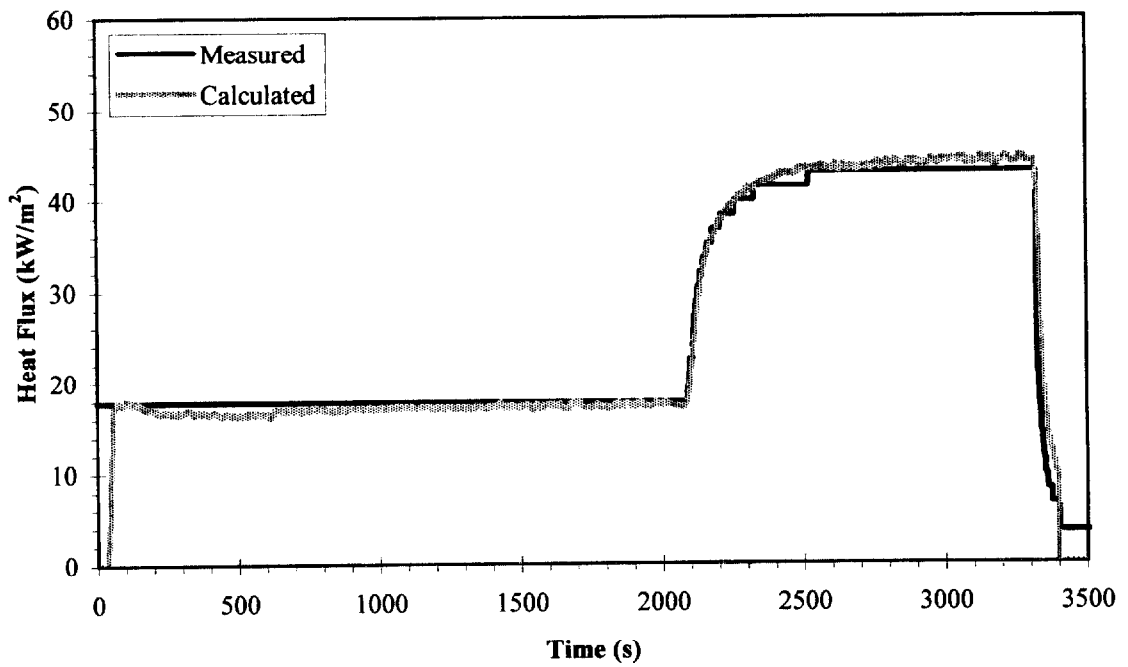
Figure 7. 15: Measured and Calculated Heat Flux – 17.8 kW/m² Increased to 43.0 kW/m².

Figure 7. 16: Temperature with Respect to Time – 28.8 kW/m².
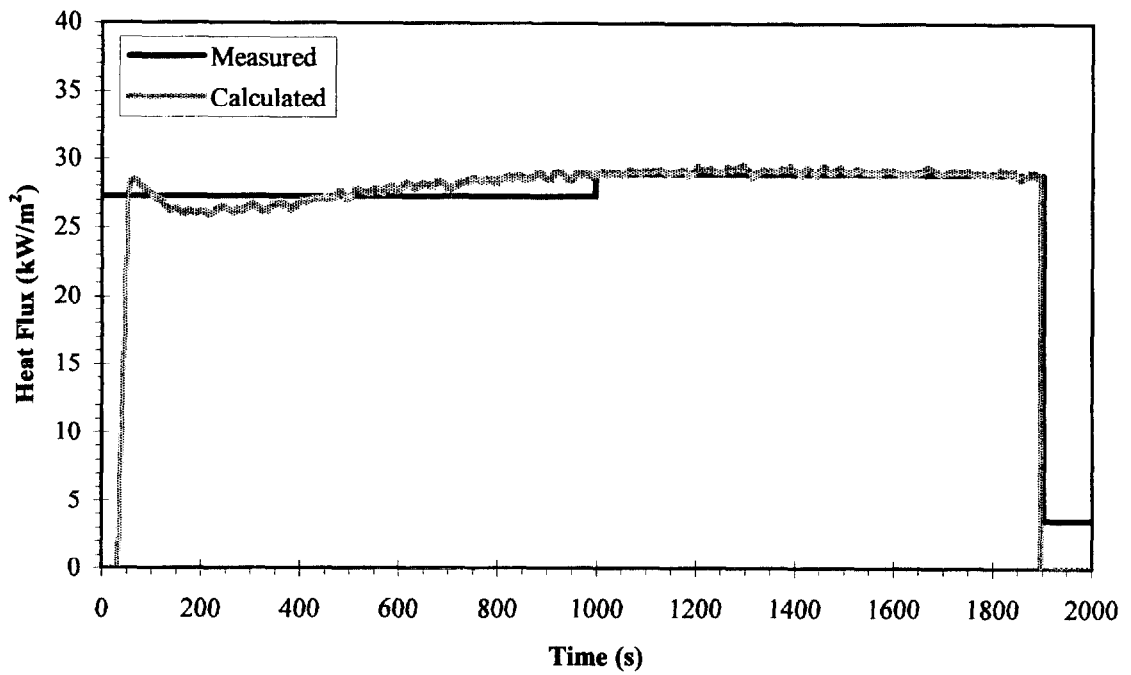
Figure 7. 17: Measured and Calculated Heat Flux – 28.8 kW/m².

135
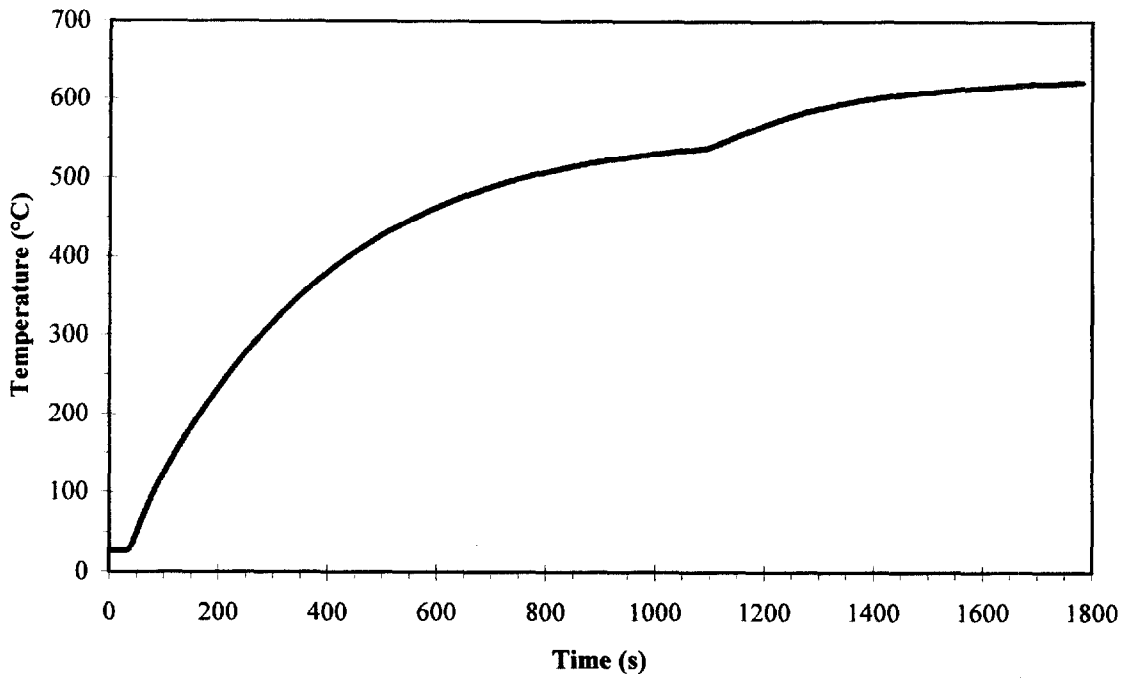
Figure 7. 18: Temperature with Respect to Time – 35.1 kW/m^2 Increased to 47.8 kW/m^2.
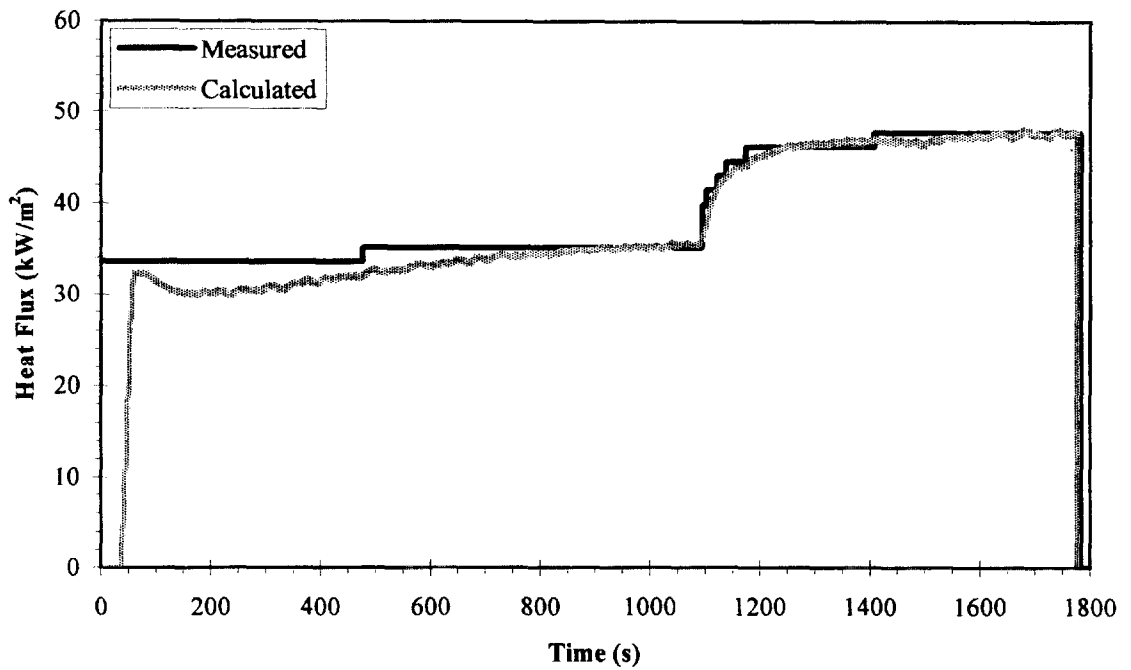
Figure 7. 19: Measured and Calculated Heat Flux – 35.1 kW/m^2 Increased to 47.8 kW/m^2.

136
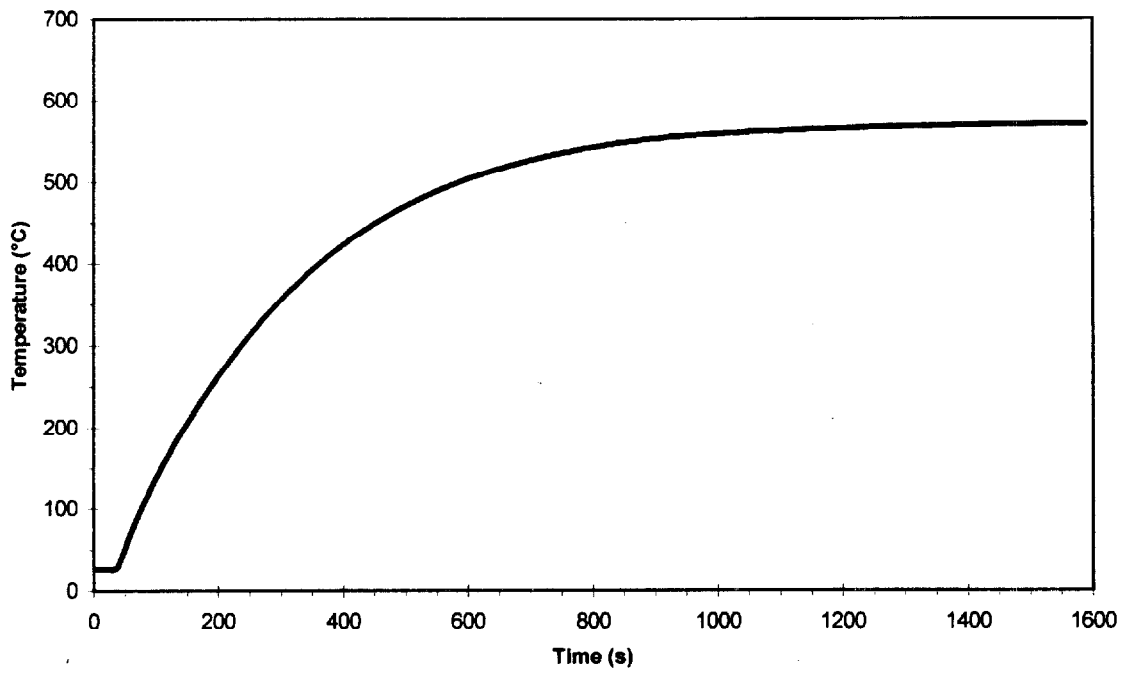
Figure 7. 20: Temperature with Respect to Time – 36.7 kW/m^2.
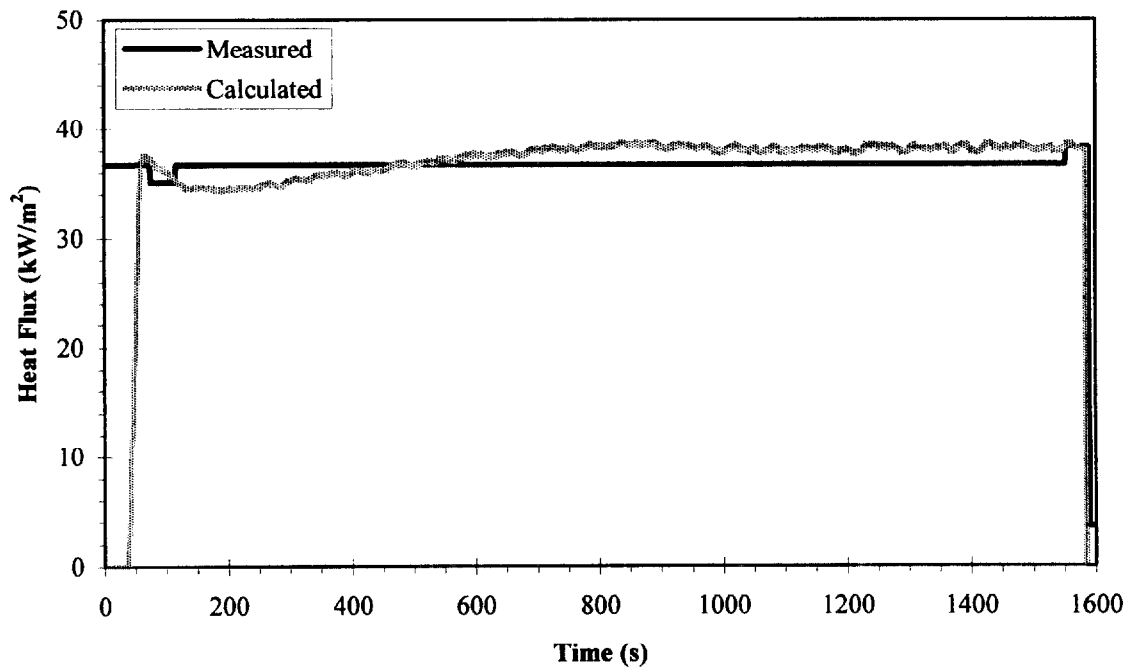
Figure 7. 21: Measured and Calculated Heat Flux – 36.7 kW/m^2.

137
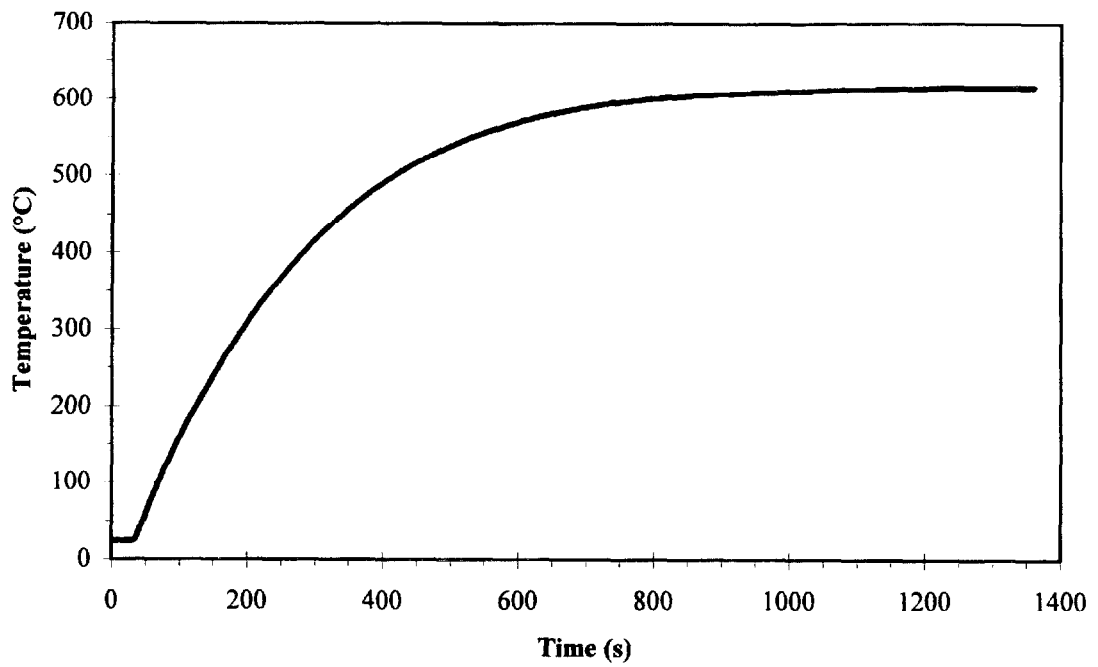
Figure 7. 22: Temperature with Respect to Time – 44.6 kW/m².

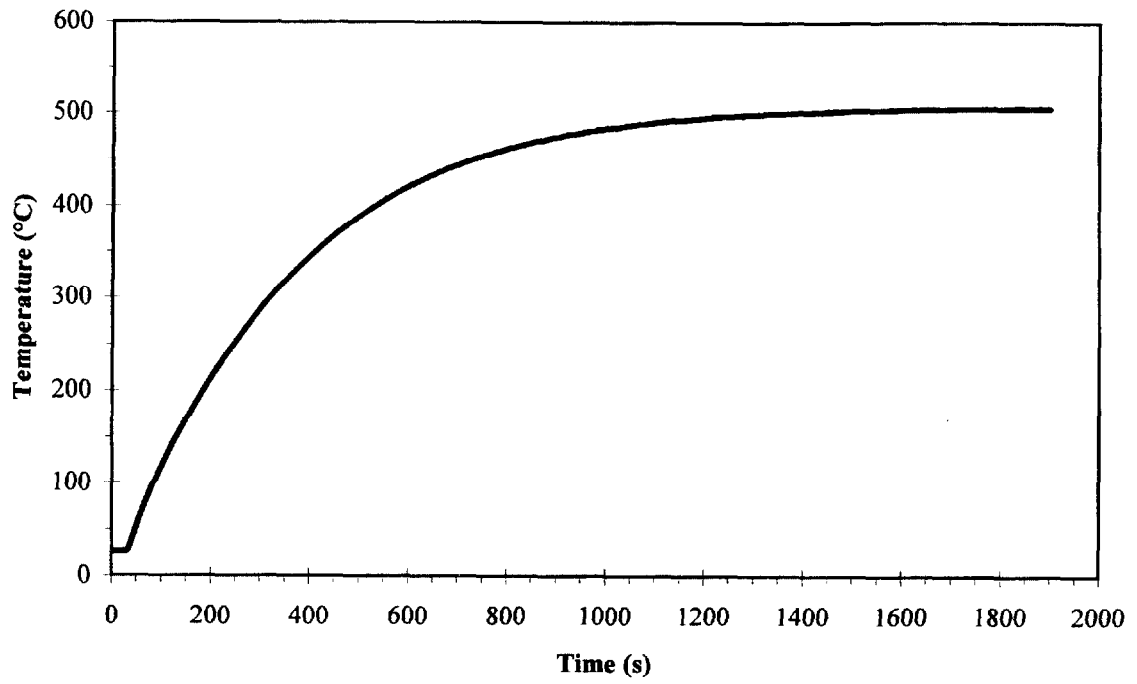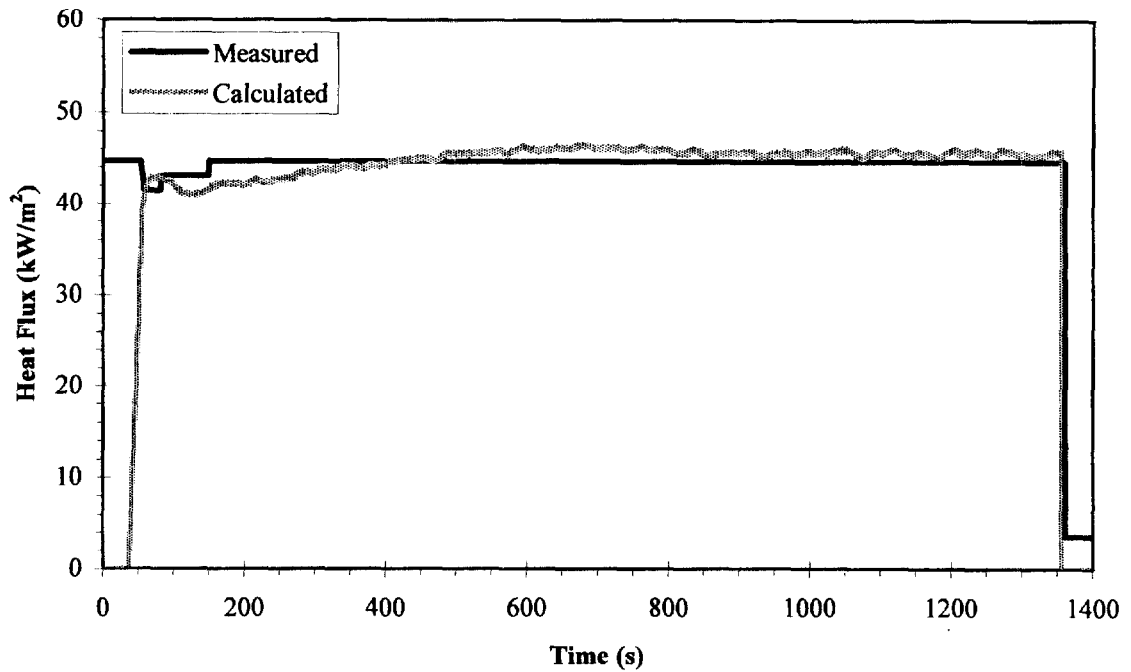**Figure 7. 23**: Measured and Calculated Heat Flux – 44.6 kW/m².
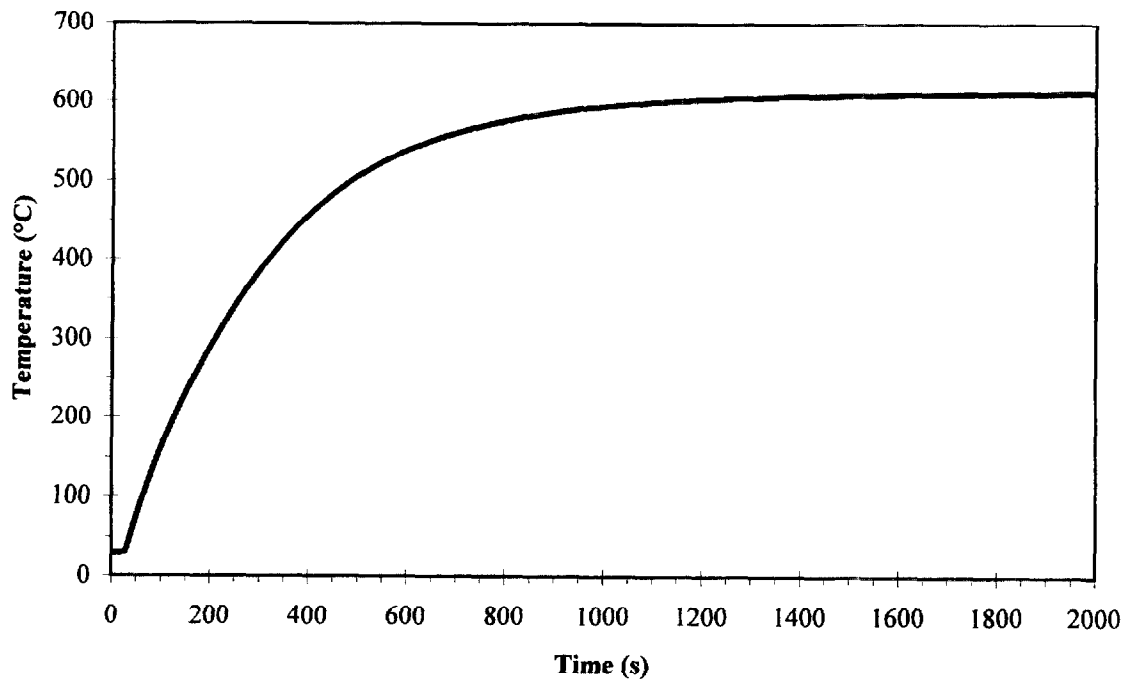
Figure 7. 24: Temperature with Respect to Time – Medtherm Coating, 46.2 kW/m^2.
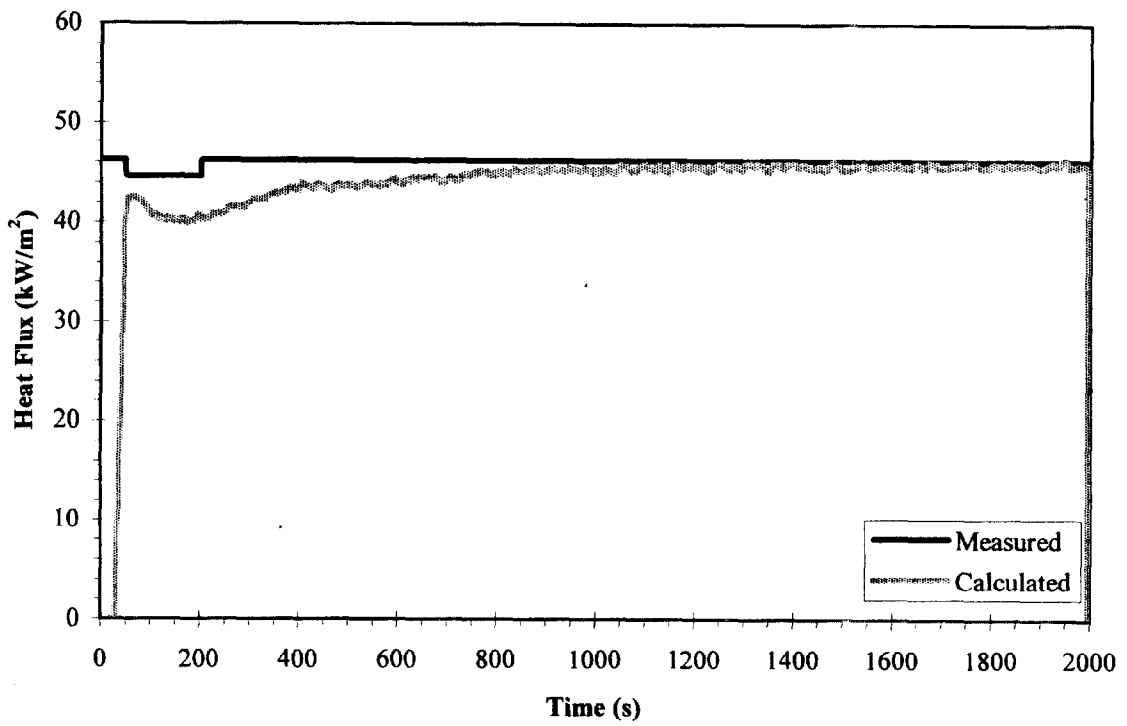
Figure 7. 25: Measured and Calculated Heat Flux – Medtherm Coating, 46.2 kW/m^2.

8. FULL-SCALE HEAT FLUX MEASUREMENTS

The same basic procedure utilized for the small steel plate in the LIFT is used to determine the incident heat flux in the full-scale room-corner test. Thermocouples were attached to the unexposed side of larger steel plates (1.2 m x 0.6 m) which were mounted to the walls and ceiling of the standard room. The heat transfer analysis used in the small scale test is almost identical to the one used for the large scale tests. However, due to the presence of the hot flames the convection and radiation terms are combined to provide a net incident heat flux from the fire plume. In order to provide steel plate heat flux measurements that are consistent with heat flux measurements from water cooled heat flux meters, a cold surface correction factor is applied. Similarly, the increased heat flux to the walls and ceiling due to the high room temperature is calculated to provide an overall room effect. The calculated heat fluxes at each thermocouple location were then used to provide complete heat flux distributions for both the initial flux from the fire plume and equilibrium conditions. This type of detailed information will significantly increase what we know about the thermal attack to materials tested in the ISO 9705 room-corner test.

8.1 Test Configuration

8.1.1 Steel Plate Assembly

Full scale testing was performed using the ISO 9705 room located at the L. S. Fire Laboratory, Italy. Steel plates were mounted in the room to determine the incident heat flux to the walls and ceiling from the ignition burner. The plates used were 1.2 m

by 0.6 m by 5 mm thick C-1018 carbon steel. Three plates were used to measure incident heat flux to the wall and two plates were used for the ceiling.

Thirty-two thermocouples were fixed to the unexposed surface of each steel plate on 15 mm centers. Due to difficulties in locating a suitable welder and to provide for relatively easy thermocouple replacement, wires were fixed in place using a small steel strip screwed to the plate as shown in Figure 8.1. A 2 mm threaded hole was provided approximately 1 cm on either side of each thermocouple location. The thermocouple junction was then pushed 0.5 to 1 cm through a 2 cm by 5 cm strip of silica blanket. The thermocouple was then placed on the plate with the junction in contact with the steel and the silica blanket between the plate and the thermocouple wire insulation. The thermocouple junction and silica blanket were then covered with a 1 mm thick strip of high-temperature mica insulation and a thin steel strip was screwed over the mica using two 2 mm diameter screws. This procedure was repeated for all 32 thermocouples.
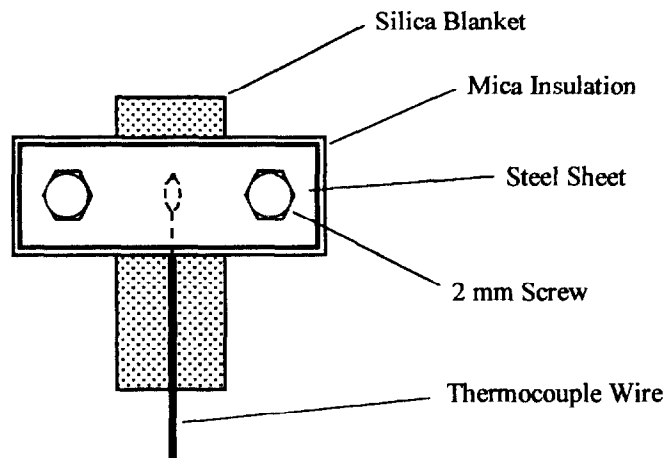
Figure 8. 1: Typical Full-Scale Plate Thermocouple Attachment.

The unexposed side of the plate was then covered with two layers of 1/2 inch ceramic fiber insulation blanket. Fifteen cm wide strips were placed between each row of thermocouple wires and 7.5 cm strips were placed along the edges of the plate. The direction of the strips was alternated as shown in Figure 8.2. The thermocouple wires were run between the ceramic fiber blanket and a 1.2 m by 0.6 m piece of 1 inch thick Rockwool insulation board and the ends were pulled through a small hole in the center of the board. The entire assembly was held together using metal angle supports which were secured using 6 mm diameter bolts screwed into threaded holes in the corner of each plate.

8.1.2 Plate Mounting

Steel frames were used to mount the plates to the walls and ceiling in the vicinity of the ignition burner. Three plates were used on the wall, with two near the ceiling and one at the floor near the burner as can be seen in Figure 8.3. A piece of ceramic fiber insulation board was placed into the frame in the empty position in order to provide a relatively flush wall surface. The flux to only one wall was measured due to symmetry. Two plates were mounted in the corner of the ceiling directly above the ignition burner as seen in Figures 8.4 and 8.5. The wall and ceiling surfaces near the burner which were not covered by the steel plates or the ceramic fiber board were covered with Rockwool insulation boards to protect the concrete walls from damage. The thermocouple wire bundles were run through holes in the concrete walls in the location of the center of each of the plates. The exposed surfaces of the steel plates were sand blasted before mounting and coated with high temperature black paint (600

°C) prior to each test to reduce the reflectivity. The exact emissivity of the paint is unknown but is assumed to be equal to 1. Siegel and Howell [45] list the emissivity of flat black paint to be 0.96 to 0.98, therefore this is a reasonable assumption.

8.1.3 Ignition Source

The burner used was the ISO 9705 standard ignition source [22]. The burner is 17 cm square with a height of 14.5 cm. The lower 10 cm of the burner is filled with 4 mm to 8 mm diameter gravel and the top 4.5 cm is filled with 2 to 3 mm diameter sand. There is a 1.4 mm layer of metal gauze placed between the two layers to keep them separated. Gas is supplied through a metal gas inlet pipe at the bottom of the burner.

The burner is placed in contact with the walls and is elevated such that the top surface of the burner is 30 cm from the floor of the room

The ISO Room/Corner Test specifies that "the net heat output shall be "100 kW during the first 10 minutes after ignition and then shall be increased to 300 kW for a further 10 minutes" [22]. The energy release rate was determined by flowing propane gas at a predetermined rate based on the heat of combustion.. The heat of combustion of propane is 46.4 kJ/g [47] and by flowing propane at the rates listed in Table 8.1, the proper theoretical energy release rate is obtained.
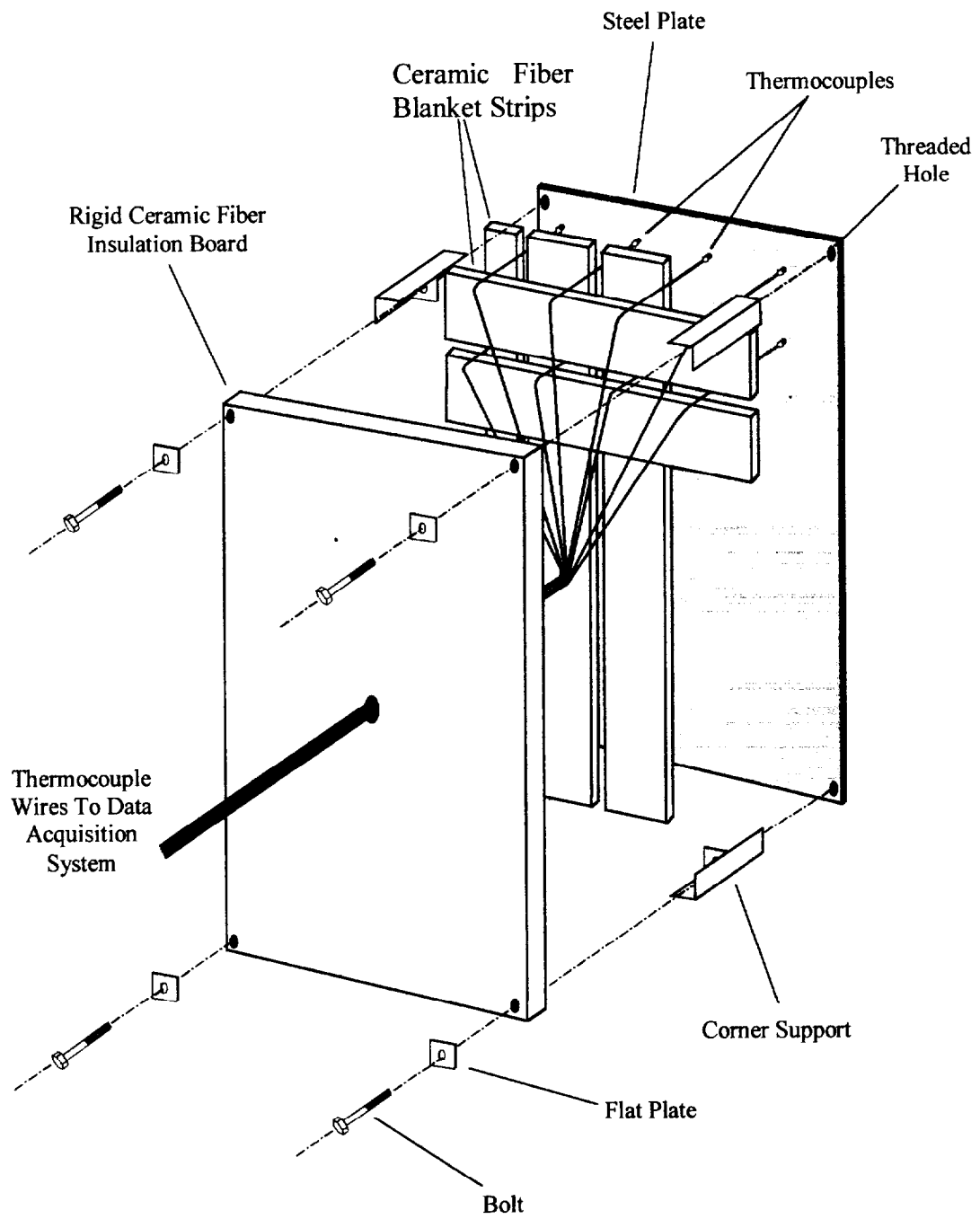
Figure 8. 2: Full Scale Test Steel Plate Assembly.
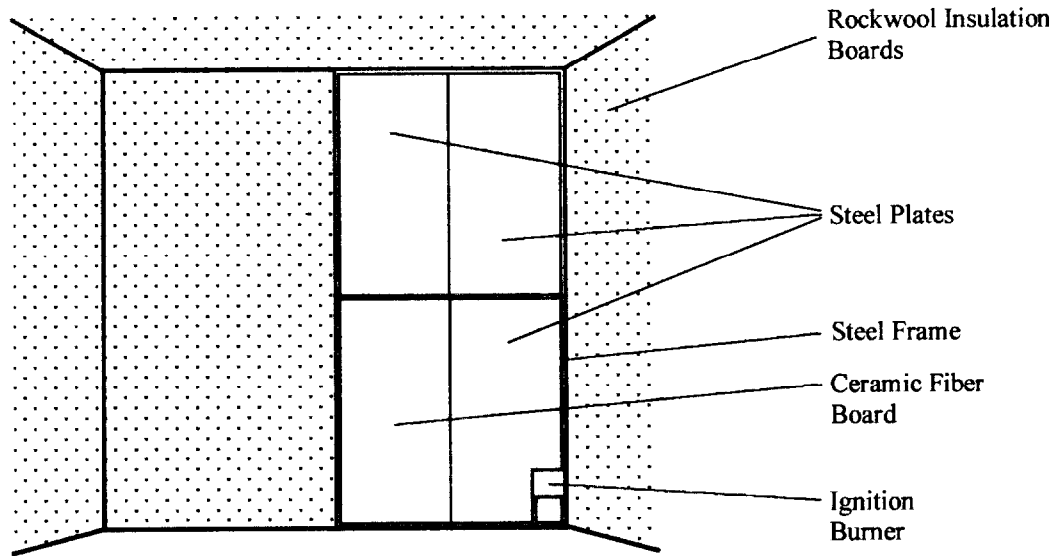
Figure 8. 3: Full-Scale Room/Corner Test Wall Heat Flux Measurement Configuration.
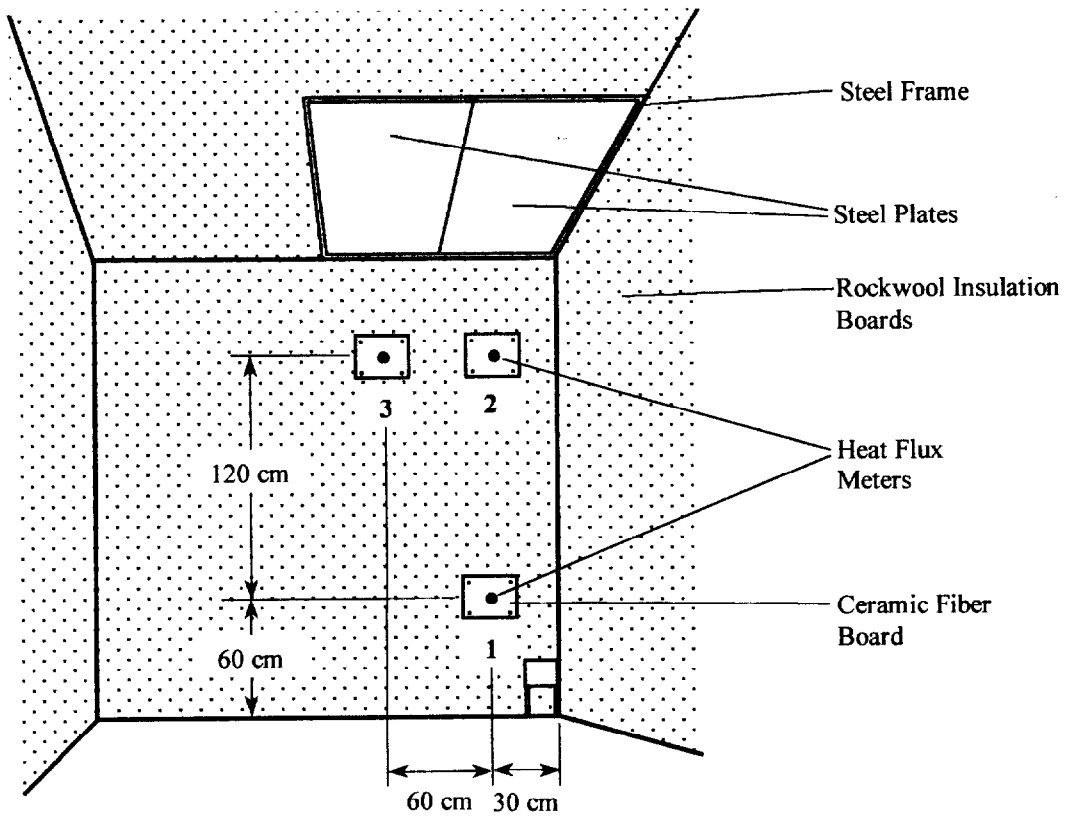
Figure 8. 4: Full-Scale Room/Corner Test Ceiling Heat Flux Measurement Configuration.

145

Table 8. 1: Propane Flow Rates Used in the Room/Corner Test.

Propane Flow g/s	Energy Release Rate kW
2.16	100
6.47	300

8.1.4 Thermocouples

A string of four thermocouples was hung from the ceiling directly in front of and 1.75 m from the wall on which the steel plates were mounted. Gas temperatures were only recorder during wall measurement tests since all available channels were needed for measuring the temperatures of the ceiling plates. The thermocouples were positioned at 235, 185, 135 and 85 cm above the floor and were shielded from the radiant flux from the flames using aluminum foil.

8.1.5 Heat Flux Meters

For the tests involving the measurement of the heat flux to the ceiling, the heat flux to the walls was measured in three different locations. The gauges were positioned in the same location as the center of the steel plates during the wall experiments (see Figure 8.4). This was due to the location of the holes in the walls through which the thermocouple wires were run. The 1 inch (2.54 cm) diameter, water cooled, Schmidt-Boelter type heat flux meters were pushed into 26 mm holes drilled into the center of small pieces of ceramic fiber insulation board. The ceramic fiber boards were then mounted to the walls using nails with the heat flux wires and plastic water cooling hoses running through the thermocouple wire holes in the wall. The Rockwool insulation

covering the remainder of the wall surface was cut out to allow for a relatively even wall surface at the flux meter locations (see Figure 8.5).
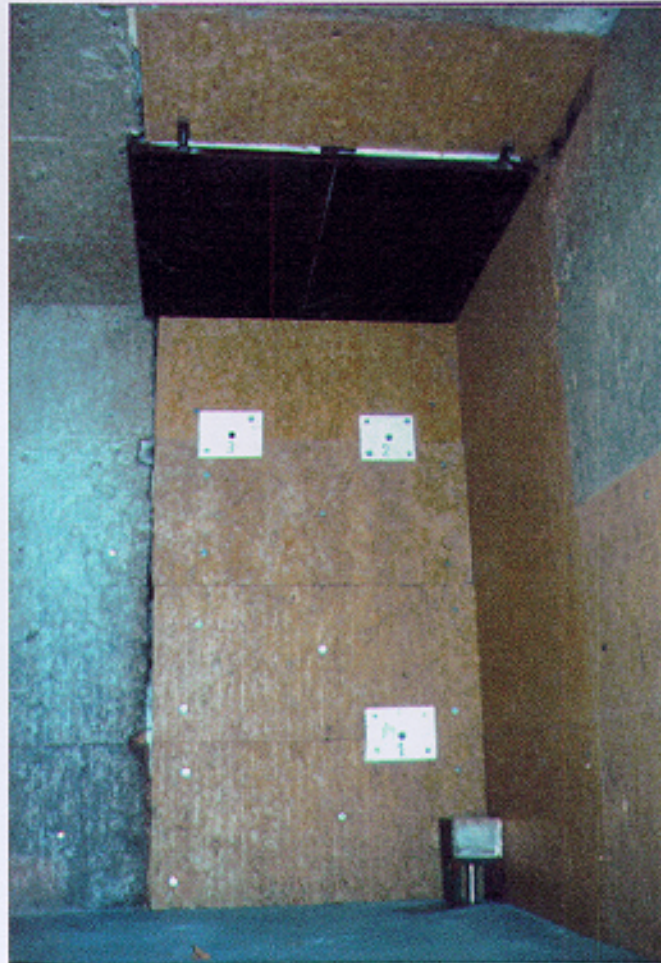
Figure 8. 5: Full-Scale Room/Corner Ceiling Test.

8.1.6 Exhaust Hood

The exhaust hood was operated at a capacity of approximately 3.5 m^3/s in accordance with the ISO 9705 Room/Corner Test standard [22].

8.1.7 Data Acquisition System

The data acquisition system and software used for the thermocouples is identical to the system used for the small-scale testing described in Section 7.2. The only difference is that three Omega® CIO-EXP32 multiplexer boards were used to accommodate the 96 thermocouples used. The heat flux meter measurements were recorded by LSF's Hewlett Packard data acquisition system.

In addition to the thermocouple and heat flux gauge measurements, photographs and video of the various tests were taken.

8.2 Test Procedure

The data acquisition systems were started approximately one minute prior to burner ignition. The steel plate temperature measurements were collected at 5 second intervals. For the ceiling tests, the heat flux from the three gauges was recorded every 3 seconds. Propane gas was flowed through the burner and ignited. Measurements were taken until equilibrium conditions were reached which was followed by a significant increase in the energy release rate. This procedure was continued a maximum of 3 times with a heat flux increase of at least 50 kW. The room was then allowed to cool to ambient, the plates were re-painted with high temperature black paint, damaged insulation on the walls was replaced and testing continued. Various tests were conducted for burner heat release rates of 50 to 300 kW. However only the 100 and 300 kW burner output levels will be analyzed here.

8.3 Heat Transfer Analysis

The total incident heat flux to any location on the steel plate is a combination of heat transfer effects. In order to accurately determine the incident heat flux from the fire plume the measured heat flux must be corrected to account for heat loss to the ceramic fiber insulation, the increased flux from the heated environment and the reduction in heat flux due to the high temperature of the plate. This corrected incident heat flux is consistent with heat flux measurements made with a water cooled heat flux meter and will allow direct comparisons to other data to be made.

8.3.1 Total Measured Heat Flux

The total incident heat flux to the large steel plates can be determined using a similar method to that used for the small-scale plate. However, due to the presence of the flames the radiant and convective heat fluxes are combined into the total incident flux from the fire plume. The measured, incident heat flux, $\dot{q}''_{i,\,meas}$, can be calculated by:

$$\dot{q}''_{i,\,meas} = \rho c \delta \frac{dT}{dt} + \varepsilon \sigma \left(T_s^{\,4} - T_\infty^{\,4}\right) - \frac{\partial}{\partial x}\left(k_{st}\frac{\partial T}{\partial x}\right)\delta - \frac{\partial}{\partial y}\left(k_{st}\frac{\partial T}{\partial y}\right)\delta \qquad (8.1)$$

where

$\rho c \delta \dfrac{dT}{dt}$ = energy storage within the steel.

$\varepsilon \sigma \left(T_s^{\,4} - T_\infty^{\,4}\right)$ = net re-radiation losses with respect to the environment.

$\dfrac{\partial}{\partial x}\left(k_{st}\dfrac{\partial T}{\partial x}\right)\delta$ = conduction heat transfer in the x-direction.

$\frac{\partial}{\partial y}\left(k_{st}\frac{\partial T}{\partial y}\right)\delta$ = conduction heat transfer in the y-direction.

Temperature measurements within the ceramic fiber insulation were not made during the full-scale experiments. Therefore the conduction losses through the insulation, $\dot{q}''_{k, ins}$, cannot be accurately determined. However these losses can be corrected for based on the small-scale plate results (see Section 8.3.2)

As in the small-scale tests, the measured, incident heat flux (Equation 8.1) is approximated by the following expression:

$$(8.2)$$

$$\dot{q}''_{i, meas} = \rho c \delta \frac{\Delta T}{\Delta t} + \varepsilon\sigma\left(T_s^{\,4} - T_\infty^{\,4}\right) - k_{st}\left(\frac{T_{x+\Delta,y} + T_{x-\Delta,y} + T_{x,y+\Delta} + T_{x,y-\Delta} - 4\cdot T_{x,y}}{\Delta}\right)\delta$$

The incident heat flux with respect to time was calculated using Equation 8.2 for each thermocouple location. The density of the steel, ρ, is 7,860 kg/m^3 and the thickness of the plate, δ, is 5.0 mm. The specific heat, c, and thermal conductivity, k_{st}, at each thermocouple node can be determined from the measured steel temperature based on Equations 7.14 and 7.5, respectively.

Equation 8.2 represents the total measured heat flux at each location. However the heat flux losses to the insulation needs to be corrected to give a more accurate representation of the total incident flux, $\dot{q}''_{i, tot}$.

150

8.3.2 Conduction Losses Through Insulation

The conduction losses through the ceramic fiber insulation, $\dot{q}''_{k,\,ins}$, were not calculated for the full-scale experiments. To calculate the total heat flux to the steel plate this loss must be added to the measured flux:

$$\dot{q}''_{i,\,tot} = \rho c \delta \frac{dT}{dt} + \varepsilon \sigma \left(T_s{}^4 - T_\infty{}^4\right) - \frac{\partial}{\partial x}\left(k_{st} \frac{\partial T}{\partial x}\right)\delta - \frac{\partial}{\partial y}\left(k_{st} \frac{\partial T}{\partial y}\right)\delta + \dot{q}''_{k,\,ins.} \qquad (8.3)$$

where

$\dot{q}''_{k,\,ins.}$ = conduction heat losses to the ceramic fiber insulation

These losses will be based on the losses in the small-scale experiments.

The peak conduction losses from the small-scale tests are presented in Table 8.2 for each incident heat flux level. The percentage of the incident heat flux is also provided and it can be seen that the losses are relatively consistent and have an average value of 5.1% of the incident. Therefore the average percentage of the incident heat flux that is lost to the ceramic fiber insulation can be considered to be about 5% ±1% of the measured flux. This conduction correction is added to the measured flux, $\dot{q}''_{i,\,meas}$, to produce the total incident flux, $\dot{q}''_{i,\,tot}$:

$$\dot{q}''_{i,\,tot} = 1.05\left(\dot{q}''_{k,\,meas}\right)$$

Table 8. 2: Percentage of Incident Heat Flux Lost to the Ceramic Fiber Insulation – Small Scale Plate Testing.

Test	Incident Heat Flux kW/m^2	Loss Through Insulation kW/m^2	Percentage
2	17.8	1.0	5.6
	43.0	2.0	4.7
3	28.8	1.5	5.2
4	35.1	1.8	5.1
	47.8	2.2	4.6
5	36.7	1.9	5.2
6	44.6	2.3	5.2
7	46.2	2.2	4.8
Average			5.1

8.3.3 Cold Surface Correction Factor

The incident heat flux from the fire plume is composed of a convective and a radiation portion. Since the temperature of the steel plate increases during testing, the convection portion of the heat flux from the plume decreases and the measured heat flux will be slightly reduced. This reduced steel plate measurement will be inconsistent with typical flux values measured by water cooled heat flux gauges. Therefore, the incident heat flux to the steel surface should be corrected for the amount of heat flux which is lost since the plates are heated.

The correction for the heat flux to a cold surface produces heat fluxes which are consistent with the incident fluxes measured by the three cooled Schmidt-Boelter heat flux gauges. These corrected heat flux calculations will also be more consistent with the flux to a sample material at ambient temperature in the beginning of the room-corner test.

The total incident heat flux to the steel plate can also be expressed as:

$$\dot{q}''_{i,\,tot} = \dot{q}''_{r,\,pl} + h_c\left(T_{pl} - T_s\right) + \sigma\left(T_R^4 - T_0^4\right) \tag{8.4}$$

where

$\dot{q}''_{r,\,pl}$ = radiant heat flux from the fire plume

$h_c(T_{pl} - T_s)$ = convective heat flux from the fire plume

    h_c is the convective heat transfer coefficient for the room (W/m$^2\cdot$K)

    T_{pl} is the plume temperature (K)

    T_s is the steel plate temperature (K)

$\sigma\left(T_R^4 - T_0^4\right)$ = net radiant flux from the heated room with respect to the initial

       room temperature

    T_R is an effective room temperature (K)

    T_0 is the initial room temperature ($\approx$ 300 K)

Immediately after the burner is ignited (t $\approx$ 0), the steel surface is still relatively

cold (ambient temperature) and the total heat flux to the plate is simply equal to the

radiant and convective heat flux from the fire plume—the temperature of the room, T_R,

and the steel, T_s, are both equal to T_0. Therefore the incident heat flux from the fire

plume to the unheated surface, $\left(\dot{q}''_{i,\,pl}\right)_{cold}$, can be expressed as

$$\left(\dot{q}''_{i,\,pl}\right)_{cold} = \left(\dot{q}''_i\right)_{cold} = \dot{q}''_{r,\,pl} + h_c\left(T_{pl} - T_0\right) \tag{8.5}$$

After a while the steel temperature, T_s, and the room temperature, T_R, become

elevated and Equation 8.4 represents the total heat flux to a heated surface $\left(\dot{q}''_{i,\,tot}\right)_{hot}$.

Combining Equation 8.4 for a heated surface with Equation 8.5 results in the following

expression for the incident heat flux from the fire plume to a cold surface.

$$\left(\dot{q}''_{i,\,pl}\right)_{cold} = \left(\dot{q}''_i\right)_{hot} - \dot{q}''_R + h_c(T_s - T_0) \tag{8.6}$$

where $\dot{q}''_R$ is the heat flux from the heated room $\left[\sigma\left(T_R^4 - T_0^4\right)\right]$. Combining Equation 8.6

with the total heat flux to the heated steel, from Equation 8.3 results in the following

expression for the incident heat flux to a cold surface.

$$\left(\dot{q}''_{i,\,pl}\right)_{cold} = \rho c \delta \frac{dT}{dt} + \varepsilon\sigma\left(T_s^4 - T_0^4\right) + \dot{q}''_{k,\,ins} + \dot{q}''_k - \dot{q}''_R + h_c(T_s - T_0) \tag{8.7}$$

where $\dot{q}''_k$ represents the conduction losses through the steel (kW/m^2) and $h_c(T_s - T_0)$ is

the cold surface correction factor. When this factor is added to the total measured heat

flux, it represents the flux that would be measured by a cooled surface such as a water

cooled heat flux meter.

In order to calculate the cold surface correction factor, the convection heat

transfer coefficient, h_c, for the room must be determined. The h_c, value for the room

can be calculated by a natural convection analysis. Therefore the method for

determining h_c presented in Section 7.3.3 can be used for the entire room. However the

length scale, l, used in Equations 7.8 and 7.9 will be the height of the room (2.4 m) as

opposed to the height of the small steel plate. The heat transfer coefficient for the room

is approximately 8.6 W/m^2·K which is consistent with typical values for natural

convection. However this value is really only applicable to the surfaces outside of the

fire plume. Janssens calculates heat transfer coefficients within the flaming regions of

the 100 and 300 kW energy release to be to be 13.8 and 15.9 W/m^2·K, respectively.

These calculations are based on forced convection calculations of h_c using the velocity

of the diffusion burners which were calculated based on the centerline temperature rise

of the flames. For simplicity the convection heat transfer for the entire room was

utilized. This results in a reduction in the heat flux from the fire plume of approximately 3 kW/m^2 for the 100 kW burner and 6 kW/m^2 for the 300 kW burner.

Equation 8.7 represents the heat flux incident to a cold surface such as the surface of a cooled heat flux meter or a sample material at ambient temperature. The added heat flux from the heated room, $\dot{q}_R''$, will be explained in the subsequent section.

8.3.4 Heated Room Effect

As each test progressed the room gas temperatures increased (see Figure 8.6). Similarly, the temperature of the interior surfaces of the walls increased. These elevated temperatures provide an added amount of radiant heat flux to the steel plates and to the sample material in the actual room-corner test. Correcting the measured equilibrium heat flux by the appropriate room feedback effect provides a more accurate measure of the incident heat flux from the ignition burner fire plume.
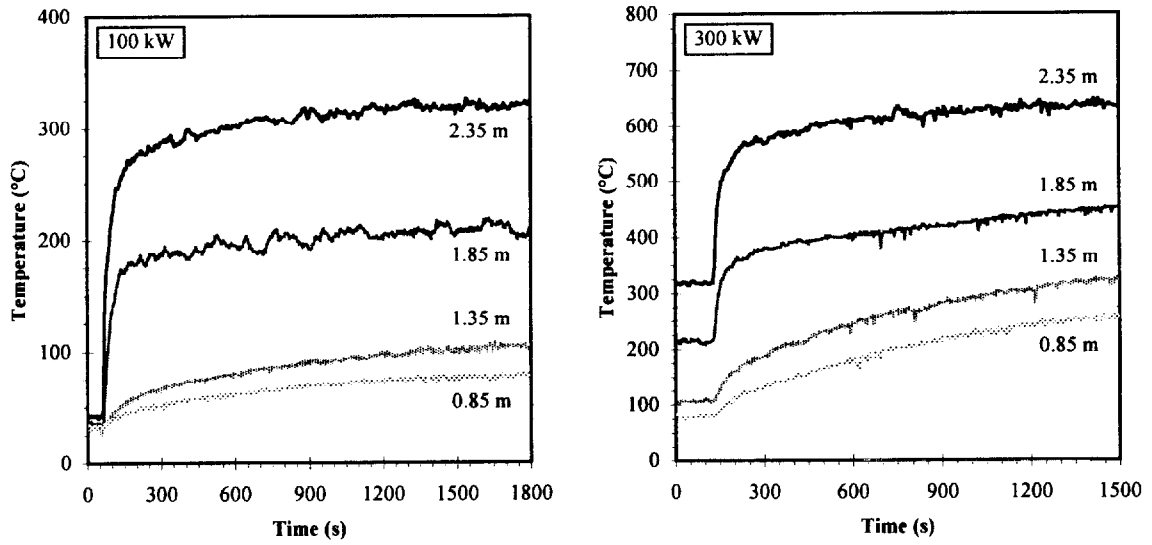
Figure 8. 6: Room Gas Temperatures for 100 and 300 kW Energy Release Rates.

The added incident heat flux from the room can be clearly seen in an example of a typical heat flux measurement as shown in Figure 8.7. The figure indicates the heat flux from the burner at 100 kW followed by an increase to 200 kW—the increase to 300 kW is not shown. Immediately following the ignition of the burner, the fire plume provides an initial incident flux to the steel plate, $\dot{q}''_{1,\ init.}$. As the room temperature increases, the heat flux increases and eventually reaches an equilibrium value, $\dot{q}''_{1,\ equil.}$.

For the initial burner output (not increased from an equilibrium state) the room effect is simply the difference between the equilibrium flux and the initial flux and can be expressed as $\sigma(T^4_{R1} - T^4_i)$. Therefore the incident heat flux from the fire plume at the first energy release rate can be expressed as

$$\left(\dot{q}''_{i,\ pl}\right)_1 = \dot{q}''_{1,\ equil.} - \sigma\left(T^4_{R1} - T^4_0\right)$$

156

After the burner output is increased, a new initial heat flux value is measured, $\dot{q}''_{2,\ init.}$.

As the room temperature increases further the heat flux also increases and eventually

reaches a new equilibrium value, $\dot{q}''_{2,\ equil.}$. The total heat flux from the heated room for

the second burner output is the new equilibrium flux minus the initial flux and the

original room effect. This results in the following incident flux from the ignition burner

fire plume:

$$\left(\dot{q}''_{i,\ pl}\right)_2 = \dot{q}''_{2,\ equil.} - \sigma\left(T_{R2}^4 - T_{R1}^4\right) - \sigma\left(T_{R1}^4 - T_0^4\right) \tag{8.8}$$

This indicates that the total added heat flux from the heated room, $\dot{q}''_R$, in Equation 8.7

is the sum of the room effects for each burner output step allowing it to be expressed as

$$\tag{8.9}$$

$$\left(\dot{q}''_{i,\ pl}\right)_{cold} = \rho c \delta \frac{dT}{dt} + \varepsilon\sigma\left(T_s^4 - T_0^4\right) + \dot{q}''_{k,\ ins} + \dot{q}''_k + h_c\left(T_s - T_i\right) - \sigma\left(T_{R1}^4 - T_0^4\right) - \sigma\left(T_{R2}^4 - T_{R1}^4\right) - \cdots$$

This flux represents the incident flux from the fire plume to a cold surface neglecting

the heat flux from the room.

Heat Flux (kW/m²)

$\dot{q}''_{2,\ equil.}$

$\sigma\left(T_{R2}^4 - T_{R1}^4\right)$

$\dot{q}''_{2,\ init.}$

Increase Burner Heat — Release Rate to 200 kW

$\dot{q}''_{1,\ equil}$

$\sigma\left(T_{R1}^4 - T_o^4\right)$

$\dot{q}''_{1,\ init.}$

Ignition of 100 kW Burner

Time (s)
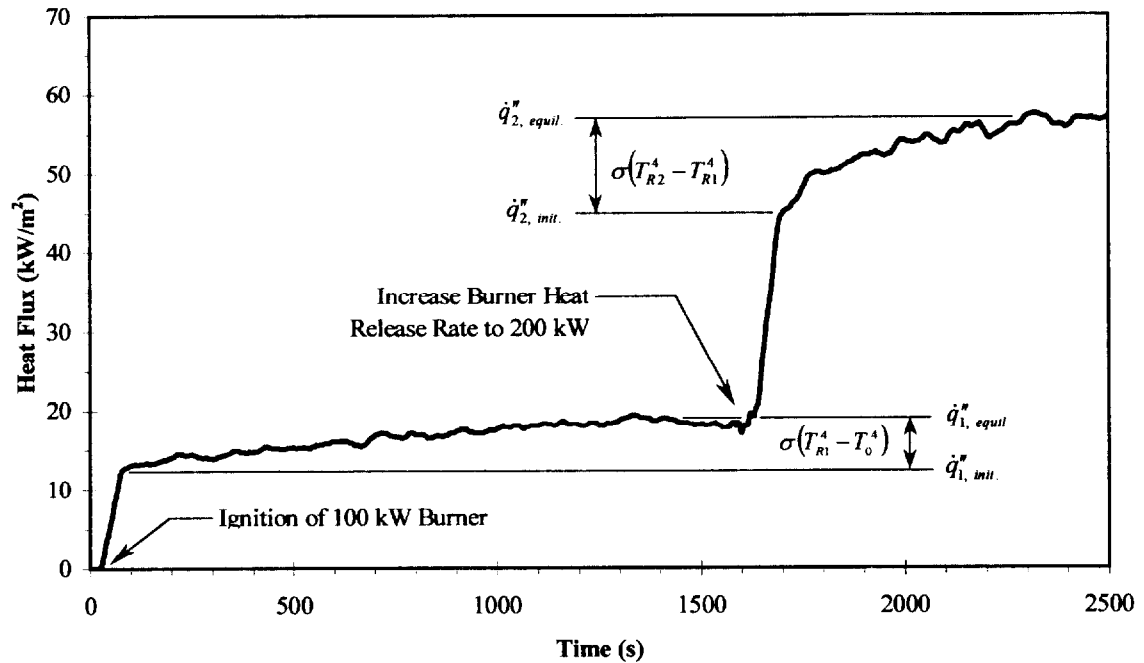
Figure 8. 7: Example of the Added Incident Heat Flux from the Heated Room – 100 kW and 200 kW Burner.

8.4 Full-Scale Test Results

Although testing was performed at burner output levels of 50 to 300 kW, only the 100 and 300 kW burner results specified by the ISO 9705 standard are analyzed here. Two tests for the measurement of the flux to the walls and one ceiling test were performed for each of the burner output levels.

Using Equations 8.2, 8.3, 8.7 and 8.9 the following incident heat fluxes to the walls and ceiling can be calculated:

- The measured heat flux from the fire plume and the heated room at equilibrium.

- The total heat flux to the steel plate including the 5% loss to the insulation.

- The total room feedback effect.

- The heat flux from the fire plume to a heated surface.

- The incident heat flux from the fire plume to a cold surface.

- The heat flux from the fire plume and the heated room to a cold surface.

The incident heat fluxes measured by the 3 Schmidt-Boelter type heat flux meters are compared with the calculated flux from the plume to a cold surface with and without the heated room effects. The flame height and general flame shape for the 100 kW and 300 kW fires are also determined using the photographs and video.

8.4.1 Heat Flux

Heat flux distributions from the 17 cm square burners at 100 and 300 kW are presented in Figures 8.8 through 8.11 where each figure shows the results of two wall tests and one ceiling test. The figures show distributions for the corrected heat flux to a cold surface, like a water cooled heat flux meter, and indicate two different incident heat fluxes: (1) the initial flux from just the fire plume and (2) the combined equilibrium flux from the fire plume and the heated room. These fluxes represent the measurements that are typically recorded in experiments and allow for comparison with the data of other researchers.

Note that the vertical height in the figures is from the floor and that the top surface of the burner is located 30 cm from the floor. The solid lines between colored areas indicate lines of constant heat flux in 10 kW/m^2 increments (*i.e.* 10, 20, 30, *etc.*)

The areas denoted by white indicate a negative heat flux or an area where no temperature measurement was made. For the wall experiments the lower left corner (where the ceramic fiber board was located) and the row of thermocouples 7.5 cm above the room floor are areas where no measurements were made. The lower thermocouples were not used due to the height of the burner. Note that the scales for the heat flux distributions begin and end 7.5 cm from the edges of the plate due to the locations of the thermocouples. Due to the fluctuations in the measured heat fluxes, as seen in Figure 8.7, average values were taken over time periods determined to be representative of the initial and equilibrium heat flux values. The fluctuations in the calculated values are due to the turbulence of the flame and the sensitivity of the data acquisition system.

The heat flux distributions for the walls show a great deal of consistency for both the 100 and 300 kW burners. The 100 kW distributions are nearly identical and the 300 kW are very similar with slightly more discrepancy.

The individual heat flux distributions are also presented in Appendix A with the lines of constant heat flux clearly identified.

Figure 8. 8: Incident Heat Flux Distribution to the Walls and Ceiling from a 17 cm Square Corner Ignition Burner at 100 kW: Fire Plume Plus Cold Surface Correction Factor.

Figure 8. 9: Incident Heat Flux Distribution to the Walls and Ceiling from a 17 cm Square Corner Ignition Burner at 100 kW: Fire Plume Plus Heated Room Feedback and Cold Surface Correction Factor.
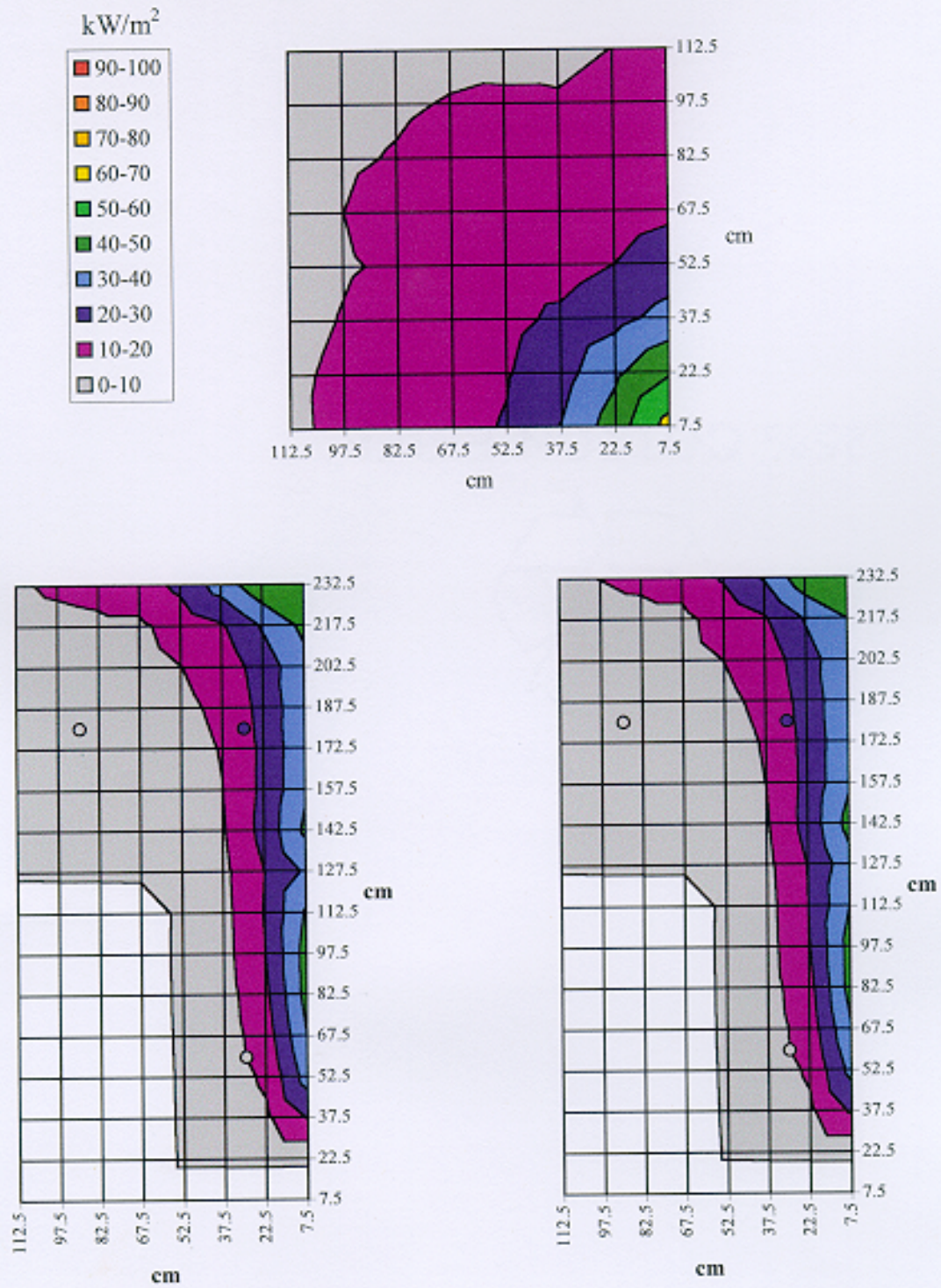
Figure 8. 10: Incident Heat Flux Distribution to the Walls and Ceiling from a 17 cm Square Corner Ignition Burner at 300 kW: Fire Plume Plus Cold Surface Correction Factor.
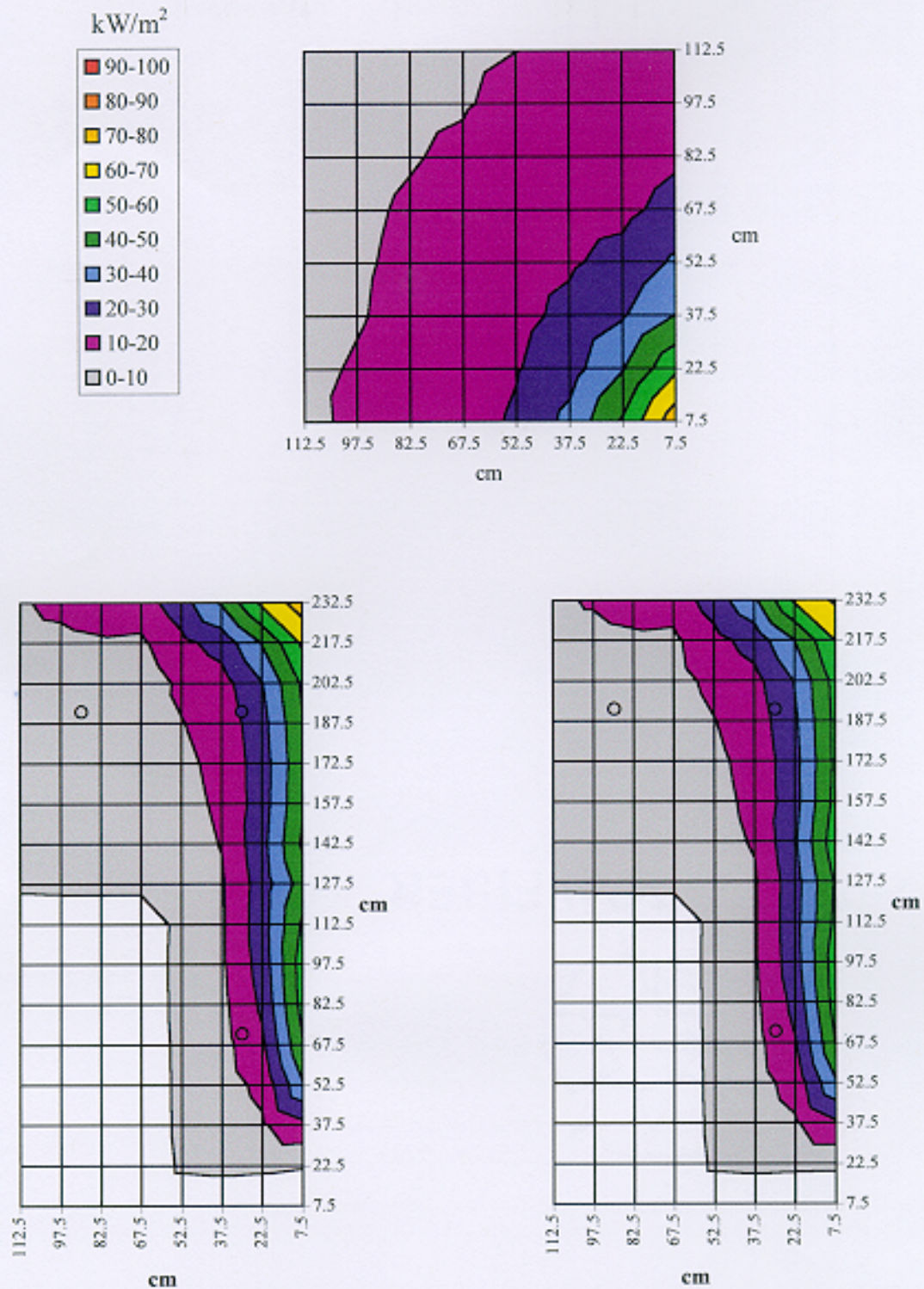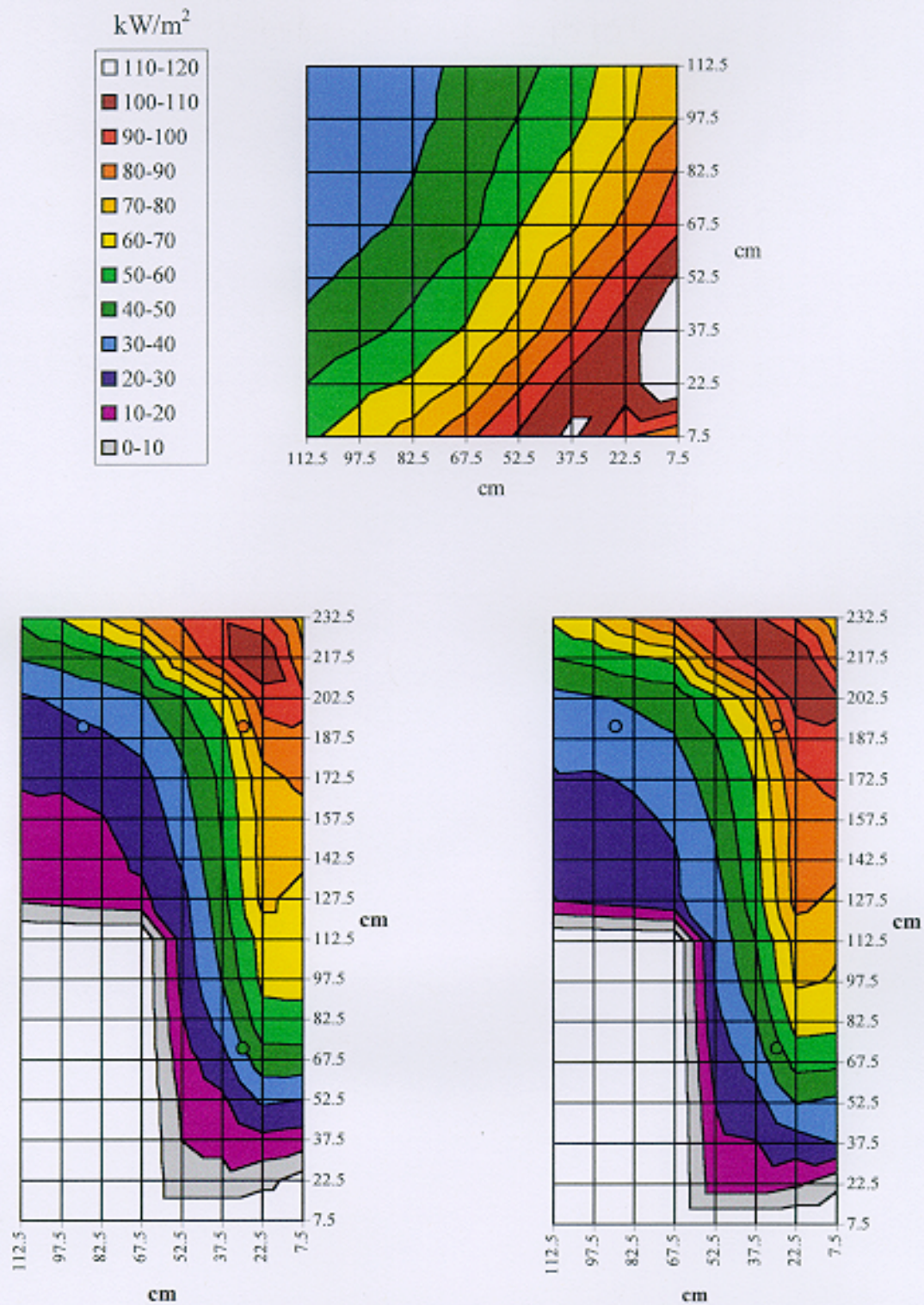
Figure 8. 11: Incident Heat Flux Distribution to the Walls and Ceiling from a 17 cm Square Corner Ignition Burner at 100 kW: Fire Plume Plus Heated Room Feedback and Cold Surface Correction Factor.
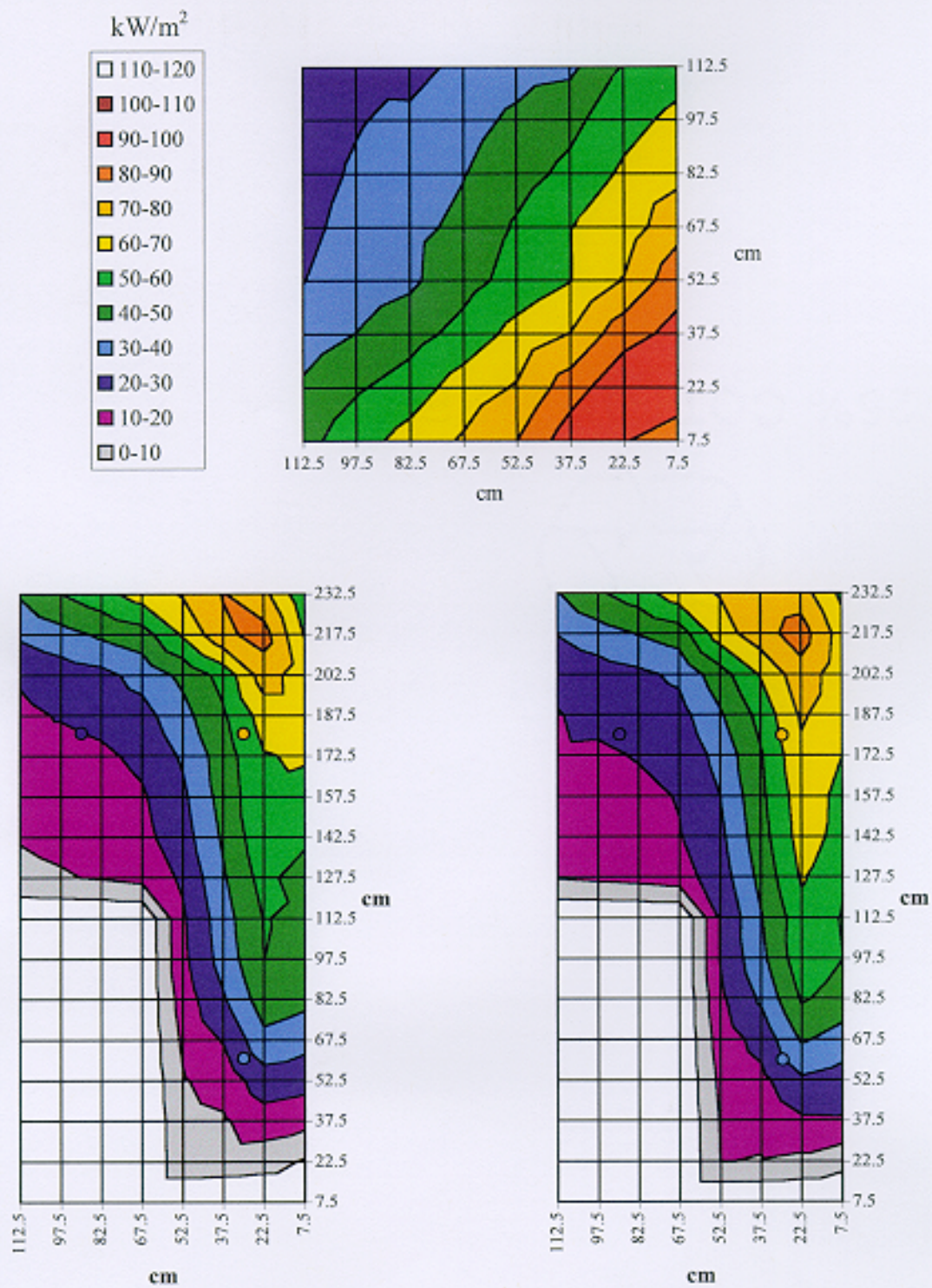
The average heat flux meter measurements are also shown in Figures 8.8 through 8.11 and are indicated in the appropriate locations by a circle (O). The color of the circle indicates the average measured heat flux using the same flux range scale as the rest of the distribution. The time dependent fluxes measured by the three heat flux meters are presented in Figure 8.12. The figure indicates that especially for the 200 and 300 kW energy release rates, room feedback effects are clearly increasing the incident heat flux to the walls. The average fire plume and equilibrium heat fluxes from the figure are presented in Table 8.3. The fire plume values represent the equilibrium values minus the total heat flux effects from room feedback. These heated room effects were determined in a similar manner as presented in Section 8.3.3.

Figure 8. 12: Heat Flux Meter Measurements for 100, 200 and 300 kW Ignition Burner Energy Release Rates.

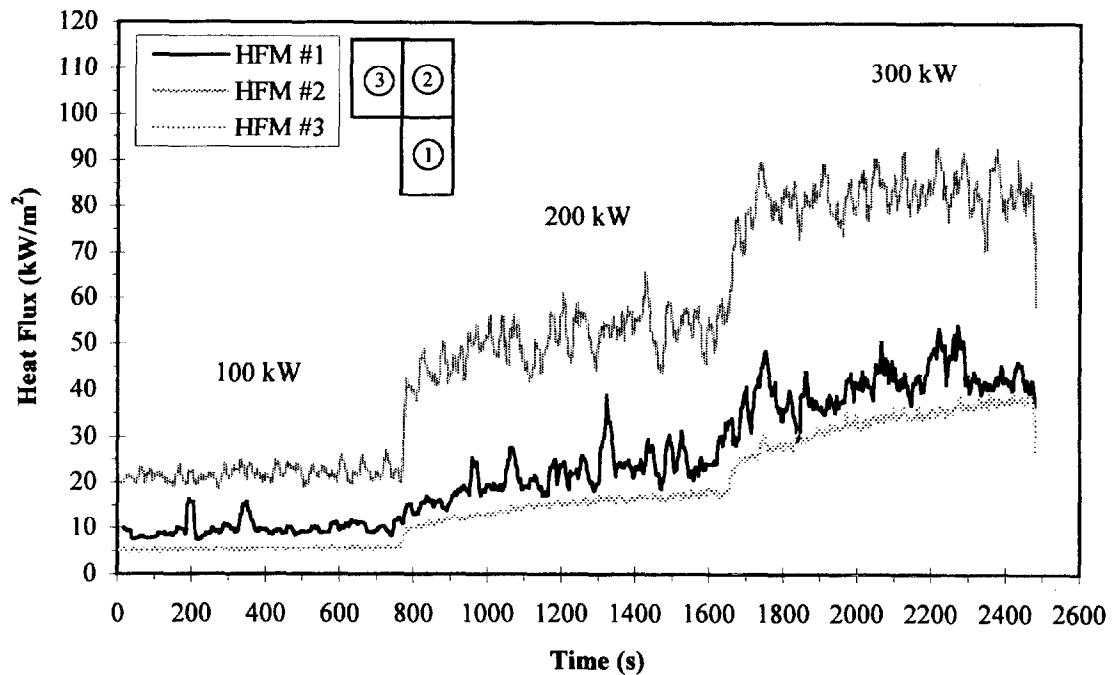**Table 8. 3**: Average Fire Plume and Equilibrium Heat Fluxes for 100 and 300 kW Burners Measured with Water Cooled Schmidt-Boelter Heat Flux Meters.

Burner Output		HFM #1	HFM #2	HFM #3
100 kW	Fire Plume	9.3	21.0	5.1
	Equilibrium	10.2	22.2	5.6
300 kW	Fire Plume	30.4	73.9	22.6
	Equilibrium	43.0	83.3	37.5

Comparison of the heat flux meter values and the steel plate measured values indicate excellent agreement, especially for the 100 kW burner. A direct heat flux comparison cannot be made since the heat flux meters are located in the middle of the four centrally located thermocouples. Therefore the average flux meter values have been displayed within the heat flux distributions and an average of the heat fluxes at the four surrounding locations was compared with the heat flux meter values. For the 100 kW burner the agreement is excellent as Figure 8.8 and 8.9 indicate. For the 300 kW burner the averages of the steel plate heat fluxes are slightly lower than the flux meter values, particularly for the upper right corner (HFM #2). This is most likely due to two effects of the cooled surface of the heat flux meter: (1) the difference in temperature between the meter and the surrounding wall and (2) water condensation. The cooled surface of the flux meters set into heated wall surface can produce inconsistencies in the boundary layer across the wall's surface which produces a slight increase in the measured heat flux. However, condensation of water from the combustion products of the fire plume on the flux meter surface provides a more significant increase in the measured heat flux. The energy produced by the conversion of gaseous water to liquid produces an increase in the heat flux to the meter which cannot be easily accounted for.

Since the flux meters were located outside of the 100 kW fire plume, there was most likely very little water condensed on the surface of the meters which explains the excellent agreement with the steel plate measurements. In the 300 kW tests the heat flux meters are located closer to and sometimes well within the fire plume where the water concentration and the associated condensation will be much higher. This results in the heat flux measured by the flux meters being higher and could account for some of the discrepancies. Nonetheless, the comparison of the steel plate measured values and the flux meter values do indicate that the methodology is valid and that the flux distributions presented are accurate. In fact since the steel plate is heated and cooling effects will not occur, the method presented hear may represent a superior method for determining the heat flux from a fire source.

Kokkala *et al.* [27] provide heat flux distributions for 100 and 300 kW burners using a 0.17 m square propane gas burner located 14.5 cm above the floor as shown in Figure 8.13. These distributions are for a burner in a 4.5 m high open corner without a ceiling, so direct comparison cannot be made with the flux distributions developed in the standard room. However below approximately 1.2 m (100 kW burner) and 1.0 m (300 kW burner) above the burner surface the results are relatively consistent. Above these heights the effects of the ceiling can clearly be seen and comparisons are no longer possible.

For the 100 kW burner, the plume width and the heat flux ranges shown in Figure 8.8 are almost identical below about 1.2 m from the burner surface. Since Kokkala's data was obtained from an open corner in a large test bay, room feedback effects would not have occurred and his data must be compared to the incident flux

from the fire plume alone (Figure 8.8). It should be noted again that the burner used by

Kokkala *et al.* was approximately 15 cm closer to the floor than the burner used in this

series of experiments. It appears that closer to the corner Kokkala measures slightly

higher values than shown in Figures 8.8. However for the steel plate the closest

measurement to the corner is 7.5 cm and the heat flux directly in the corner is unknown.

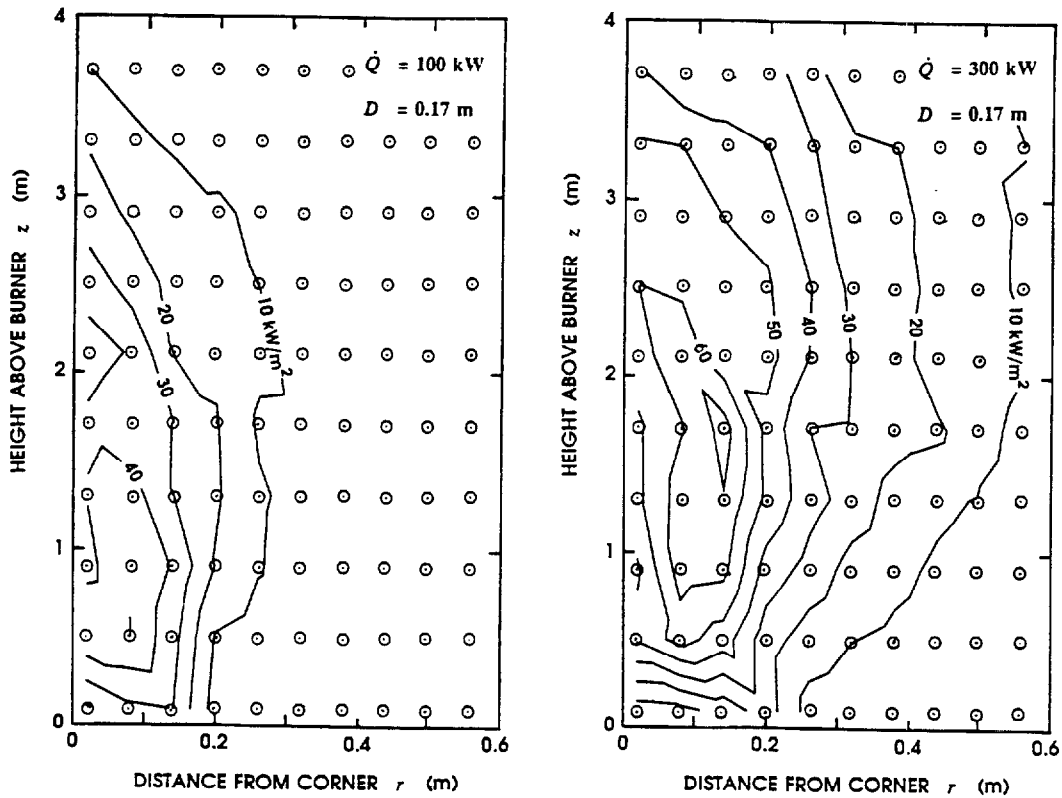**Figure 8. 13 (a & b)**: Heat Flux Distributions to the Wall from a 17 cm x 17 cm Propane Gas Burner Located in the Corner with Energy Release Rates of 100 and 300 kW [27].

There appears to be more discrepancy between the 300 kW distributions

(Figures 8.10) than the ones for 100 kW. Below about 1.0 m above the burner the

plume width and heat flux ranges are relatively consistent. However Kokkala's data

indicates slightly higher heat fluxes near the corner intersection. The lower fluxes with the steel plates are possibly due to the experimental room arrangement, but the differences are not incredibly large. The open corner experiments allow slightly more air to be entrained into the fire plume which could produce a hotter fire and therefore more heat flux. In addition the differences could be directly related to the ceiling effects. At lower elevations the open corner heat fluxes are slightly higher, but at higher elevations (near the ceiling height) the room fluxes are significantly higher. However, the differences that do exist are most likely due to the fact that the data collected by Kokkala was through the use of cooled heat flux meters and condensation from the combustion products most likely occurred.

Janssens [23] calculated the average incident heat flux from the fire plume of a 0.17 m square ignition burner at both 100 and 300 kW energy release rates. His calculated heat flux for the 100 kW output, 44.4 kW/m^2, is consistent with the measured flux directly in the corner and at the wall ceiling intersection (see Figure 8.8). For a heat release rate of 300 kW, Janssens calculates a fire plume heat flux of 47.1 kW/m^2. Figure 8.10 indicates a heat flux of 47 kW/m^2 at approximately 60 to 80 cm above the center of the burner. Above this region the heat flux increases rapidly and reaches over 80 kW/m^2 near the ceiling.

Janssens was attempting to provide an average heat flux from the entire ignition burner fire plume. Based on the measured values, his average 100 kW heat flux seems too high while his average 300 kW flux seems a little low. A more detailed analysis needs to be conducted but a preliminary examination of Figures 8.8 and 8.10 indicates

that an average heat flux of 35 kW/m^2 and 50 kW/m^2 may be more appropriate for the 100 kW and 300 kW burner release rates, respectively.

At this time no correlations have been developed for this corner burner heat flux data. Unfortunately this type of analysis was beyond the time frame of this report. However, the data for the 50 to 300 kW energy release rates will be examined in more detail in a subsequent report and appropriate correlations will be proposed.

8.4.2 Flame Length

The average flame lengths are determined based on visual observation, photographs and video. The 100 kW heat release rate exhibited a flame height that was approximately consistent with the ceiling with very little horizontal flame extension. On the other hand the 300 kW fire displayed significant flame extension along the ceiling. In fact visual observations and analysis of the ceiling heat flux distribution (Figure 8.10) indicates that the flames did not extend from the corner in a radial manner—there appeared to be increased local extension of the flames along the wall-ceiling interface.

The average flame length is determined by observing the peak and continuous flame regions from the video. According to Zukoski [50], the intermittency (I) of a fire plume is defined as "the fraction of time during which at least part of the flame lies above a horizontal plane located at elevation Z above the burner". Zukoski also defines the average flame height, Z_f, as the height at which $I = 0.5$. His analysis of the average flame heights for various heat release rates indicates that the average flame height is located in the center of the intermittent region—between $I = 1.0$ (continuous flame

region) and $I = 0$ (no flame). Therefore, the average flame length can be determined by taking an average of the maximum and minimum observed flame lengths.

The minimum and maximum flame volume heights were determined by recording the length for successive frames on the video. Since the flames are beneath a ceiling the flame tips can fluctuate between below the ceiling and along the ceiling interface, especially for the 100 kW burner (see Figure 8.14-a). For the 300 kW burner both the minimum and maximum flame lengths are along the wall-ceiling interface (see Figure 8.14-b). Since the ceiling is 2.1 m above the burner, the total recorded flame length (Z_f) is the vertical flame height (Z_v) plus any horizontal flame extension. The horizontal flame length (Z_h) is measured from the corner-ceiling intersection and no correction is made for the distance between the center of the burner and the wall. The observed minimum, maximum and average flame lengths for the 100 and 300 kW burners are presented in Table 8.4. It should be noted that the maximum flame length for the 300 kW burner may be slightly lower than the actual value due to the wall of the room causing some obstruction to the view of the video camera.
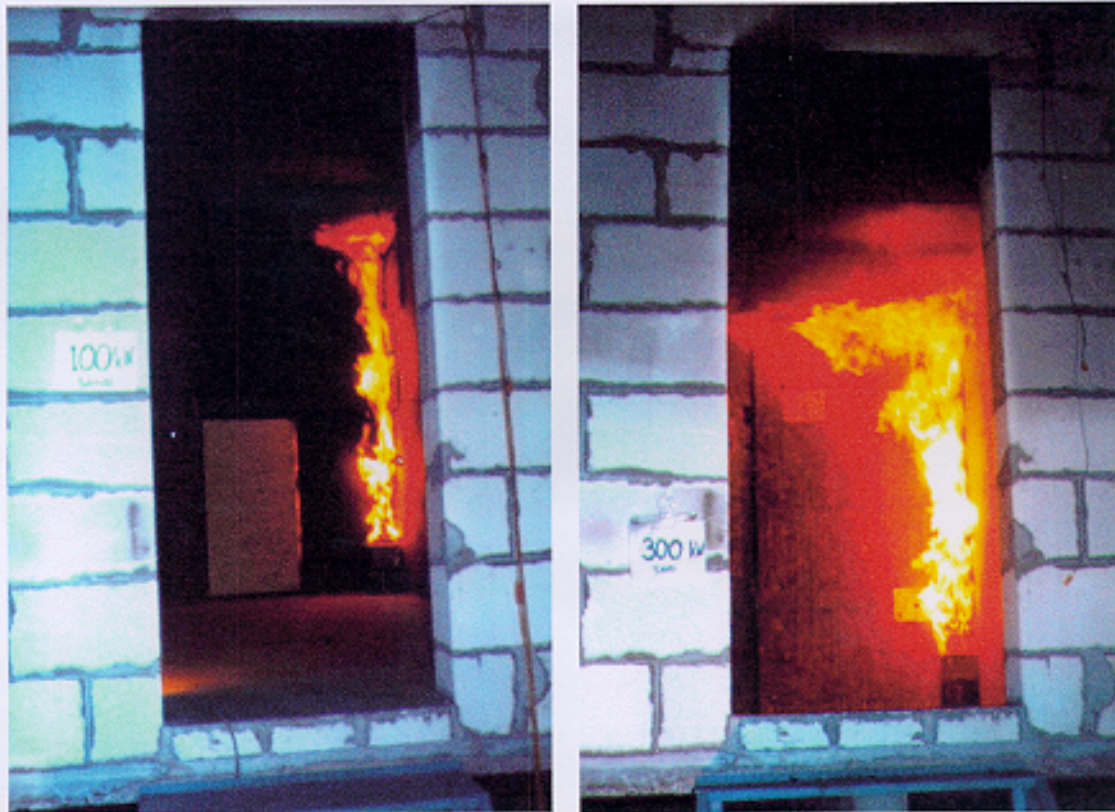
Figure 8. 14 (a & b): 100 kW and 300 kW Ignition Burner Flames.

Table 8. 4: Minimum, Maximum and Average Flame Lengths for the 0.17 m Burner in the Corner of the ISO 9705 Standard Room: 100 and 300 kW.

Heat Release Rate kW	$Z_{f, min}$ m	$Z_{f, max}$ m	$Z_{f, avg}$ m	Z_h m
100	1.5	2.6	2.1	0
300	2.6	4.4 *	3.5	1.4

* May be slightly lower than actual due to obstruction by the door.

The observed flame lengths and the flame lengths calculated by the correlations in Section 6.1 are presented in Table 8.5 where Z_f represents the total length of the flame:

$$Z_f = Z_v + Z_h$$

It is evident that there is a great deal of discrepancy between the different correlations.

Since the observed height of the 100 kW burner flame is just at the wall ceiling

interface it is difficult to determine if it is classified as an open corner flame or a ceiling

jet flame. It can be deduced that the ceiling will have a significant effect on the plume

flow (as can be seen in the heat flux distribution) and the flame will be more consistent

with a ceiling jet flame. Nonetheless, the Heskestad/Kokkala and Alpert correlations

and the calculation by Janssens all provide reasonable calculations of the 100 kW flame

height. For the 300 kW flame, the flame is clearly a ceiling jet flame and the Heskestad

and Delichatsios correlation provides a good approximation of the flame height.

However the Heskestad/Kokkala correlation provides the best approximation even

though it was developed for the open corner.

Table 8. 5: Calculated and Experimentally Observed Flame Heights for 100 and 300 kW Heat Release Rates Using a 0.17 m Square Burner in the Standard ISO Test Room.

Correlation		Flame Length, Z_f (m)	
		100 kW	300 kW
Open Corner	Hasemi & Tokunaga	2.41	5.01
	Kokkala	2.98	4.21
	Heskestad/Kokkala	2.19	3.59
	Janssens	1.96	4.00
Ceiling Jet	Alpert	2.20	3.17
	Heskestad & Delichatsios	2.37	3.69
Experimental		2.1	3.5

8.4.3 Plume Approximations

A comparison of the average flame heights in Table 8.4, the flame shapes from Figure 8.14 and the heat flux distributions in Figures 8.8 and 8.10, indicates that the flame volume from the ignition burner can be generally characterized by the area where the heat flux distribution is above 30 kW/m^2 (see Figure 8.15). For both heat release rates the main flame volume appears to be above the top of the burner surface by about 20 to 30 cm. This is relatively consistent with Figure 8.14 and is most likely due to the fact that the air and propane do not mix and react immediately after the gas leaves the burner. This analysis only represents a preliminary observation and needs to be confirmed by test results from various burner sizes and heat release rates.
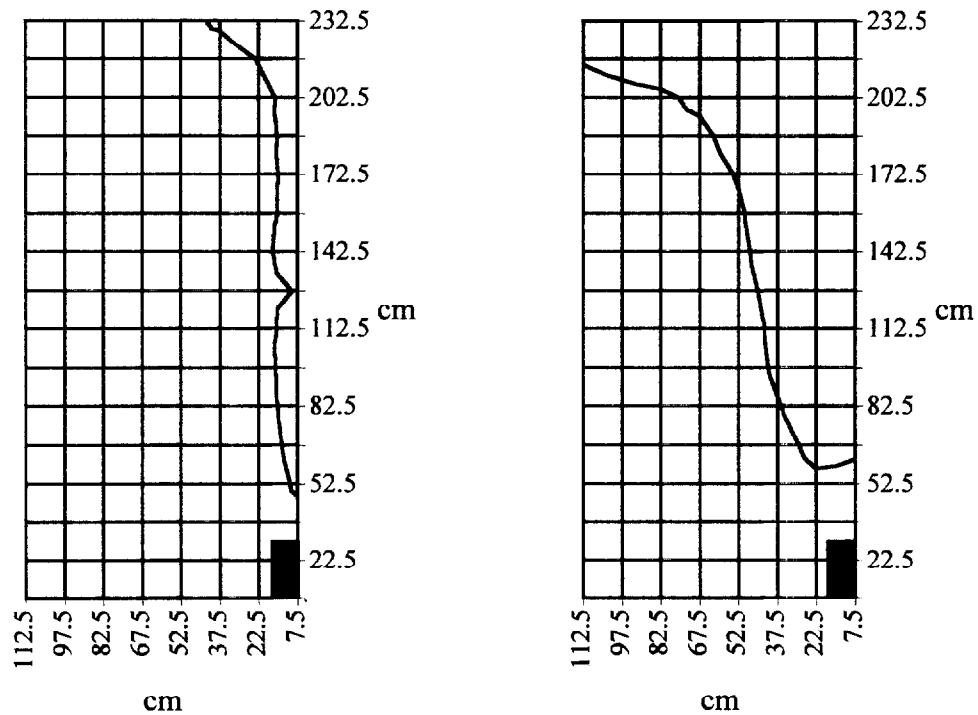
Figure 8. 15 (a & b): Flame Shape Generalizations for the 100 and 300 kW Burners Based on a Heat Flux Distribution Greater Than 30 kW/m^2.

Using average incident heat fluxes of 35 and 50 kW/m^2 from Section 8.4.1 over this approximated flame shape may be a more appropriate method of modeling the plumes than the one currently used in Quintiere's model. As mentioned above, correlations for the incident heat flux as well as the flame length will be examined in a future steady.

9. CONCLUSIONS

A systematic method has been developed for determining material fire properties. The method does not appear to be perfect for all of the materials but does provide a more structured way of determining the properties. Previous material property determinations have been random and specific to the experiment. This methodology represents a preliminary step towards a universal means of developing the modeling properties of any material.

Quintiere's fire growth model provides reasonable predictive results of the ISO 9705 Room-Corner test. As previous analysis has indicated, wood materials are predicted very well. Thermoplastic materials are predicted well provided that the material test data are modified with a reduced energy release rate per unit area to account for the removal of the material from the wall-ceiling orientation by melting, dripping and other effects. Further testing and analysis will have to be performed to increase the power of the reduced burn time prediction. The properties of most of the thermoplastic LSF materials had to be adjusted beyond what was originally anticipated.

A methodology has been established that provides accurate representation of time-resolved material data from the Cone Calorimeter including heat of combustion, heat of gasification and total energy per unit area. A refined ignition model was developed to account more exactly for radiation effects and long time ignition behavior. This leads to a more appropriate way to extrapolate ignition data to determine the critical heat flux for ignition.

A correlation based on linearized upward flame spread continues to give good predictive results for the time to flashover for 36 materials. The individual non-

176

conformity of one material is easily explained. The empirical correlation is further expanded to address burnout effects and still provides excellent results. However, the anticipated asymptote of zero that is expected appears to be shifted slightly negative. The inclusion of more materials into the existing database should strengthen the correlation and help to provide more clear demarcations of asymptotes and borderline materials.

The model indicates that the heat flux from the ignition burner to the sample material is about 60 kW/m^2. However the work by Kokkala and Janssens and results of these full-scale experiments shows that for the 100 kW burner a heat flux value of 40 kW/m^2 may be more appropriate. For the 300 kW burner the heat flux increases vertically from 30 kW/m^2 to about 80 kW/m^2 in the corner close to the ceiling.

The heat flux from the flames impinging on the ceiling and spreading along the wall ceiling interface can clearly be seen. The figures in Section 8 indicate that the ceiling heat flux is substantially higher than for the walls and that the flux along the wall-ceiling interface is higher than in the central portions of the corner. The test results indicate that the peak heat flux from the burner flames does indeed occur at the ceiling. Peak ceiling values of 60 kW/m^2 and 95 kW/m^2 are measured for the 100 and 300 kW burners, respectively.

These heat flux results provide new knowledge into the actual thermal attack to a material tested in the ISO 9705 room/corner test. The 100 kW ignition burner heat flux used in Quintiere's flame spread model is clearly too high. These full-scale results provide the means for developing a more appropriate method for modelling the performance of real materials.

The full-scale results also indicate that the flame height used in the model for the 100 kW burner (1.3 m) is too low. The experimental results indicate that the flames from this burner have an average height of 2.1 m above the burner which exactly corresponds with the height of the ceiling.

These is also a preliminary indication that the flame shape for the ignition burners can be associated with a heat flux of 30 kW/m^2. However, further analysis will have to be conducted to either verify or contradict this theory.

Further analysis for the full range of ignition burner energy release rates must still be completed. It is anticipated that incident heat flux and with respect to height and overall flame length correlations will be developed from this data. These correlations can then be input into Quintiere's flame spread model to increase its overall accuracy.

APPENDIX – Heat Flux Distributions

The heat flux distribution for the 100 and 300 kW energy release rates are presented again in the following appendix for clarity. The distributions indicate lines of constant heat flux in 10 kW/m^2 increments (*i.e.* 10, 20, 30, *etc.*) from a 0.17 m square burner in the corner with the surface 30 cm from the floor. The figures shown represent

1. The incident heat flux from the fire plume corrected for the flux to a cold surface (*i.e.* a water cooled heat flux meter).

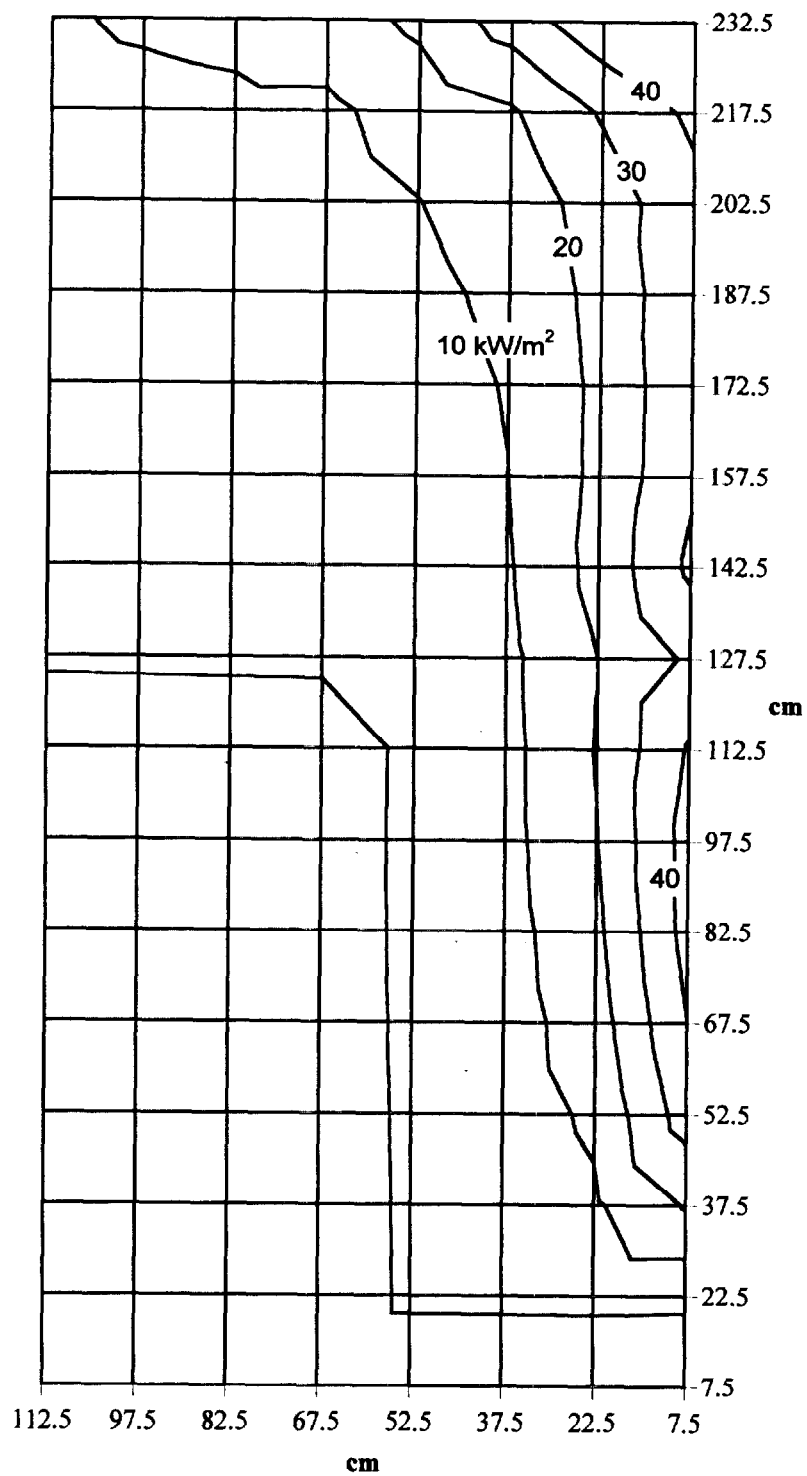2. The incident heat flux from the fire plume and the heated room corrected for a cold surface.

Figure A.1: Incident Fire Plume Heat Flux Distribution to a Cold Wall--
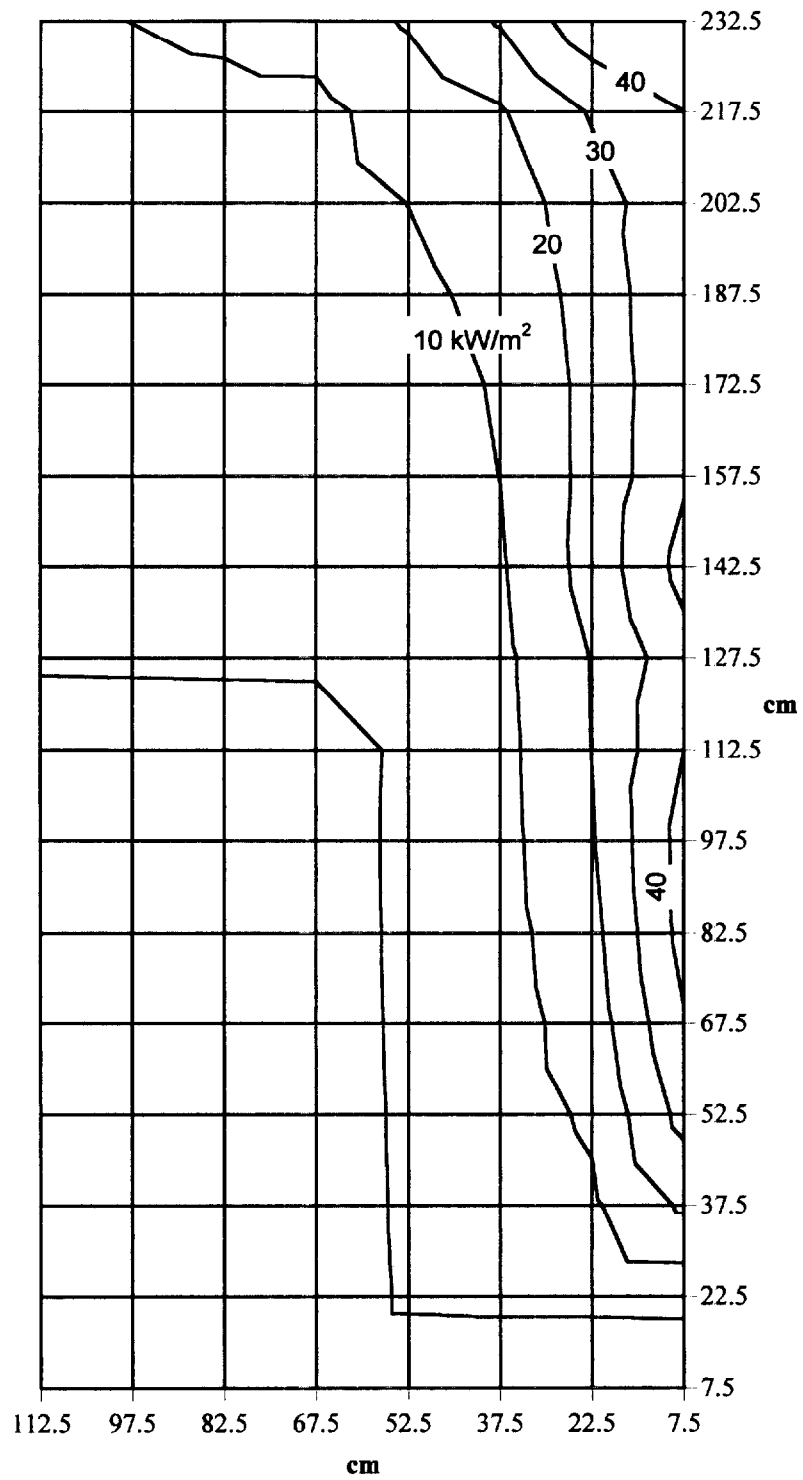0.17 m x 0.17 m Square Burner at 100 kW, Top Surface 30 cm From the Floor

Figure A.2: Incident Fire Plume Heat Flux Distribution to a Cold Wall--
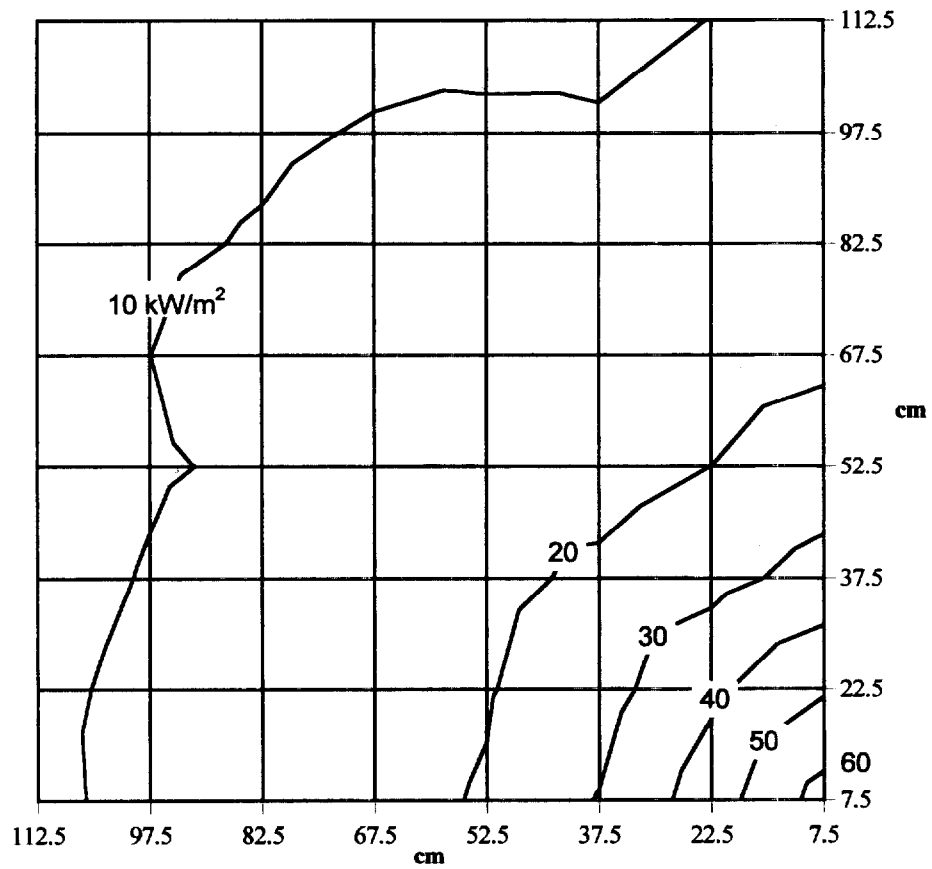0.17 m x 0.17 m Square Burner at 100 kW, Top Surface 30 cm From the Floor

181

Figure A.3: Incident Fire Plume Distribution to a Cold Ceiling--
0.17m x 0.17 m Square Burner at 100 kW, Top Surface 30.0 cm From the Floor
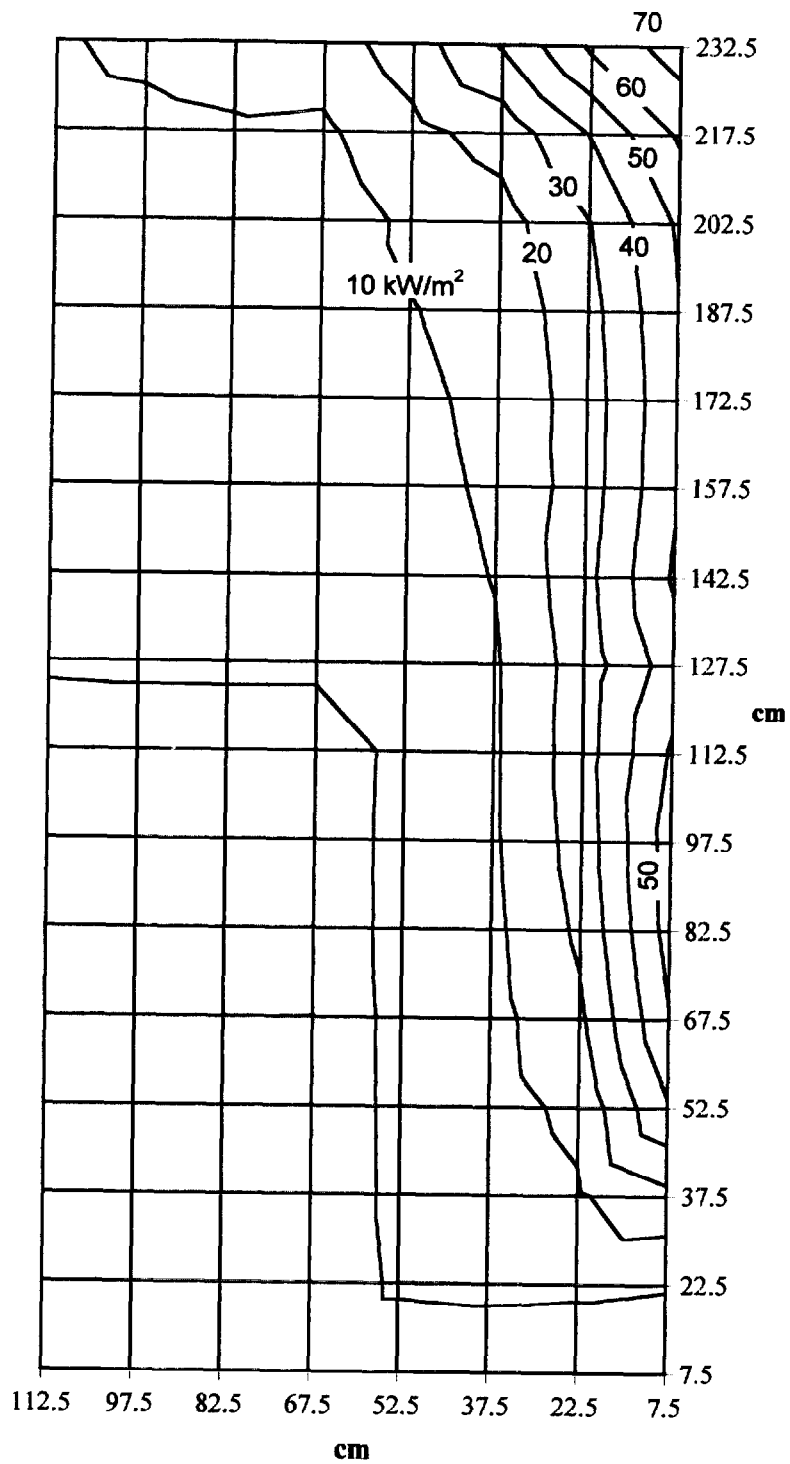
Figure A.4: Incident Fire Plume and Room Feedback Heat Flux Distribution
to a Cold Wall--0.17 m x 0.17 m Square Burner at 100 kW,
Top Surface 30 cm From the Floor

183

Figure A.5: Incident Fire Plume and Room Feedback Heat Flux Distribution
to a Cold Wall--0.17 m x 0.17 m Square Burner at 100 kW,
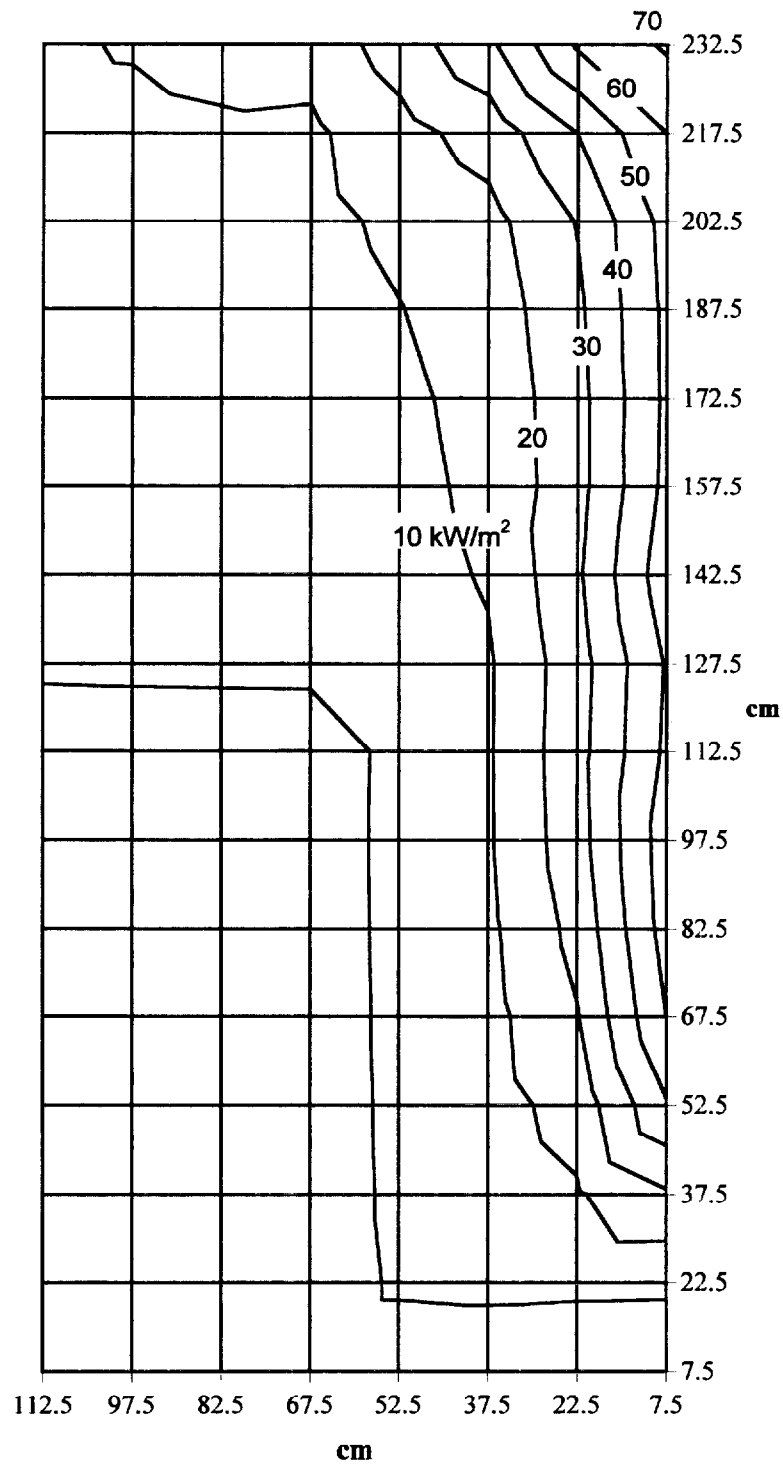Top Surface 30 cm From the Floor
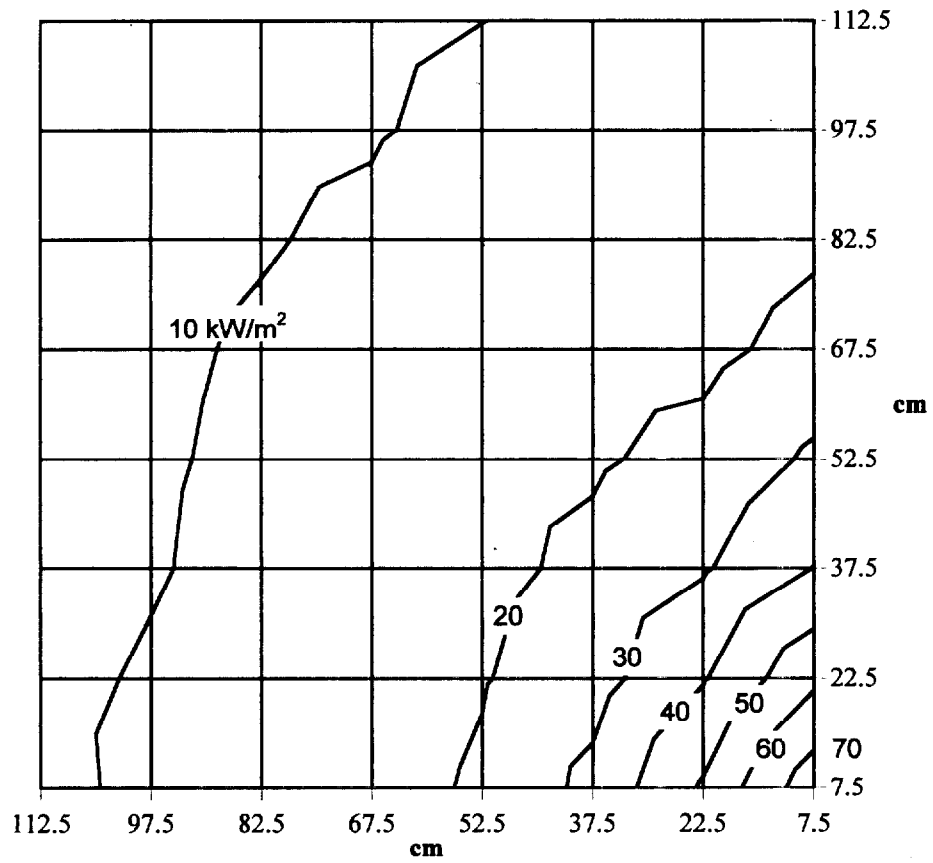
184

Figure A.6: Incident Fire Plume and Room Feedback Heat Flux Distribution
to a Cold Ceiling--0.17 m x 0.17 m Square Burner at 100 kW,
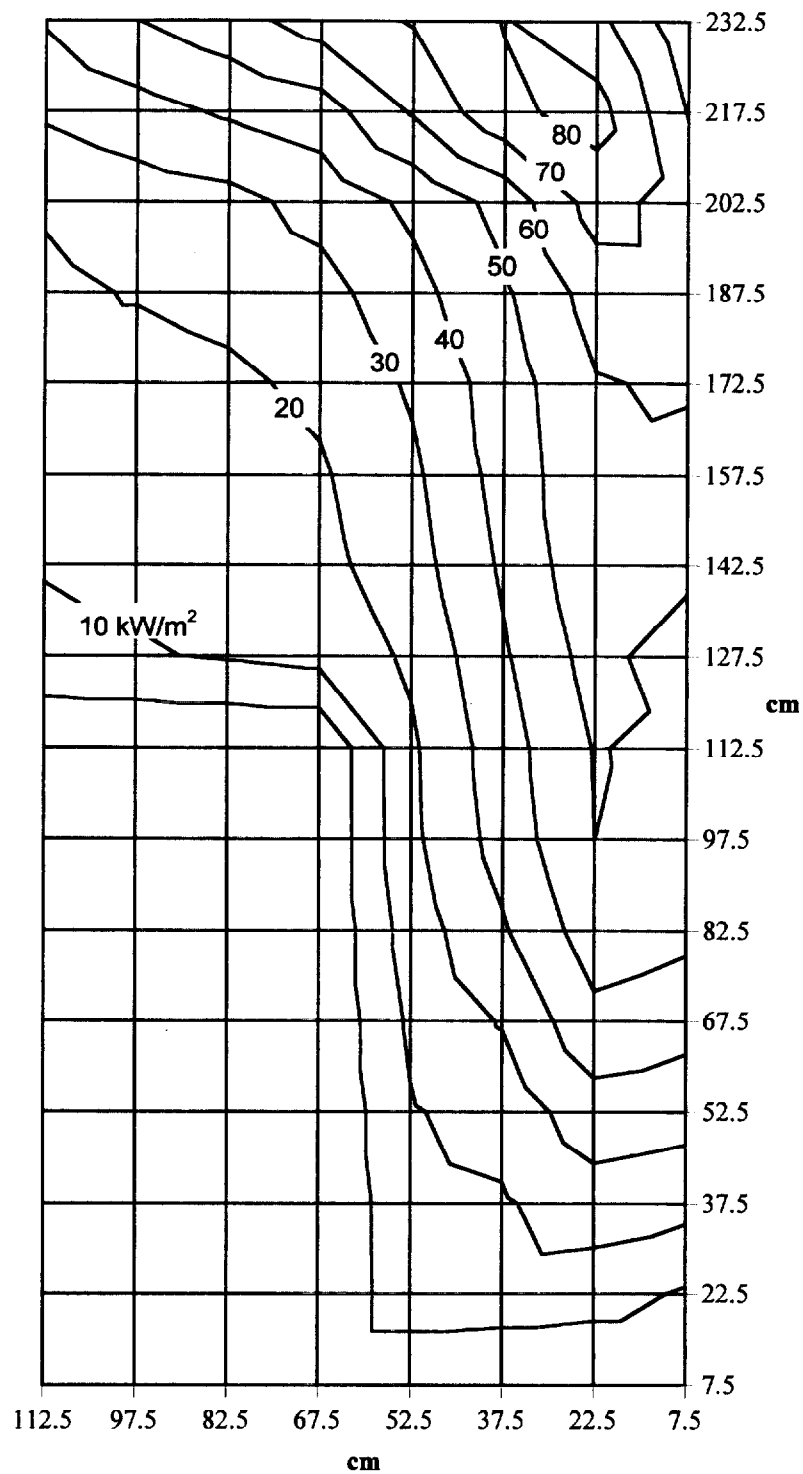Top Surface 30 cm From the Floor

185

Figure A.7: Incident Fire Plume Heat Flux Distribution to a Cold Wall-- 0.17 m x 0.17 m Square Burner at 300 kW, Top Surface 30 cm From the Floor
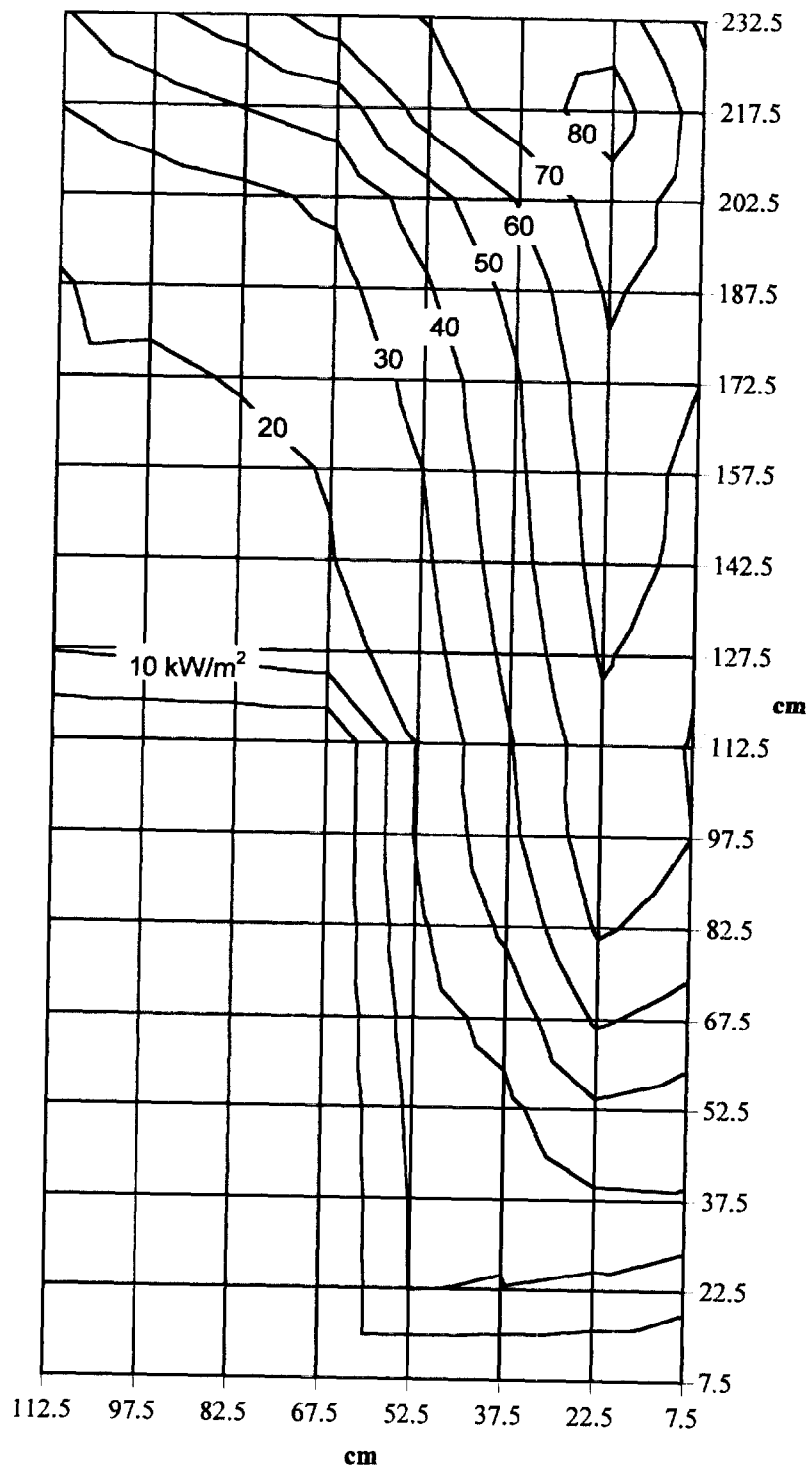
Figure A.8: Incident Fire Plume Heat Flux Distribution to a Cold Wall--
0.17 m x 0.17 m Square Burner at 300 kW, Top Surface 30 cm From the Floor

Figure A.9: Incident Fire Plume Distribution to a Cold Ceiling--
0.17m x 0.17 m Square Burner at 300 kW, Top Surface 30.0 cm From the Floor

Figure A.10: Incident Fire Plume and Room Feedback Heat Flux Distribution
to a Cold Wall--0.17 m x 0.17 m Square Burner at 300 kW,
Top Surface 30 cm From the Floor

189

Figure A.11: Incident Fire Plume and Room Feedback Heat Flux Distribution to a Cold Wall--0.17 m x 0.17 m Square Burner at 300 kW, Top Surface 30 cm From the Floor
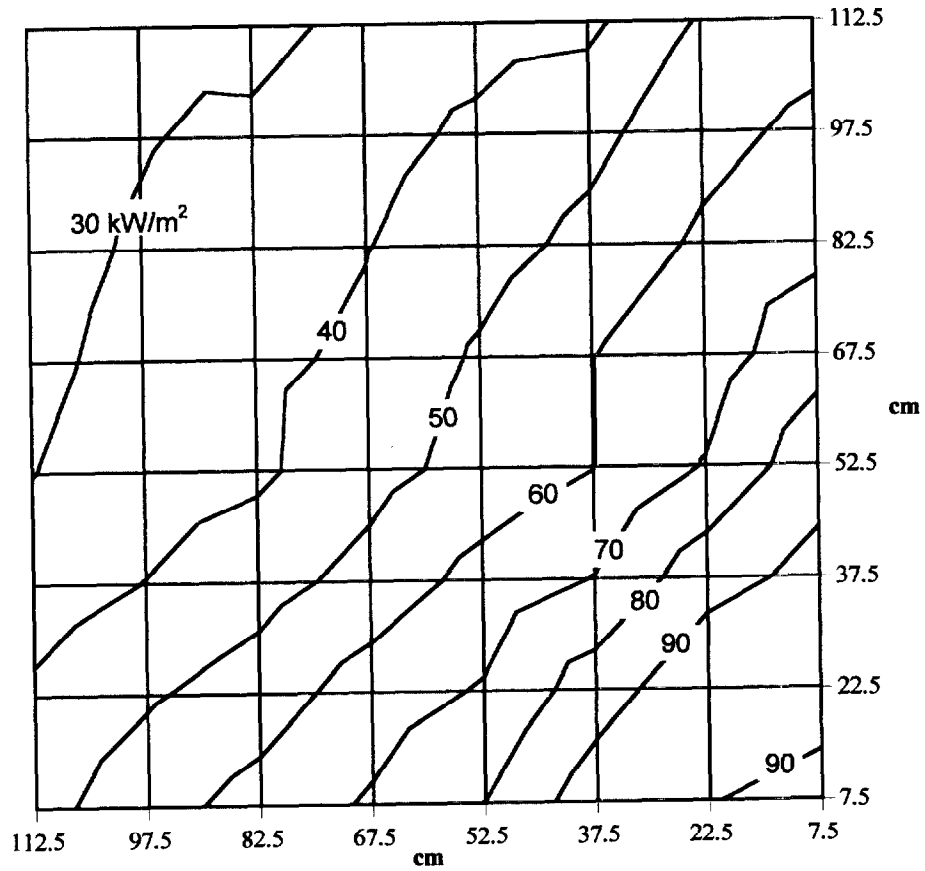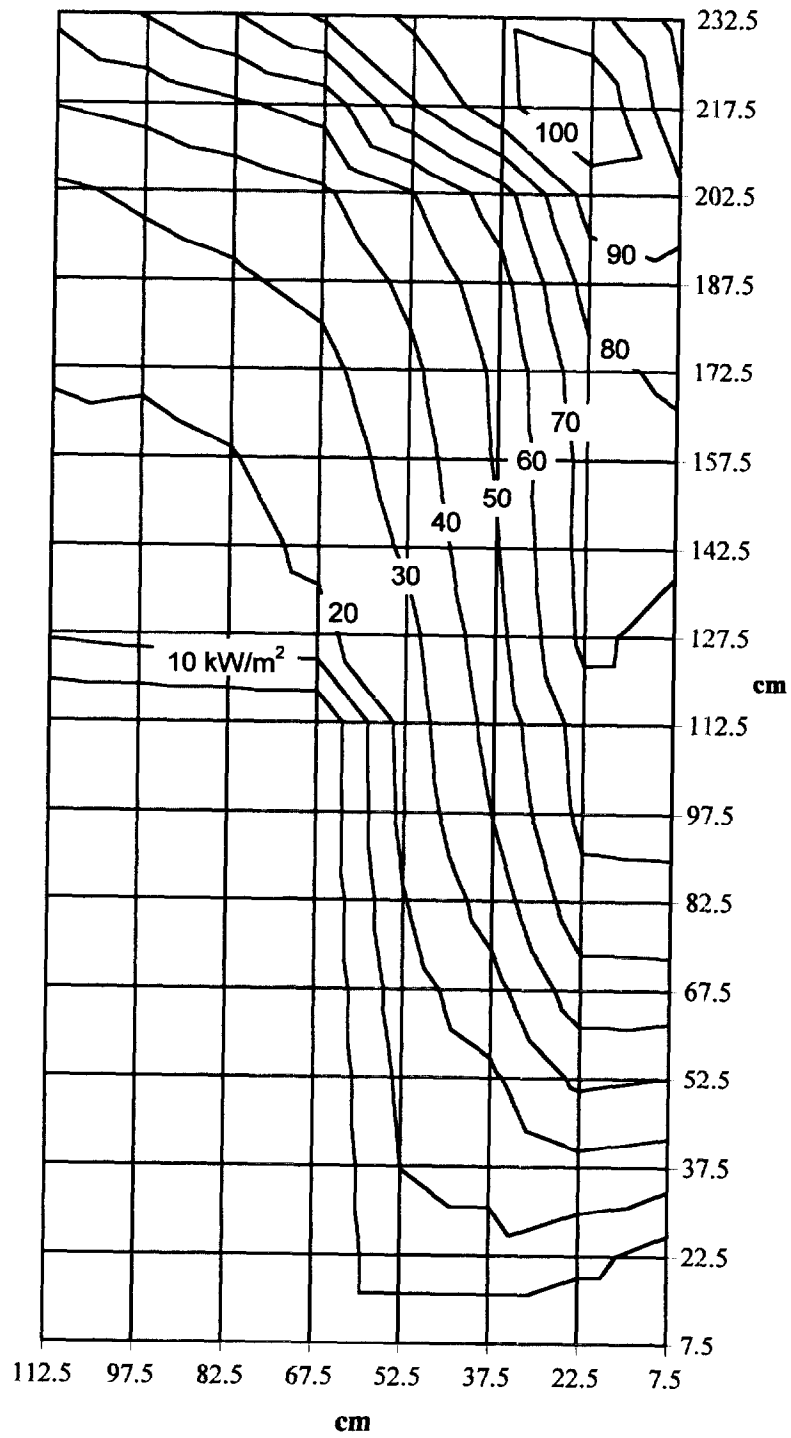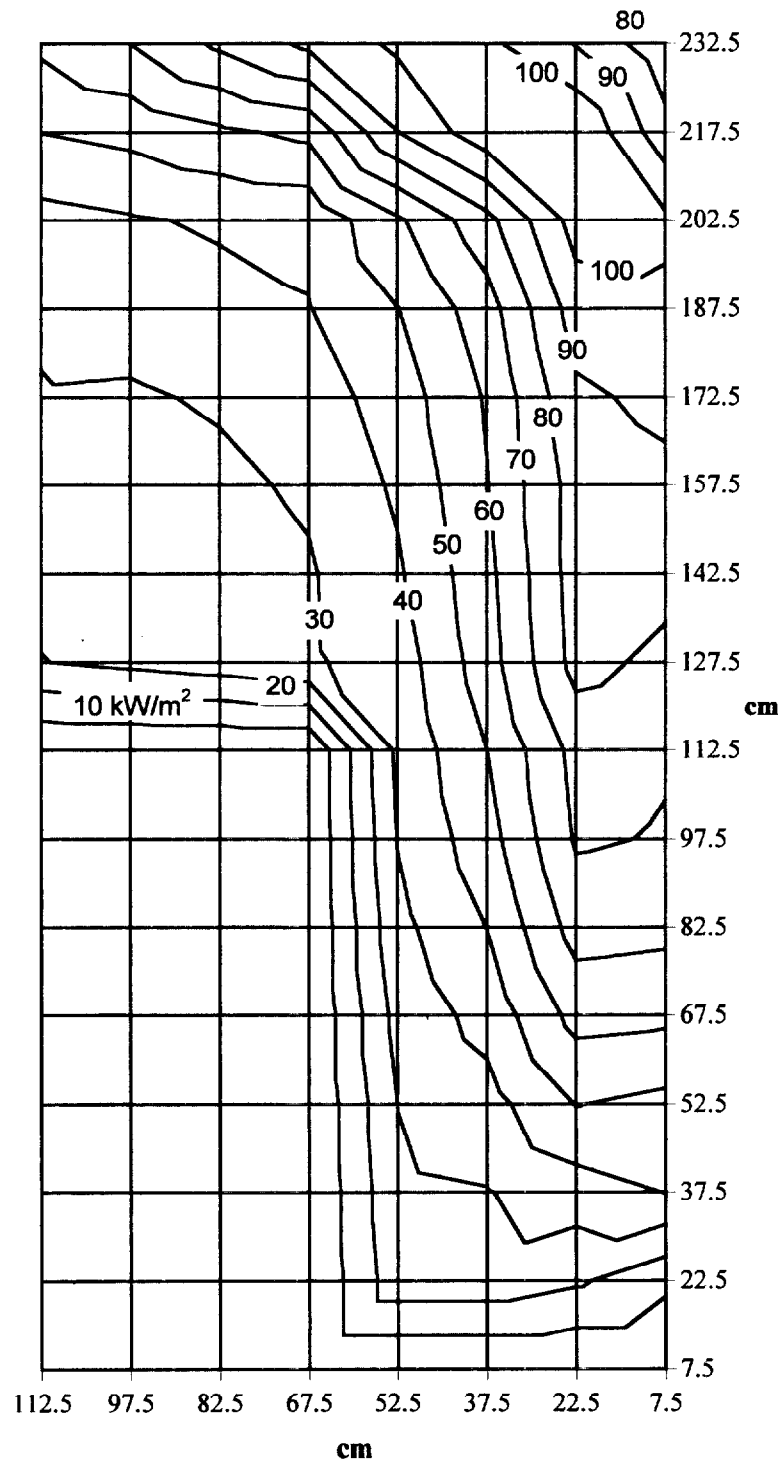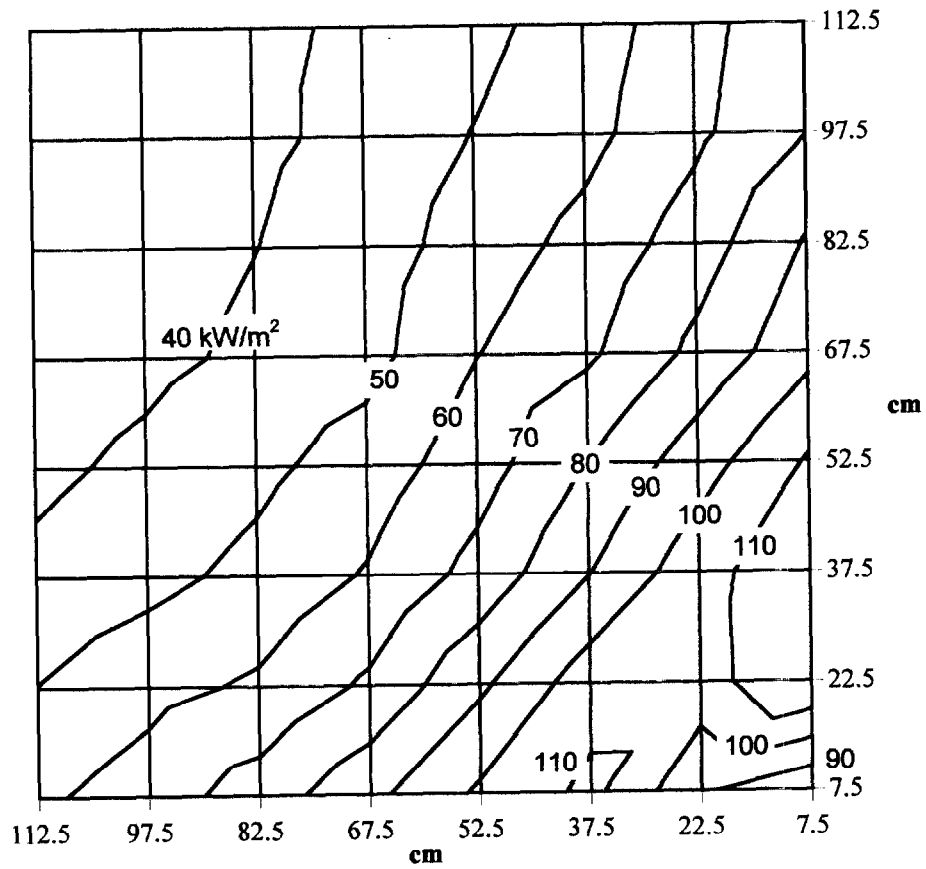
190

Figure A.12: Incident Fire Plume and Room Feedback Heat Flux Distribution
to a Cold Ceiling--0.17 m x 0.17 m Square Burner at 300 kW,
Top Surface 30 cm From th Floor

191

REFERENCES

1. ASTM E 1321-93, "Standard Test Method for Determining Material Ignition and Flame Spread Properties", *Annual Book of ASTM Standards*, American Society for Testing and Materials, Philadelphia, 1993, pp. 1055 to 1076.

2. ASTM E1354-90, "Standard Test Method for Heat and Visible Smoke Release Rates for Materials and Products Using and Oxygen Consumption Calorimeter", *Annual Book of ASTM Standards*, American Society for Testing and Materials, Philadelphia, 1990, pp. 803 to 817.

3. *ASM Metals Reference Handbook*, Third Edition, ASM International, ed. Bauccio, Michael, 1993.

4. Atreya, A., "Convection Heat Transfer", *SFPE Handbook of Fire Protection Engineering*, National Fire Protection Association, Quincy, MA, 1988, pp. 1-65 to 1-91.

5. Atreya, A., "Pyrolysis, Ignition and Fire Spread on Horizontal surfaces of Wood", Ph.D. Thesis, Harvard University, Cambridge, MA, 1983.

6. Babrauskas, Vytenis, "Flame Lengths Under Ceilings", *Fire and Materials*, Volume 4, Number 3, 1980, pp. 119 to 125.

7. Back, G., Beyler, C., DiNenno, P. and tatem, P., "Wall Incident Heat Flux Distributions Resulting From an Adjacent Fire", Fire Safety Science—Proceedings of the Fourth International Symposium, ed. T. Kashiwagi, IAFSS, 1994.

8. Beyler, C., "Fire Plumes and Ceiling Jets", *Fire Safety Journal*, Volume 11, 1986, pp. 53 to 75.

9. Cleary, T. G. & Quintiere, J. G., "A Framework fur Utilizing Fire Property Tests", *Fire Safety Science*, Proceedings of the 3rd Inter national Symposium, ed. G. Cox & B. Langford, Elsevier Applied Science, London, 1991, pp. 647 to 656.

10. Dillon, S. E., Kim, W. H. & Quintiere, J. G., "Determination of Properties and the Prediction of the Energy Release Rate of Materials in the ISO 9705 Room-Corner Test", Department of Fire Protection Engineering, University of Maryland, College Park, MD, June 1998.

11. Drysdale, Dougal, *An Introduction to Fire Dynamics*, John Wiley & Sons, Chichester, 1994.

12. Gross, D. "Measurements of Flame Lengths Under Ceilings", NISTIR 88-3835, 1988.

13. Hasemi, Y. "Experimental Wall Flame Heat Transfer Correlations for the Analysis of Upward Wall Flame Spread", *Fire Science and Technology*, Vol. 4, No. 2, 1994, pp. 75 to 90.

14. Hasemi, Y. & Tokunaga, T., "Modeling of Turbulent Diffusion Flames and Fire Plumes for the Analysis of Fire Growth", Fire Dynamics and Heat Transfer, American Society of Mechanical Engineers, 21st Annual Heat Transfer Conference, Seattle, WA, July 24 – 28, 1983.

15. Hasemi, Y. & Tokunaga T., "Some Experimental Aspects of Turbulent Diffusion Flames and Buoyant Plumes from Fire Sources Against a Wall and in a Corner of Walls", *Combustion Science and Technology*, Volume 40, 1984, pp. 1 to 17

16. Haynes, G. A., "Analysis of a Model to Predict Flame Spread Over a PMMA Wall in a compartment", M.S. Thesis, Department of Fire Protection Engineering, University of Maryland, College Park, Maryland, 1996.

17. Heskestad, G., *Fire Safety Journal*, 5, 1983, pp. 109-114.

18. Holman J. P., *Heat Transfer*, Seventh Edition, Mc-Graw Hill, Inc., 1990.

19. Hopkins, Jr. D. & Quintiere J. G., "Material Fire Properties for Thermoplastics", *Fire Safety Journal*, 26 (3), 1996, pp. 241-268.

20. Incropera, Frank P., & DeWitt, David P., *Fundamentals of Heat and Mass Transfer*, Third Edition, John Wiley & Sons, New York, 1990.

21. Ingason, Haukur & de Ris, John, "Flame Heat Transfer in Storage Geometries", in H. Ingason, Dept. of Fire Safety Engineering, Rep. LUTVDG/(TVBB-1013), Lund University, Sweden, 1996.

22. ISO 9705, International Standard, "Fire Tests—Full Scale Room Test for Surface Products", First Edition, Reference Number ISO/TC92/WG7/N124, 1993-05-15.

23. Janssens, M., "Predictions of ISO 9705 Room/Corner Test Using a Simple Model", Interscience Communications Limited, Fire and Materials, Proceedings of the 4th International Conference and Exhibition., 1995, pp. 73 to 83.

24. Janssens.

25. Kim, Woon Hyung & Quintiere, J. G., "Applications of a Model to Compare Flame Spread and Heat Release Properties of Interior Finish Materials in a Compartment", International Symposium on Fire Science and Technology, Seoul, November 12 – 14, 1997.

26. Kokkala, M. A., "Characteristics of a Flame in an Open Corner of Walls", *Interflam '93*, Inter Science Communications Limited, London, UK, 1993, pp. 13 to 24.

27. Kokkala, M. Göransson, U. & Söderbom, J., "EUREFIC – Large Scale Fire Experiments in a Room with Combustible Linings", SP Report 1990:41, Swedish National Testing and Research Institute, Boras, 1990.

28. Kokkala, Matti, Göransson, Ulf & Söderbom, Johan, "Five Large-Scale Room Fire Experiments: Project 3 of the EUREFIC Fire Research Programme", Technical Research Centre of Finland, Espoo, 1992.

29. Kutateladze, S. S. & Borishanskii, V. M., *Consise Encyclopedia of Heat Transfer*, Pergamon Press Ltd., Oxford, 1966.

30. Long, Dick T., Jr., "An Evaluation of the Lateral Ignition and Flame Spread Test for Material Flammability Assessment for Micro-Gravity Environments", M.S Thesis, University of Maryland, Department of Fire Protection Engineering, College Park, MD, 1998.

31. Mowrer, F. W. & Williamson, R. B., "Flame Spread Evaluation for Thin Interior Finish Materials", *Fire Safety Science*, Proceedings of the 3rd Inter national Symposium, ed. G. Cox & B. Langford, Elsevier Applied Science, London, 1991, pp. 689 to 698.

32. Ohlemiller, T., Cleary, T. & Shields, J., "Effect of Ignition Conditions on Upward Flame Spread on a Composite Material in a Corner Configuration", (private communications, to be publised).

33. Quintiere, J. G., "Estimating Fire Growth on Compartment Interior Finish Materials", Department of Fire Protection Engineering, University of Maryland, College Park, MD, 1995.

34. Quintiere, J. G, "Fire Tests and Hazard Evaluation", 7th International Research and Training Seminar on Regional Development Planning for Disaster Prevention— Improved Firesafety Systems in Developing Countries, October 17, 1994, Tokyo, Japan.

35. Quintiere, J. G., "Modeling Room Corner Tests", Heat Release and Fire Hazard, Proceedings of the First Japan Symposium, Volume 1, Tsukuba, Japan, May, 1993.

36. Quintiere, J. G., "A Simulation Model for Fire Growth on Materials Subject to a Room/corner Test", *Fire Safety Journal*, Volume 18, 1992.

37. Quintiere, J. G., Haynes, G. & Rhodes, B. T., "Applications of a Model to Predict Flame Spread Over Interior Finish Materials in a Compartment", *Journal of Fire Protection Engineering*, Volume 7, Number 1, 1995, pp. 1 to 13.

38. Quintiere, J. G., Hopkins, M. & Hopkins, D. Jr., "Fire Hazard Prediction for Textile Wall Materials", Final, ATMI, January, 1995.

39. Quintiere, J. G., Hopkins, M. & Hopkins, D. Jr., "Room-Corner Fire Prediction for Textile Wall Materials", International Conference on Fire Research and Engineering, BFRL and SFPE, Orlando Marriot International, FL, Sept. 10 –15, 1995.

40. Quintiere, J. G. & Iqbal, N., "An Approximate Integral Model for the Burning Rate of a Thermoplastic-like Material", *Fire and Materials*, Vol. 18, 1994, pp. 89 to 98.

41. Quintiere, J. G. and Lee, C. H., Ignitor and Thickness Effects on Upward Flame Spread", *Fire Technology*, Volume 34, Number 1, March 1998, pp. 39-59.

42. Quintiere, J. G. & Rhodes, B. T., "Fire Growth Models for Materials", *Fire Safety Journal*, 26 (3), 1996, pp. 221-240.

43. Rhodes, B. T., "Burning Rate and Flame Heat Flux for PMMA in the Cone Calorimeter", M. S. Thesis, Department of Fire Protection Engineering, University of Maryland, College Park, Maryland, May, 1994.

44. Rockett, J. A., "Conduction of Heat in Solids", *SFPE Handbook of Fire Protection Engineering*, National Fire Protection Association, Quincy, MA, 1988, pp. 1-49 to 1-64.

45. Siegel, R. & Howell, J. R., *Thermal Radiation Heat Transfer*, Second Edition, McGraw-Hill Book Company, New York, 1981.

46. Su, Chen-Hsiang, "Downward and Lateral Flame Spread in Roland Apparatus Phase 5", M. S. Degree Scholarly Paper, Department of Fire Protection Engineering, University of Maryland, college Park, Maryland.

47. Tewarson, Archibald, "Generation of Heat and Chemical Compounds in Fires", *SFPE Handbook of Fire Protection Engineering*, National Fire Protection Association, Quincy, MA, 1988, pp. 1-179 to 1-199.

48. Thomas, Philip & Karlsson, Björn, "On the Lengths of Flames Under Ceilings", Department of Fire Safety Engineering, Lund University, Sweden, 1990.

49. Thureson, Per, "Fire Tests of Linings According to Room/Corner Test, ISO 9705", Swedish National Testing and research Institute, Fire Technology, Report 95R22049, January, 1996.

50. Zukoski, E. E., "Properties of Fire Plumes", *Combustion Fundamentals of Fire*, Ed. Cox., G. Academic Press, London, 1995.

51. LS Fire Laboratories, "Roland Programme", ISO/TC92/SC2/WG3/N244, Paris, pril 25, 1994, pp. 1 – 27.

52. Quintiere, J. G. & Cleary, T. G., "Heat Flux from Flames to Vertical Surfaces", *Fire Technology*, Second Quarter, 1994, pp. 209 to 231.

53. Hasemi, Y, Yoshida, M, Takashima, S., Kikuchi, R. & Yokobayashi, Y., "Flame Length and Flame Heat Transfer Correlations in Corner-Wall and Corner-Wall-Ceiling Configurations", *Interflam '96*, Inter Science Communications Limited, London, UK, 1996, pp. 179 to 188.

NIST-114
(REV. 11-94)
ADMAN 4.09

U.S. DEPARTMENT OF COMMERCE
NATIONAL INSTITUTE OF STANDARDS AND TECHNOLOGY

(ERB USE ONLY)

ERB CONTROL NUMBER | DIVISION

MANUSCRIPT REVIEW AND APPROVAL

PUBLICATION REPORT NUMBER | CATEGORY CODE

NIST-GCR-98-756

INSTRUCTIONS: ATTACH ORIGINAL OF THIS FORM TO ONE (1) COPY OF MANUSCRIPT AND SEND TO THE SECRETARY, APPROPRIATE EDITORIAL REVIEW BOARD.

PUBLICATION DATE | NUMBER PRINTED PAGES

August 1998

TITLE AND SUBTITLE (CITE IN FULL)
Analysis of the ISO 9705 Room/Corner Test: Simulations, Correlations and Heat Flux Measurements

CONTRACT OR GRANT NUMBER
60NANB2D1266

TYPE OF REPORT AND/OR PERIOD COVERED
Thesis

AUTHOR(S) (LAST NAME, FIRST INITIAL, SECOND INITIAL)
Dillon, S.E.
University of Maryland
College Park, MD 20742

PERFORMING ORGANIZATION (CHECK (X) ONE BLOCK)

☐ NIST/GAITHERSBURG
☐ NIST/BOULDER
☐ JILA/BOULDER

LABORATORY AND DIVISION NAMES (FIRST NIST AUTHOR ONLY)

SPONSORING ORGANIZATION NAME AND COMPLETE ADDRESS (STREET, CITY, STATE, ZIP)

U.S. Department of Commerce
National Institute of Standards and Technology
Gaithersburg, MD

PROPOSED FOR NIST PUBLICATION

☐ JOURNAL OF RESEARCH (NIST JRES)
☐ J. PHYS. & CHEM. REF. DATA (JPCRD)
☐ HANDBOOK (NIST HB)
☐ SPECIAL PUBLICATION (NIST SP)
☐ TECHNICAL NOTE (NIST TN)

☐ MONOGRAPH (NIST MN)
☐ NATL. STD. REF. DATA SERIES (NIST NSRDS)
☐ FEDERAL INF. PROCESS. STDS. (NIST FIPS)
☐ LIST OF PUBLICATIONS (NIST LP)
☐ NIST INTERAGENCY/INTERNAL REPORT (NISTIR)

☐ LETTER CIRCULAR
☐ BUILDING SCIENCE SERIES
☐ PRODUCT STANDARDS
☒ OTHER NIST-GCR

PROPOSED FOR NON-NIST PUBLICATION (CITE FULLY) ☐ U.S. ☐ FOREIGN

PUBLISHING MEDIUM

☒ PAPER
☐ DISKETTE (SPECIFY)
☐ OTHER (SPECIFY)
☐ CD-ROM

SUPPLEMENTARY NOTES

ABSTRACT (A 2000-CHARACTER OR LESS FACTUAL SUMMARY OF MOST SIGNIFICANT INFORMATION. IF DOCUMENT INCLUDES A SIGNIFICANT BIBLIOGRAPHY OR LITERATURE SURVEY, CITE IT HERE. SPELL OUT ACRONYMS ON FIRST REFERENCE.) (CONTINUE ON SEPARATE PAGE, IF NECESSARY.)

A simulation model is implemented in order to predict the fire performance of materials in the ISO 9705 Room-Corner Tests. These materials were tested by the L S Fire Laboratories of Italy, and the data they provided is Analyzed in this report. A method was established to define materials properties including the heat of combustion, heat of gasification, thermal inertia, ignition temperature and the total energy released per unit area. These methods were developed from refinements in a theoretical model of ignition and in resolving time dependent effects in the Cone Calorimeter. The materials examined consist of some of the most difficult to analyze because they melt, drip, expand and de-laminated from the wall and ceiling configuration of the room-corner test. Corrections have been included in the simulation modeling to account for these effects. The correction involves reducing the total energy content per unit area of the material to accordingly reduce its contribution as a wall-ceiling oriented element. An empirical correlation based on a linearized upward flame spread model is shown to provide excellent comparison to the flashover time in the full-scale ISO test. Accurate heat flux measurements from the ignition burner at an energy release of 100 and 300 kW were made from full-scale room-corner tests. Corrections to these heat flux measurements provide the incident heat flux from the burner fire plume and from a combination of the plume and the thermal feedback of the heated room. Detailed heat flux distributions along the walls and ceiling in the vicinity of the ignition burner are provided.

KEY WORDS (MAXIMUM OF 9; 28 CHARACTERS AND SPACES EACH; SEPARATE WITH SEMICOLONS; ALPHABETIC ORDER; CAPITALIZE ONLY PROPER NAMES)

corner tests; fire data; fire growth; fire models; gas burners; heat flux; material properties

AVAILABILITY

☒ UNLIMITED ☐ FOR OFFICIAL DISTRIBUTION - DO NOT RELEASE TO NTIS
☐ ORDER FROM SUPERINTENDENT OF DOCUMENTS, U.S. GPO, WASHINGTON, DC 20402
☒ ORDER FROM NTIS, SPRINGFIELD, VA 22161

NOTE TO AUTHOR(S): IF YOU DO NOT WISH THIS MANUSCRIPT ANNOUNCED BEFORE PUBLICATION, PLEASE CHECK HERE.

☐

ELECTRONIC INFORMS